DEVELOPMENT OF A NOVEL BREATHALYZER FOR THE DETECTION OF SARS-COV-2 AND OTHER RESPIRATORY ILLNESSES

By

LIAM JOHN WHITE

A dissertation submitted to the

School of Graduate Studies

Rutgers, The State University of New Jersey

In partial fulfillment of the requirements

For the degree of

Doctor of Philosophy

Graduate Program in Mechanical and Aerospace Engineering

Written under the direction of

German Drazer and Edward P. DeMauro

And approved by

_____

_____

_____

_____

New Brunswick, New Jersey

October 2025

ABSTRACT OF THE DISSERTATION

Development of a Novel Breathalyzer for the Detection of SARS-CoV-2 and Other Respiratory Illnesses

by LIAM JOHN WHITE

Dissertation Director: German Drazer and Edward P. DeMauro

A respiratory-illness detecting breathalyzer inspired by a trap impactor has been developed to collect viral-particle-containing water droplets. A label-free nanowell-based impedance sensor was used to detect the binding between SARS-CoV-2 spike proteins and antibodies as the sensing platform for the breathalyzer. The sensor demonstrated a 1.5 pM limit of detection and displayed the ability to differentiate between SARS-CoV-2 and MERS-CoV spike proteins used with SARS-CoV-2 antibodies. After characterizing the sensing platform, the trap impactor was designed to optimize the amount of virus deposited on the sensor surface. Multiple generations of trap impactors were developed and characterized by their removal and trap efficiencies. Experiments were performed using water and olive oil droplets as test aerosols, and constructed efficiency curves demonstrated that increasing the trap ratio (the trap opening clearance divided by the depth) resulted in an increase in trap efficiency, with the optimal tested impactor achieving 94%. However, some impactor designs displayed efficiencies that decreased with increasing particle inertia, which was unexpected. To explain this phenomenon and to better understand what drives particle capture inside trap impactors, the axisymmetric flow field was investigated using high-speed shadowgraphy, particle image velocimetry, and hotwire anemometry. The flow field investigation revealed that decreasing the trap ratio resulted in increases in turbulent

kinetic energy, and the regions of high turbulence could alter particle trajectories, preventing them from entering the trap and decreasing the trap efficiency. Numerical simulations were performed using ANSYS Fluent to construct the flow field inside the particle traps that could not be viewed experimentally. The simulations demonstrated that the increase in turbulent kinetic energy was due to the wall jet escaping from the particle trap mixing with the incoming jet, and was exacerbated for decreasing trap ratios. The experimental flow fields, turbulent kinetic energy fields, and power spectral densities were used to validate the simulations, with fair agreement. However, more work is needed to improve the simulations. The reduction in trap efficiency for low trap ratios is hypothesized to be due to the wall jet separating from the surfaces of the trap and mixing with the incoming jet for small trap opening clearances. Also, further reducing the trap opening clearance can create regions of enhanced shear between the edge of the jet and the trap entrance channel walls that can break up the jet structure. The optimal trap geometry is proposed to reduce jet mixing and is obtained by reducing the trap depth, increasing the trap diameter, and rounding the trap edges.

ACKNOWLEDGMENTS

I would like to first thank Professor German Drazer and Professor Edward P. DeMauro for their supervision and guidance during my five years working in their labs. I would also like to thank the committee members, Professor Hao Lin, and Professor Jeffrey Zahn, for their support. Special acknowledgment is also given to Milan Simonovic for his help in the machine shop. I'd like to thank my labmates and friends for their support and friendship gained over complaining about experiments, devouring all-you-can-eat sushi, and, at times, playing too much foosball. Special acknowledgement is given to Tomas Rojas Carvajal for his help with the experimental setup for the particle image velocimetry experiments. Also, my PhD experience would not have been complete without the Project SUPER and JJ Slade undergraduate students I mentored in our labs, Samantha Welsh and Manny Correia.

I would like to thank my mother, Shirley, and my sister, Meghan, for their love and support. This work could not have been done without a strong foundation at home.

A very special thank you is given to my wife, Isabella, who has supported me through my entire PhD journey. At times when experiments were not going according to plan and I found myself in the lab until late at night, you would stay awake for me and always greet me at the door with a warm meal. Marrying you was the easiest decision of my life, but I never thought it would happen while I was still in school! I cannot thank you enough for all of the love and support you have given me and for how patient you have been over the past five years.

Lastly, I need to thank my father, who taught me the value of hard work and how to be a man. Dad, you are the only person I have ever wanted to impress, and I think about you every day.

TABLE OF CONTENTS

LIST OF TABLES

LIST OF FIGURES

CHAPTER 1
AEROSOL SCIENCE AND SARS-COV-2

1.1 Introduction

1.1.1 Basic Concepts in Aerosol Science

Suspended in the air are microscopic particles invisible to the naked eye. These particles can be solid or liquid and are generated from vehicle exhaust, cooking, arc welding, granite cutting, nebulizers, sneezing, coughing, breathing, and talking, among other sources. Solid or liquid particles ranging in size between 0.001 to 100 μm are called aerosol particles or particulate matter. Aerosols are of particular interest in the areas of atmospheric sciences, combustion, manufacturing, and airborne pathogens. These particles can maintain their structural integrity from a few seconds to a few years [1]. Interest in aerosol science and the impact of particulate matter on human health has increased in recent years due to the effects of industrialization, climate change, and especially airborne pathogens due to the SARS-CoV-2 (Covid-19) pandemic.

One of the most important characteristics of aerosols is their size. Aerosol particle sizes can range in orders of magnitude, affecting the time they are suspended in the air and their potential impact on the human respiratory system. Solid particles have a large variety of shapes and have a range of densities depending on the particle's porosity. The dynamic shape factor, χ, characterizes the geometry of nonspherical particles. It is the ratio of the resistive drag force of the nonspherical particle to that of the spherical particle with the same volume and velocity. The equation for the drag force on a spherical particle is shown below,

$$\mathrm{F_d} = \frac{3\pi\mu\mathbf{V}\mathrm{d}}{\mathrm{C_c}}, \tag{1.1}$$

where μ is the fluid dynamic viscosity, V is the relative fluid velocity, d is the particle diameter, and C_c is the Cunningham slip correction factor. The dynamic shape factor is then given by

$$\chi = \frac{F_d}{3\pi\mu V d_e}, \tag{1.2}$$

where d_e is the equivalent particle diameter for a particle with the same volume. Some common shape factors are shown below in Table 1.1.

Shape	**Dynamic Shape Factor, χ**
Sphere	1.00
Cube	1.08
Cylinder (L/D = 4)	
axis horizontal	1.32
axis vertical	1.07
Cluster of Spheres	
2 chain	1.12
3 chain	1.27

Table 1.1: Dynamic shape factors for different particles [1].

Liquid droplets are typically characterized as spheres with densities equivalent to the original media.

The geometric diameter is not the only length scale used in aerosol science, as the aerodynamic and Stokes diameters are two commonly used equivalent diameters [1]. The aerodynamic diameter is the diameter of a spherical particle with the density of water (1000 kg/m^3) that has the same settling velocity as the particle of interest. The Stokes diameter is the diameter of a sphere with the same density and settling velocity as the particle. Aerodynamic diameter is more commonly used for filtration and separation devices. For spherical

particles, the aerodynamic diameter is given below,

$$d_a = d_p \sqrt{\frac{\rho_p}{\rho_0}}, \tag{1.3}$$

where d_p is the particle geometric diameter, ρ_p is the particle density, and ρ_0 is the density of water.

Aerosol concentration is the collection of aerosols suspended in a medium, and it is divided into number and mass concentration. Aerosol concentration is routinely used when discussing the air quality through the air quality index, or AQI. The AQI is a combination of the mass concentrations of multiple air quality monitors that can affect respiration, such as particle pollutants, Ozone, Carbon Monoxide, and Nitrogen Dioxide, among others [2, 3]. An AQI less than 100 is considered acceptable, whereas values from 101-150 are considered ”unhealthy for sensitive groups,” and an AQI greater than 200 is very unhealthy for all individuals. The number concentration, like the AQI, is the number of particles in a given volume of gaseous media, and the mass concentration is the total mass of the aerosols in the given volume. Diving deeper into the number and mass concentrations is the particle distribution. Monodisperse distributions contain particles of one uniform size, whereas polydisperse distributions have a range of particle sizes. Devices that take advantage of differences in particle inertia can separate particles based on their size.

1.1.2 Inertial Impactors

Inertial impactors are devices that separate particles from a flow stream based on size. They are used in airborne particle sampling, air quality monitoring, and biological sample filtering, among other applications [4, 5, 6, 7, 8]. Impactors use a converging nozzle to accelerate a flow and place an obstacle in its path, such as a flat plate, to remove particles above a specific size. Consider the motion of aerosol particles transported in a flow stream. Particles with high inertia are less likely to follow the flow when an obstacle is encountered and may even collide with it. The dimensionless number characterizing a particle’s

inertia is known as the Stokes number and will be explained in further detail in chapter 3. Impactors use a nozzle to accelerate the flow impinging on a flat plate, and particles with sufficiently high inertia will collide with it shown in Figure 1.1

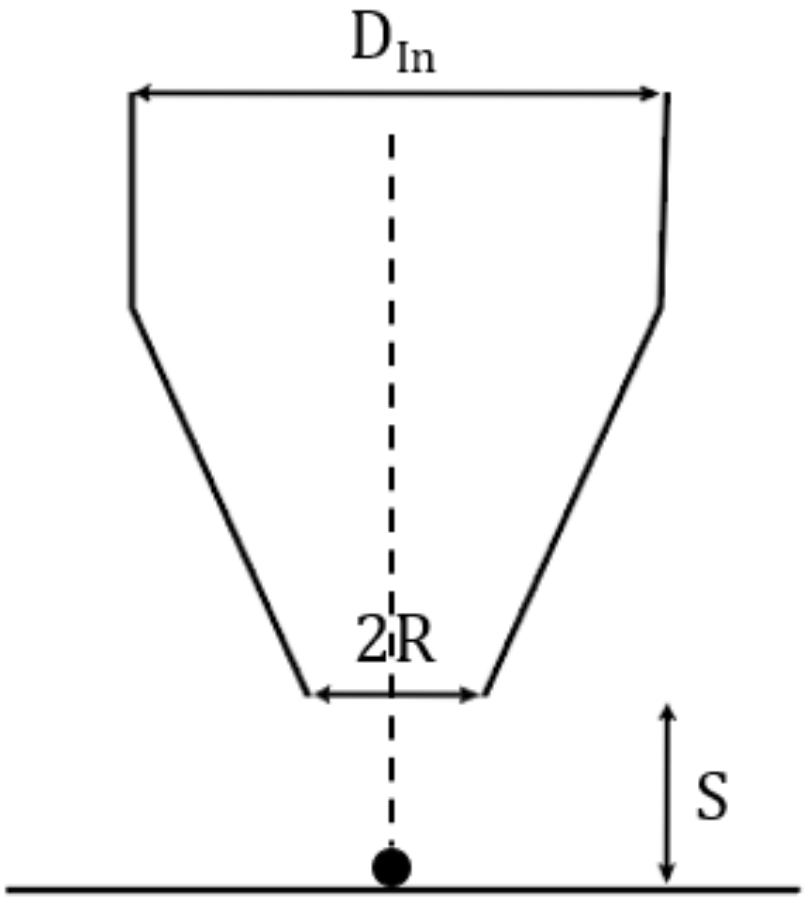

Figure 1.1: Schematic of flat plate inertial impactor.

where D_{In} is the inlet diameter, 2R is the outlet diameter, and S is the distance between the end of the nozzle and the impaction plate.

The first impactor was reported to have been developed in 1860 by Pouchet Aeroscope for investigating airborne particles and diseases by looking at the collected particles under a microscope [9]. The first impactors used flat plates to collect particles removed from the flow, and it was not until 1945 that a new development was introduced, known as a cascade impactor, which, by integrating multiple impactors in succession could provide informa-

tion on the particle size distribution [10]. In fact, tuning the geometry of the successive test stages could remove particles of various sizes from the flow at different sections and give information about the particle size distribution depending on the particles removed at each stage. Many studies have been performed using single-stage and cascade impactors, with the impactor performance being graded by its efficiency, which is the percentage of particles removed from the flow [5, 6, 8, 11, 12, 13, 14, 15, 16, 17, 18, 19, 20, 21].

The trap impactor is a variation of the flat plate impactor introduced in 1988 by Biswas and Flagan [22] (see Figure 1.2). The trap is a recessed region added to the center of a flat plate where particles are expected to be collected. This configuration allows particles to be trapped in a collection site for easier examination in applications such as biosensors or air and water quality monitors [23, 24, 25, 26, 27, 28, 29, 30]. However, the trap impactor configuration increases the number of geometric parameters that may affect efficiency.

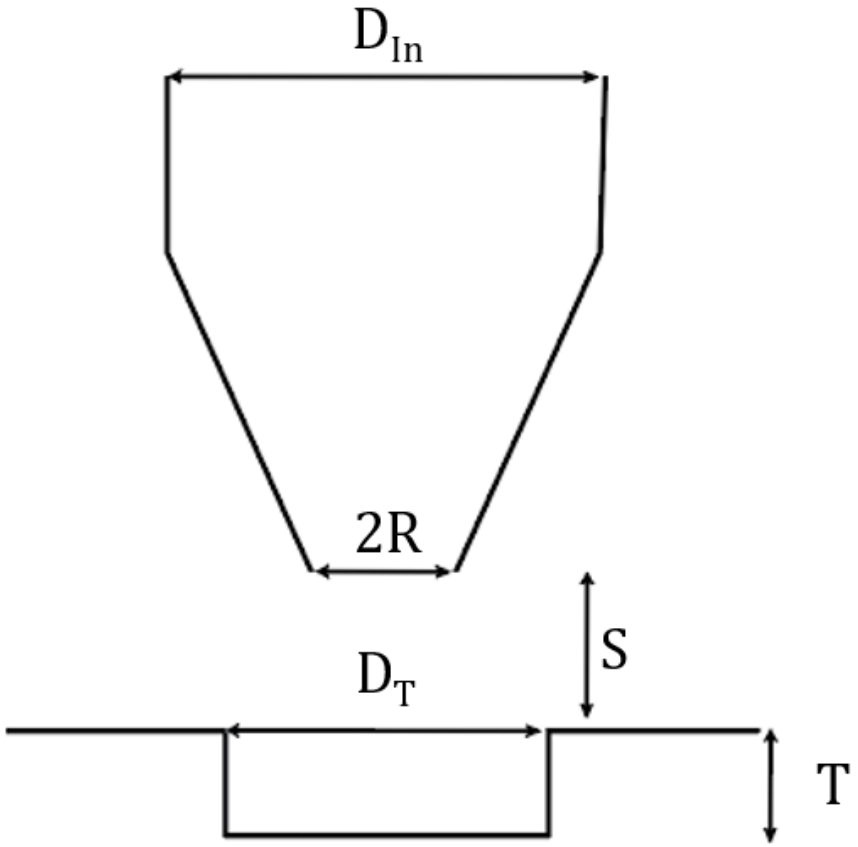

Figure 1.2: Trap impactor schematic.

Here, D_T is the trap diameter and T is the trap depth. Typical non-dimensional geometric parameters for trap impactors are $D_T/2R$, called the diameter ratio; S/2R, known as the gap ratio; and T/2R, known as the depth ratio. In this thesis, we will characterize the trap geometry by the trap ratio (TR), which is the trap opening clearance divided by the trap depth, and will be discussed in chapter 4.

1.2 Motivation

1.2.1 Impact of the Covid-19 Pandemic

The Covid-19 pandemic swept across the world in 2020, and the novel respiratory illness has since claimed the lives of 7.1 million people worldwide [31]. Measures were taken

to limit the spread of the disease through mask mandates, social distancing, and, eventually, lockdowns. Aerosols generated in the respiratory tract drive the disease's spreading mechanism [32]. When people speak, sing, cough, or sneeze, these laced water droplets are expelled through the mouth and nose and ejected into the air.

Respiratory aerosols are classified by their generation site, and the smaller the droplets, the deeper in the respiratory tract they are produced [33, 32, 34]. Bronchiolar aerosols are generated through the bronchiole fluid film burst mechanism, where a liquid bridge in terminal bronchioles is fragmented into droplets during inhalation and carried into the alveoli [33, 35]. Bronchial aerosols are produced on exhalation when high-velocity expelled air disturbs the mucous lining of the bronchioles and shears the mucous into fine aerosols. Laryngeal aerosols are produced during speech through vocal fold vibrations [33]. Oral aerosols are produced from saliva between the lips and epiglottis [33].

Droplets larger than 100 μm will have more mass and settle onto surfaces within 1 m of the emitter [32]. Surfaces contaminated by exhaled droplets are termed fomites. These droplets can spread the disease only if the subjects are within 0.2 m while talking or within 0.5 m while coughing [32, 36]. Smaller droplets, however, will stay suspended in the air for longer periods of time and are more likely to be inhaled by others and spread the disease. Figure 1.3 below summarizes the spreading mechanism of Covid-19 and the generation sites of the different types of aerosols.

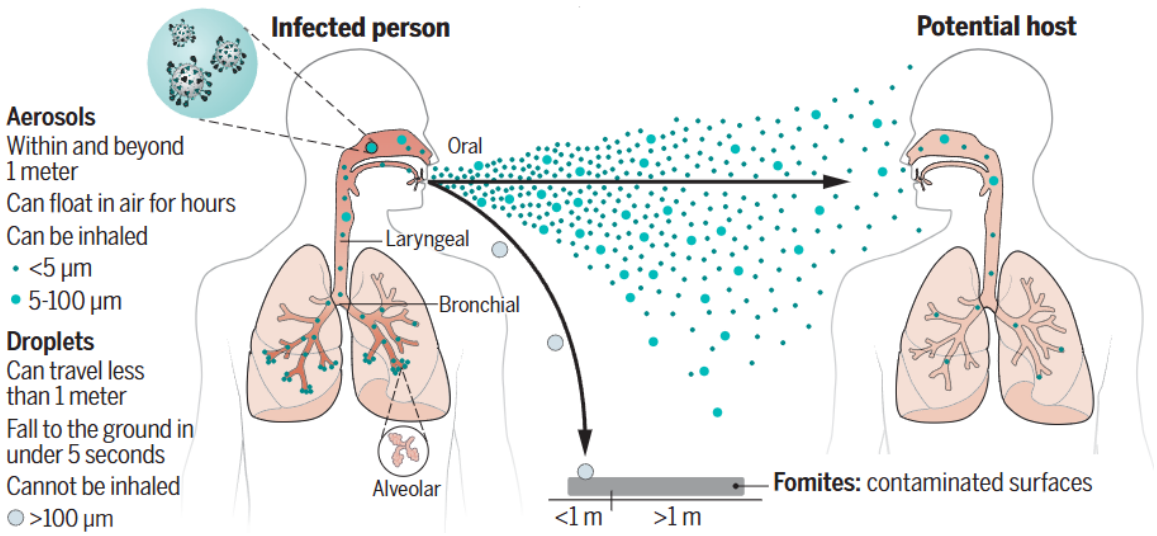

Figure 1.3: Schematic of exhaled aerosol transmission mechanisms. From [32]. Reprinted with permission from AAAS.

Multiple studies have found that viral load varies with droplet size, with smaller particles having a higher concentration of virus [37, 38, 39, 40, 41, 42]. Specifically, it has been shown that particles smaller than 5 µm can contain up to 8.8 times the number of viral copies contained in larger particles [38]. Studies investigating the particle size distribution in exhaled breath have also demonstrated that particles < 5 µm have a much higher number concentration than larger particles [34, 43, 44]. The combination of small droplets having a long residence time in the air, a high viral load, and the largest number concentration all potentially work in concert to proliferate the spread of respiratory illnesses.

One of the paramount tasks to slow down or stop the spread of the virus was to develop devices to detect the presence of Covid in individuals. Multiple tests were created utilizing RNA/DNA molecular analysis, biosensors, antibody/antigen testing, and clinical imaging [45, 46, 47, 48]. Still, all had drawbacks, such as invasive and uncomfortable procedures, long collection times, high sample volumes, and poor portability [49, 50, 51, 52, 53].

1.3 Novel Breathalyzer Trap Impactor

To address these issues, this thesis proposes a novel breathalyzer using a trap impactor to collect viral Covid particles encased in exhaled aerosols (see Figure 1.4).

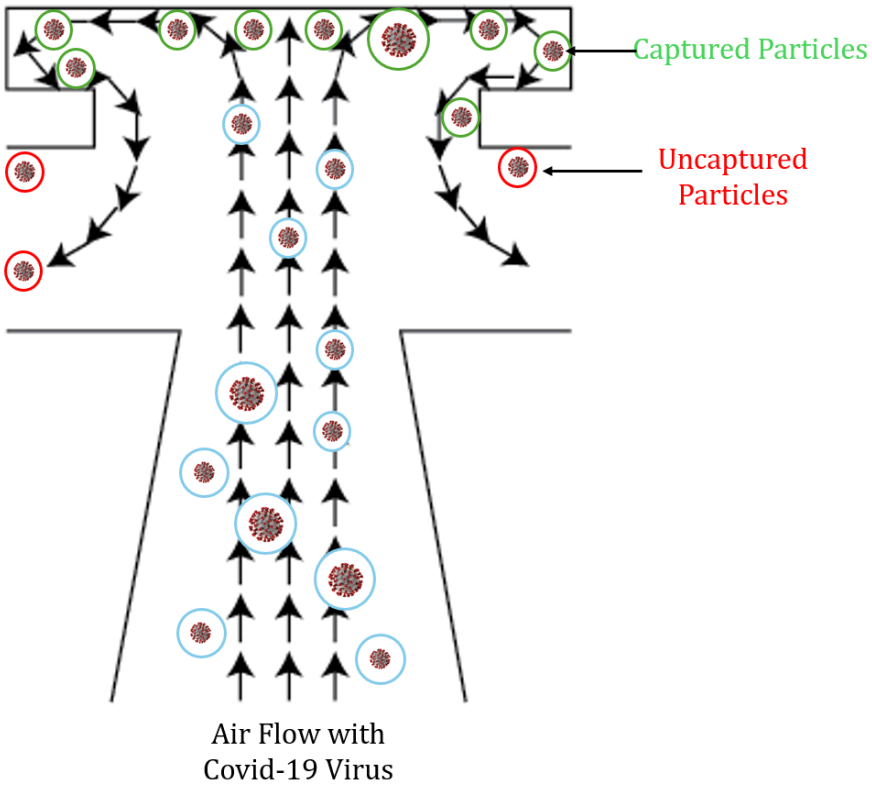

Figure 1.4: Schematic of the trap impactor used for collecting water droplets encasing Covid-19 virus.

This solution is easy to use, especially for those with difficulty self-administering tests, as users only blow through the inlet and do not have to subject themselves to painful or uncomfortable collection methods.

A flat plate is placed after the nozzle with a cavity in the center acting as the trap. Some particles in the flow will enter the trap, deposit on its surfaces, and be collected, whereas others may not enter the trap or may enter and exit the trap, and are missed. Unlike other impactors, the main priority of this design is not only to remove particles from the flow but to optimize for deposition inside the trap. Hence, the viral particles would be readily

available for detection. The geometry is tailored to maximize capture for inlet pressures similar to human exhalation.

To first test the viability of the trap impactor as a breathalyzer, we characterized a label-free nanowell-based impedance sensor that can detect the binding between a target disease antibody and antigen. This sensor is placed inside the particle trap, and the transported viral particles are deposited on the sensor for detection. Different impactor nozzle designs were then optimized to increase particle inertia and enhance particle capture. The acceleration nozzle is designed to increase particle inertia thus enhancing particle deposition in the trap, and at the same time, it should maintain sufficiently high flow rates to increase the total amount of virus available for capture. The nozzles were modeled and 3D printed, and experimental flow rates are compared with predictions. Experiments with varying trap geometries were then performed to determine the nozzle and trap combination that maximizes efficiency. Preliminary experiments using water droplets resulted in potential effects from evaporation making the interpretation of the results challenging. To reduce these effects, olive oil droplets were used instead. The olive oil particle distribution is characterized through two methods: microscopy after allowing a cloud of droplets to settle under gravity, and using an optical particle sizer. A model for predicted efficiency for the trap impactors was developed from impactor theory, experimental efficiency data in the literature, and the measured particle distributions. We determined that modifying the trap impactor geometry, specifically increasing the trap ratio, is a critical parameter for maximizing trap efficiency. Interestingly, designs with low trap ratios performed poorly even when particles had high inertia, which was not thoroughly investigated in the literature. To determine what could be responsible for the poor impactor performance, the flow field between the nozzle exit and the trap was experimentally examined to determine potential mechanisms responsible for the decrease in efficiency. Finally, numerical simulations were conducted to develop an understanding of the flow field inside the particle traps that could not be visualized with experiments.

The nanowell sensor is characterized in chapter 2. The impactor flow field and particle dynamics are discussed in chapter 3. The experimental setup, design, and methodology for the impactor efficiency characterization are explained in chapter 4. Impactor efficiency results using water droplets and olive oil particle size distributions are explored in chapter 5. The prediction model and experimental efficiency results for impactors using olive oil droplets as test aerosols are detailed in chapter 6. The experimental setup for the impactor flow field investigation is described in chapter 7. High-speed shadowgraphy, particle image velocimetry, and hotwire anemometry were used to study the impactor flow field, and the results are presented in chapter 8. Numerical simulations studying the flow field in the entire impactor, with emphasis on the particle trap, are explored in chapter 9. Trap efficiency reduction mechanisms are explored in chapter 10, and we introduce the optimal trap geometry. Finally, in chapter 11, the conclusions of this dissertation are summarized, and future work is proposed.

CHAPTER 2
NANOWELL SENSOR FOR ANTIBODY/ ANTIGEN BINDING DETECTION

2.1 Introduction

The respiratory illness detection mechanism for the breathalyzer is based on a microfabricated, label-free nanowell impedance sensor previously used to detect stress hormones and cytokines in serum [54, 55, 56, 57, 58, 59]. In order to assess the potential of this sensor to detect SARS-CoV-2, we have tested its performance using SARS-CoV-2 spike proteins suspended in either Phosphate-Buffered-Saline (PBS) or artificial saliva, in independent experiments.

2.2 Materials and Methodology

2.2.1 Impedance Sensor Methodology

The sensor is a 5×5 array of nanowells microfabricated over a 20 µm × 20 µm area consisting of two opposing gold electrodes separated by an aluminum oxide layer. Antibodies are first injected and adsorbed on the surface of the nanowells by applying an AC electric field. A sample protein in solution is then introduced, and the impedance between electrodes is monitored through lock-in amplifiers to determine the presence of the antigen that corresponds to the adsorbed antibodies, that is the formation of antibody-antigen pairs. The schematic cross-section view of a single well in the array is shown in Figure 2.1a, indicating the two gold layers acting as electrodes and separated by a thin dielectric layer of aluminum oxide. Figure 2.1b shows antibodies adsorbing to the surface of a nanowell in the presence of the AC field. As the antigens in solution are introduced to the sample and bind to the antibodies (Figure 2.1c), the impedance across the electrodes increases. The equivalent circuit model is shown in Figure 2.1d and e, where $\mathrm{R_s}$ is the solution resis-

tance, $\mathrm{R_s}$ is the polarization resistance, $\mathrm{C_{dl}}$ is the double-layer capacitance, and $\mathrm{C_{oxide}}$ is the oxide layer capacitance. The nanowell characterization is discussed in detail in previous research by Mahmoodi et al [59]. Measurable increases in impedance indicate the presence of antigen-antibody pairs after introducing the test sample. Although the impedance changes are obtained by measuring current, the first stage of the lock-in amplifier is a mixer that compares the reference voltage with the signal measured. Thus, we first need to convert the signal to a voltage for the lock-in amplifier to process the data further. The circuit topology is shown in Figure 2.1e. The signal is converted to a voltage after passing through the current amplifier. Therefore, in some figures, voltage is used as the unit for presenting preliminary results. However, since voltage depends on the amplifier gain, impedance is a more intrinsic and normalized property of the sensors themselves. Consequently, in most figures, voltage values are converted to impedance, expressed in units of Ω, using the formula below,

$$\mathrm{Z} = \frac{0.1}{2\sqrt{2} \cdot \mathrm{V_{output}} \times 10^{-6}}.$$

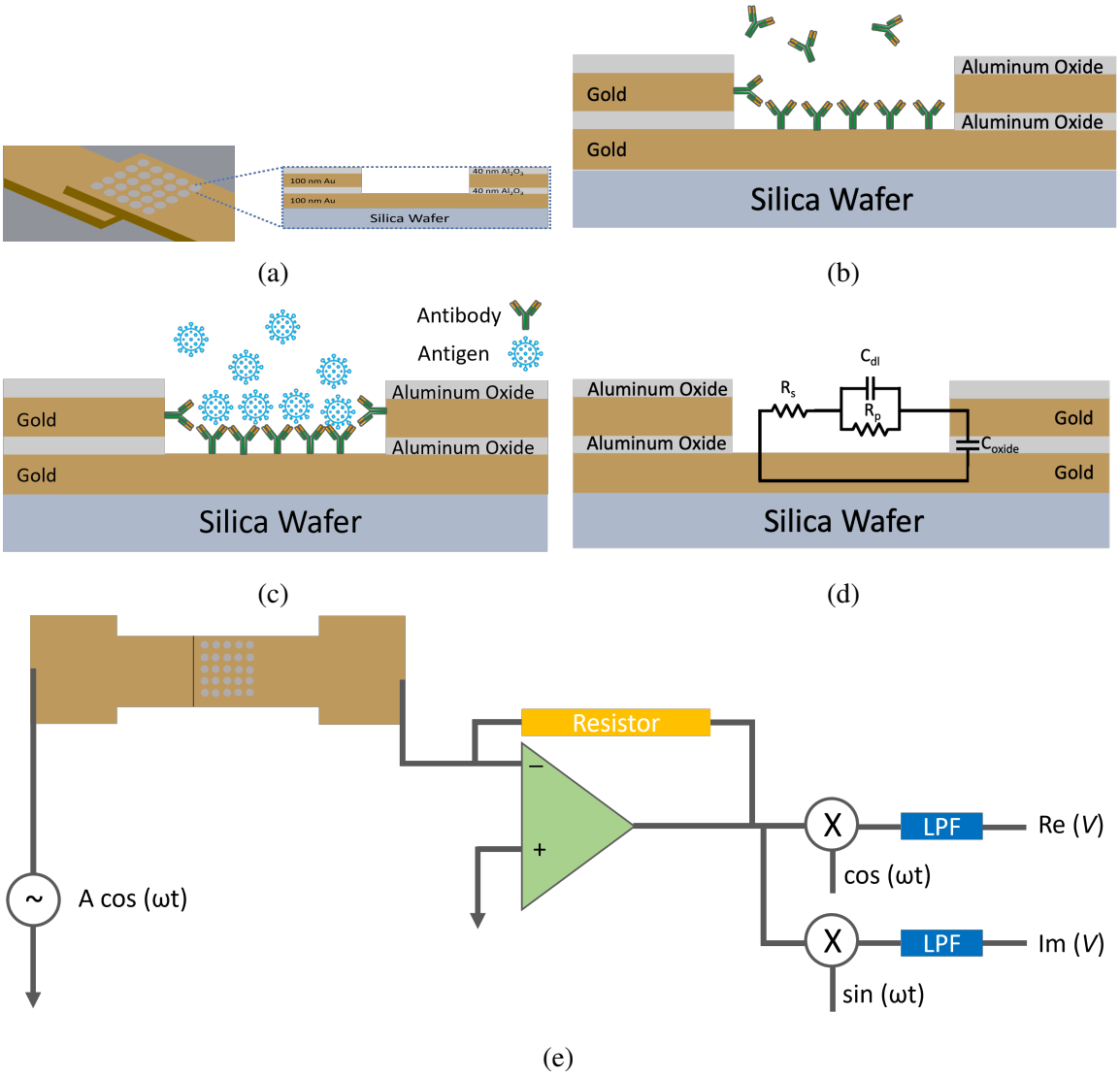

Figure 2.1: (a) Cross-sectional view of a single nanowell. (b) Cross-sectional view of single nanowell adsorbing antibodies. (c) Cross-sectional view of the nanowell adsorbing target protein. (d) Equivalent circuit model. (e) Equivalent circuit of the measurement platform using a lock-in amplifier.

2.2.2 Sensor Fabrication

The nanowell sensor fabrication process is explained in detail in Ref. [27], but a brief description is as follows and is shown in Figure 2.2a. The sensor is prepared on 7.62 cm-diameter, 500 µm-thick fused silica substrates. Two alternating layers of gold and aluminum oxide were deposited onto the wafer through e-beam and atomic layer deposition,

respectively, and are shown as Steps 1-4. The first and second layers of gold overlap in a small 20 µm $\times$ 20 µm area, and they act as the electrodes in the sensor. After depositing the four metal layers, the wells are patterned in the overlapping area by multiple wet etching steps that penetrate through the top three metal layers and down to the original gold layer, as shown in Step 5. The antibodies, antigen, and buffer solutions reside inside the wells (shown in zoomed-in view of Step 5), where the lock-in amplifier measures the impedance across the two gold layers acting as electrodes. A polydimethylsiloxane fluidic cell is glued to contain the liquids. To connect the impedance sensor to other electronic equipment, electrically conductive wires are attached to the gold layers by conductive epoxy , and the completed sensor is shown in Figure 2.2b. The zoomed-in images are of the microscopic view of the patterned nanowell array.

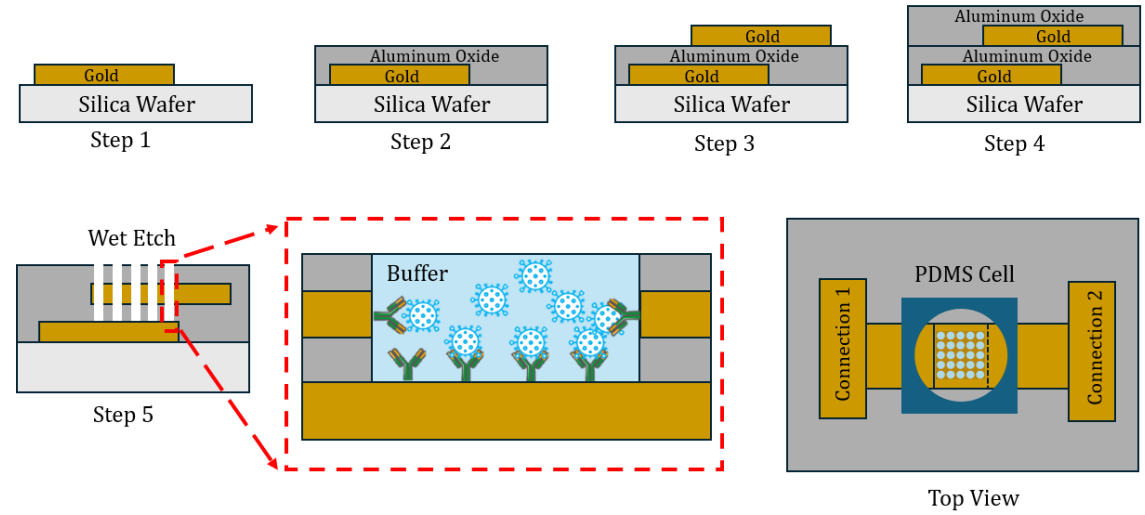

(a)

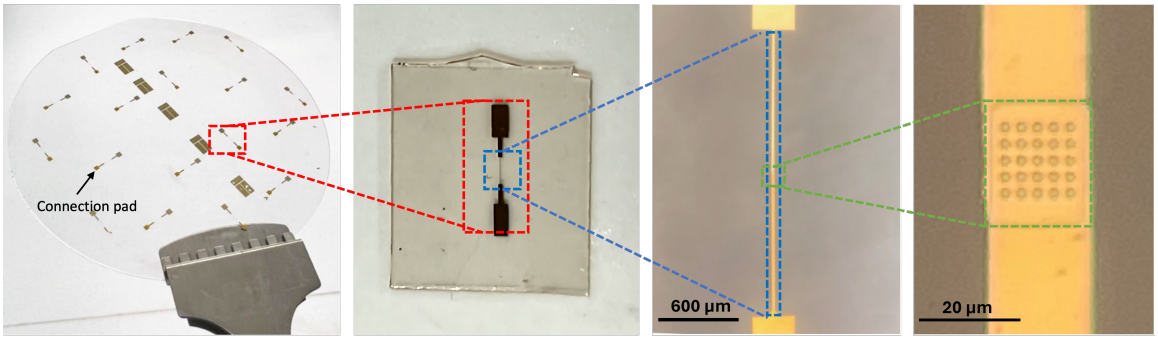

(b)

Figure 2.2: (a) Sensor fabrication process - Step 1: first gold layer deposition, 2: first aluminum oxide layer deposition, 3: second gold layer, 4: second alumium oxide layer, 5: wet etch down to first gold layer; (b) From left to right: 1. View of a fabricated wafer; 2. Single nanowell sensor; 3. Microscope view of electrodes; 4. Microscope view of 5 $\times$ 5 well-shaped arrays.

2.3 Experimental Setup

2.3.1 Experimental Procedure

The device detects binding between target antibodies and antigens by monitoring the changes in impedance between the two gold electrodes in real-time. Numerous sensors are used in the experiments discussed in this dissertation. The following is the step-by-step procedure to record the change in impedance. Note that, after each step, the sensor is allowed to rest, undisturbed, for 10 minutes.

First, the sensor is connected to the lock-in amplifier and is supplied with a 100 mV, 1 MHz AC signal. Then, 5 μL of 1X PBS are injected into the empty nanowell to create the liquid environment. Next, 3 more μL of 1X PBS are added. Then, 3 μL of the target antibodies are injected. If the antibodies adsorb successfully, an increase in the impedance should be recorded by the lock-in amplifier. The power is then turned off and all liquid is removed from the nanowell via pipette. The sensor is therefore considered dry, with the antibodies still adsorbed to the sensor walls. The power is then restored, and 5 μL of 1X PBS are added, followed by 3 more μL to recreate the liquid environment. Lastly, 3 μL of the target antigen prepared at the concentration of interest are injected into the sensor to record the change in impedance over ten minutes.

We used a potentiostat to characterize the impedance spectrum of the biosensor devices [56]. We performed impedance measurement tests ranging from 10 Hz to 3 MHz on numerous sensors and observed that beyond 100 kHz, the impedance reaches a constant value and becomes dominated by resistance. Thus, we choose to operate at a frequency of 1 MHz to monitor changes in ionic resistance due to antigen binding [56].

2.3.2 Reagent Preparation

Experiments utilize monoclonal and polyclonal SARS-CoV-2 antibodies. Figure 2.3 shows the sensor response to the adsorption of the monoclonal and polyclonal antibodies in artificial saliva. We can conclude that there is no significant difference in the types of antibodies used, as the response curves behave similarly and overlap. Therefore, both types of antibodies are used throughout this dissertation.

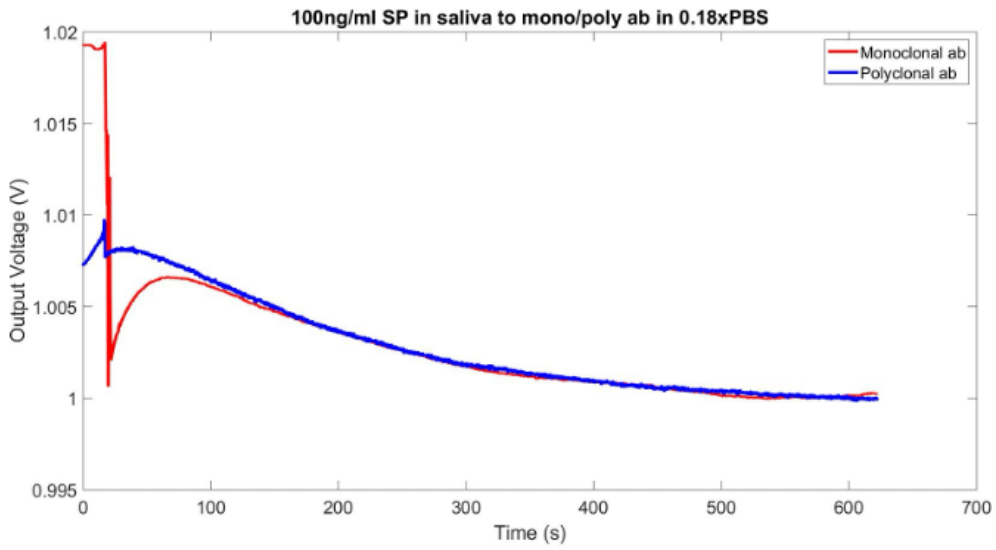

Figure 2.3: Comparison of output voltage in response to monoclonal and polyclonal antibodies. Due to the curves having very similar behavior and overlapping, we conclude there is no significant difference between the types of antibodies used.

The antibodies were prepared in a concentration of 100 µg/mL first using 1X PBS, and then later in 0.18X PBS, as will be explained in section 2.4. The target protein was the wild-type SARS-CoV-2 spike protein prepared in artificial human saliva, having concentrations ranging from 0 ng/mL to 1000 ng/mL (0 - 7.5 nM, spike protein molecular weight = 134 kDa). After characterizing the sensor with SARS-CoV-2 antibodies and spike protein, SARS-CoV-2 antibodies were used with MERS-CoV spike proteins to demonstrate protein specificity. These experiments determined if the sensor can differentiate between the target protein (SARS-CoV-2) and a different protein that should not bind with the antibodies. The specificity tests were performed using the MERS-CoV spike protein prepared in 0.18X PBS at a 1000 ng/mL concentration with SARS-CoV-2 antibodies prepared in 0.18X PBS.

Figure 2.4 displays the results from preliminary experiments of SARS-CoV-2 spike protein prepared in 0.18X PBS and artificial saliva buffers binding with SARS-CoV-2 antibodies prepared in 0.18X PBS. The behavior of the output voltages over time for the four curves is similar, as after the sharp decrease in voltage near 20s, the output voltage slowly decreases before slightly increasing at the end of the experiments. The artificial saliva

output voltage does not have a markedly different behavior than the 0.18X PBS results, and thus, we determined that either 0.18X PBS or artificial saliva could be interchangeable protein buffers.

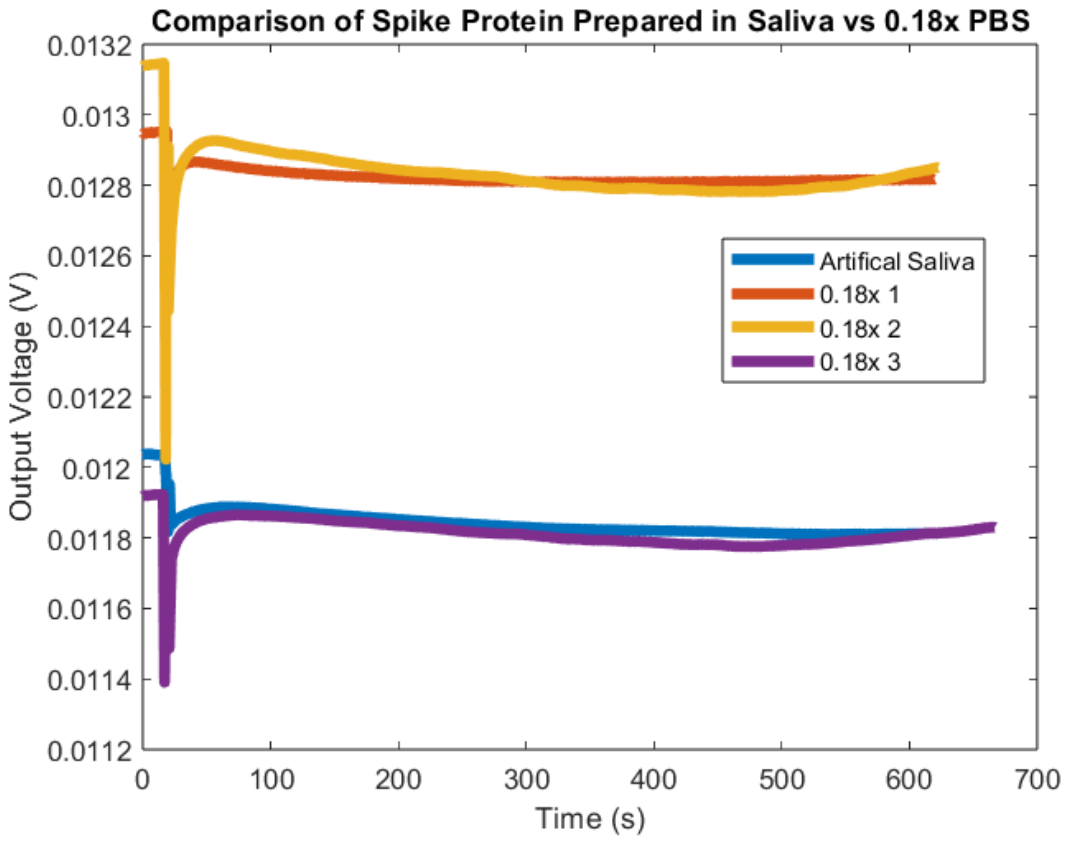

Figure 2.4: Comparison between SARS-CoV-2 spike protein antigen prepared in artificial saliva and 0.18X PBS. The antigen prepared in artificial saliva, shown in blue, has a similar output to the antigens prepared in 0.18X PBS.

2.3.3 Real-Time Measurments and Impedance Change Methodology

As mentioned previously, the lock-in amplifier measures the change in impedance in real-time. Figure 2.5 displays the real-time impedance for the addition of 1X PBS to the empty sensor (red) to create the liquid environment, antibodies (blue), and 1000 ng/mL SARS-CoV-2 spike-protein antigen (yellow) over a ten-minute period. The PBS curve shows a slowly decaying impedance due to the increased conductivity generated by the PBS. The antibody and antigen curves display a sharp increase in impedance, referred to as

impedance shifting, at approximately 25s. This increase is due to the pipette tip disturbing the sensor as the solution is injected. After the sharp rise, the impedance decreases dramatically after the pipette is removed and the liquid environment stabilizes. After the antibodies enter the sensor, they are adsorbed onto the nanowell walls and demonstrate that the nanowell is functioning, confirmed by the increase in impedance from t $\approx 50 - 500$ s. Similarly, after the impedance shift for the antigen injection, the impedance increases due to the antigen binding to the antibody. This increase in impedance signifies the presence of SARS-CoV-2 spike protein.

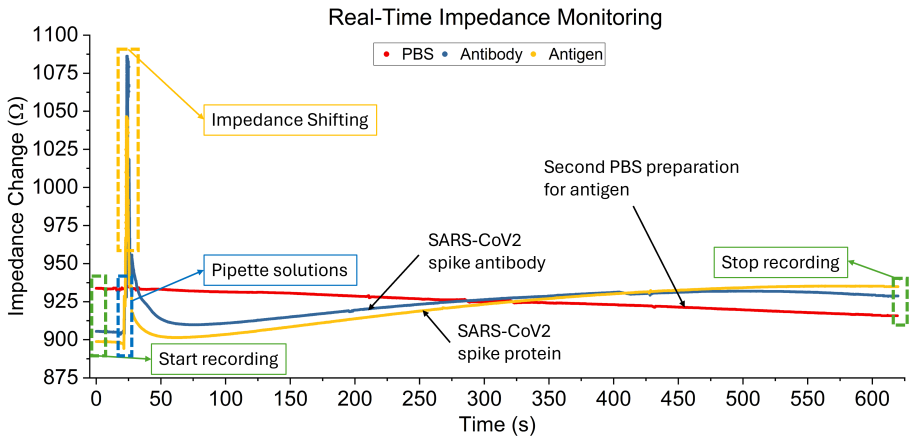

(a)

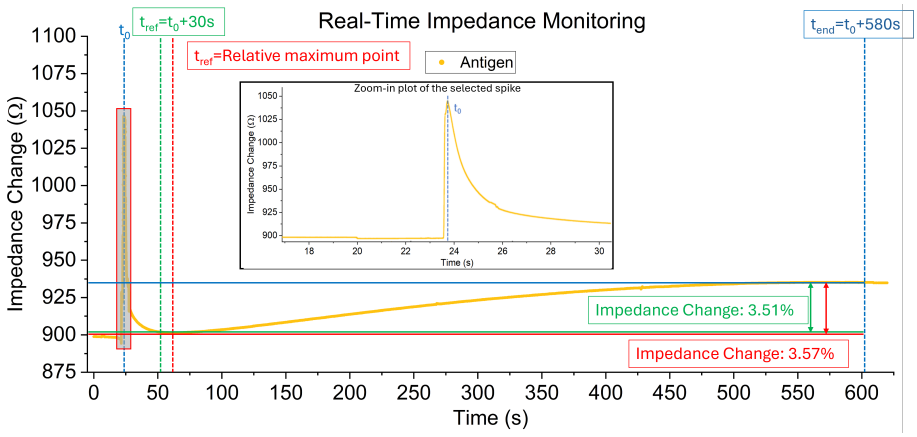

(b)

Figure 2.5: (a) Example impedance curves for the addition of PBS, antibody, and antigen across a ten-minute period, b) Comparison of the two data analysis methods to calculate the change in impedance.

During benchtop experiments, the impedance can be monitored in real-time, and confir-

mation of an increasing impedance can indicate the presence of the target protein. However, when the sensor is used in the breathalyzer, only a binary positive or negative result will be delivered after a predetermined incubation period. Due to this criterion, we established that a positive result, detection of the target protein, is determined if the change in impedance exceeds a threshold value. We then had to determine two key factors: how to calculate the change in impedance and the value of the threshold.

We employed two methods to calculate the change in impedance. Figure 2.5b presents an isolated view of the spike protein response curve. Every experiment has a slightly different pipette insertion time after the voltage has started recording. To accommodate for this, three specific times will be used to characterize the impedance change: t_0, $\mathrm{t}_{\mathrm{ref}}$, and $\mathrm{t}_{\mathrm{end}}$. In both methods, t_0 is the location of the last impedance shift, and the end time is defined as $\mathrm{t}_{\mathrm{end}} = \mathrm{t}_0 + 580\mathrm{s}$. The reference time is defined as $\mathrm{t}_{\mathrm{ref}} = \mathrm{t}_0 + 30\mathrm{s}$ in the first method. In contrast, the second method uses the time corresponding to a relative minimum observed after t_0 as $\mathrm{t}_{\mathrm{ref}}$ [54, 56, 59]. The change in impedance is then given by:

$$\Delta \mathrm{z} = (\mathrm{Z}_{\mathrm{t}_{\mathrm{end}}} - \mathrm{Z}_{\mathrm{t}_{\mathrm{ref}}})/\mathrm{Z}_{\mathrm{t}_{\mathrm{end}}}. \tag{2.1}$$

In Figure 2.5b, we show that the first method provides a relative impedance change of 3.51% and with the second method the relative change is 3.57%.

Figure 2.6 shows the impedance change in response to the concentration of spike protein ranging from C = 0 - 1000 ng/mL with varying $\mathrm{t}_{\mathrm{ref}}$, which was 30s after T_0 in Figure 2.5b, and $\mathrm{t}_{\mathrm{end}}$, 580s after T_0 in Figure 2.5b. C = 0 ng/mL is the negative control, as there are no spike proteins present in the buffer. Due to Figure 2.6 being plotted on a semi-log scale, C = 0 ng/mL is plotted at $\mathrm{C} = 10^{-4}$ ng/mL for visualization purposes. Figure 2.6a highlights that a reference time that coincides with the impedance shift has an increase in impedance change at C = 10 ng/mL that is unseen for the other reference times and may be unsuitable (used $\mathrm{t}_{\mathrm{end}} = \mathrm{t}_0 + 580\mathrm{s}$). Reference times between 10-60s all give similar results; therefore, 30s was chosen for these experiments. Figure 2.6b shows that the mag-

nitude of the impedance change increases with increasing end time (used $\mathrm{t_{ref}} = \mathrm{t_0} + 30\mathrm{s}$). Therefore, we used 580s for the end time, as it was the maximum time that could be used for all experiments.

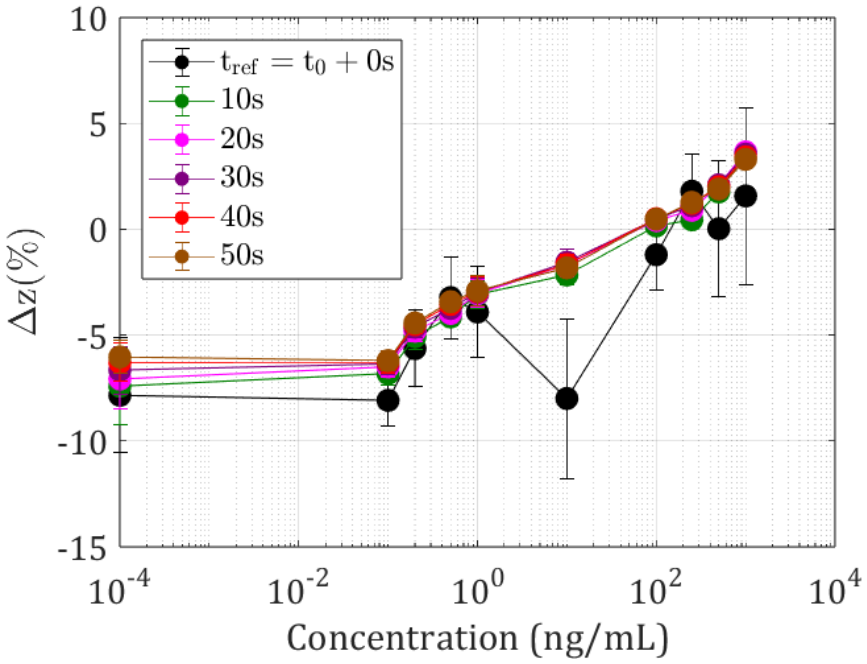

(a)

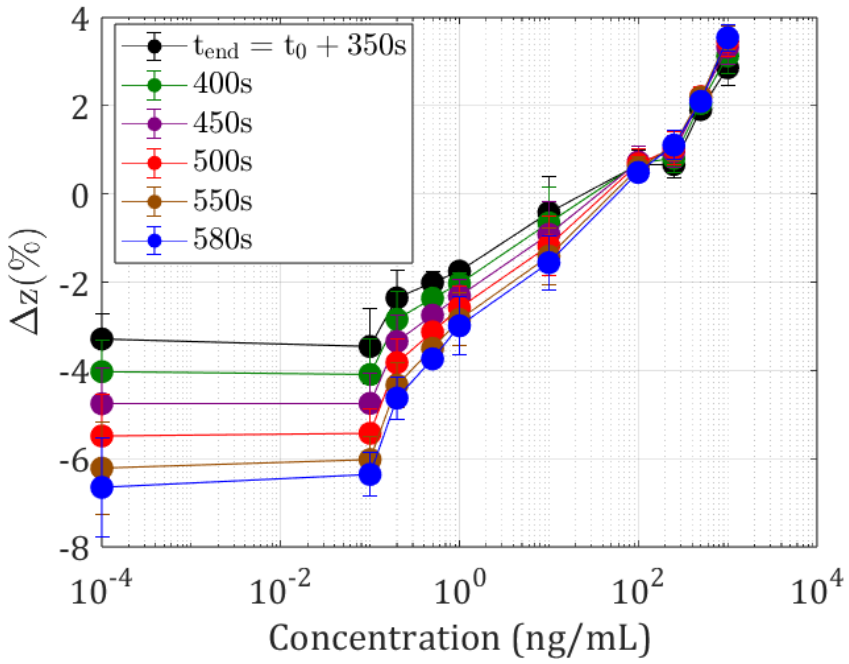

(b)

Figure 2.6: Impedance change for spike protein concentrations ranging from 0 ng/mL - 1000 ng/mL as functions of a) T_{ref} and b) T_{end}. C = 0 ng/mL (negative control) is plotted at C = 10^{-4} ng/mL for visualization purposes.

2.4 SARS-CoV-2 Detection Limit Results

After establishing the impedance change methodology, the threshold for a positive test result is determined through the limit of detection. The limit of detection (LOD) is the lowest concentration of protein that has a statistically different impedance change compared to the negative control. The LOD is used to evaluate the effectiveness of different diagnostic tests, as a lower LOD can detect smaller samples of virus that less sensitive measurements could not. The measured impedance change at the limit of detection is then the threshold value, and any impedance change greater than the threshold results in a positive test result. To establish the detection limit for the sensor using SARS-CoV-2 antibodies and spike protein, various concentrations were tested with multiple sensors. The devices are fragile and were only used for three tests maximum before being discarded. Initial experiments used antibodies prepared in 1X PBS and spike protein in artificial human saliva. Figure 2.7 shows titration curves using the two methods outlined above, with a) using the set reference time of $\mathrm{t_{ref}} = \mathrm{t_0} + 30\mathrm{s}$, and b) using the $\mathrm{t_{ref}}$ as the relative minimum observed after $\mathrm{t_0}$. The dynamic range for these experiments was C = 50 - 500 ng/mL, as well as the negative control of C = 0 ng/mL. Both plots show the impedance change becoming increasingly positive with increasing concentration. This is expected as more spike proteins are available to bind to the antibodies to further increase the impedance. Detection limits are calculated as 200 ng/mL (1.5 nM) for both methods, as it is the lowest concentration that does not overlap with the error for C = 0 ng/mL (plotted at C = 10 ng/mL for visualization purposes). The error bars are generated using the standard deviation of the impedance changes. A 200 ng/mL detection limit is not ideal, as other biosensors have demonstrated LODs on the order of 10^{-6} to 10 ng/mL [49, 50, 51, 52, 53].

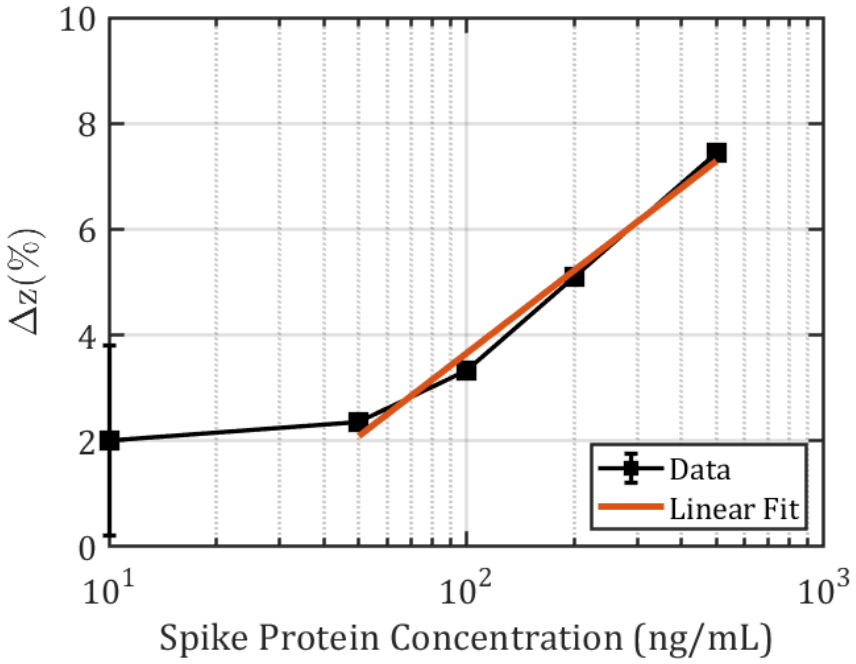

(a)

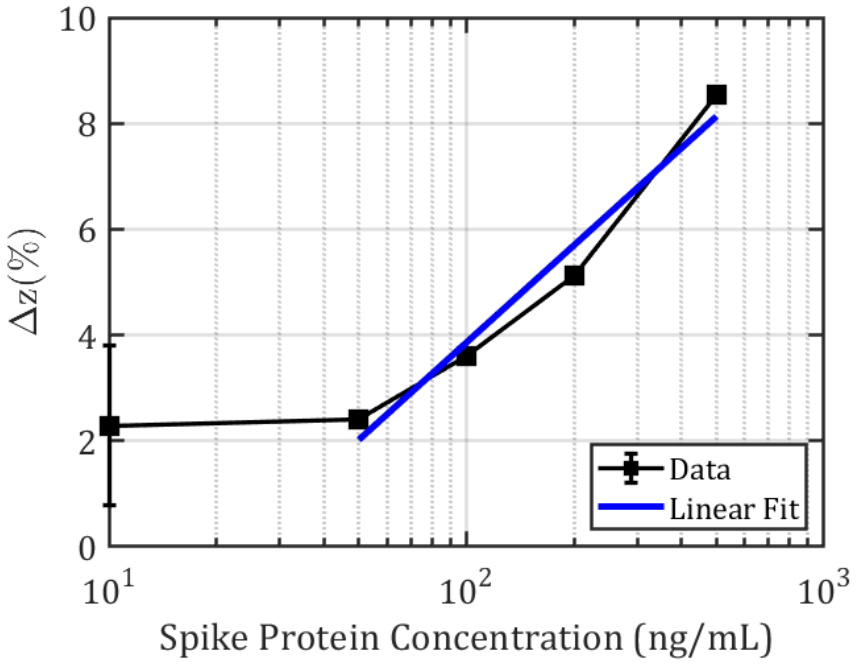

(b)

Figure 2.7: Impedance change for antibodies prepared in 1X PBS and spike protein in artificial human saliva in concentrations ranging from 50 - 500 ng/mL dynamic range. a) Impedance change calculated using method 1, resulting in a 200ng/mL (1.5nM) detection limit; linear fit: (Z) = -6.74 + 5.18 x C, $R^2 = 0.99$, b) Impedance calculated using method 2 with a 200 ng/mL detection limit; linear fit: (Z) = -8.36 + 6.11 x C, $R^2 = 0.97$. $\star$ denotes negative control (C = 0 ng/mL) plotted at C = 10 ng/mL for visualization purposes. N = 5 for C = 0 ng/mL and N = 1 for all other concentrations.

A potential explanation for the large LOD value is the mismatch in impedance between the 1X PBS and artificial saliva. Higher concentrations of PBS have larger salt concentrations and ultimately lower impedance. A lower baseline impedance could potentially reduce the effects of the impedance increase when the antigens bind to the antibodies, thus resulting in the relatively high LOD. To investigate the effects of impedance imbalance, Figure 2.8a shows the output voltage from the sensor for PBS concentrations ranging from 0.1 to 1X and artificial saliva. Here, the output voltage is reported as the signal is converted to voltage after passing through a current amplifier. The previous figures have reported results in units of ohms (Ω) using Equation 2.1. It is clear that the output voltage baseline increases with increasing PBS concentration, and the saliva curve (dark blue) is between 0.1 and 0.2X PBS. We then chose to quantify the PBS concentration that most closely resembles the saliva baseline, a regression curve using the voltage at t = 300 s is shown in Figure 2.8b. The equivalent concentration is found to be 0.18X PBS through interpolation.

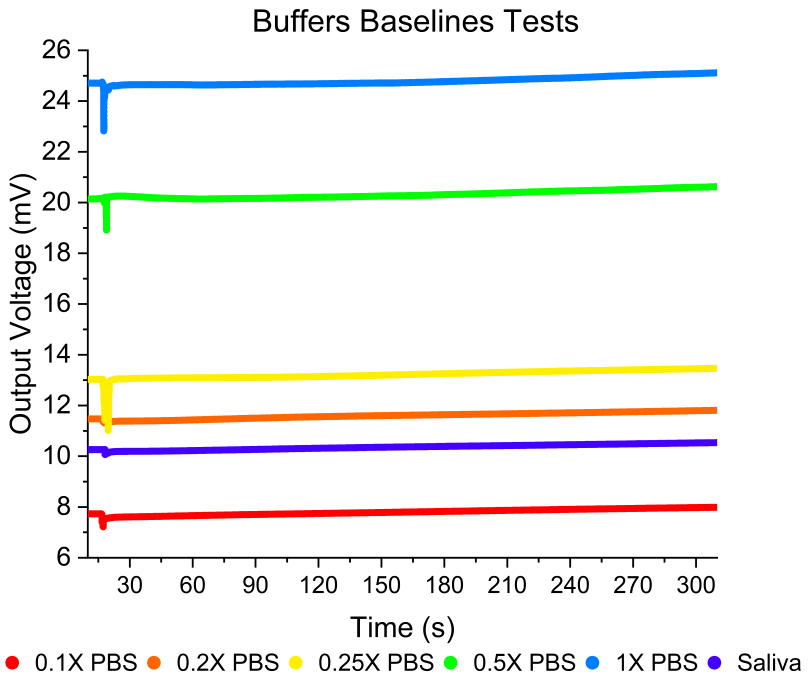

(a)

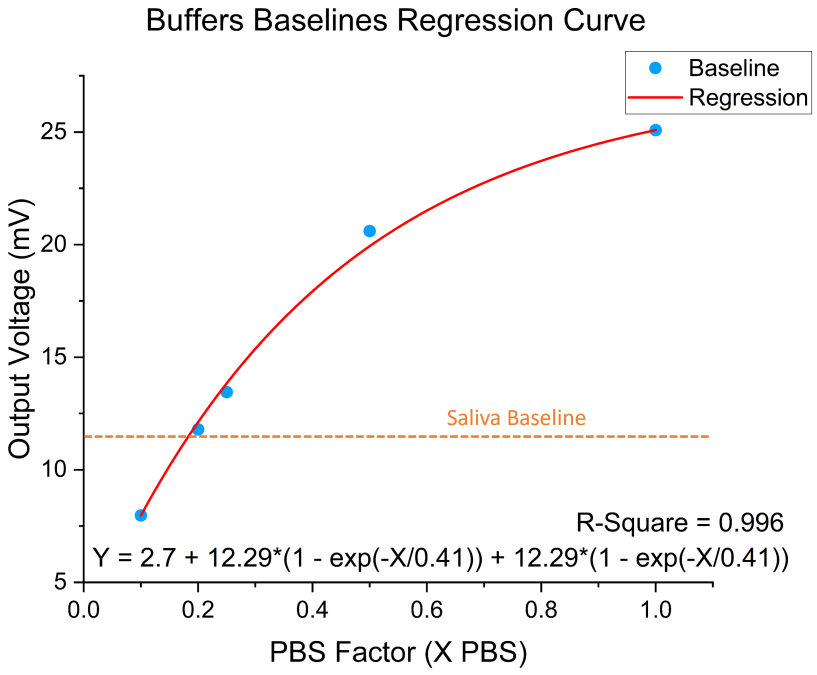

(b)

Figure 2.8: a) Nanowell output voltage over five minutes for varying concentrations of PBS, b) Regression curve using voltage at t = 300 s to match the PBS concentration with the artificial saliva baseline. Through interpolation, matching concentration is found to be 0.18x PBS.

After establishing the matching PBS concentration, subsequent experiments were performed with the antibodies prepared in 0.18X PBS. Titration curves using the fixed time interval and relative minimum t_{ref} impedance change methods are shown in Figure 2.9a and b, respectively. Compared to the titration curves using 1X PBS, controlling for the buffer impedance greatly increases the magnitude of the impedance change. Whereas the previous experiments yielded a LOD of 200 ng/mL (1.5 nM), the method using $t_{ref} = t_0 + 30s$ has an LOD of 0.2 ng/mL (1.5 pM) using a 0.05 significance level, which is a three-order-of-magnitude improvement. The significance level is the probability that the result (0.2 ng/mL is the limit of detection) is incorrect, and the result is instead a false positive. A significance level of 0.05 means the probability of the LOD being greater than 0.2 ng/mL is 5%. Using an even higher significance level of 0.0001, which is a higher degree of confidence, the detection limit is 1 ng/mL (7.5 pM), which is still significantly better than the LOD using 1X PBS. Using the relative minimum analysis method, a significance level of 0.05 yields a detection limit of 0.5 ng/mL (3.75 pM), which is slightly worse than the first method. However, the LOD is the same as the first method with a 0.0001 significance level. The previous LODs were the lowest concentration of spike protein that had a statistically significant impedance change compared to the negative control using the Tukey test with an assigned significance level as mentioned previously. The theoretical limits of detection can also be projected by using the linear fits shown in Figure 2.9. Theoretical LODs correspond to the spike protein concentrations at the intersections of the linear fits with the negative control. We obtained 0.13 ng/mL (0.975 pM) and 0.33 ng/mL (2.475 pM) for the first and second methods, respectively. From these results, we conclude that 0.18 PBS is a more suitable buffer for the SARS-CoV-2 antibodies.

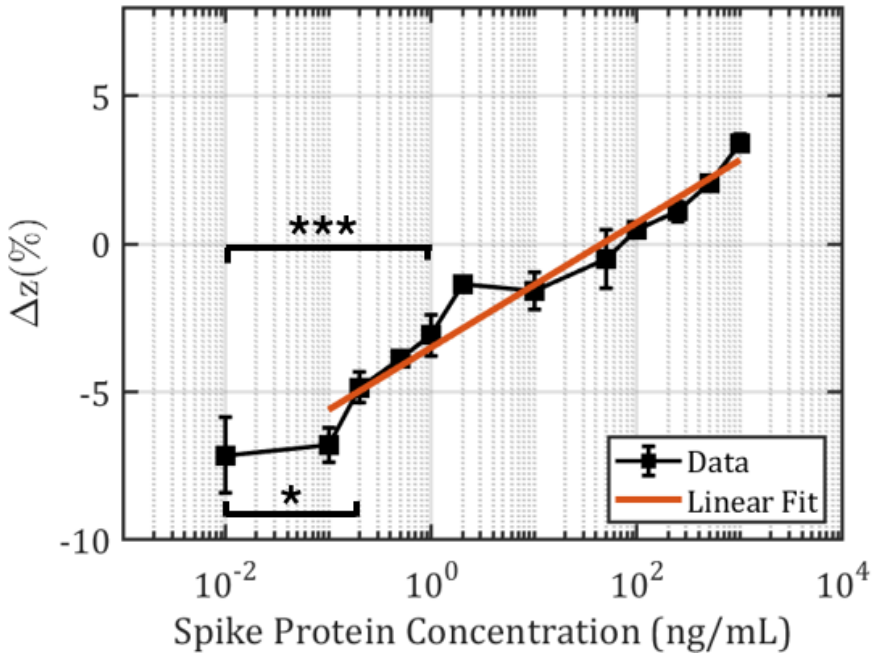

(a)

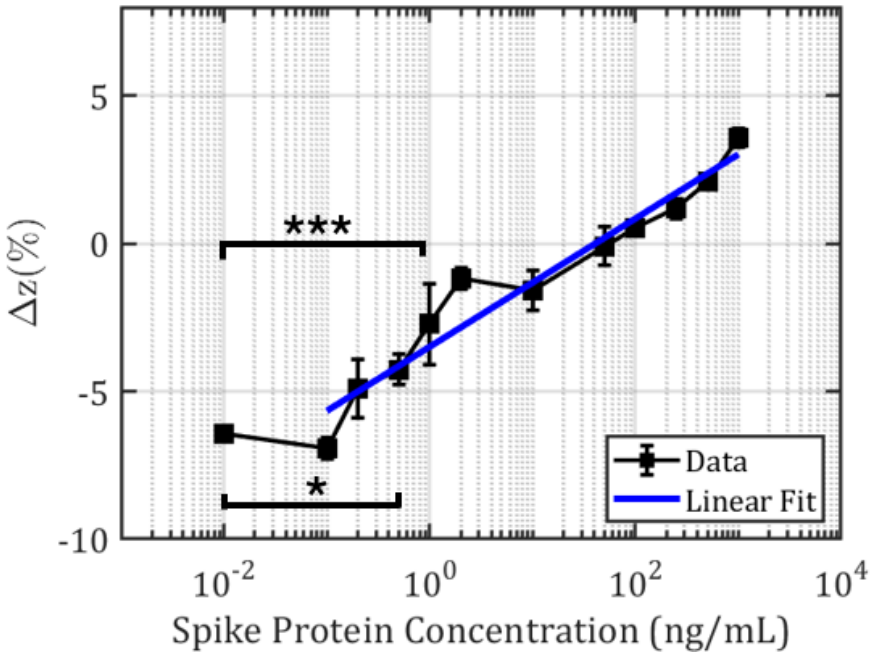

(b)

Figure 2.9: Impedance change for antibodies prepared in 0.18X PBS and spike protein in artificial human saliva in concentrations ranging from 0.01 - 1000 ng/mL dynamic range. a) Impedance change calculated using method 1; linear fit: (Z) = 3.49 - 2.17 x log(C), $R^2 = 0.94$, b) Impedance calculated using method 2; linear fit: (Z) = 3.49 - 2.11 x log(C), $R^2 = 0.95$. $\star$ denotes negative control (C = 0 ng/mL) plotted at C = 0.01 ng/mL for visualization purposes. $\star P \leq 0.05$; $\star\star\star P \leq 0.0001$, N = 2 for C = 0 ng/mL, N = 5 for C = 50 ng/mL, N = 3 for all other concentrations.

After determining the limit of detection for the nanowell sensor using SARS-CoV-2 spike proteins prepared in artificial saliva with antibodies prepared in 0.18X PBS, we compared the LOD to commercially available, over-the-counter tests such as the Abbott BinaxNOW Covid-19 Antigen Card Home Test and the Abbott Panbio Covid-19 Antigen Rapid Test Device. The BinaxNow and Panbio limits of detection were reported as 140.6 and 158 TCID_{50}/mL, which is the concentration of virus needed to infect 50% of a cell culture [60, 61, 62]. The TCID_{50}/mL can be converted to ng/mL by multiplying by the ratio of SARS-CoV-2 antigen to virion, which is 0.89 pg per TCID_{50} and then multiplying by 1000 to convert pg to ng [63]. The corresponding LODs in ng/mL for the BinaxNow and Panbio tests are 0.13 and 0.14 ng/mL, which are similar to the 0.2 ng/mL limit of detection of the nanowell sensor.

2.5 MERS Specificity Results

Thus far, the sensor has demonstrated the ability to detect a binding event between SARS-CoV-2 antibodies and spike proteins. We then needed to demonstrate that the sensor can differentiate between the target and a different protein by performing specificity experiments. In these experiments, the sensors are prepared with SARS-CoV-2 antibodies, as before, but MERS-CoV spike proteins were used in the final step instead of the SARS-CoV-2 spike proteins in the previous experiments. MERS was chosen as the alternative spike protein to demonstrate specificity because it is from the same *Betacoronavirus* genus as SARS-CoV-2 [64]. To correctly differentiate between MERS-CoV-2 and SARS-CoV-2 spike proteins, the MERS spike proteins and SARS-CoV-2 antibodies should not bind, and the impedance should, therefore, not increase. The experimental procedure is the same as the previous experiments; however, the MERS-CoV spike proteins are prepared in 1000 ng/mL concentrations in 0.18X PBS instead of artificial saliva.

The specificity results are shown in Figure 2.10 and match the expected trends for a negative test result. One 250 ng/mL SARS-CoV-2 result is shown in red, two 1000 ng/mL

MERS-CoV results are shown in black and orange, and 2 1X PBS (negative control) are shown in blue and green. All curves are normalized to their impedance at 50 s to account for variations in impedance baselines across the different experiments. The SARS-CoV-2 result has an increasing impedance due to the antigen-antibody binding, whereas all other results have decreasing impedance due to the enhanced conductivity of the PBS buffer. Similarity in the impedance changes for the negative control and MERS-CoV results highlights that the sensor does not detect a binding event between the SARS-CoV-2 antibodies and the MERS-CoV spike proteins and demonstrates the ability to distinguish between the two spike proteins. This result is powerful as it demonstrates the ability of the sensor to correctly identify patients with the target disease while correctly ignoring others.

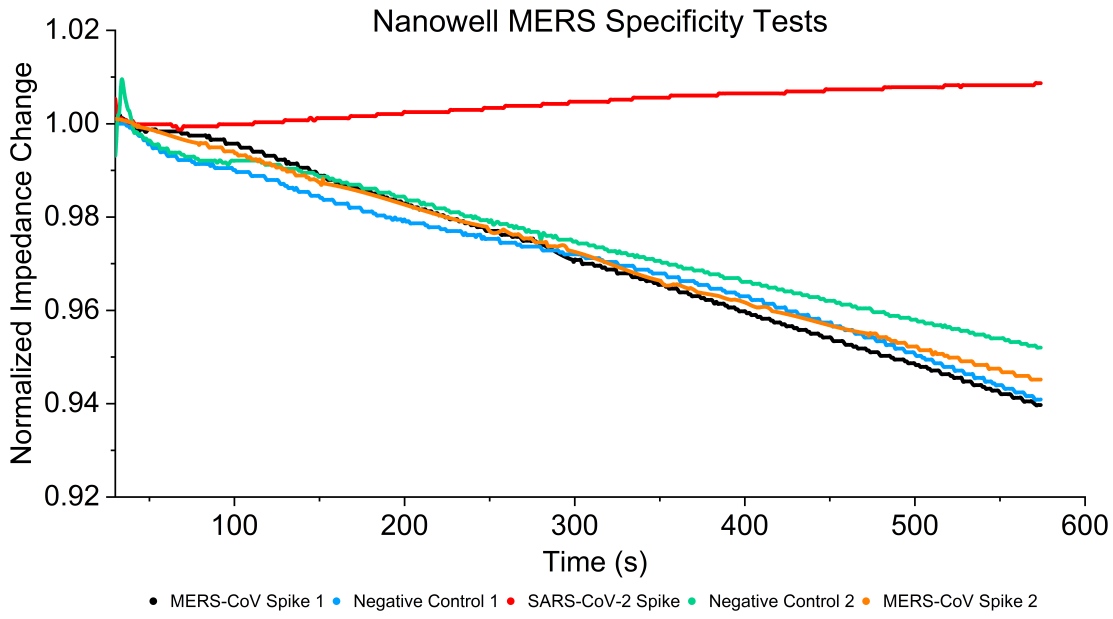

Figure 2.10: Comparison of impedance change over time for sensors prepared with SARS-CoV-2 antibodies and either MERS spike protein, SARS-CoV-2 spike protein, or 1x PBS (negative control). The negative control and MERS impedance curves overlap and have nearly identical decreases in impedance and are distinct from the SARS-CoV-2 spike protein curve, thereby demonstrating specificity between the two proteins.

It has been established that the nanowell impedance sensor can detect SARS-CoV-2 spike protein with a 0.2 ng/mL (1.5 pM) limit of detection and is similar to commercially available at-home testing kits. As a breathalyzer, the water droplets from exhaled breath

carrying viral particles will transport the target antigen to the sensor. Next steps will be to incorporate the sensor into the breathalyzer by embedding it into the particle trap and studying the impactor flow field and particle dynamics to optimize the particle capture efficiency and maximize protein delivery.

Portions of this chapter are reproduced from my previously published article: Zhuolun Meng, Liam White, Pengfei Xie, Hassan Raji, S. Reza Mahmoodi, Aris Karapiperis, Hao Lin, German Drazer, Mehdi Javanmard, Edward P. DeMauro, A label-free nanowell-based impedance sensor for ten-minute SARS-CoV-2 detection, Lab on a Chip, 2025, DOI: 10.1039/D5SD00002E, with permission from the Royal Society of Chemistry.

I am listed as the second author on this article, but contributed equally and am credited as a co-first author.

CHAPTER 3
FLOW FIELD AND PARTICLE DYNAMICS

3.1 Introduction

This chapter investigates how aerosols transported by a jet impinging normally on a particle trap can be collected for virus detection by the nanowell sensor. Liquid droplets suspended in exhaled breath travel through a converging nozzle and exit as multiphase flow in a round jet. After the jet exits the nozzle, it normally impinges on the cavity called the particle trap, and particles with sufficient inertia will deposit inside.

3.2 Isentropic Flow Relations

The Reynolds number characterizes the flow regime and is the ratio of inertial forces to viscous forces, and is given below,

$$\mathrm{Re} = \frac{\rho V D_c}{\mu}, \tag{3.1}$$

where ρ is the fluid density, μ is the dynamic viscosity of the fluid, V is the fluid velocity, and D_c is the characteristic length of the flow. The Reynolds number is one factor that determines how the flow will behave inside the breathalyzer.

The breathalyzer comprises a converging nozzle and a particle trap. As users blow into the nozzle, increasing the particle Stokes number, the nondimensional number that represents the particle's inertia, is imperative to increase the likelihood of collecting the exhaled droplet. To achieve this, the nozzle's cross-sectional area should decrease, increasing the fluid velocity and, subsequently, the Stokes number. As the fluid emerges from the nozzle, it will expand into the surrounding air at the nozzle exit. Because the changes in the flow are gradual, we will assume the flow is isentropic, meaning the flow is adiabatic and reversible,

so we can use the isentropic flow relations to assess the effects of compressibility.

The isentropic flow relations allow us to calculate the Mach number for a flow in a converging nozzle. The Mach number (M) is the ratio of the speed of the flow to the speed of sound of the fluid at the operating temperature, shown below,

$$\mathrm{M} = \frac{\mathrm{V}}{\mathrm{c}}. \tag{3.2}$$

Compressibility effects can be ignored if the Mach number is less than 0.3 and the density of the fluid is, therefore, considered constant [65]. When a user blows in the nozzle, they supply the converging nozzle with an airstream at a certain inlet pressure, P_0, and the air will exit the nozzle at atmospheric pressure, P. The corresponding pressure difference and nozzle geometry will determine the fluid velocity. The user blowing into the nozzle can be represented as a stagnation chamber connected to a converging nozzle that exhausts to atmospheric pressure. The fluid velocity at the nozzle inlet relative to the outlet is slow and therefore the user can be represented by a stagnation chamber with nozzle inlet pressure, P_0, as the stagnation pressure. A cartoon of the user representing a stagnation chamber is shown below in Figure 3.1.

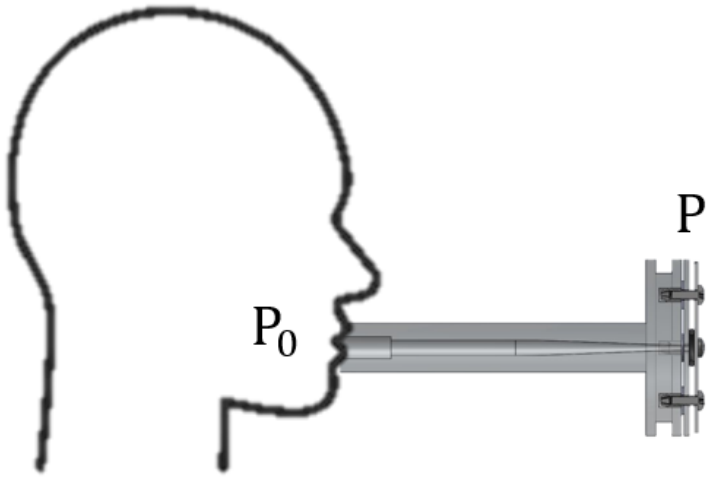

Figure 3.1: Cartoon representation of a user blowing into the impactor as a stagnation chamber inlet stagnation pressure, P_0, and outlet pressure, P.

For a given inlet and outlet pressures, the isentropic flow relation is,

$$\frac{\mathrm{P}_0}{\mathrm{P}} = [1 + \frac{\gamma - 1}{2}\mathrm{M}^2]^{\frac{\gamma}{\gamma - 1}}, \tag{3.3}$$

where γ is the ratio of the specific heats of constant pressure-to-constant volume for air. Humans can typically exhale between 0.5 - 3.5 psi [66, 67], with adults exhaling with greater pressure than children. Assuming an exhalation temperature of 95° F [68], the ratio of specific heats for air is 1.4. Figure 3.2 shows the Mach number as a function of inlet pressure and reveals that the flow is incompressible for inlet pressures less than 1 psi, which is within the user range.

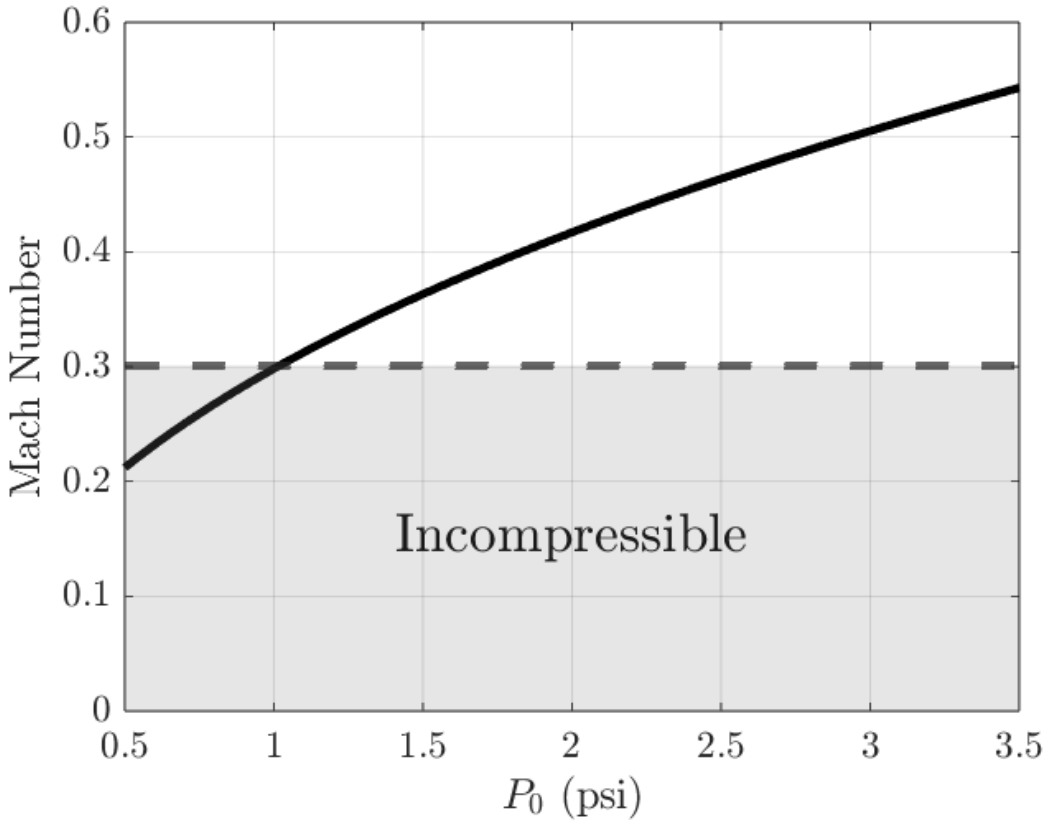

Figure 3.2: Mach number as a function of inlet gauge pressure.

3.3 Impactor Axisymmetric Flow Field

After verifying that compressibility effects can be ignored, we conclude that the behavior of the air as it flows in the impactor is governed by the incompressible Navier-Stokes momentum equation without body forces shown below,

$$\rho\frac{\mathrm{D}\mathbf{u}}{\mathrm{Dt}} = -\nabla \mathrm{P} + \mu\nabla^2\mathbf{u}, \tag{3.4}$$

where $\mathbf{u}$ is the fluid velocity, P is pressure, and t is time. Gravitational effects can be ignored due to the Froude number,

$$\mathrm{Fr} = \frac{\mathrm{V}}{\sqrt{2\mathrm{gR}}}, \tag{3.5}$$

being much larger than one for flow velocities and characteristic lengths used throughout this dissertation. The characteristic flow velocities for the impactor will be the average velocities exiting the converging nozzle, and the characteristic lengths will be the outlet diameters of the nozzles. Throughout this dissertation, we will limit the inlet pressures to the nozzle to less than 1.5 psi, as this is around the typical values we can expect from a user. The characteristic velocities will then be between 5 and 100 m/s for the nozzle diameters between 1.5 and 3 mm, and the rationale for using these nozzle diameters will be explained in chapter 4.

Due to the impactor geometry having radial symmetry, the incompressible continuity and momentum equations can be rewritten in axisymmetric, cylindrical coordinates in component form, shown below,

$$\frac{1}{\mathrm{r}}\frac{\partial(\mathrm{ru_r})}{\partial \mathrm{r}} + \frac{\partial \mathrm{u_z}}{\partial \mathrm{z}} = 0, \tag{3.6}$$

$$\frac{\partial \mathrm{u_r}}{\partial \mathrm{t}} + (\mathbf{u}\cdot\nabla)\mathrm{u_r} = -\frac{1}{\rho}\frac{\partial \mathrm{P}}{\partial \mathrm{r}} + \nu(\nabla^2\mathrm{u_r} - \frac{\mathrm{u_r}}{\mathrm{r}^2}), \tag{3.7}$$

$$\frac{\partial \mathrm{u_z}}{\partial \mathrm{t}} + (\mathbf{u} \cdot \nabla)\mathrm{u_z} = -\frac{1}{\rho}\frac{\partial \mathrm{P}}{\partial \mathrm{z}} + \nu\nabla^2\mathrm{u_z}, \tag{3.8}$$

where $\mathrm{u_r}$ and $\mathrm{u_z}$ are the radial and axial components of velocity, respectively. An axisymmetric flow field has no dependence on the azimuthal angle, φ. Therefore, rotating about the centerline has no impact on the flow field, and the flow field is only a function of the pressure gradient, distance from the centerline (r), and axial distance from the inlet (z). A schematic of the impactor coordinate system is shown in Figure 3.3.

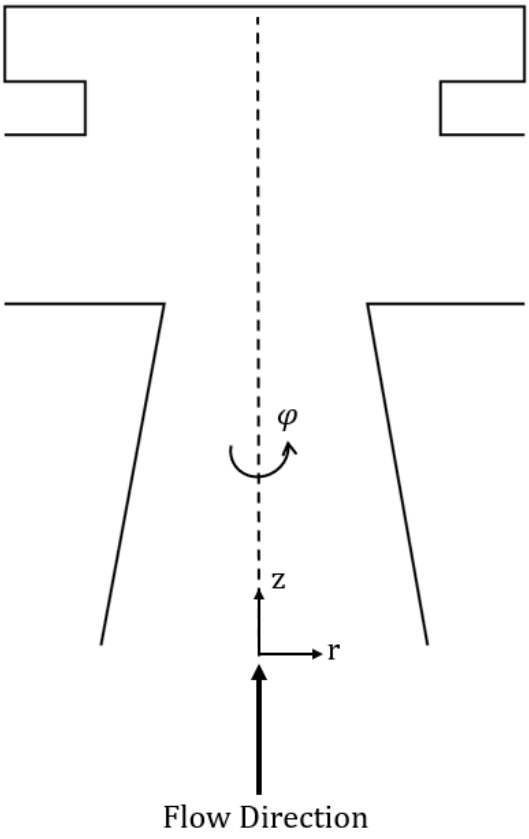

Figure 3.3: Impactor cylindrical coordinate system.

The impactor can be split into three sections: the converging nozzle, the round jet, and the trap.

3.3.1 Converging Nozzle

Uniform flow enters the nozzle at velocity $\mathrm{u_0}$. As the flow moves through the contraction, it will accelerate due to the reduced cross-sectional area, and the centerline velocity, $\mathrm{u_c}$, will be the maximum. Due to the boundary layer development at the walls, the originally uniform velocity profile will evolve to a flattened parabolic profile downstream. Compared to nozzles with constant diameters, the boundary layers in the converging nozzle will be thinner due to the favorable pressure gradient in the presence of the contraction. This favorable pressure gradient blunts the development of the boundary layer, and the velocity profile has a flatter peak than typical fully-developed pipe flows. If the Reynolds number is large enough ($\mathrm{Re} > 2300$) and the flow is turbulent, the profile will be even flatter. This flattened profile is the result of the erratic local velocities accelerating and decelerating parts of the flow, so the overall profile is more uniform than parabolic. The flatter the velocity profile, the more similar the average velocity is to the uniform velocity, whereas in fully-developed pipe flows, the average velocity is twice the centerline velocity. The velocity profile development in the nozzle is shown in Figure 3.4.

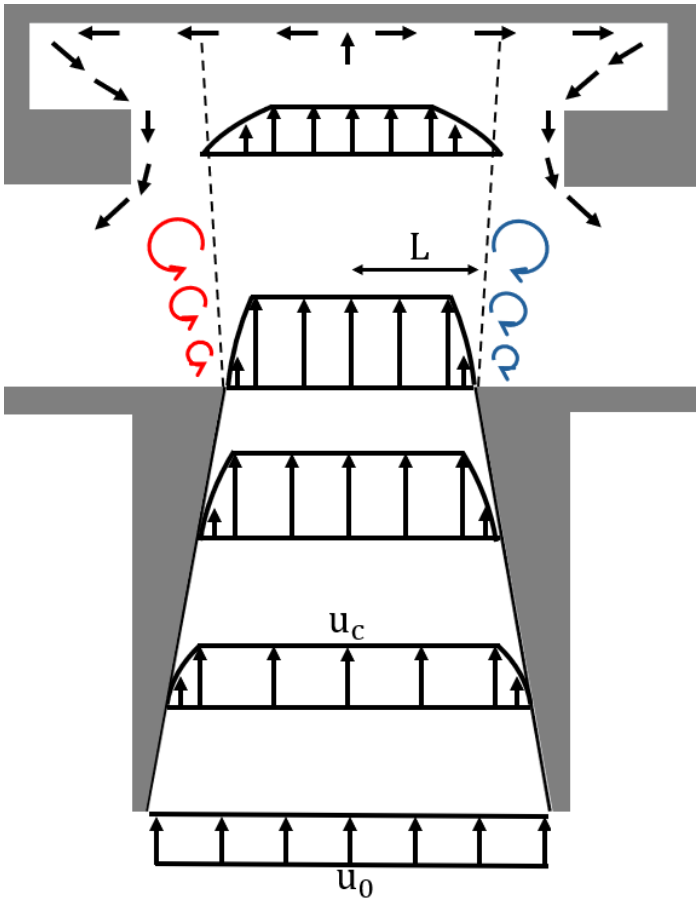

Figure 3.4: A schematic of the predicted impactor flow field. The nozzle inlet has uniform velocity, u_0, and the profile becomes a blunted parabolic distribution due to the boundary layer development and decreasing cross-sectional area. u_c is the centerline velocity. The fluid emerges from the nozzle as a round jet and entrains ambient fluid to expand its width. L is the jet width, which is half of the radial distance to the location with axial velocity that is 1% of the centerline velocity. Due to the velocity gradient between the jet and ambient air, the Kelvin-Helmholtz instability is present, which generates counter-rotating vortices at the edge of the jet. The jet then enters the trap, expands radially outward to the trap walls, reverses direction, and exits the trap.

3.3.2 Round Jet

When the flow emerges from the converging nozzle, it will be an axisymmetric round jet. The Reynolds number for the jet is based on the nozzle outlet diameter as the characteristic length scale and the average velocity at the outlet. As the jet travels downstream, ambient air will be entrained into the jet due to the favorable pressure gradient towards the centerline of the jet. The entrained fluid causes the size of the jet to increase, as determined by L, the

radial distance to the location where the axial velocity is 1% of the centerline velocity (denoted by the dotted lines in Figure 3.4) [65]. As the jet moves downstream, the shear layer at the edges moves inward towards the centerline, similar to a boundary layer in internal flow. In this thesis, the distance between the jet exit and the particle trap are small, and the shear layers do not meet at the centerline. Therefore, the jet is underdeveloped.

Another characteristic of the round jet arises from the shear layer. The velocity gradient at the jet edge results in the formation of toroidal vortices due to the Kelvin-Helmholtz instability. The Kelvin-Helmholtz instability exists in regions of a fluid with a velocity shear and leads to enhanced momentum transfer in the fluid. As the instability progresses, there is a vortex sheet at the interface [65], creating toroidal vortices. In Figure 3.4, the blue circles indicate the clockwise rotating component of the vortices, and the red circles indicate the counterclockwise motion.

3.3.3 The Trap

As the jet enters the trap region, the velocity will decrease due to the presence of the solid wall at the bottom of the trap, where the centerline velocity will come to rest. This stagnation point will propagate an adverse pressure gradient upstream and decrease the jet velocity. The areas of the jet not along the centerline will move radially outward at the back of the trap due to the no-penetration condition. The flow will turn and reverse direction at the solid boundaries along the trap walls and ultimately exit the trap in the opposite direction of the incoming flow. This reverse flow can potentially interact with the incoming jet and will be explored in chapter 7.

3.4 Particle Dynamics

Understanding the motion of the particles in the flow is crucial to studying impactor performance. The particle-laden flow is assumed to be dilute enough so that we can ignore particle-particle and particle-fluid interactions. The liquid droplets can be treated as rigid

spheres due to the Capillary number,

$$\mathrm{Ca} = \frac{\mu \mathrm{V}}{\sigma}, \tag{3.9}$$

where σ is the surface tension between water and air, being much less than one for the range of characteristic velocities used in this dissertation.

Consider first the motion of a particle settling under gravity in quiescent air. The equation of motion for the particle is

$$\mathrm{m_p}\frac{\mathrm{dV_p}}{\mathrm{dt}} = \mathrm{F_D} - \mathrm{F_G}, \tag{3.10}$$

where $\mathrm{m_p}$ is the mass of the particle, V_p is the particle velocity, F_D is the drag force opposing the motion of the particle, and F_G is the force due to gravity. Spherical particles with diameters in the micrometer range in quiescent air will be under the influence of Stokes drag (Re < 1) given below,

$$\mathrm{F_d} = \frac{3\pi\mu \mathrm{U D_p}}{\mathrm{C_c}}, \tag{3.11}$$

where $\mathrm{D_p}$ is the particle diameter, U is the relative velocity between the fluid and particle, and again, C_c is the Cunningham slip correction factor. The slip correction factor accounts for particle diameters approaching the mean-free path of the particles constituting the bulk fluid and is given below,

$$\mathrm{C_c} = 1 + \frac{2.52\lambda}{\mathrm{D_p}}, \tag{3.12}$$

where λ is the mean free path of the gas. The mean free path of air at 20° and atmospheric pressure is 0.066 μm and 0.07 μm at 95°F and atmospheric pressure for human exhalation conditions [1, 69]. For particles between 1 and 10 μm, the Cunningham slip correction factor is between 1.2 and 1, and therefore, a correction factor of 1 will be used throughout

this dissertation. At length scales approaching the mean free path, the fluid is treated as a collection of molecules. The particles are then subjected to collisions from the individual molecules comprising the surrounding fluid and will experience a reduction in drag.

For spherical droplets, the Stokes drag force accounts for the difference between the internal and external viscosities as shown below,

$$\mathrm{F_d} = 2\pi\mu \mathrm{U D_p} \frac{3\epsilon + 2}{2(\epsilon + 1)}, \tag{3.13}$$

where ϵ is the effective viscosity and is the ratio of the internal (droplet) viscosity to the external (bulk fluid) viscosity [70]. However, the correction is negligible for droplets with high viscosity relative to the bulk fluid, such as water droplets in air. The viscosity of water at 95°F is $7.2 \times 10^{-4}\,\mathrm{Pa \cdot s}$, whereas air is $1.91 \times 10^{-5}\,\mathrm{Pa \cdot s}$, which is nearly 40 times larger, and therefore, Equation 3.11 is appropriate.

Returning to the equation of motion, the force due to gravity in a viscous fluid is shown in Equation 3.14,

$$\mathrm{F_G} = \frac{(\rho_P - \rho_g)\pi(\mathrm{D_p})^3 g}{6}, \tag{3.14}$$

where ρ_p is the density of the particle, ρ_g is the density of the surrounding fluid, and g is the acceleration due to gravity. The terminal settling velocity is the maximum velocity attained by the particle and occurs when the drag force and gravitational forces are equal, and is given below,

$$\mathrm{V_{TS}} = \frac{\rho_p \mathrm{D_p^2} g \mathrm{C_c}}{18\mu} = \tau g \tag{3.15}$$

where τ is the particle relaxation time, which is the time it takes for the particle to adjust, or relax, to its new velocity when disturbed by a force. Due to the density of water being over 800 times larger than that of air, we have ignored the contribution of the air density to the gravitational force. If the particle has an initial velocity, $\mathrm{V_0}$, the distance the particle

will travel before coming to rest is the stopping distance

$$S = V_0 \tau. \tag{3.16}$$

We now introduce the Stokes number (St), which is the ratio of the particle's stopping distance to the characteristic length of the flow, L_c,

$$St = \frac{S}{L_c} = \frac{V_0 \tau}{L_c}. \tag{3.17}$$

The Stokes number characterizes the inertia of the particle to that of the flow. Particles with high Stokes numbers have high relative inertia and cannot react quickly to changes in the flow, whereas particles with low Stokes numbers can. Point particles with a negligibly small Stokes number would essentially follow the flow streamlines. This is the most critical dimensionless parameter for impactors, as the particle Stokes number helps predict if a particle will collide with an obstruction, such as a flat plate. The equation for the impactor Stokes number is

$$St = \frac{\rho_p V_0 D_p^2 C_c}{18 \mu R}, \tag{3.18}$$

where 2R, the nozzle exit diameter, is the characteristic length. $\sqrt{St}$ will be used throughout this dissertation as it represents the non-dimensional particle diameter.

CHAPTER 4
EXPERIMENTAL SETUP AND DESIGN

4.1 Impactor Design

After verifying the flow is incompressible (see section 3.2), the next objective was to determine the optimal nozzle exit diameter. The inlet diameter is 4.4 mm, the size of a standard straw. The continuity equation dictates that the air flow rate through any cross-section in the nozzle is constant and is given below,

$$\mathrm{Q} = \mathrm{VA}, \tag{4.1}$$

where V is the average fluid velocity, and A is the cross-sectional area. Previously, the isentropic flow relation (Equation 3.3) was used to determine the outlet Mach number for the given inlet and outlet pressures (P_0 and P, respectively) for the nozzle, assuming the upstream pressure was the stagnation pressure with a slow-moving flow. The continuity equation can be coupled with Bernoulli's equation,

$$\mathrm{P}_0 + \frac{\rho \mathrm{V}_0^2}{2} = \mathrm{P} + \frac{\rho \mathrm{V}^2}{2}, \tag{4.2}$$

which states that the total pressure is constant along a streamline for incompressible, inviscid, and steady flow. P_0 and V_0 represent the nozzle inlet pressure and velocity, and the resultant outlet velocity, V, at atmospheric pressure at the outlet can be determined by

$$V = \frac{1}{A}[\frac{2\Delta P}{\rho}(\frac{1}{A^2} - \frac{1}{A_0^2})^{-1}]^{1/2}, \tag{4.3}$$

where ΔP is the difference between the inlet and outlet pressures. The schematic representing the converging nozzle is shown in Figure 4.1.

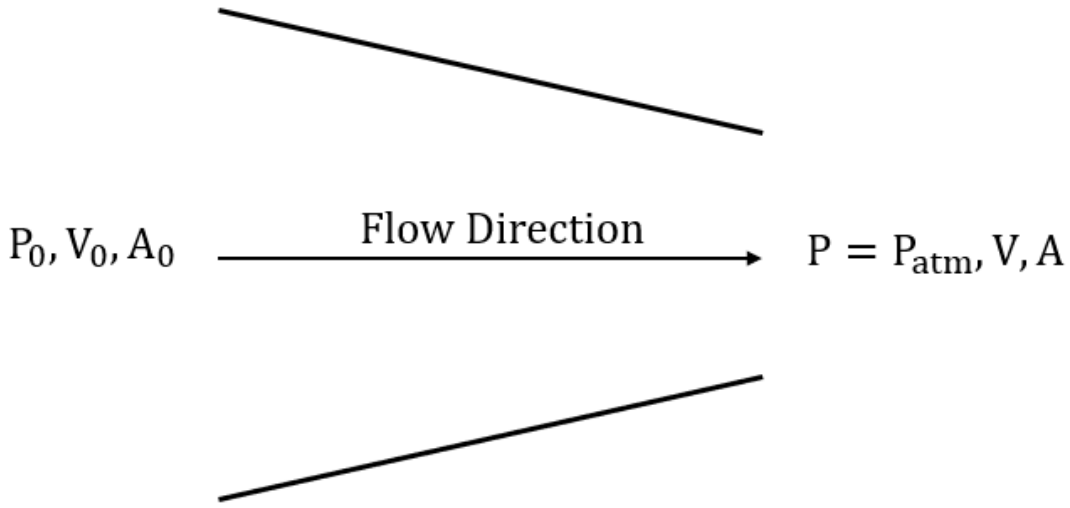

Figure 4.1: Schematic representation of a converging nozzle with inlet values denoted by 0 subscripts.

Parametrizing Equation 4.3 in terms of the outlet area A, the resultant air flow rate through the impactor can be determined as a function of the nozzle outlet diameter, 2R, and is shown in red in Figure 4.2 with a 1 psi pressure differential.

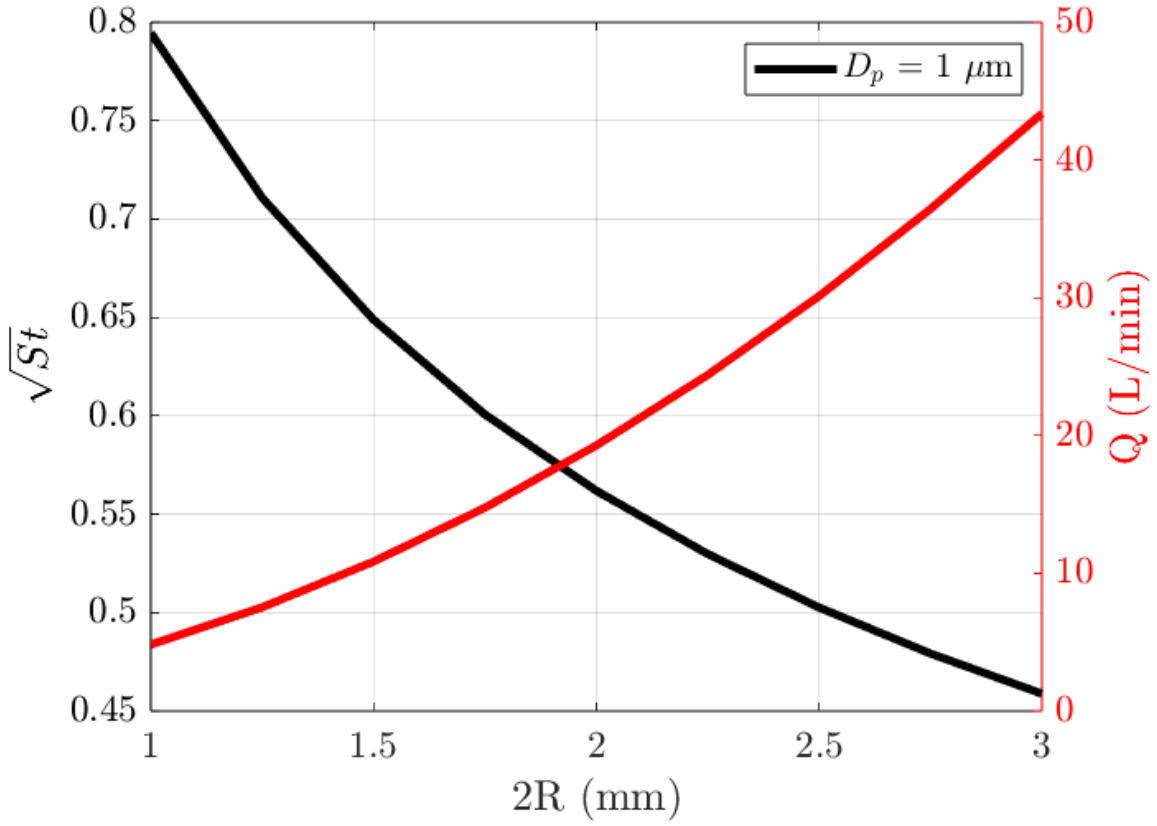

Figure 4.2: $\sqrt{\mathrm{St}}$ and air flow rate as functions of nozzle outlet diameter with a 1 psi pressure differential between the inlet and outlet. $\sqrt{\mathrm{St}}$ uses a 1 µm particle diameter.

The air flow rate increases with 2R, and for a fixed particle concentration in the air, the total amount of particles available for capture increases as well. However, as 2R increases, $\sqrt{\mathrm{St}}$ decreases due to its inverse relationship with 2R, shown in black in Figure 4.2 for a 1 µm particle diameter. Although more particles are available for capture at high flow rates, the particles have reduced inertia and are less likely to be deposited on the collection site. A compromise was made to maximize the potential number of deposited particles, and nozzle diameters of 1.5, 2.3, and 3 mm are used throughout this thesis, as Stokes numbers greater than 0.5 are considered ideal for particle capture. The 1.5 mm nozzle has the largest $\sqrt{\mathrm{St}}$ but the lowest air flow rate, whereas the 3 mm nozzle has the lowest $\sqrt{\mathrm{St}}$ and the highest air flow rate. The 2.3 mm nozzle was chosen as a compromise.

The impactors were printed with a Formlabs Form 3 stereolithography 3D printer.

Stereolithography printers have higher resolution (25 μm layer-height) than other 3D printing methods, such as fused deposition modeling (FDM), and it was important to maintain a relatively smooth internal nozzle geometry to reduce turbulence due to surface roughness. The nozzle geometry begins with the inlet and slowly tapers to the outlet. A spline was drawn to create the nozzle taper, and care was taken to ensure no abrupt reductions in the cross-sectional area that could disturb the flow or create additional flow restrictions. The impactor plate (flat plate with orifice) was also modeled and printed as a simple disk with a through-hole in the center to act as the entrance to the trap. In total, the impactor components are the nozzle, the impactor flat plate with orifice, an o-ring, a collection square, the acrylic backing, and the outlet filter, and their placement and function are discussed below. The flow enters the nozzle and is accelerated through the contraction, as shown in Figure 4.3.

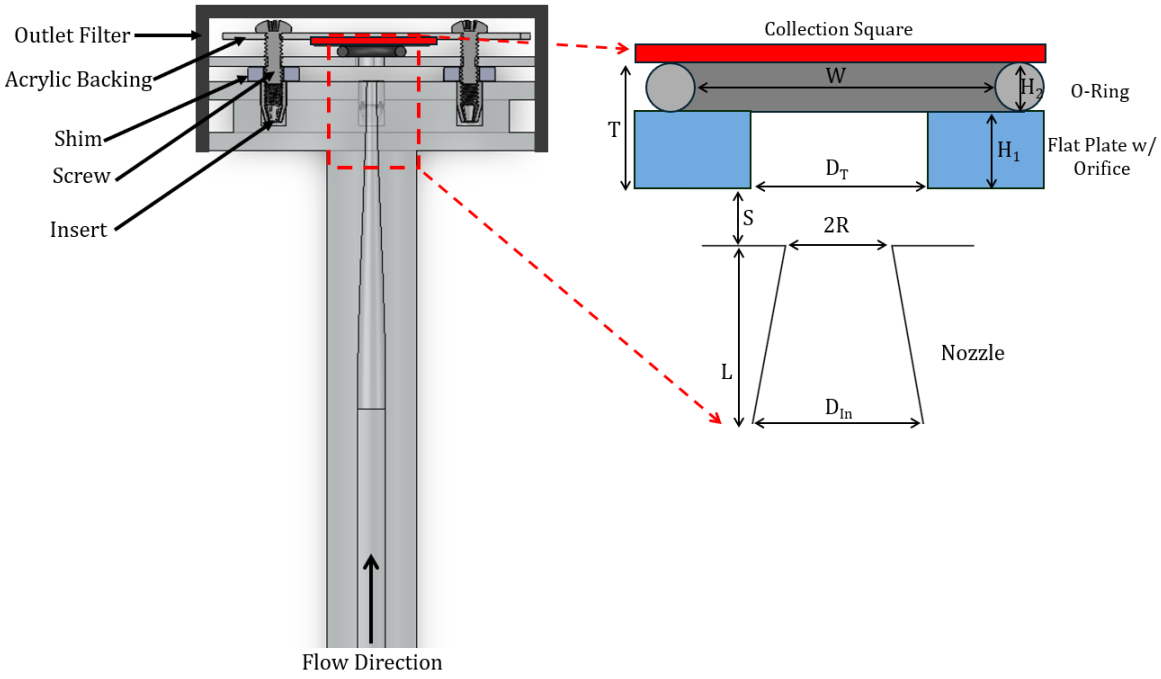

Figure 4.3: Cross-sectional view of impactor.

A schematic of the impactor cross-section is presented in the inset in Figure 4.3, showing the cylindrical trap created by the orifice in the impactor plate and the compressed o-ring between the plate and collection square. The nozzle inlet diameter is D_{In} = 4.4 mm,

the nozzle length is L = 127 mm, the o-ring thickness is H_2 = 2.2 mm, and the o-ring diameter is W = 10 mm. The impactor dimensions were chosen to mimic a typical straw and to make it easy for the user to hold and blow into the device. The nozzle outlet diameter, 2R, is varied, as is the distance between the nozzle exit and the flat plate, S, the flat plate thickness, H_1, and the trap-entrance diameter, D_T. A shim separates the end of the nozzle and the impactor plate to set the distance S. The collection square covers the back of the o-ring to collect particles deposited on the back of the trap. The acrylic backing, collection square, o-ring, flat plate, and shims are screwed into the nozzle with threaded inserts. As the screws are tightened and compress the components, the o-ring experiences a small, negligible deformation in its thickness (the nominal o-ring thickness is used for geometric considerations). The outlet filter is wrapped around the outlet and secured with an elastic band to collect any droplets with low enough St that follow the streamlines past the impactor plate. The trap ratio (TR) characterizes the nozzle-to-trap aspect ratio and is given by,

$$\mathrm{TR} = \frac{D_T - 2R}{T} \tag{4.4}$$

The numerator, $D_T - 2R$, is the trap opening clearance, and T is the total trap depth.

4.2 Water Aerosolization Setup

Initial experiments used water droplets to characterize the impactor efficiency, that is, how well the impactor removes particles of a given Stokes number. All components of the experimental setup are shown below in Figure 4.4 and Figure 4.5, and the air pre-conditioning and droplet generation systems will be explained in detail.

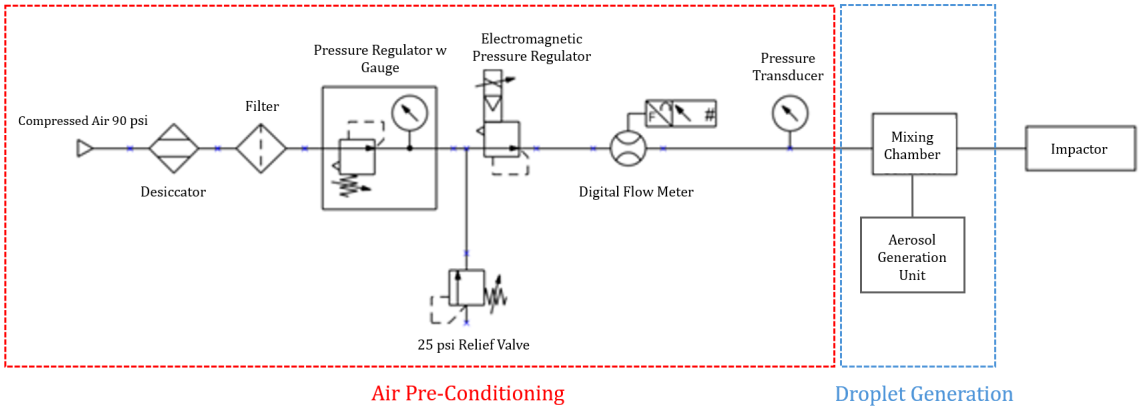

Figure 4.4: Experimental setup schematic.

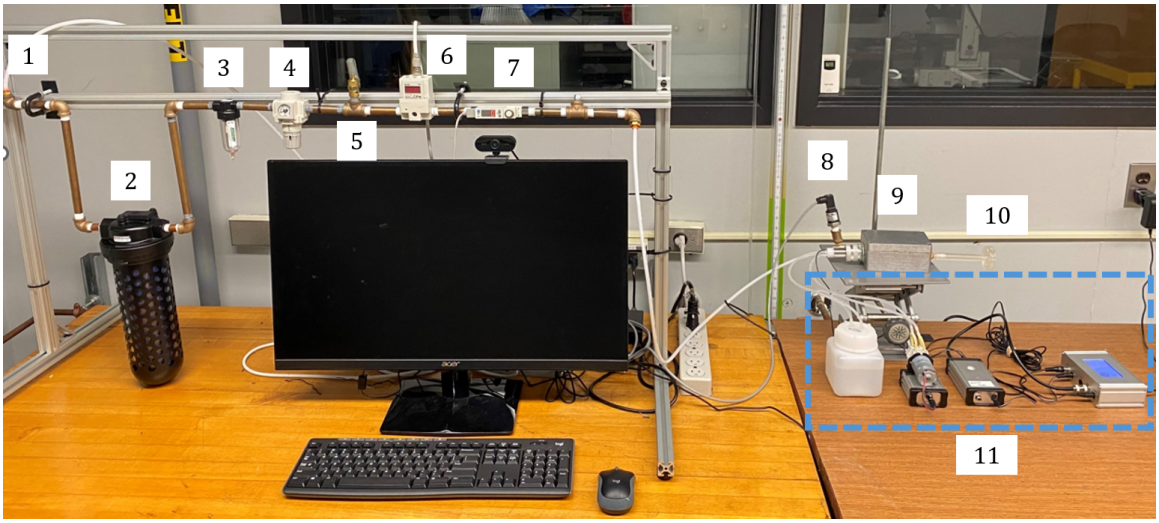

Figure 4.5: The experimental setup consists of 1) compressed air, 2) desiccator, 3) filter, 4) pressure regulator with gauge, 5) 25 psi relief valve, 6) electromagnetic pressure regulator, 7) digital flow meter, 8) pressure transducer, 9) mixing chamber, 10) impactor, 11) water droplet generation unit.

Air Pre-Conditioning: Compressed air is supplied to the system at 90 psi, after a desiccator removes excess moisture. A filter is placed after the desiccator to remove particles and other contaminants larger than 5 μm. An analog pressure regulator reduces the air pressure to 18 psi. A 25 psi relief valve is added downstream and actuates in the event of a spike in air pressure to prevent the components from being damaged. An electromagnetic flow regulator (EMR, SMC ITV 1000) adjusts the pressure by opening and closing a solenoid valve controlled through LabVIEW and a National Instruments Data Acquisition (DAQ)

system with -10 to 10 V analog input (National Instruments NI-9263) and output voltage (NI-9201) modules. After the electromagnetic regulator, a digital flow meter (SMC PFM7 Digital Flow Switch) is also connected to LabVIEW. The flow rate is the pertinent metric in the operation of the impactor, as it is directly related to the impactor outlet velocity, which determines the Stokes number. The upstream pressure at the EMR is varied to set the desired air flow rate. A pressure transducer is connected before the air inlet of the aluminum mixing chamber (152.4 $\times$ 76.2 $\times$ 101.6 mm).

Droplet Generation: The mixing chamber has two inlets and one outlet. Inlet 1 is connected to the conditioned air, inlet 2 is connected to the water droplet generation system, and the outlet outputs the droplet-laden airstream to the impactor. Water droplets are generated using the Tekceleo P&S-360 nebulizer, with a schematic shown below in Figure 4.6 and a picture of the generation system shown in Figure 4.7.

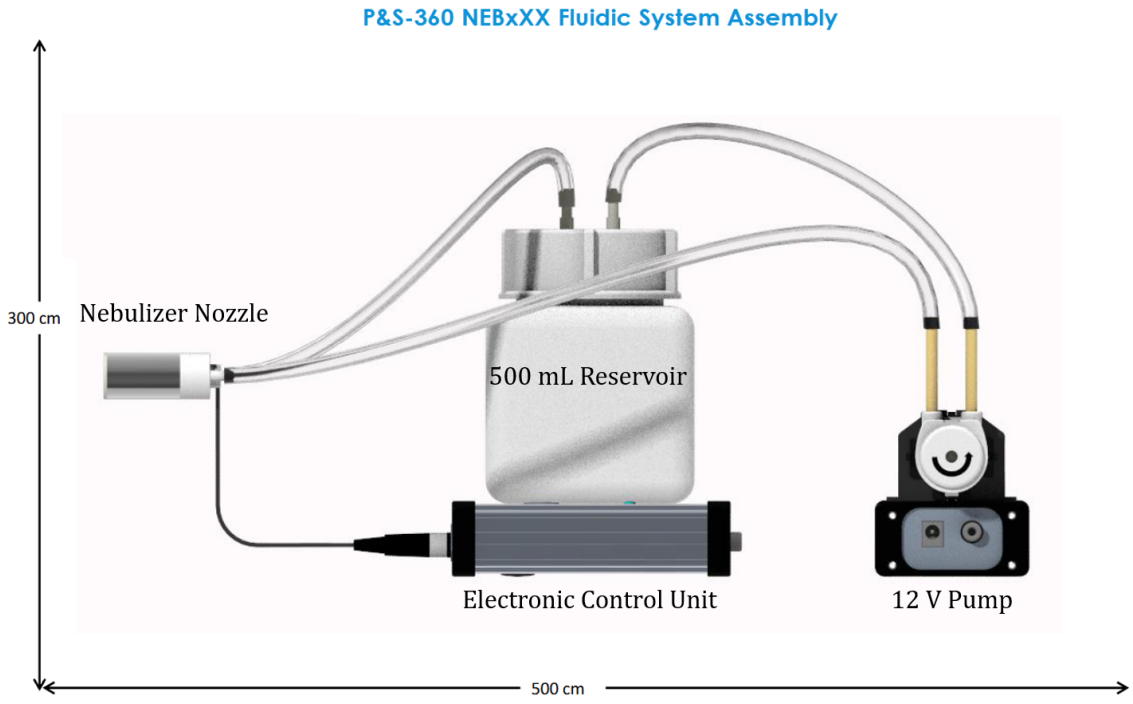

Figure 4.6: Water droplet generation setup using the Tekceleo P&S-360 electronic sprayer kit. Reproduced from Tekceleo.

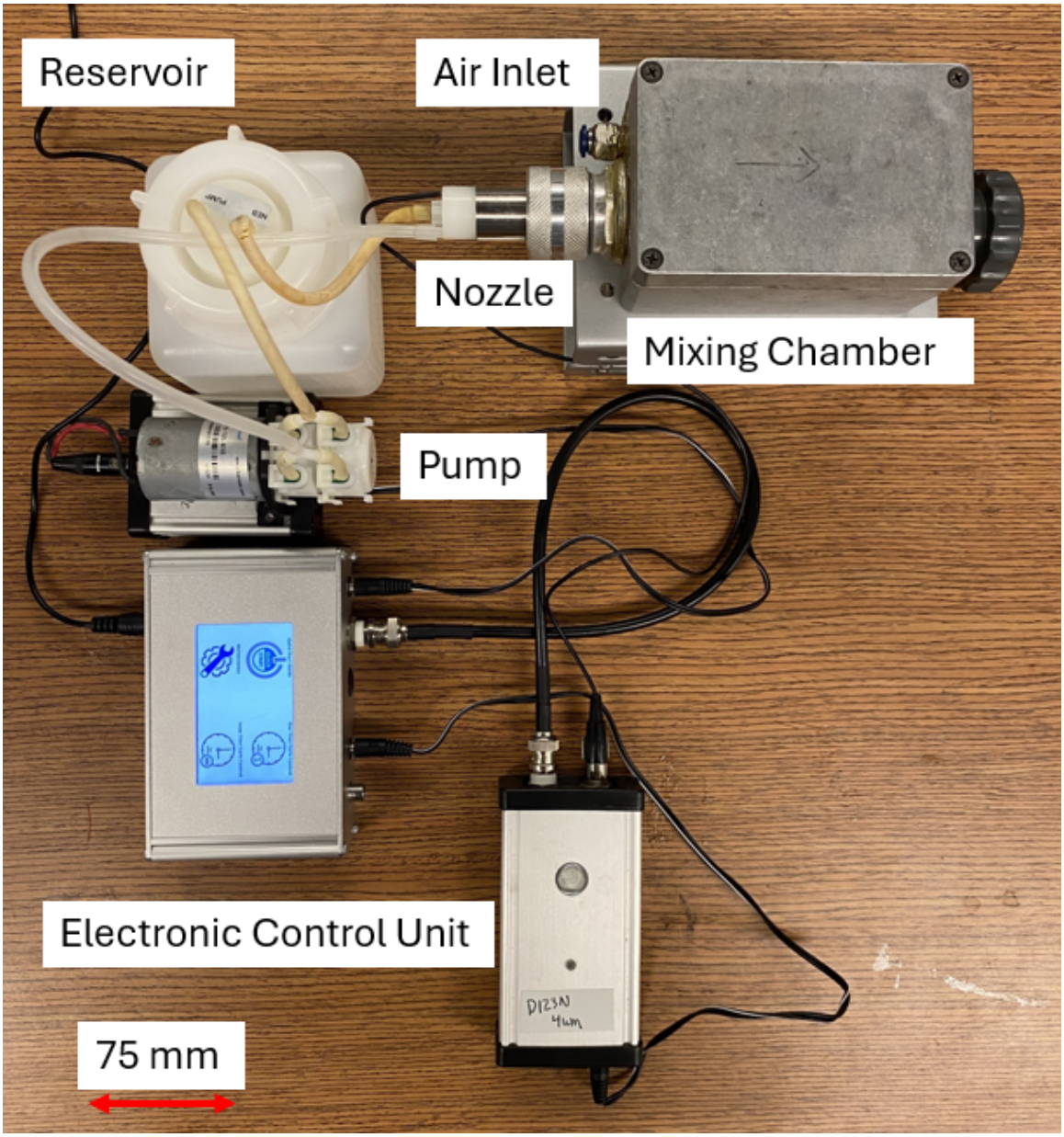

Figure 4.7: Picture of Tekceleo P&S-360 electronic sprayer kit.

The nebulizer is a vibrating mesh generator that nominally creates 4 μm water droplets. Deionized water is circulated at 155 mL/min by a 12 V pump from the 500 mL liquid reservoir to the pump, through the nebulizer, and back to the reservoir. When the water reaches the nebulizer nozzle, it is held in a small chamber inside the aluminum housing. The droplets are generated using a low-power piezoelectric effect. A mesh substrate is vibrated over the water, and as it makes contact, it forces the water through the mesh,

creating 4 μm droplets. The electronic control unit (ECU) regulates the duty cycle and linearly changes the nebulizer and pump water flow rates to ensure the nebulizer is constantly primed. The water flow rate was constant for all experiments at 1 mL/min (+/- 0.2 mL/min), but the nebulization time varied depending on the air flow rate of interest. The nebulizer nozzle is inserted into inlet 2 through a chord grip connection. Inside the mixing chamber, the water droplets combine with the dry air, creating a uniformly distributed particle-laden flow transported to the impactor nozzle.

4.3 Olive Oil Atomization Setup

Subsequent experiments were performed using olive oil droplets. Olive oil droplets were used to address the potential complication of water droplet evaporation. The experimental setup for the olive oil characterization experiments is shown below in Figure 4.8.

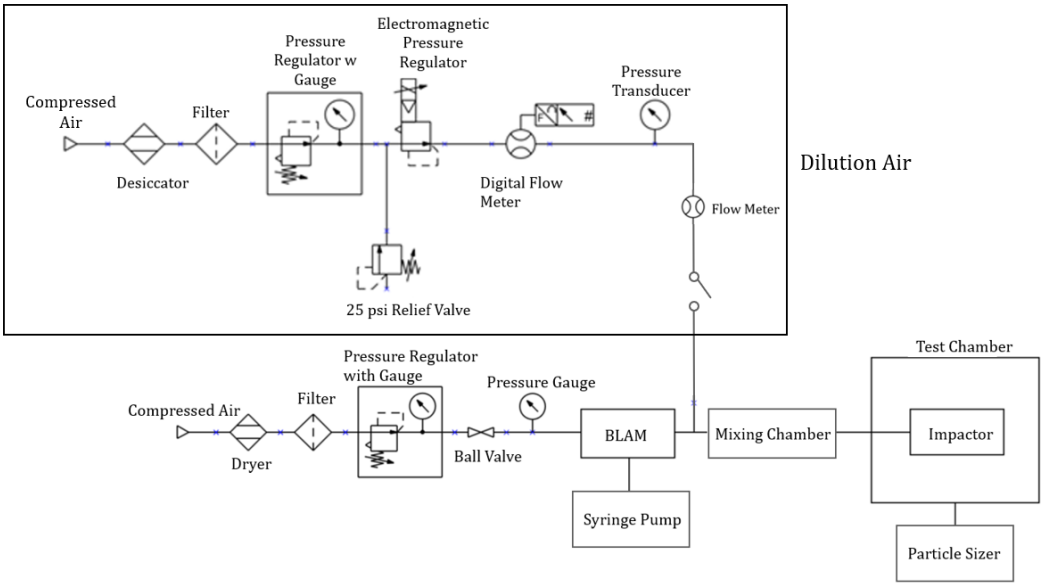

(a)

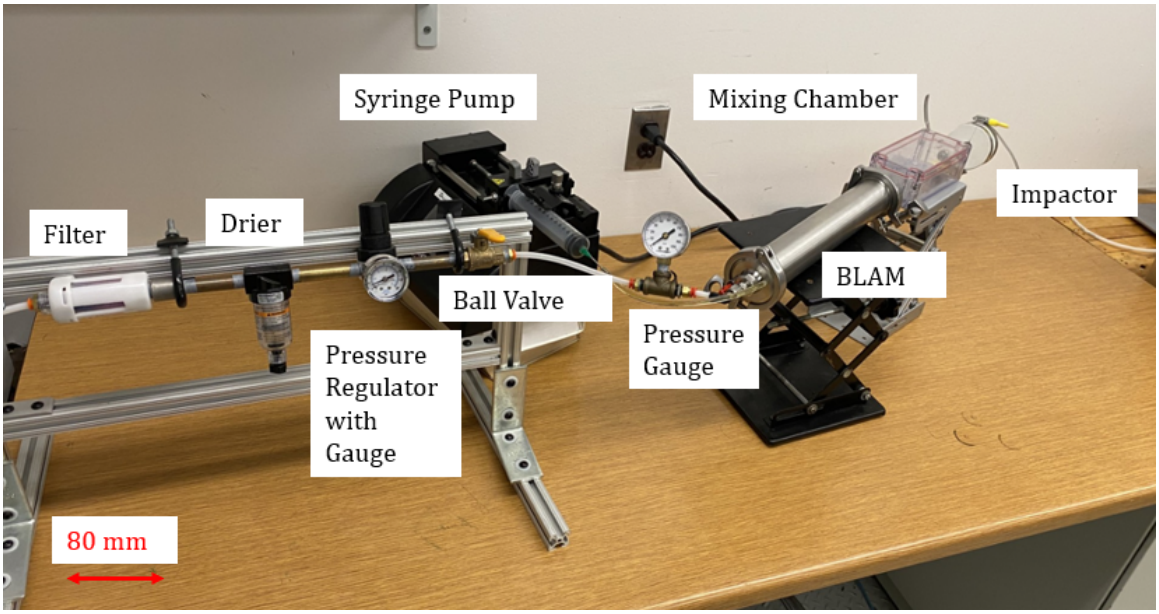

(b)

Figure 4.8: a) Schematic of olive oil efficiency experimental setup, b) Picture of setup before dilution air from water droplet setup is used.

The experimental setup is similar to the water droplet setup, using compressed air, a desiccator, and a filter to pre-condition the air. The pressure regulator and gauge are used to control the downstream pressure. A ball valve is added to allow the conditioned air

to flow into the rest of the setup. A second pressure gauge is added before the Blaustein Atomizer (BLAM) to measure its inlet pressure.

Blaustein Atomizer (BLAM) The BLAM generates the olive oil aerosols. The pre-conditioned air is introduced into the air inlet fitting, and a Harvard Apparatus syringe pump feeds the BLAM olive oil at a constant flow rate of 5 mL/min into the liquid feed port. The olive oil then enters the atomization nozzle through the liquid feed tube. Inside the atomization system are four nozzles that create high-speed jets to shear the liquid into fine droplets. However, unlike the Tekceleo nebulizer used in the water droplet experiments, the atomized olive oil droplets are polydisperse, and the distribution is a function of the pressure gradient across the BLAM inlet and outlet. The BLAM is placed on its side and connected to the aerosol pipe that guides the droplets to a different mixing chamber from the water droplet setup with one inlet and one outlet. This configuration allows for higher droplet concentration and larger aerosols to enter the mixing chamber and, ultimately, the impactor.

4.3.1 Olive Oil Aerosolization Procedure

We developed the following two-step process in order to generate repeatable particle distributions for impactor characterization. First, the olive oil test aerosols are injected into the mixing chamber for 15 seconds. The resulting particle distribution inside the mixing chamber is assumed to be statistically identical for each experiment. Then, the BLAM output is disconnected from the mixing chamber inlet and replaced by the airline from the pre-conditioned air in the water droplet experiments (dilution air). The rationale for this procedure is that the droplet distribution generated by the BLAM is a function of its pressure gradient and, subsequently, its air flow rate. The BLAM air flow rate must be constant to keep the particle distribution constant. In order to be able to vary the Stokes number of the aerosol particles and characterize impactor efficiency, the impactor flow rate must be variable. Therefore, the secondary air line replaces the BLAM air line to vary the air flow rate while allowing the BLAM flow rate to be constant in the first step. This process

is repeated up to 10 times to ensure an adequate droplet mass has been injected into the impactor ($\approx$ 8 mg). The outlet filter used for the air droplet experiments is replaced with a 3D printed enclosure and HEPA filter shown in Figure 4.9 that collects droplets larger than 0.3 µm that are not removed by the trap or flat plate.

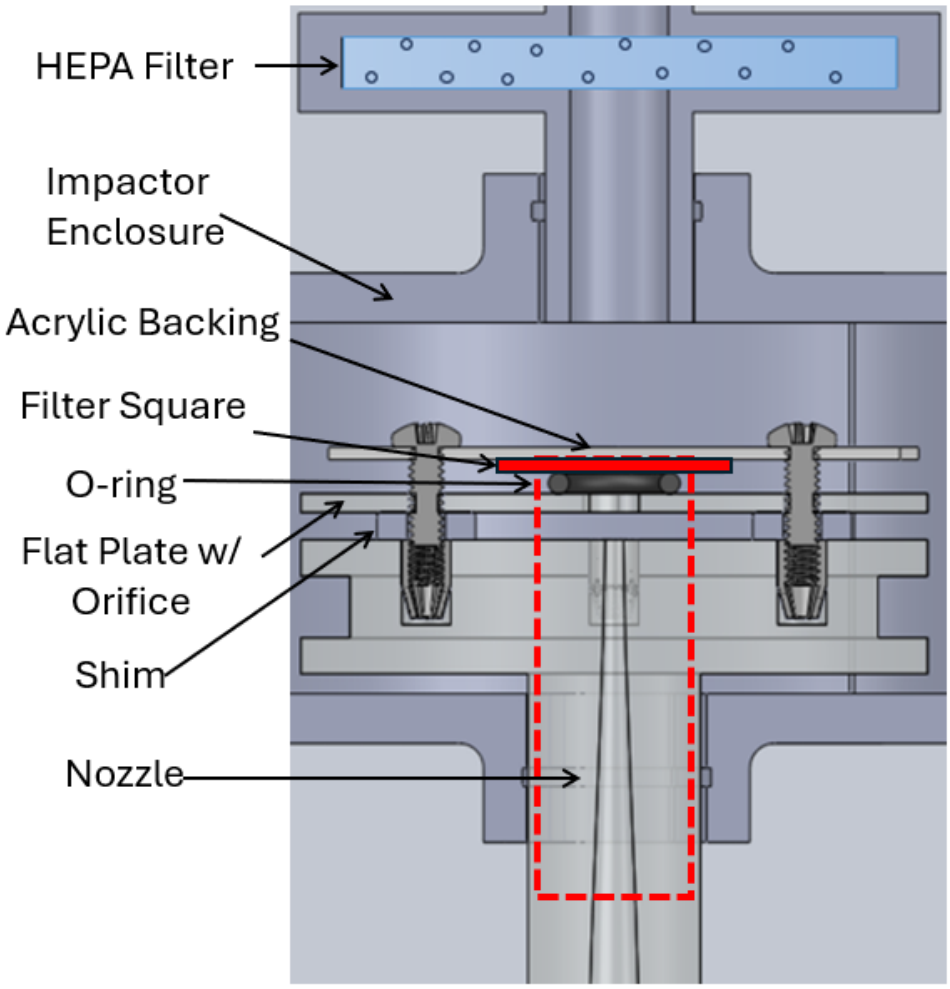

Figure 4.9: Schematic of impactor with enlosure and HEPA filter.

4.4 Particle Sizing Setup Units

It is imperative to characterize the particle size distribution exiting the nozzle because this distribution ultimately determines impactor efficiency. We used two methods to measure the olive oil particle size distribution exiting the nozzle.

4.4.1 Droplet Microscopy

The first method utilizes a Nikon Eclipse Ti-U inverted microscope to examine the olive oil droplets that have settled on a glass slide. The impactor nozzle is placed in a polystyrene chamber (254 × 381 × 163 mm) and a glass slide (76 × 25 × 2 mm) is placed on the chamber floor. The nozzle injects the droplet-laden stream into the chamber using the two-step method described above. The droplets settle under gravity and onto the slide for approximately seven minutes. When the droplets settle on the glass slide, a contact angle (θ) is formed by the olive oil-air-glass interface. A schematic is shown below in Figure 4.10.

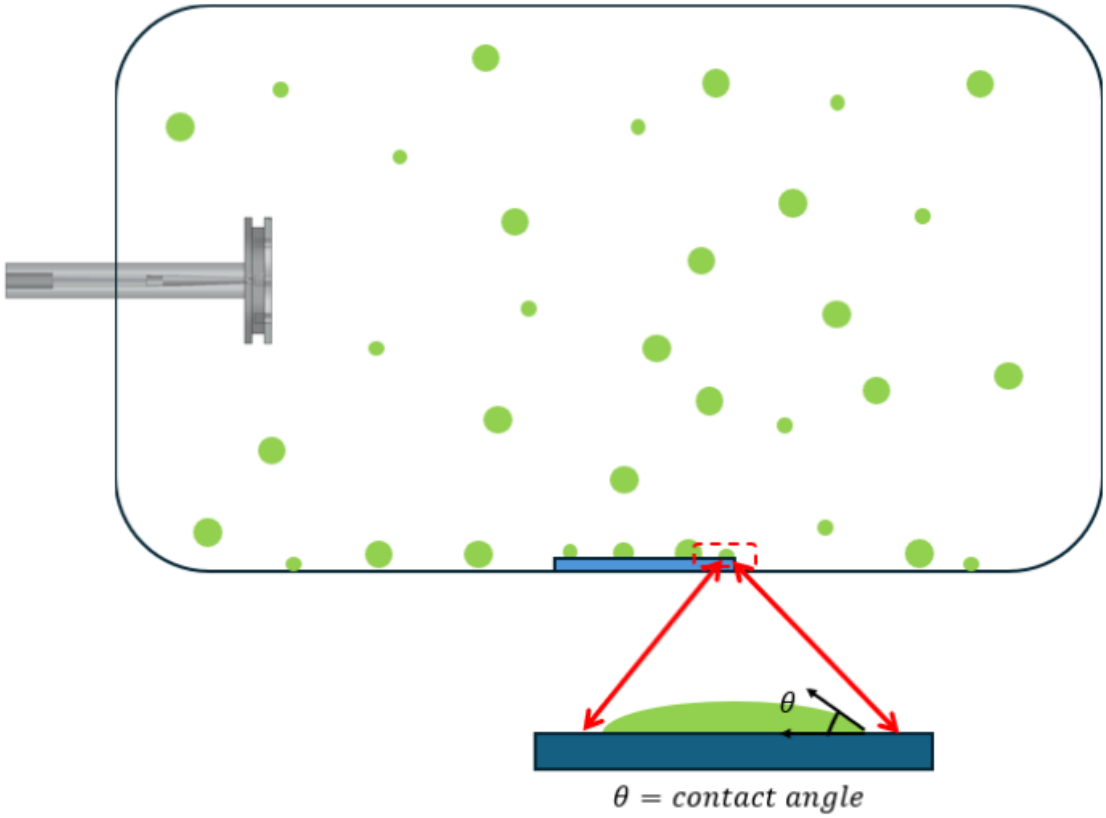

Figure 4.10: Schematic of olive oil droplets settling onto glass slide.

After the droplets have settled onto the slide, the slide is removed and placed on the stage of the inverted microscope. A 10x magnification objective lens, an extra 1.5x magnification lens, and a light source are used to view the droplets. A picture of the microscope

setup is shown in Figure 4.11. A Hayear 5MP camera is mounted in the auxiliary port to take images of various parts of the glass slide. A calibration slide was used to determine that each pixel is ≈ 0.5 µm $\times$ 0.5 µm. These images are then analyzed in MATLAB to determine the recorded droplet diameters and reconstruct the particle size distribution as shown in Figure 4.12.

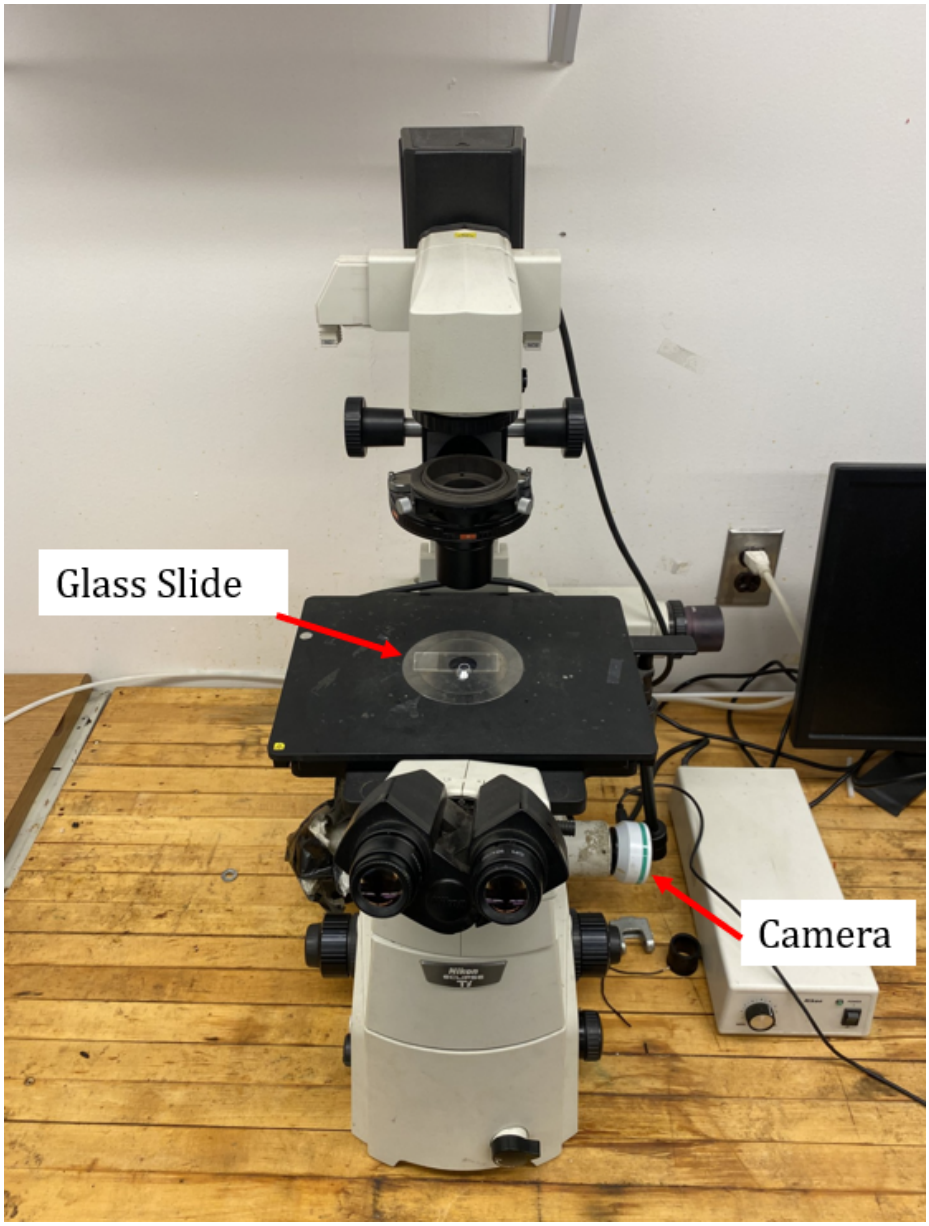

Figure 4.11: Picture of the inverted microscope used to measure the olive oil droplets on a glass slide.

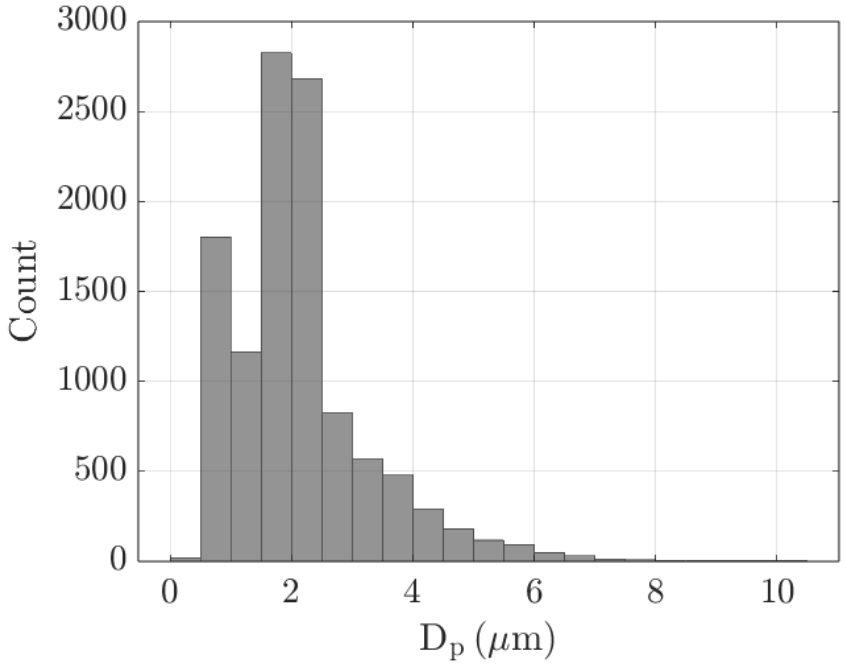

Figure 4.12: Particle size distribution of olive oil droplets deposited on a glass slide as measured by the inverted microscope.

4.4.2 Optical Particle Sizer

A second method to determine the particle size distribution was employed using a TSI Optical Particle Sizer Model 3330 (particle size range 0.3 to 10.53μm using an index of refraction of 1.44 for olive oil, and size resolution of 5% at 0.5 μm per ISO 21501-1, the industry standard for determining particle size distributions through single particle light interaction methods). The experimental setup is similar to the droplet settling experiments, except now the glass slide is removed, and the particle sizer samples the droplets inside a larger chamber (356 $\times$ 438 $\times$ 280 mm). An outlet port is added to the chamber that leads into the particle sizer inlet. The droplet-air mixture is injected into the chamber for 10 seconds and allowed to rest undisturbed for 30 seconds before the air is sampled. 30 seconds is not long enough for the largest particles (10 μm) to settle to the bottom of the, and settling effects are assumed to be negligible. The device has an internal pump that samples the air at 1 L/min. The light scattered by the droplets is determined by the droplet

diameters. A laser diode, collimating lens, and cylindrical lens shape the beam into a thin sheath intersecting the aerosol stream. The light scattered by the droplets is collected by an elliptical mirror and focused onto the photodetector, where the signal is processed and the particle size is determined. A refractive index of 1.44 is used for olive oil to correct the particle sizes, as the device is calibrated for latex spheres. Although the olive oil droplets are liquid, they are assumed to be rigid due to the low Capillary numbers discussed in chapter 3. Particles are automatically assigned to discrete bins ranging from 0.3 - 10.53 μm, and the particle size distribution can be constructed similarly to Figure 4.12.

4.5 Impactor Efficiency Methodology

Impactor efficiency is measured gravimetrically by weighing the different impactor components before and after each experiment. The mass of water, or olive oil, deposited on each item is determined and used to calculate the percentage of mass removed from the flow. An Ohaus Adventurer AX124/E precision balance with a measurement uncertainty of 0.2 mg was used to weigh each component. The weighted components are the nozzle (m_n), impactor plate (m_p), collection square ($m_{trap,b}$), and outlet filter (m_f). The o-ring is not measured due to repeated measurements indicating a negligible change in mass. The total mass of water injected into the system is, therefore, $m_t = m_n + m_p + m_{trap,b} + m_f$. A picture of the impactor components is shown below in Figure 4.13, and the combined impactor and impactor plate are shown in Figure 4.14.

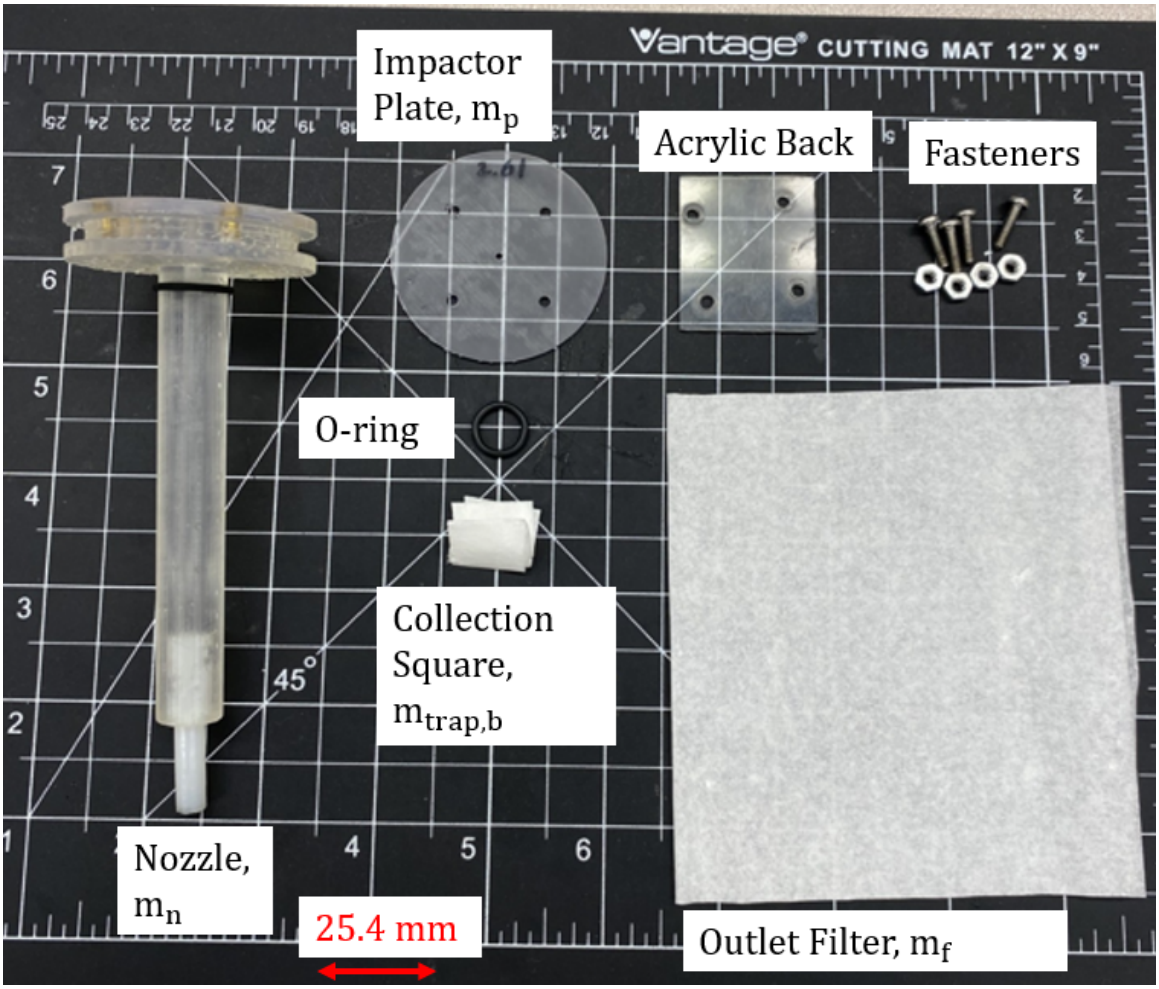

Figure 4.13: Impactor components used for water droplet efficiency experiments.

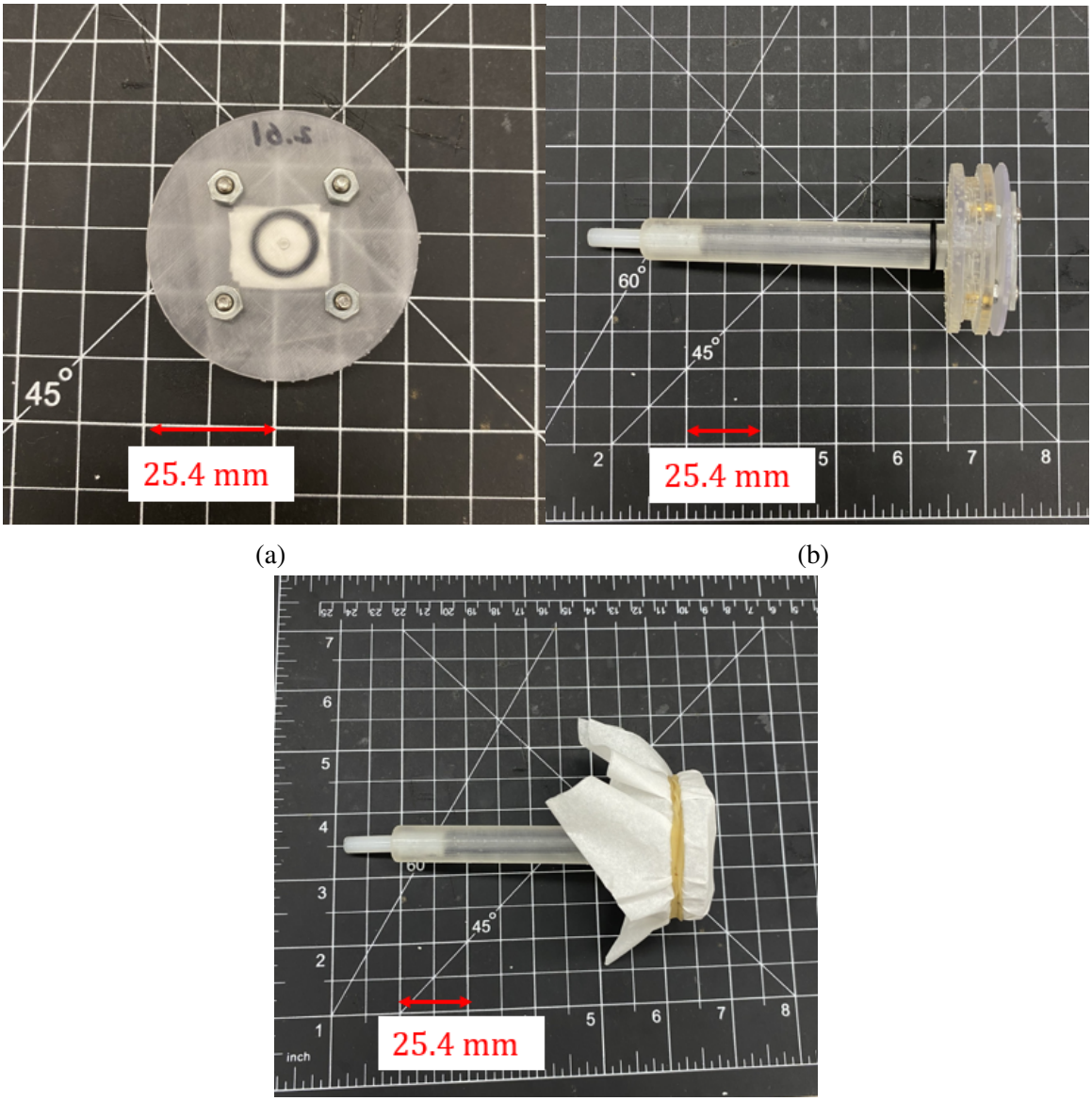

(a) (b)

(c)

Figure 4.14: a) Assembled impactor plate, b) Assembled impactor without filter, c) Assembled impactor.

For the olive oil droplet experiments, m_f represents the mass in the HEPA filter, and the enclosure is not weighed due to a negligible change in mass. The assembled impactor used for the olive oil experiments is shown in Figure 4.15b.

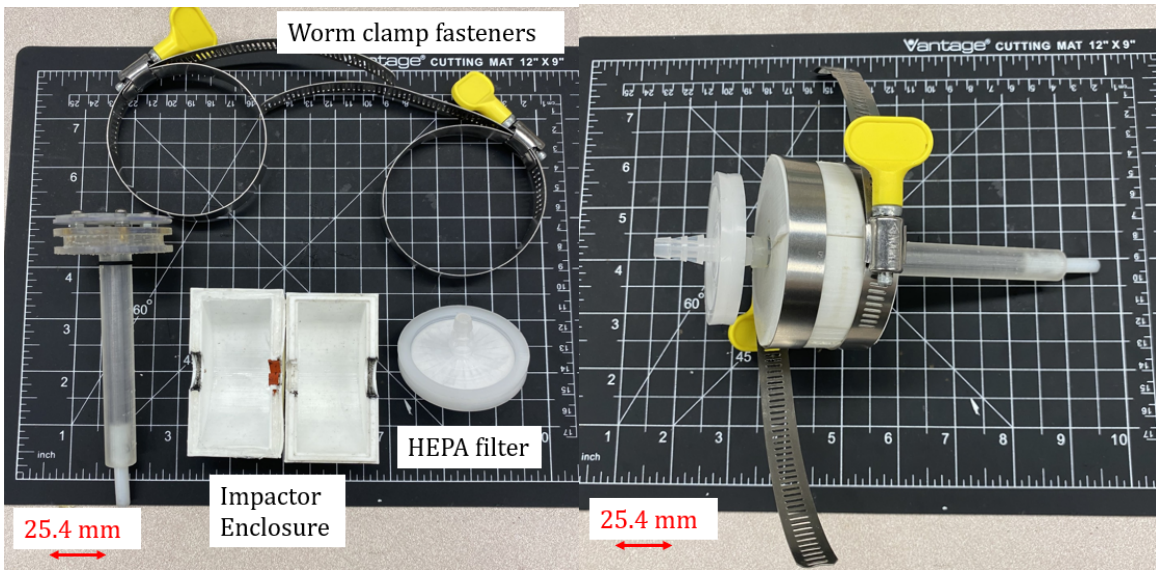

(a) (b)

Figure 4.15: a) Assembled impactor and disassembled enclosure used for olive oil experiments, b) Combined impactor

Droplets can accumulate on the interior and the outer wall of the nozzle. To remove the mass on the outer wall, it is wiped with a fiberglass cloth. The nozzle is then weighed again, and this measurement provides the mass of droplets only deposited on the interior surface, denoted as m_i. The difference between the initial nozzle mass and the internal mass is the droplet mass that was on the end of the nozzle, $m_{n,l} = m_n - m_i$. The impactor plate is also weighed a second time to account for droplets depositing on the top surface and not inside the trap. Measuring the impactor plate a second time after wiping the top surface gives the mass of droplets on the trap walls, $m_{trap,\,w}$.

Two efficiencies are calculated for each trial: removal (η_R) and trap (η_{Trap}) efficienies, as defined below,

$$\eta_R = 1 - \frac{m_f}{m_t - m_i}. \tag{4.5}$$

$$\eta_{Trap} = \frac{m_{trap,\,b} + m_{trap,\,w}}{m_t. - m_i} \tag{4.6}$$

Removal efficiency is the standard measure of impactor efficiency and the percentage of mass removed from the flow. Trap efficiency is the percentage of mass collected inside the trap. Only the droplets that exit the nozzle are considered for the removal and trap efficiencies. Wall losses are droplets removed from the flow exiting the nozzle but not collected inside the trap, and their corresponding fraction is,

$$W = \eta_{\text{R}} - \eta_{\text{Trap}} \tag{4.7}$$

The wall losses account for the nozzle and plate losses. Experiments using flat plates instead of traps were performed as well and only the removal efficiency is calculated in that case.

4.6 Uncertainty Analysis

4.6.1 Air Flow Rate Uncertainty Analysis

The digital flow meter has a nominal uncertainty of 5 L/min, which is too high for this application. However, the flow rate displayed by the digital flow meter was compared to multiple rotameters with high agreement and much smaller uncertainty. Specifically, four rotameters were used and their specifications are shown in Table 4.1. The rotameters have units of standard cubic feet per hour (SCFH) and are converted to L/min using a temperature of $20°$C and atmospheric pressure.

Rotameter	**Range [L/min]**	**Uncertainty (u_c) [L/min]**	**Q Measured [L/min]**
Dwyer VFA-41	0.05 - 0.5	0.01	0.5 - 1
Dwyer RMA-4	0.5 - 5	0.1	2 - 5
Dwyer VFA-5-SSV	2 - 20	0.5	6 - 20
Dwyer VFA-8-BV	5 - 50	2.35	21 - 30

Table 4.1: Rotameters used to compare against digital flow meter.

For varying air flow rates through the 1.5 mm nozzle, the digital flow meter and analog rotameter were added in series, and their measured flow rates are compared in Figure 4.16. The line of best fit is shown, and high agreement between the digital and analog devices is displayed, highlighting that the digital uncertainty is far lower than the reported 5 L/min. For convenience, the digital flow meter is used throughout this thesis.

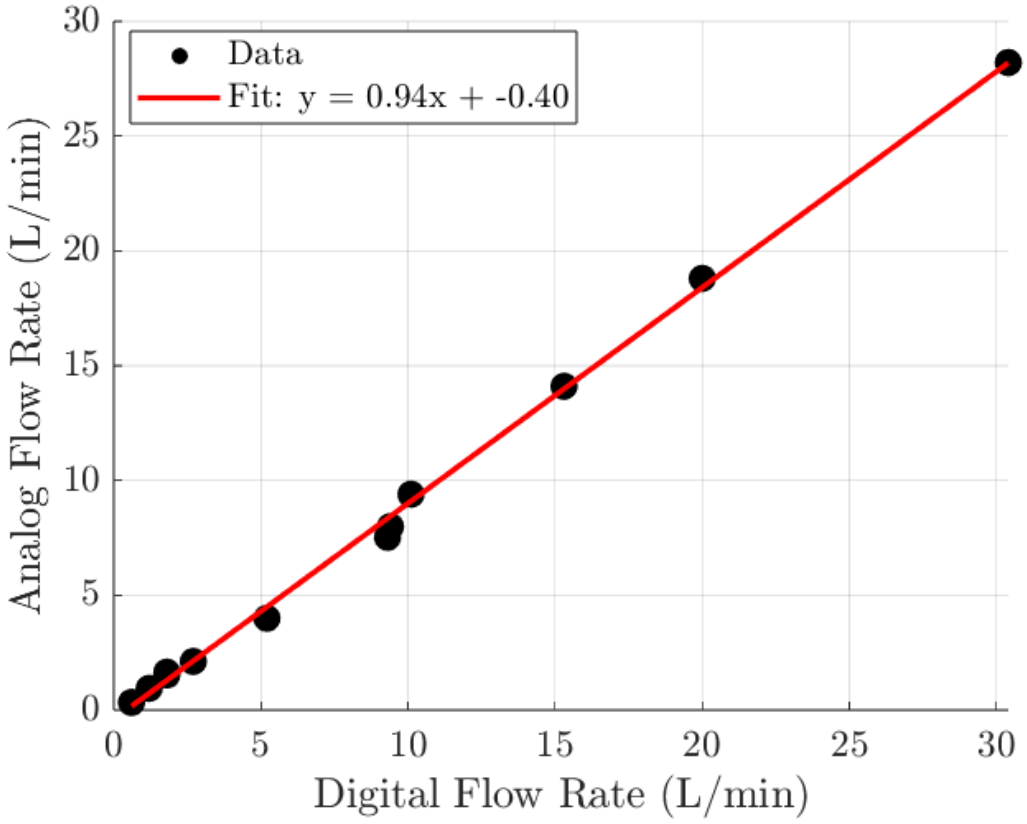

Figure 4.16: Comparing the flow rates measured by the digital flow meter and different rotameters.

The line of best fit is then used to convert the flow rate measured by the digital flow meter to the flow rate of the rotameters with lower uncertainties. The flow rate uncertainty, u_Q is calculated below as

$$u_Q = \sqrt{(\Delta Q)^2 + u_c^2}, \tag{4.8}$$

where ΔQ is the maximum difference in flow rate measurements and acts as a systematic error, and u_c is the uncertainty of the rotameter used. The digital flow rate measurement uncertainties are shown in Figure 4.17 for flow rates between 0.5 and 30 L/min and are significantly lower than the nominal 5 L/min. The large increases in error observed at 5 and 20 L/min is due to the increases in u_c between different rotameters.

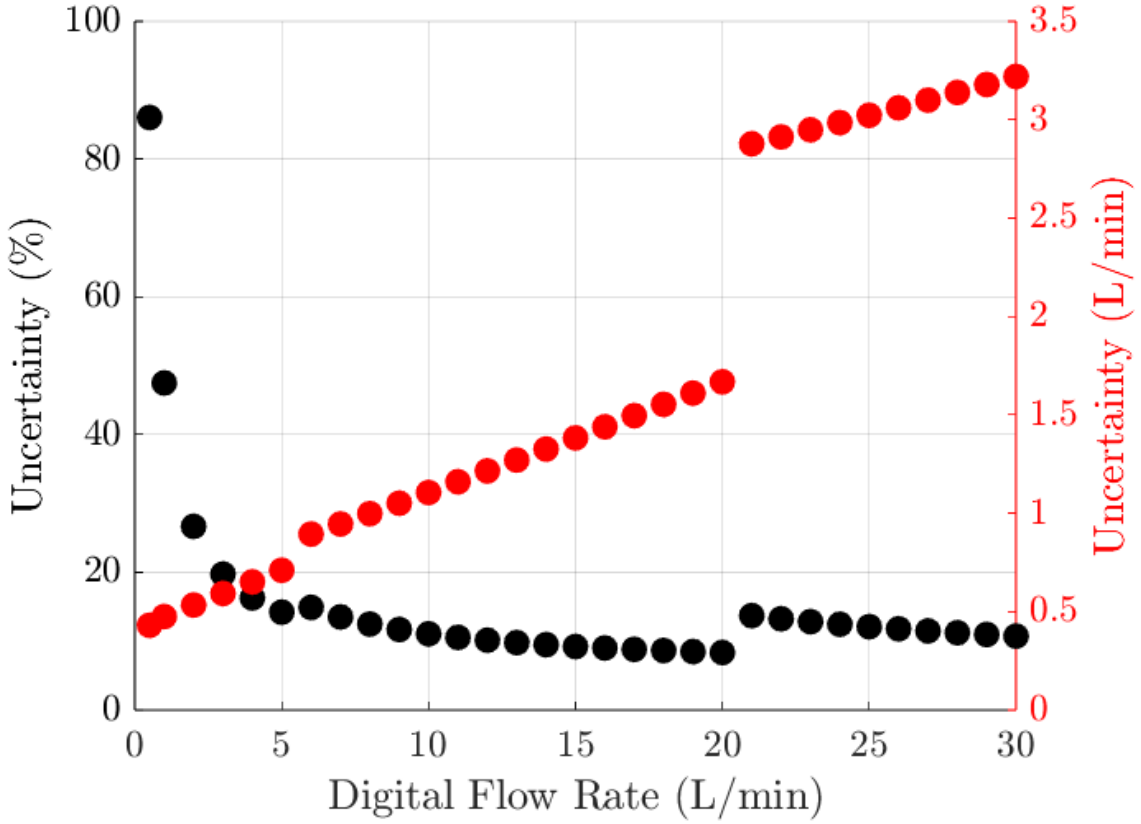

Figure 4.17: Comparing the flow rates measured by the digital flow meter and different rotameters.

4.6.2 Stokes Number Uncertainty

The uncertainty in the Stokes number is calculated using error propagation. The Stokes number for impactors is given by Equation 3.18. There are two main contributors to the Stokes number uncertainty: the outlet velocity and the particle size. The outlet velocity uncertainty is the same as the flow rate uncertainty, u_Q divided by the area of the nozzle

outlet, and the particle diameter has a nominal uncertainty of 5% due to the particle sizer. Air density, Cunningham slip correction, air dynamic viscosity, and nozzle radius are assumed to be known with certainty. The resultant uncertainty in the Stokes number is given by,

$$u_{St} = \sqrt{(u_{V_0}\frac{\rho_P D_P^2 C_c}{18\mu R})^2 + (u_{D_P}\frac{\rho_P V_0 D_P C_c}{9\mu R})^2} \tag{4.9}$$

4.7 Pressure vs Flow Rate Measurements

After configuring the experimental setup, initial experiments were performed to measure the effect of the gap size (S) on the flow rate for the 1.5 mm nozzle. Experiments were performed by varying the inlet pressure and measuring the resultant air flow rate with gap sizes of 0.1, 0.7, 1.4, 2.1, and 2.6 mm with a flat plate as the obstruction, and also for the free jet. In these experiments, single-phase air is used without the aerosol generation system. The results are shown below in Figure 4.18, along with the predicted air flow rate for the free jet for the 1.5 mm nozzle using Equation 3.3. The error bars are the corresponding errors shown in Figure 4.17. The experimental error bars overlap with the predictions, except for the 0.1 mm gap, where there is a significant decrease in flow rate. This is potentially due to a strong adverse pressure gradient created by the proximity of the flat plate to the nozzle exit. From these results, the gap thickness will be at least 0.7 mm.

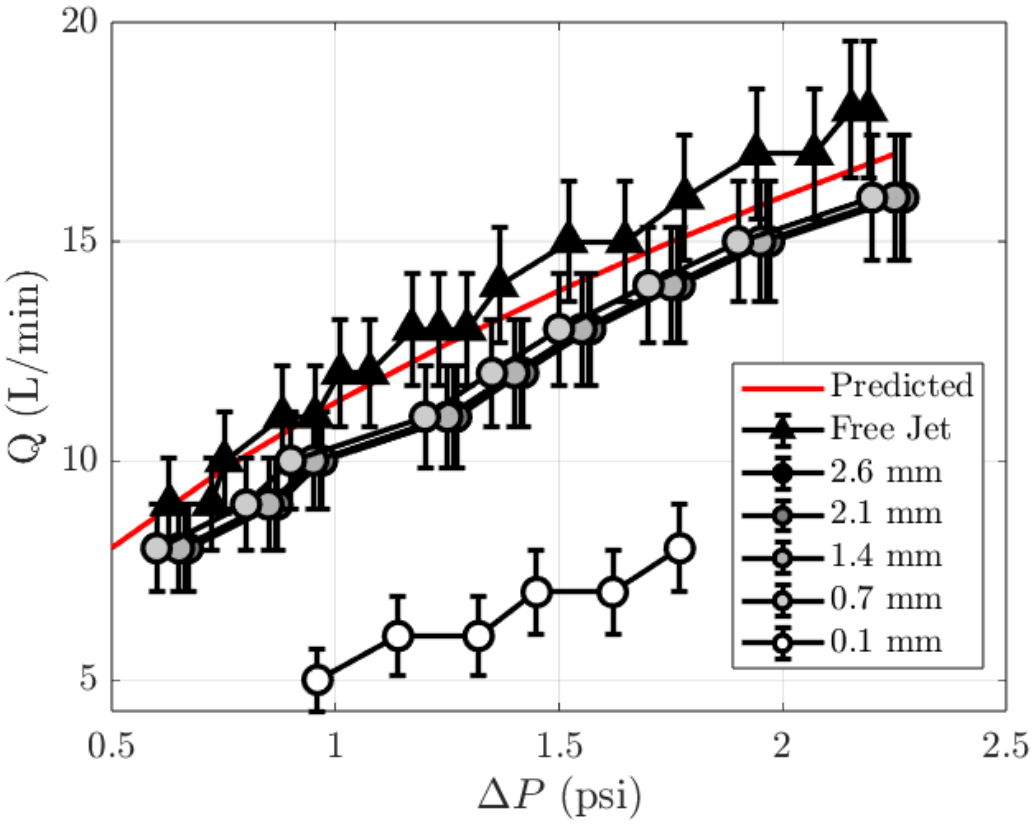

Figure 4.18: Nozzle flow rate as a function of inlet pressure for various gap thicknesses. Experimental values are compared with the predicted values for a nozzle without the presence of a flat plate.

CHAPTER 5

IMPACTOR EFFICIENCY

5.1 Introduction

Figure 5.1 shows the nanowell collecting water droplets generated by the Tekceleo nebulizer, as described in section 4.2, over a 10s runtime. The well is initially empty, but within 0.1s, the first droplets are captured. As more droplets are captured, they start to coalesce and form a large droplet in the well, and after 10s, the well is filled. These images demonstrate that the impactor is able to collect the water droplets in the nanowell, but it does not provide any quantitative information about how efficiently it can trap the droplets.

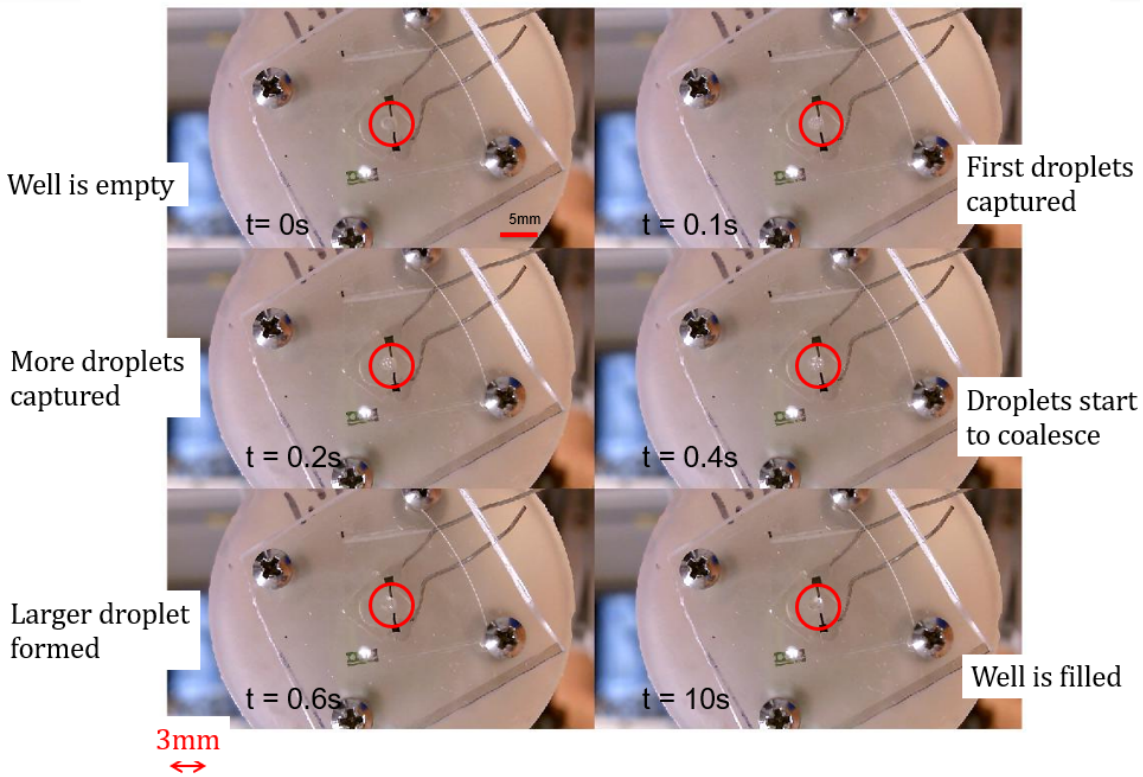

Figure 5.1: Pictures of water droplets collecting inside nanowell. The nanowell is initially empty but is filled within 10s.

As discussed in section 4.5, impactor efficiency is the percentage of particles that are

removed from the flow. Many studies have characterized impactor efficiency as a function of Stokes number. The square root of the Stokes number is used more commonly as it provides the dimensionless particle diameter. As the Stokes number increases, the particles have more inertia and are less likely to follow the streamlines and avoid the flat plate or particle trap.

5.1.1 Flat Plate Impactors

As mentioned, flat plate impactors use flat plates placed normal to the jet exit, and particles with enough inertia impinge on it. The prevalent geometric parameters of these designs are the nozzle outlet diameter, 2R, and the distance between the end of the nozzle and the plate, S. An ideal impactor has a threshold Stokes number, St_c, where all particles with $St \geq St_c$ will collide with the plate and be removed, and all others will evade the plate. This step-function model is shown below.

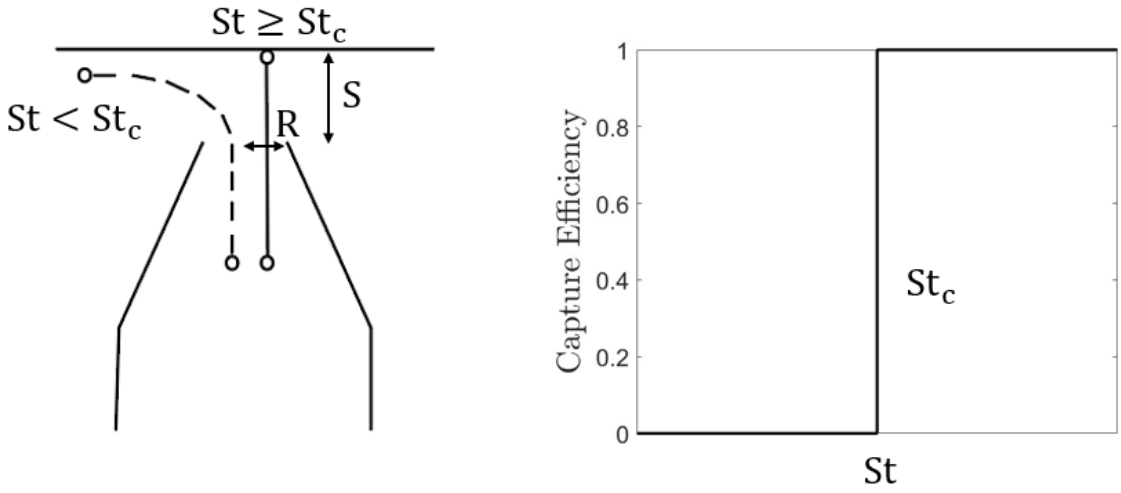

Figure 5.2: Theoretical capture efficiency model for a flat plate impactor.

Marple's seminal work on impactors included design criteria for developing impactors with sharp efficiency curves resembling the theoretical step-function model. In practice, impactors will not have a step-function increase from 0 to 100% efficiency due to the slight differences in particle diameter and the radial location of the particles in the jet. These

criteria stated that S/2R $\geq$ 1 [71, 72, 7]. However, it has been demonstrated that round impactors, with impaction plates placed between one and five nozzle radii from the nozzle exit (S/2R = 0.5 - 2.5), exhibit a removal efficiency that increases with $\sqrt{\text{St}}$ and reaches approximately 100% at $\sqrt{\text{St}_\text{C}} \approx 0.5$ [11, 12, 13, 14, 15, 16, 17, 18, 19, 20, 21]. Conversely, Grinshpun *et al.* [73] demonstrated that if S/2R decreases below 0.5, 100% efficiency can be reached for $\sqrt{\text{St}_\text{C}}$ as low as ≈ 0.2. However, as S/2R decreases, the adverse pressure gradient due to the proximity of the plate to the nozzle increases and can require larger inlet pressures, as demonstrated in chapter 4.

5.1.2 Trap Impactors

Trap impactors have increased complexity due to their geometry. The trap impactor was introduced to reduce the effects of particles impacting on the flat plate, but rebounding and being re-entrained back into the flow. Implementing the trap could collect particles inside the cavity and prevent this issue. However, including the trap increased more dimensional considerations. Typical non-dimensional geometric parameters for trap impactors are S/2R, known as the gap ratio; D_T/2R, called the diameter ratio; and T/2R, known as the depth ratio. Different trap designs used throughout the literature are presented in Figure 5.3.

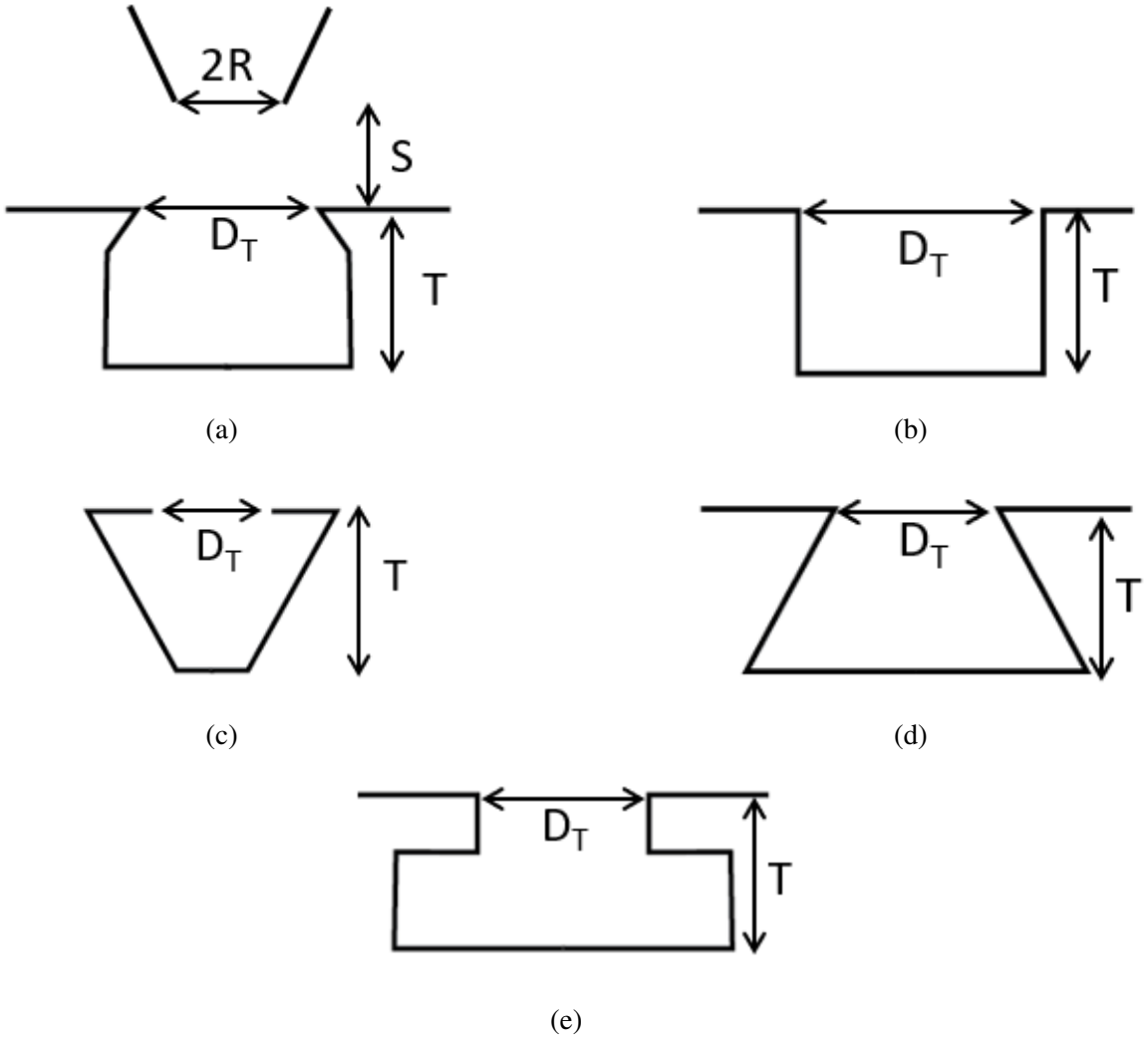

Figure 5.3: Different trap designs: (a) [22], (b) [74], (c) [15], (d) [75] conical, (e) [75] cylindrical. Reproduced from [76].

It has been shown that the trap geometry can alter the impactor efficiency curve. Biswas and Flagan[22] first introduced the trap impactor in 1988 and found that a diameter ratio $D_T/2R = 1.4$ and gap ratio $S/2R = 2$ gives spurious results where the efficiency did not monotonically increase with increasing particle inertia. However, when the diameter ratio increased to $D_T/2R = 1.9$, the results resembled a typical impactor and reached 80% efficiency at $\sqrt{St} \approx 0.8$.

Kim *et al.* [74] developed trap impactors and tested designs with $D_T/2R = 1.9$, 2.7, and 3.2, all with $S/2R = 1.2$. All three designs reached 80% efficiency but at $\sqrt{St} \approx 1$. Tsai and

Cheng [15] used a variation of a trap impactor with an orifice placed on top of the trap (see Figure 5.3c). They found that the efficiency decreased with decreasing $D_T/2R$ for similar $\sqrt{St}$. They also demonstrated that as the efficiency decreased, their wall losses increased. Wall losses were defined as particles that were removed from the flow but did not deposit inside the trap. The authors hypothesized that this increase in wall losses was due to the flow exiting the trap depositing the particles on the back side of the nozzle.

Chang *et al.* [75] used straight, conical, and cylindrical cavities (see Figure 5.3b, d, e) and found that the conical and cylindrical cavities had higher efficiency than the straight cavity. They also show that at the highest $\sqrt{St}$, the efficiency slightly decreases, which they attribute to the solid particles bouncing out of the trap. The trap impactors used in this thesis resemble the cylindrical traps introduced by [75].

5.2 Water Droplet Efficiency Results

Initial experiments using 4 μm water droplets as test aerosols were conducted using three impactors with geometries given in Table 5.1.

2R (mm)	TR	$D_T/2R$	S / 2R	T / 2R	Q_{air}(L/min)
1.5	0.59	2.7	1.5	2.9	1 - 12
2.3	0.54	2	1	1.9	0.4 - 18
3	1.19	2.7	1.5	1.4	0.5 - 25

Table 5.1: Trap impactor parameters for 2R = 1.5, 2.3, and 3mm nozzles.

The nebulizer nominally generates a monodisperse distribution of 4 μm droplets. Therefore, the Stokes number can only be altered by varying the nozzle outlet velocity. The removal and trap efficiency curves for the three impactors are presented below.

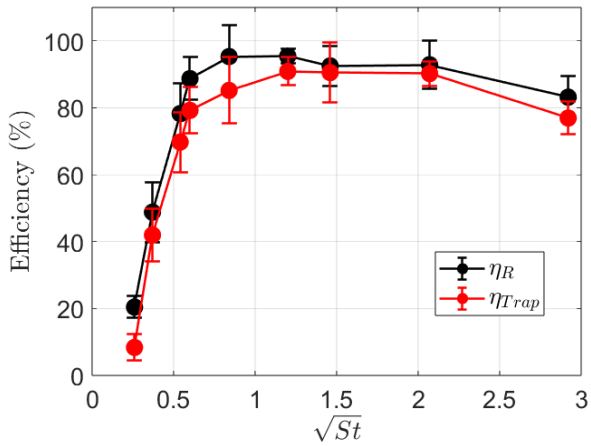

(a)

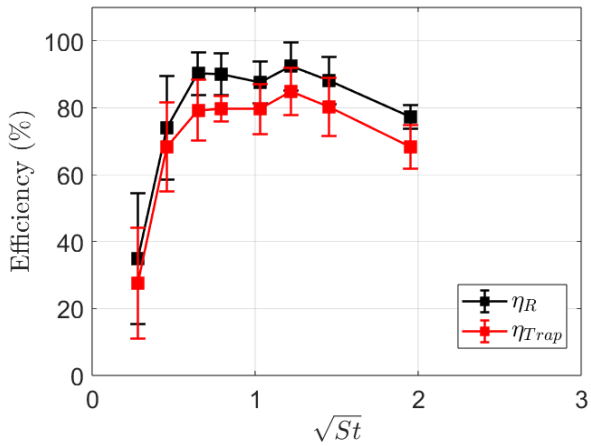

(b)

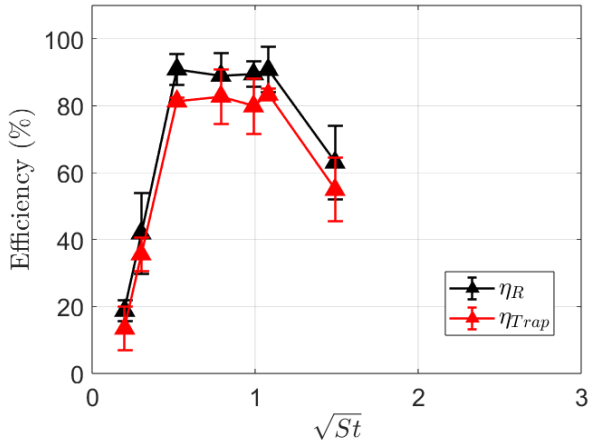

(c)

Figure 5.4: Removal and trap efficiencies as functions of $\sqrt{\text{St}}$ for a) 1.5 and b) 2.3, and c) 3 mm impactors.

The error bars are generated using the student-t distribution with a 95% confidence interval. The trap efficiency (η_{Trap}, shown in red) agrees with the removal efficiency (η_{R}, shown in black), demonstrating that the water droplets removed from the flow are mostly deposited inside the trap. For all curves, as the $\sqrt{\text{St}}$ increases, removal efficiency increases and reaches 90% efficiency at $\sqrt{\text{St}} \approx 0.5$. This result is similar to the flat plate impactor studies reported in the literature. However, the efficiency decreases for large values of the $\sqrt{\text{St}}$ for all the different impactors. This result is unexpected as the removal efficiency should increase monotonically with $\sqrt{\text{St}}$. η_{R} for the three impactors is shown below to highlight the different $\sqrt{\text{St}}$ values at which the efficiency decreases for each impactor.

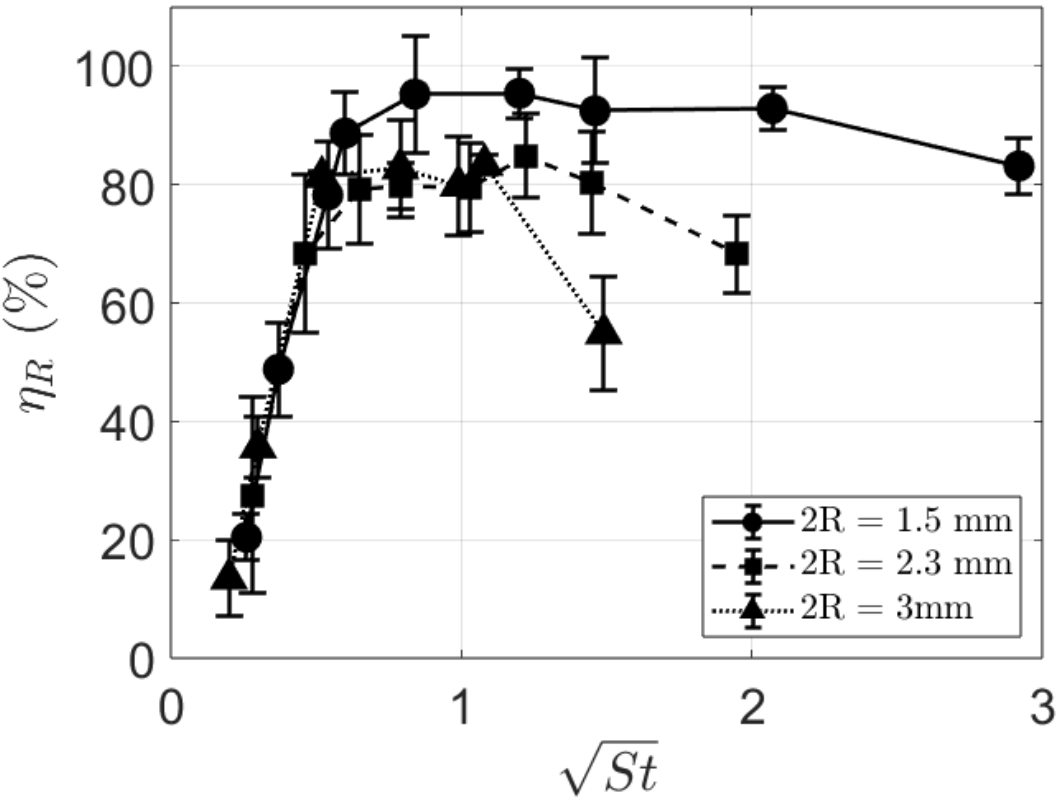

Figure 5.5: Removal efficiency as a function of $\sqrt{\text{St}}$ for the 1.5, 2.3, and 3 mm impactors.

Although the error bars overlap between $\sqrt{\text{St}}$ = 2.1 - 2.9., a clear trend is observed for 2R = 1.5 mm as the removal efficiency decreases from 93% to 83%. Similarly, 2R = 2.3 mm has a reduction in efficiency from 88% to 77% between $\sqrt{\text{St}}$ = 1.5 and 2.0. The most drastic

decrease is observed for 2R = 3 mm as the removal efficiency decreases from 83% to 55% between $\sqrt{\text{St}}$ = 1.1 and 1.5.

When plotted as a function of Re, removal efficiency decreases for Re $\approx$ 14000 for all impactors, as seen in Figure 5.6. The Reynolds number for the impactors is given by,

$$\text{Re} = \frac{2\rho \text{VR}}{\mu}. \tag{5.1}$$

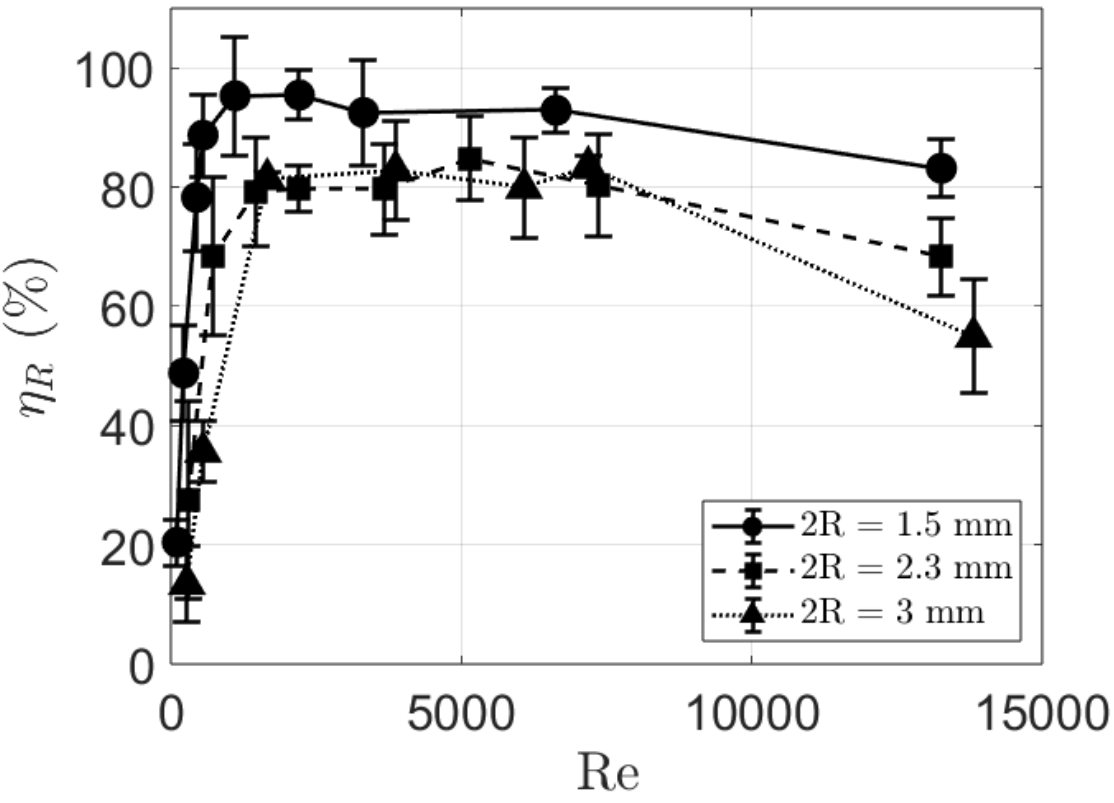

Figure 5.6: Removal efficiency as a function of Re for the 1.5, 2.3, and 3 mm impactors.

This result highlights that the removal efficiency is potentially affected by the flow field created by the trap, as the Re characterizes the flow regime. Another possibility is that droplet evaporation is exacerbated with increasing Reynolds number. The Reynolds number increases with velocity and, therefore, the air flow rate. As the air flow rate increases, the total volume of air available to evaporate the droplets increases. Water nebulization

times and air run times were recorded to measure the total mass of air and water for each experiment and to determine the water-air mass ratio. Dry air at 20° C has a maximum moisture content of 0.015 kg of water per kg of air [77]; therefore, theoretically, a water-air mass ratio approaching this threshold will have droplets susceptible to evaporation as the dry air could increase droplet evaporation as they are transported through the impactor.

The water-air mass ratio for efficiency experiments is shown in Figure 5.7. The mass ratio is high for Re $<$ 1,000, and evaporative effects can be assumed to be negligible. However, as Re increases between 7,000 and 14,000, the water-air mass ratio approaches the carrying capacity shown in Figure 5.8. At Re $\approx$ 14,000, 2R = 3 mm has a mass ratio of 0.04 and is the closest to the carrying capacity. This is correlated with the largest decrease in removal efficiency demonstrated in Figure 5.6. 2R = 1.5 and 2.3 mm have mass ratios of 0.08 and 0.06, respectively, and have reductions in removal efficiency, but are not as pronounced as 2R = 3 mm. These results demonstrate that the decrease in removal efficiency can potentially be due to the reduction in the water-air mass ratio at higher Re and increasing evaporative effects. Droplet evaporation confounds the removal and trap efficiency results due to the droplet diameters and, subsequently, the droplet Stokes numbers decreasing during the experiments.

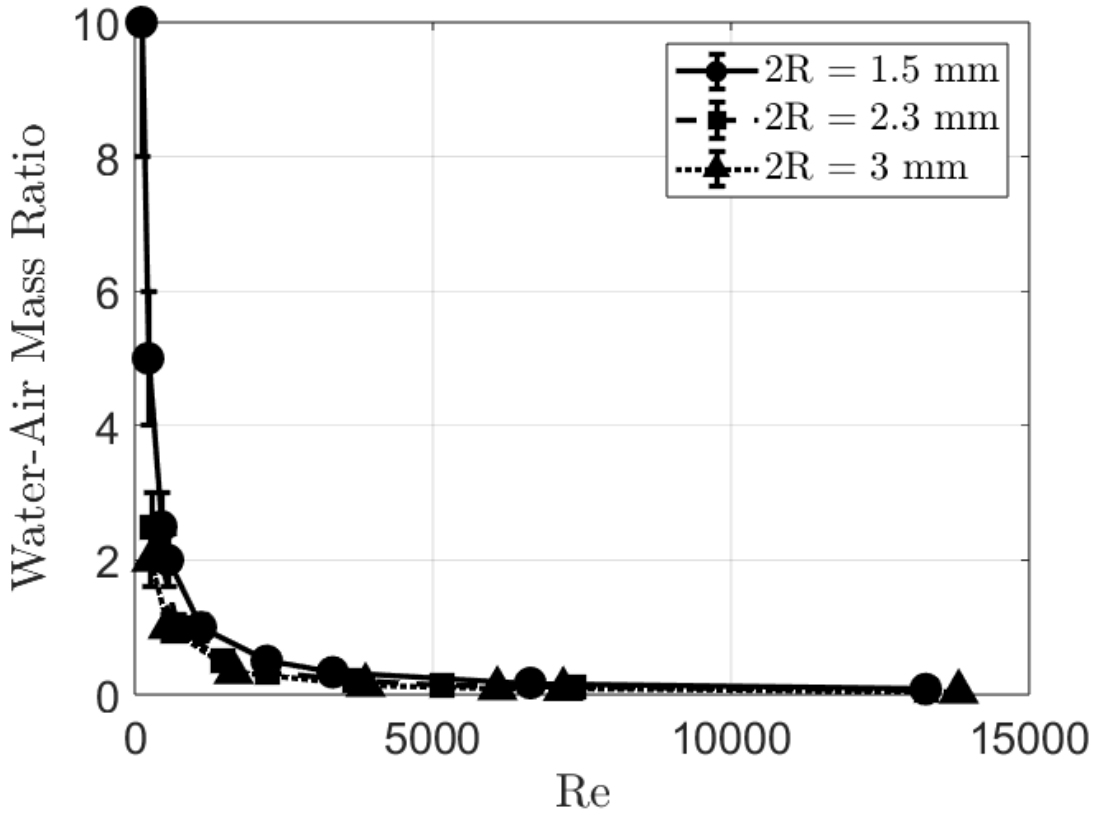

Figure 5.7: Water-air mass ratio of water droplets in dry air at 20° C as a function of Re for efficiency experiments.

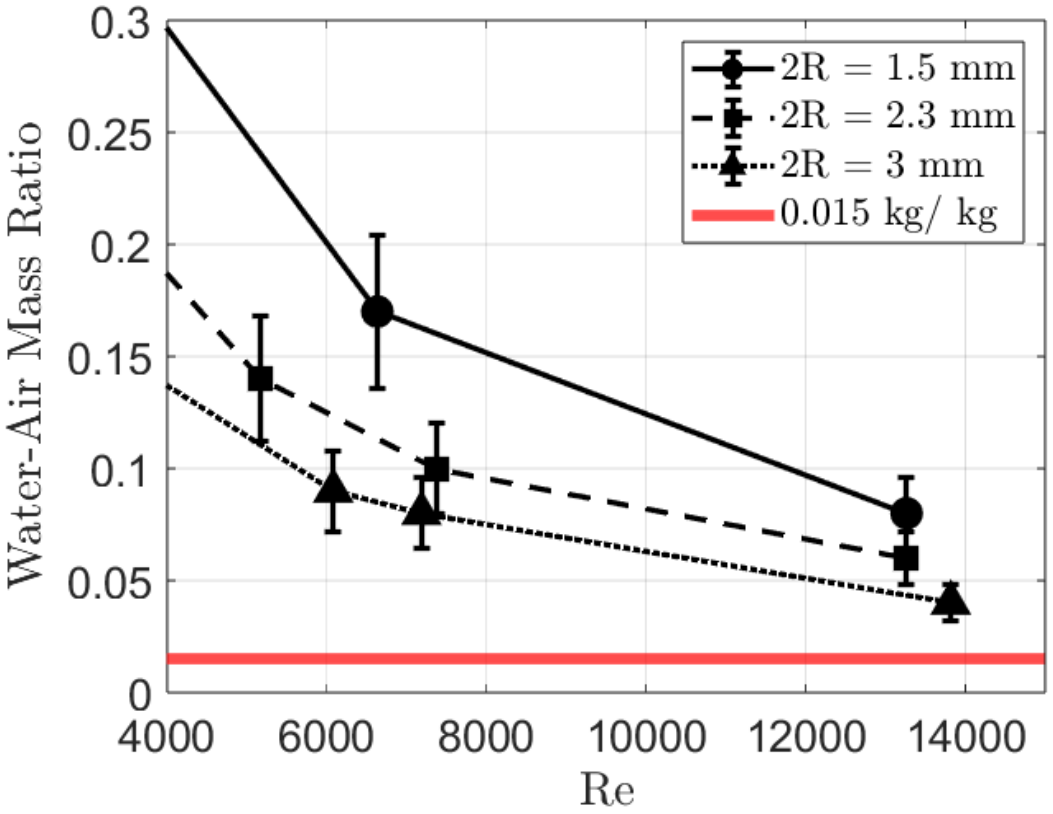

Figure 5.8: Water-air mass ratio for Re between 4000 and 14000.

5.3 Olive Oil Droplet Characterization

5.3.1 Microscopy Particle Size Distribution

To reduce the effects of evaporation, olive oil droplets were used as test aerosols due to their lower vapor pressure [78, 1]. Unlike the Tekceleo nebulizer utilized to generate the water droplets, the BLAM generates a polydisperse distribution of olive oil droplets that needs to be characterized. The first method to characterize the distribution uses a microscope and settling chamber, as described in subsection 4.4.1. After the droplets settle on the glass slide, the images are analyzed in MATLAB using the image processing toolbox and the imfindcircles computer vision algorithm. Before and after images of the droplet identification procedure are shown below in Figure 5.9.

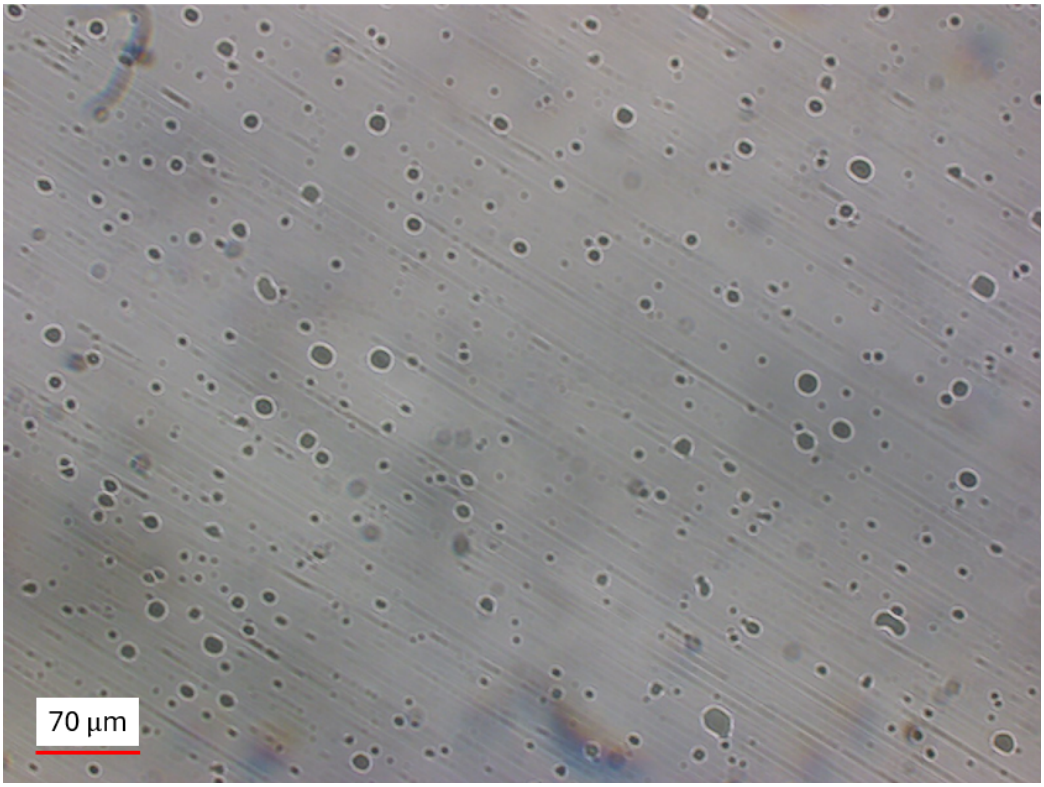

(a)

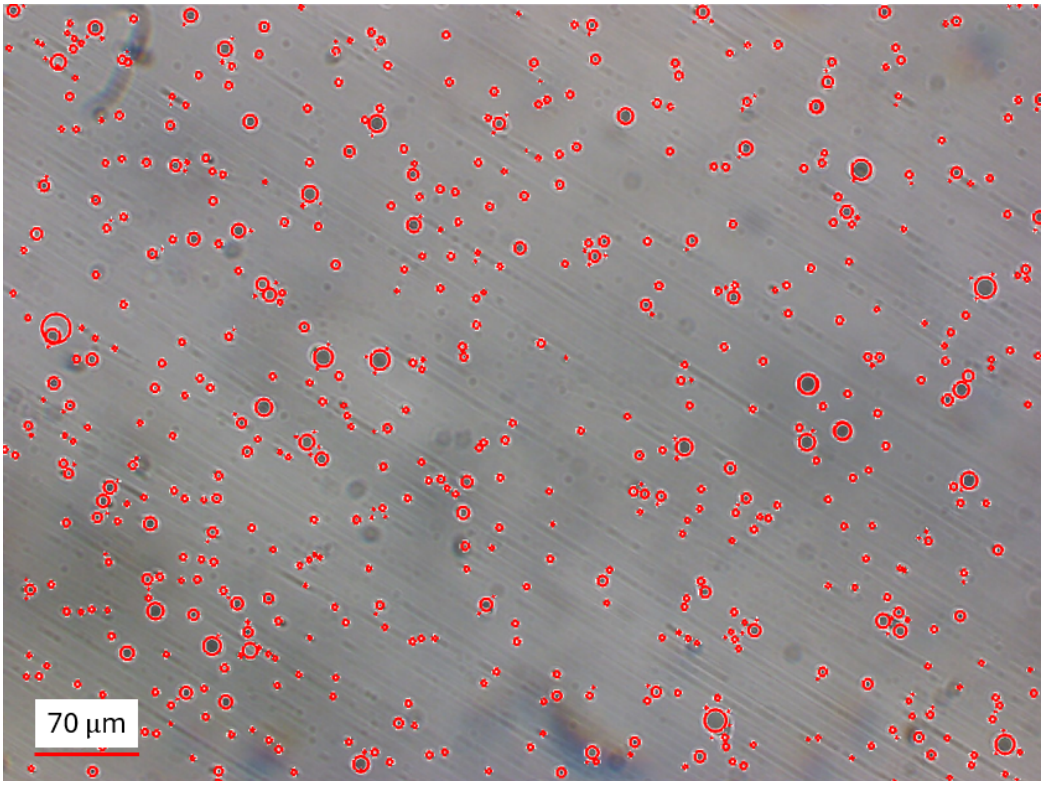

(b)

Figure 5.9: Olive oil droplets deposited on a glass slide from 1.5 mm nozzle and 3 L/min flow rate.

After the droplets are identified, the droplet radii are calculated by modeling the droplets deposited on the slide as spherical caps. As the droplets contact the glass slide, they spread and form a 30° contact angle at equilibrium.

To determine the contact angle of the olive oil droplets on the glass slide in air, we used a micropipette to deposit a single droplet onto a glass slide and weighed it before and after to determine the mass and subsequently the droplet volume. We then placed the glass slide on the microscope stage and measured the droplet radius, A. A schematic of the droplet on the glass slide is shown in Figure 5.10. The contact angle could then be calculated from the spherical cap having the same volume as the droplet using Equation 5.2.

$$V_{cap} = \frac{\pi}{3}(\frac{A}{\sin\theta})^3(2+\cos\theta) - (1-\cos\theta)^2 \tag{5.2}$$

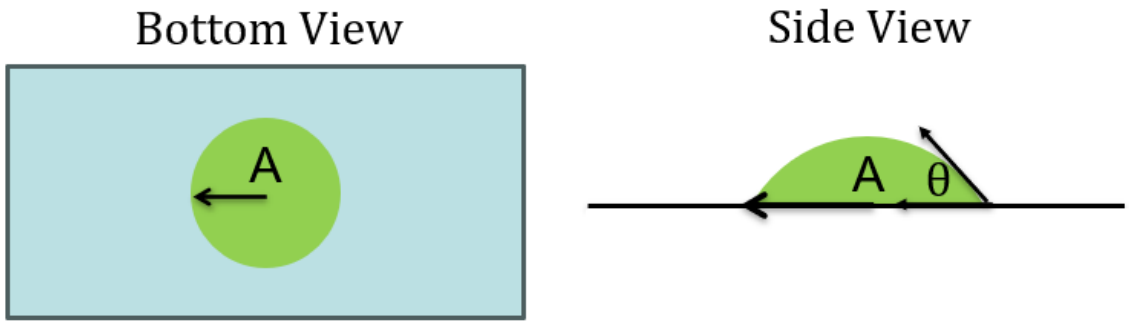

Figure 5.10: Schematic of spherical cap formed by the olive oil droplet on the glass slide.

After four trials, contact angles of 25, 29, 29, and 30° were calculated, and a contact angle of 30° was used throughout.

Returning to characterizing the particle size distribution, images taken with the inverted microscope and camera show a circular cross-section from the bottom view of the slide, but this diameter is not the original droplet diameter. The measured diameter would equal the original droplet diameter only if the contact angle were 90 °. To determine the original droplet diameter, D_p, the spherical cap volume is first calculated, and then D_p can be cal-

culated as,

$$D_p = (\frac{6V_{cap}}{\pi})^{1/3}. \tag{5.3}$$

After converting the circle radii to the droplet radii, histograms are generated to analyze the droplet size distribution by number. The number distributions shown below in Figure 5.11 are for the 1.5 mm nozzle and a 3 L/min air flow rate. Figure 5.11a has bin widths of 1 pixel, and Figure 5.11b has bin widths of 0.5 μm. The distribution of the particle diameter in μm highlights that the particle diameters are centered around 2 μm by number, and taper off for the larger particle diameters with very few particles larger than 5 μm.

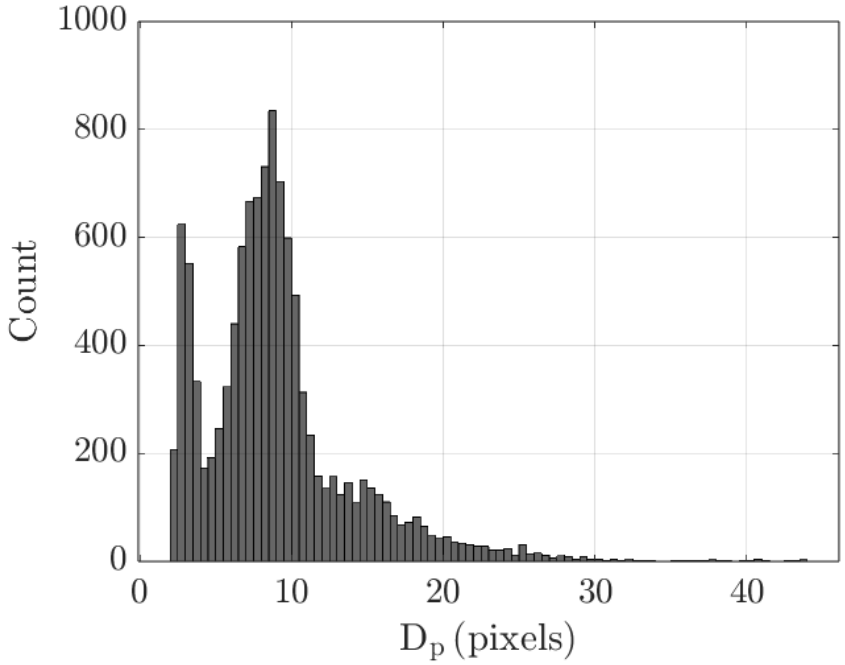

(a)

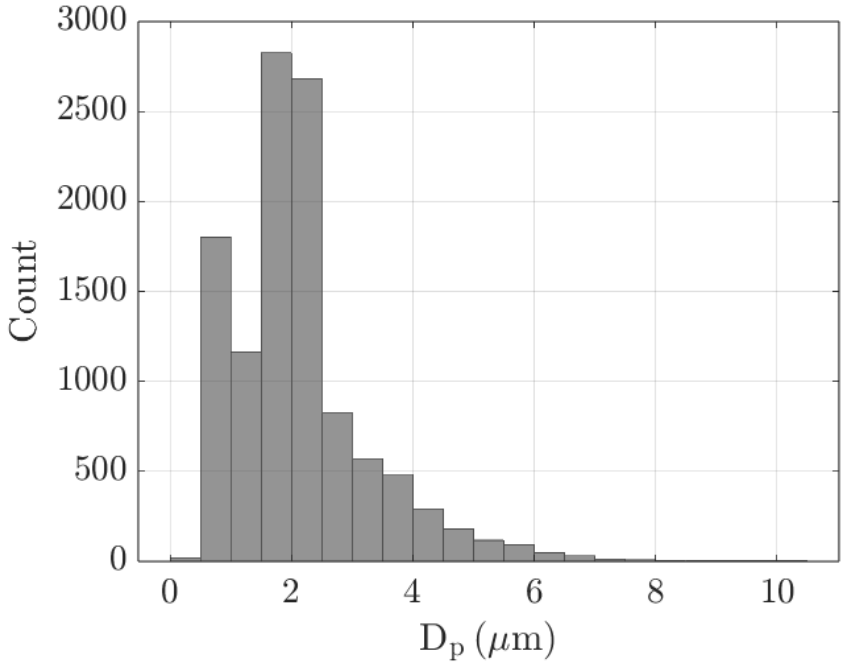

(b)

Figure 5.11: Particle size distribution of olive oil droplets identified by MATLAB on a glass slide. Droplet diameter in a) pixels, b) µm.

Due to the significant variation in droplet diameters, droplets will travel different ver-

tical distances over the seven-minute settling period. Larger droplets will settle faster than smaller ones, potentially representing a higher fraction than the population. To account for this, the distribution is normalized by the predicted vertical displacement for each diameter. The droplet settling velocity was calculated in section 3.4 and is reproduced below,

$$V_{TS} = \frac{\rho_p D_p^2 g C_c}{18\mu}. \tag{5.4}$$

The vertical displacement, y, is then

$$y = V_{TS}\Delta t, \tag{5.5}$$

where Δt is seven minutes. Droplets settle onto the glass slide over seven minutes, and the settling chamber has a height of h = 163 mm, therefore, all droplets larger than 3.75 μm can settle on the glass slide during this time. However, particles smaller than 3.75 μm may not all settle on the slide because they need more time to reach a vertical displacement as large as h, as highlighted below in Figure 5.12.

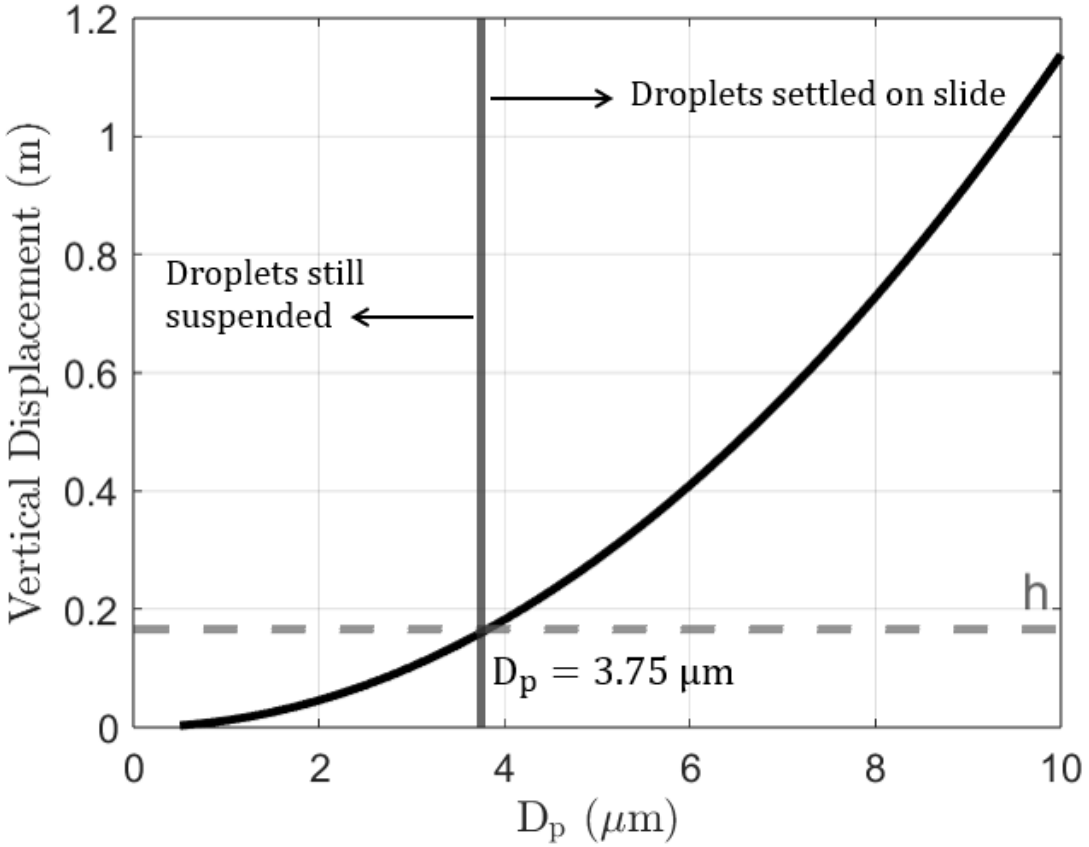

Figure 5.12: Settling distance as a function of particle diameter.

To account for the particles that will not fully settle on the glass slide, the particle distribution is normalized by the vertical displacement, which is proportional to the square of the particle diameter. This model assumes the particles are uniformly distributed in the chamber, start from rest, and move downward at their settling velocity. All particles with diameters larger than 3.75 µm are assumed to reach the glass slide and are not treated with the normalization factor. Particle counts are normalized by the square of the ratio of 3.75 µm particles to the particle size of interest. For example, if there are two 3.75 µm particles identified on the glass slide, and ten 2 µm particles, the normalization factor would be 5^2 and the ten 2 µm particle count would increase to 50. The normalization factor, N_i for particle with diameter $D_{p,i}$ is shown below,

$$N_i = \left(\frac{n_i}{n_{3.75}} \right)^2 \tag{5.6}$$

where $n_{3.75}$ and n_i are the number of 3.75 μm and $D_{p,i}$ droplets identified on the slide, respectively. A comparison of the original and normalized distributions is shown below in Figure 5.13. The histograms are replaced with scatter plots for convenience.

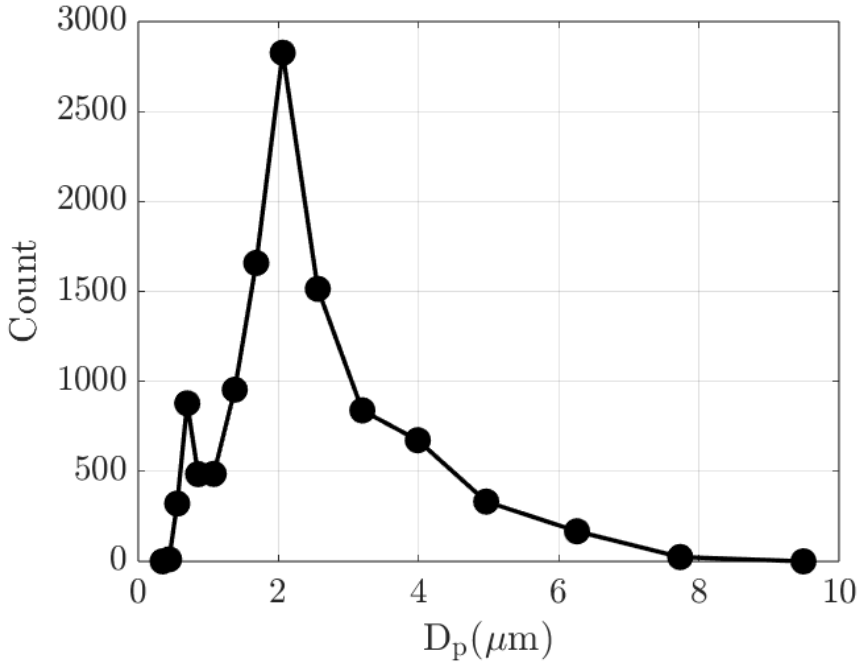

(a)

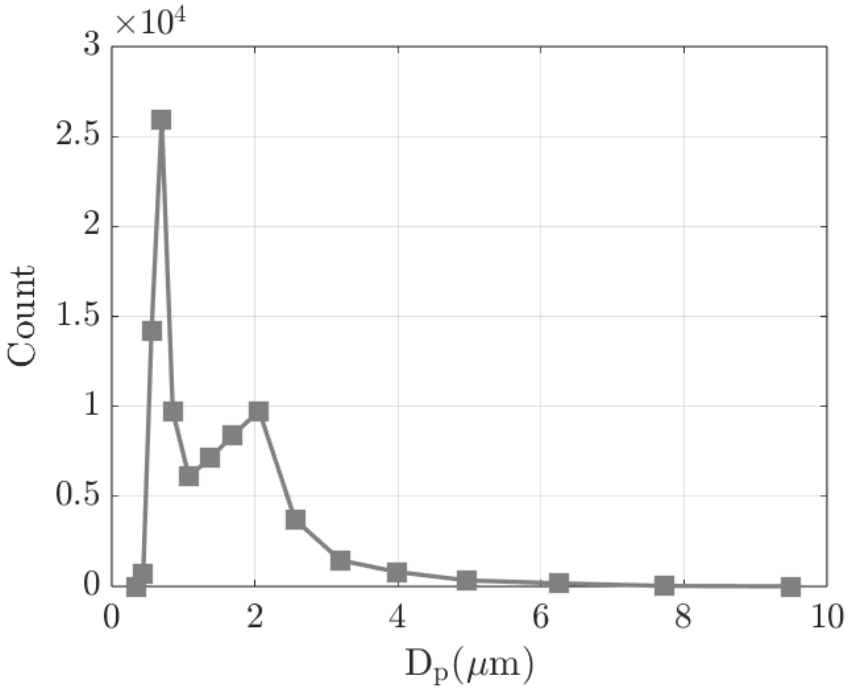

(b)

Figure 5.13: Particle size distribution by counts for a) original distribution and b) normalized distribution.

Figure 5.13a highlights that the distribution peaks around 2 μm, and has very few particles

less than 0.554 μm or greater than 6.260 μm. However, after the normalization is applied, the distribution peaks at 0.554 μm, as the normalization heavily weighs the smaller particles that may not reach the glass slide. The bins are shown in the table below, where ΔD_p is the bin width. These bins are set by the TSI Optical particle sizer used in the next section to compare the distribution measurement methods.

Bin	$D_p(\mu m)$	$\Delta D_p(\mu m)$
1	0.346	0.092
2	0.438	0.094
3	0.554	0.136
4	0.697	0.152
5	0.853	0.158
6	1.076	0.288
7	1.376	0.312
8	1.682	0.302
9	2.060	0.452
10	2.561	0.552
11	3.197	0.718
12	3.988	0.866
13	3.965	1.086
14	6.260	1.504
15	7.732	1.44
16	9.491	2.078

Table 5.2: Bins used for droplet distributions.

So far, this dissertation has discussed the particle size distribution based on number. However, the efficiency measurement methodology is based on particle mass, so the particle size distribution by mass is more important to analyze [1]. The mass-specific particle

size distribution is calculated by dividing the total mass in each bin by the total mass sampled. Further, the probability density function is the likelihood of a particle having a particular size, and can represent the distributions by dividing the number and mass distributions by the corresponding bin width. This defines the particle size distribution (PSD) integral as unity. The Mass PSDs for the 1.5 mm 3L/min original distribution and the distribution normalized by the settling distance are shown below in Figure 5.14. The normalized Mass PSD has a much sharper peak at 2 μm compared to the broad peak ranging from 2-5 μm for the original particle size distribution. Compared to the particle counts, the particle size distribution by mass demonstrates that although many more small particles are in the distribution, they do not account for most of the mass. This result highlights that an impactor with a polydisperse distribution does not have to capture most of the particles to capture most of the mass.

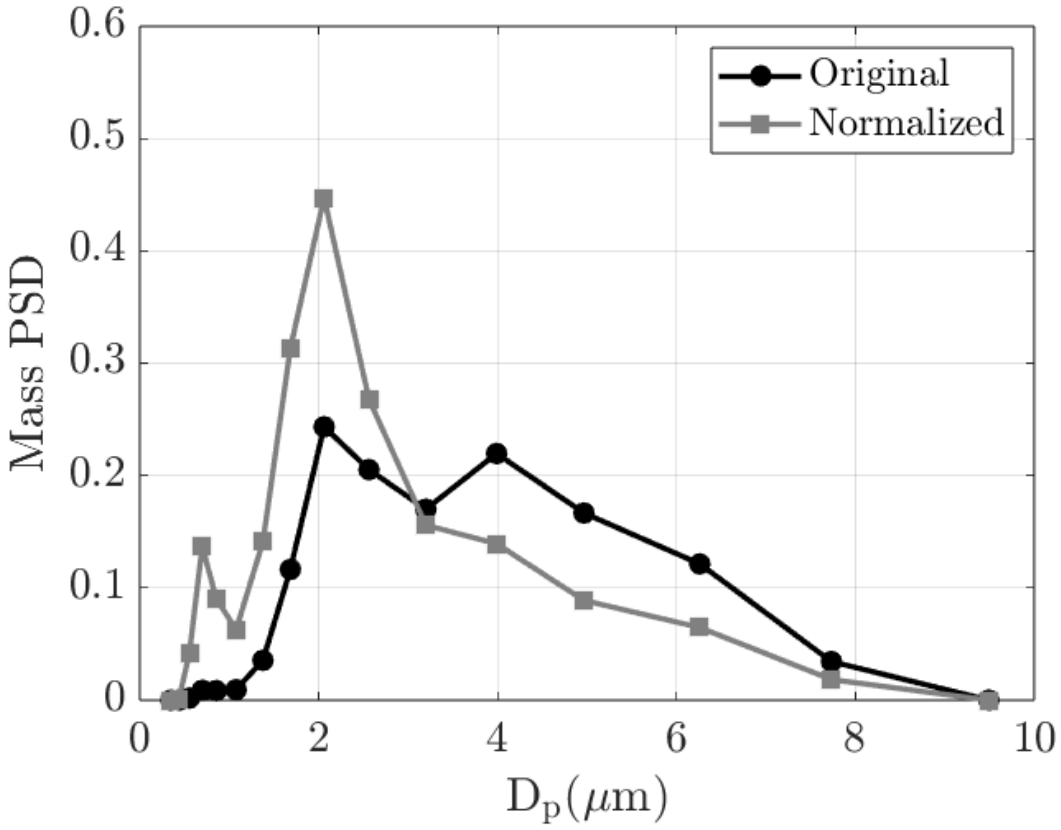

Figure 5.14: Comparison of Mass PSD for original and normalized distributions.

5.3.2 Optical Particle Sizer Particle Distributions

The particle size distributions determined using the glass slide method were compared to the TSI Optical Particle Sizer using the method outlined in subsection 4.4.2. Below in Figure 5.15 is a comparison between the Mass PSD for the 1.5 mm nozzle with a 3 L/min flow rate for the original and normalized distributions using the glass slide method, and the results from the particle sizer.

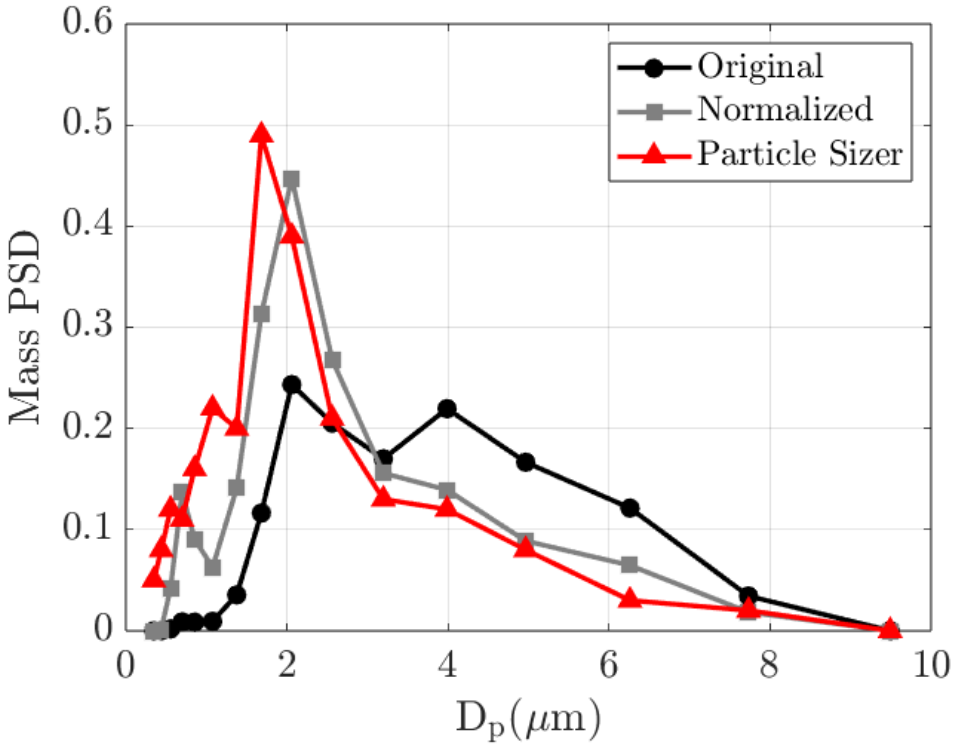

Figure 5.15: Comparison of Mass PSD for 1.5 mm nozzle and 3 L/min flow rate for microscope methods and particle sizer.

It is clear that the normalized distribution more closely resembles the particle sizer results. This highlights that particles stay suspended in the chamber and do not have enough time to settle on the glass slide. Normalizing the distribution by settling distance makes the results better resemble the particle sizer, which is an established measurement technique. This is a very useful result as analyzing the glass slide with a microscope is a cheaper alternative to the optical particle sizer and allows other groups to measure distributions without expensive

or niche equipment. Other normalizations could be applied to find a model to match the particle sizer data best, such as the particles not starting at the terminal velocities, but this is outside the scope of this dissertation. The remainder of this dissertation will use the particle sizer for distribution measurements, as it is a more generally accepted measurement technique.

Measurements were made across the three impactor nozzles with various air flow rates. The nozzle and flow rate combinations sampled are listed in the tables below.

2R (mm)	Q_{air} (L/min)	2R (mm)	Q_{air} (L/min)	2R (mm)	Q_{air} (L/min)
1.5	1	2.3	2	3	3
	2		2		3
	3		3		5
	5		5		10
	8		8		15
	12		12		20
	15		15		25
	17		20		30

Table 5.3: Nozzle and air flow rates sampled with particle sizer.

The average Mass PSDs measured by the particle sizer across three realizations for each nozzle and flow rate combination are shown below in Figure 5.16. Each nozzle displays a peak in Mass PSD around 2 μm with the distributions rapidly tapering off for particles larger than 6 μm. Each distribution slightly changes with air flow rate as well—the 1.5 mm nozzle experiences the least change compared to the 2.3 and 3 mm nozzles. All nozzles have peaks in their distributions at 1.683 μm. The 1.5 mm nozzle has its maximum mass PSD of 0.51 for a 1.5 mm air flow rate, the minimum flow rate tested. The 2.3 and 3 mm nozzles, however, have maximums of 0.59 and 0.66 at 20 and 30 L/min, respectively, the

maximum flow rates tested. These results highlight that the mass PSD is not consistent with air flow rate across the different nozzle sizes. The 2.3 and 3 mm nozzles have similar behavior also for particles larger than 3 μm, consistently decreasing as air flow rate increases, whereas the 1.5 mm nozzle is relatively unchanged. This behavior can potentially be explained by the larger particles having more inertia than the smaller particles at higher air flow rates and colliding with the nozzle walls, resulting in a low-pass filter effect, also known as aerodynamic overfocusing. Aerodynamic overfocusing is the effect seen when particles with high inertia and velocities in the radial direction deviate from their paths and move closer to the nozzle centerline [79, 80, 81, 82].

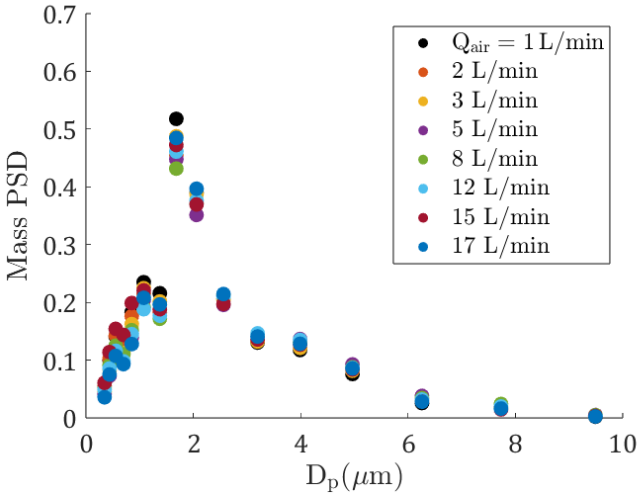

(a)

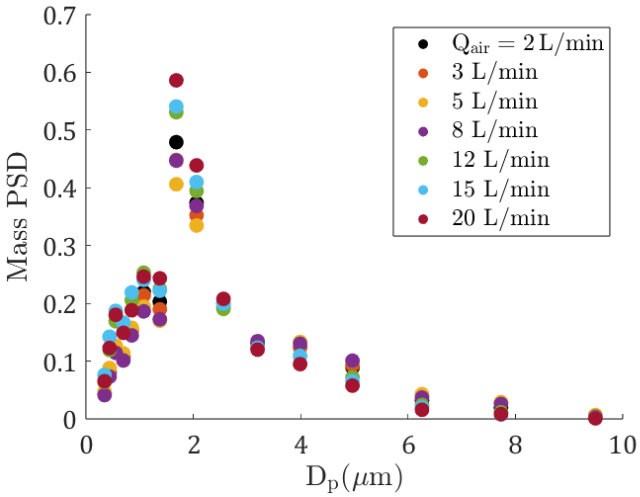

(b)

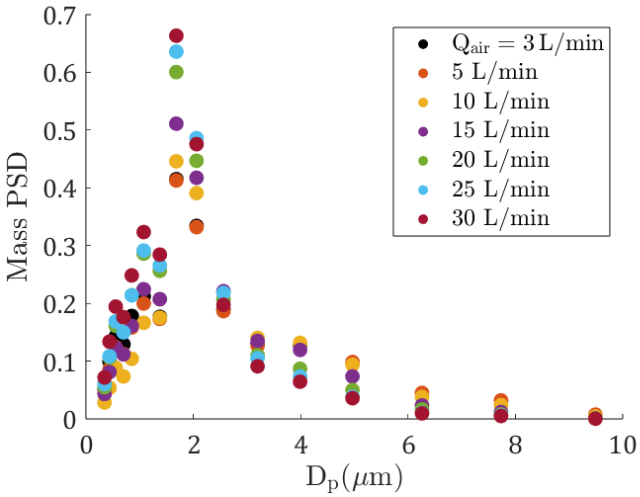

(c)

Figure 5.16: Mass PSD for multiple air flow rates for a) 1.5 mm nozzle, b) 2.3 mm nozzle, c) 3 mm nozzle.

To characterize the Stokes number for the different particle distributions, the average $\sqrt{\mathrm{St}}$ by mass, $\langle\sqrt{St}\rangle$, will be used. The expression for $\langle\sqrt{St}\rangle$ is given below,

$$\langle\sqrt{St}\rangle = \sum_i m_i Dp_i \sqrt{\frac{\rho_p C_\mathrm{i}}{18\mu}} \sqrt{\frac{V_0}{R}}, \tag{5.7}$$

where, for a given particle size distribution, $\mathrm{m_i}$ is the percentage of total mass for particle diameter Dp_i and $\mathrm{C_i}$ is the Cunningham slip correction factor for Dp_i (see section 3.4). The slip correction factor had a negligible effect on $\langle\sqrt{St}\rangle$ and will be a constant of 1.

Figure 5.17 compares $\langle\sqrt{St}\rangle$ using the average particle distribution, denoted as $\langle\sqrt{St}\rangle_\mathrm{a}$, with the measured individual distribution obtained for each experimental condition, $\langle\sqrt{St}\rangle_\mathrm{m}$ for the three nozzles individually (a-c), and all results combined (d). The high agreement between the average and individual values shows that the distributions do not appreciably change with the flow rate for the 1.5 mm nozzle ($\mathrm{R}^2 = 0.95$). The 2.3 mm nozzle shows similar agreement ($\mathrm{R}^2 = 0.93$). The 3 mm nozzle has slightly worse but still a fair agreement ($\mathrm{R}^2 = 0.89$). The average distribution for all nozzles and flow rates is presented in Figure 5.17d with similar variation. Only small variations are observed in the particle distribution, potentially demonstrating that the changes in the mass PSD for larger particles seen in Figure 5.16b and c are negligible when calculating the average Stokes number by mass. Table 5.4 provides example values of mass accumulation for the different components for the 1.5 mm, TR = 0.77 impactor. As the flow rate increases, a larger fraction of the mass is deposited inside the nozzle, as shown in the increase in $\mathrm{m_i}$. However, the distribution seems relatively unchanged across the different flow rates, and the particles can be assumed to be filtered equally, independent of their size.

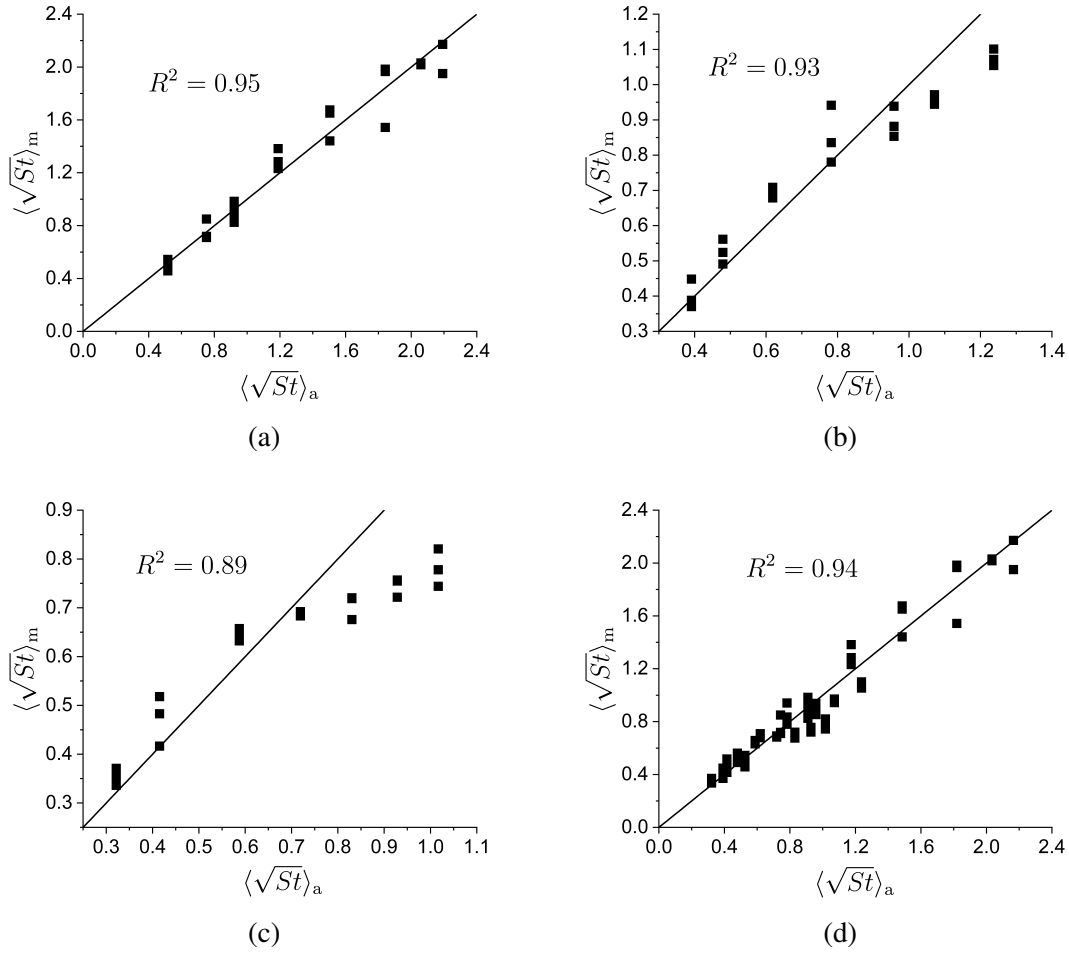

Figure 5.17: Comparison of average and individual $\langle\sqrt{St}\rangle$ for a) 1.5 mm nozzle, b) 2.3 mm nozzle, c) 3 mm nozzle, d) all nozzles.

$Q_{air}(L/min)$	$m_n(mg)$	$m_i(mg)$	$m_p(mg)$	$m_{trap,b}(mg)$	$m_{trap,w}(mg)$	$m_h(mg)$
5	0.7	0.0	1.4	1.5	1.0	2.3
8	3.0	0.0	3.2	3.0	2.5	1.4
8	2.6	0.0	2.5	3.9	1.8	1.9
8	2.0	0.0	2.6	3.9	2.7	1.7
8	2.1	0.0	2.8	3.6	1.5	2.1
12	6.6	0.0	1.0	4.4	0.4	1.0
12	4.1	0.0	2.5	4.0	2.2	1.3
12	2.5	0.1	2.6	4.1	2.3	1.0
12	1.9	0.3	2.8	4.4	2.1	1.6
15	1.8	0.2	0.9	4.1	0.6	0.4
15	2.2	0.4	1.5	6.0	1.4	0.9
15	3.4	0.4	2.3	6.4	1.6	1.1
15	4.3	0.3	1.7	5.0	1.1	1.8
17	3.2	1.5	0.3	6.8	0.3	1.2
17	2.9	1.5	1.0	7.4	0.6	1.2
17	2.3	0.6	1.2	6.1	1.2	1.1
17	3.7	1.6	1.2	4.4	0.7	0.7

Table 5.4: Sample values for mass accumulation on different components for the 1.5 mm, TR = 0.77 impactor.

CHAPTER 6
PREDICTED AND EXPERIMENTAL OIL DROPLET IMPACTOR EFFICIENCY

6.1 Introduction

Typical impactors are calibrated using monodisperse aerosols. Monodisperse aerosols allow the particle Stokes number to be isolated only as a function of velocity. However, the experiments in this dissertation use a polydisperse particle distribution characterized in the previous chapter. The rationale for using polydisperse distributions is that they are more common in applications where the impactor can be used as a particle trap. The particle distribution expelled from humans, in particular, is highly polydisperse [83, 84]. For a fixed velocity, the Stokes numbers will vary due to the range of particle sizes. Recalling inertial impactor theory introduced in chapter 5, there is a theoretical critical Stokes number where particles with $\mathrm{St} \geq \mathrm{St_c}$ are removed from the flow. For monodisperse aerosols, the theoretical efficiency curve is a step-function from 0 to 100% at $\mathrm{St_c}$. For a polydisperse distribution, there will be particles with St greater than and less than $\mathrm{St_c}$, and the efficiency curve is not a step-function, but a sigmoidal curve. For a fixed particle distribution, as the velocity increases, the size of the smallest particle with $\mathrm{St} \geq \mathrm{St_c}$ will decrease, and a higher fraction of the total particle mass will be removed. The smallest velocity for which the largest particle have $\mathrm{St} \geq \mathrm{St_c}$, would result in a small, but larger than 0% efficiency. If the velocity is continuously increased, then once the smallest particle has $\mathrm{St} \geq \mathrm{St_c}$, the removal efficiency will be 100%, and the efficiency curve will be S-shaped. The smaller the variation in the particle distribution, the closer the efficiency curve will be to the step-function of corresponding to a monodisperse aerosol.

6.1.1 Predicted Efficiency Model

Studies calibrating flat plate impactors with monodisperse aerosols found that impactors with impaction plates placed between one and five nozzle radii from the nozzle exit (S/2R = 0.5 - 2.5), exhibit a removal efficiency that increases with $\sqrt{\mathrm{St}}$ and reaches approximately 100% at $\sqrt{\mathrm{St}} \approx 0.5$ [11, 12, 13, 14, 15, 16, 17, 18, 19, 20, 21]. To characterize the performance of the trap impactors using polydisperse olive oil distributions, the experimental efficiencies will be compared to theoretical efficiencies using $\sqrt{\mathrm{St_c}} = 0.5$. This prediction model assumes that all particles with $\sqrt{\mathrm{St_c}} \geq 0.5$ will be perfectly removed from the flow.

Equation 5.7 shows that for a given particle distribution, the corresponding average square root of the Stokes number ($\langle\sqrt{\mathrm{St}}\rangle$) is a linear function of $\sqrt{\mathrm{V_0/R}}$. For any value of the average square root of Stokes number by mass, it is then possible to calculate the corresponding individual Stokes number (and its square root) for any given particle size using the value of $\sqrt{\mathrm{V_0/R}}$, including those sizes corresponding to the midpoint of each bin using Equation 3.18.

Similarly, for a given $\langle\sqrt{\mathrm{St}}\rangle$, it is possible to calculate the critical particle size $\mathrm{D_p^*}$ for which its individual square root of the Stokes number is $\sqrt{\mathrm{St}}$ = 0.5. Conversely, for any given particle size, we can calculate the corresponding value of the average square root of the Stokes number of the distribution for which that bin size has $\sqrt{\mathrm{St}}$ = 0.5 by

$$\langle\sqrt{\mathrm{St}}\rangle = (\sum_{\mathrm{i}} \mathrm{m_i D_{p,i}})(\frac{0.5}{\mathrm{D_p}}), \tag{6.1}$$

where $\mathrm{D_p}$ is the particle size of interest.

Once the critical particle size is determined, we can obtain the predicted efficiency as the fraction of particles with sizes equal to or larger than the critical size. As an example, consider the case shown in Figure 6.1 when $\mathrm{D_p^*}$ = 4.97 μm, corresponding to $\sqrt{\mathrm{V_0/R}}$ = 59.70 $[\frac{1}{\mathrm{s}}^{1/2}]$ and $\langle\sqrt{\mathrm{St}}\rangle_{\mathrm{a}}$ = 0.28, where $\langle\sqrt{\mathrm{St}}\rangle_{\mathrm{a}}$ is the average square root of Stokes by mass using the average particle size distribution for all nozzles and flow rates as defined

in subsection 5.3.2. The vertical line indicates the critical particle size, D_{p}^{*}. The predicted efficiency,η_{P}, for $\langle\sqrt{\mathrm{St}}\rangle_{\mathrm{a}}$ = 0.28 is then the fraction of the mass contained in particles with $\mathrm{D_p} \geq \mathrm{D_p}^{*}$ which can be calculated from the bins on the Mass PSD that lie to the right of the vertical line, as indicated. Specifically, for $\langle\sqrt{\mathrm{St}}\rangle_{\mathrm{a}}$ = 0.28, the predicted efficiency is 8%. As the value of $\langle\sqrt{\mathrm{St}}\rangle_{\mathrm{a}}$ increases, the size of the smallest particles removed from the flow decreases, and thus, the predicted efficiency increases.

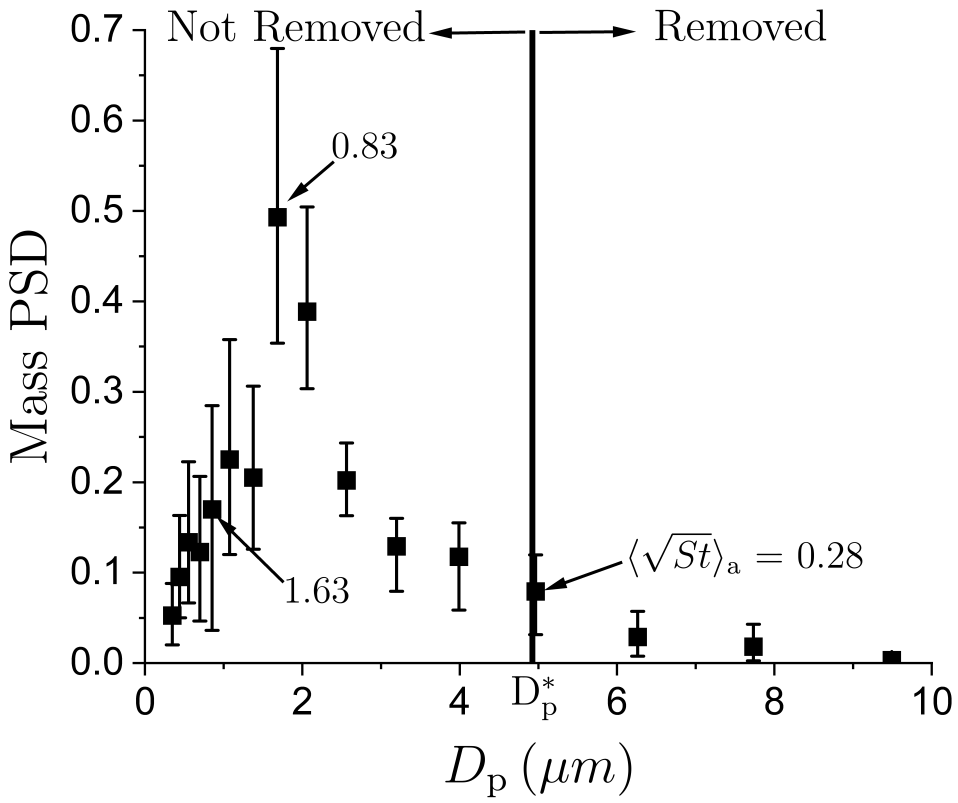

Figure 6.1: Average Mass PSD for all nozzles and flow rates. Arrows indicate $\langle\sqrt{St}\rangle_{\mathrm{a}}$ where critical particle diameter, D_{p}^{*}, has $\sqrt{\mathrm{St}} = 0.5$.

The predicted removal efficiencies for the average and individual distributions are shown in Figure 6.2. Due to the high agreement between $\langle\sqrt{St}\rangle_a$ and $\langle\sqrt{St}\rangle_m$ in Figure 5.17, the four predicted efficiency curves overlap. The predicted efficiencies are 0% for $\langle\sqrt{St}\rangle < 0.2$ and increase to $\approx 80\%$ at $\langle\sqrt{St}\rangle = 1$ and reach a maximum of 98% at $\langle\sqrt{St}\rangle = 2.8$. The gradual increase in efficiency is due to fractions of the total particle mass with $\sqrt{St} \geq 0.5$

compared to the step-function increase predicted for a monodisperse distribution.

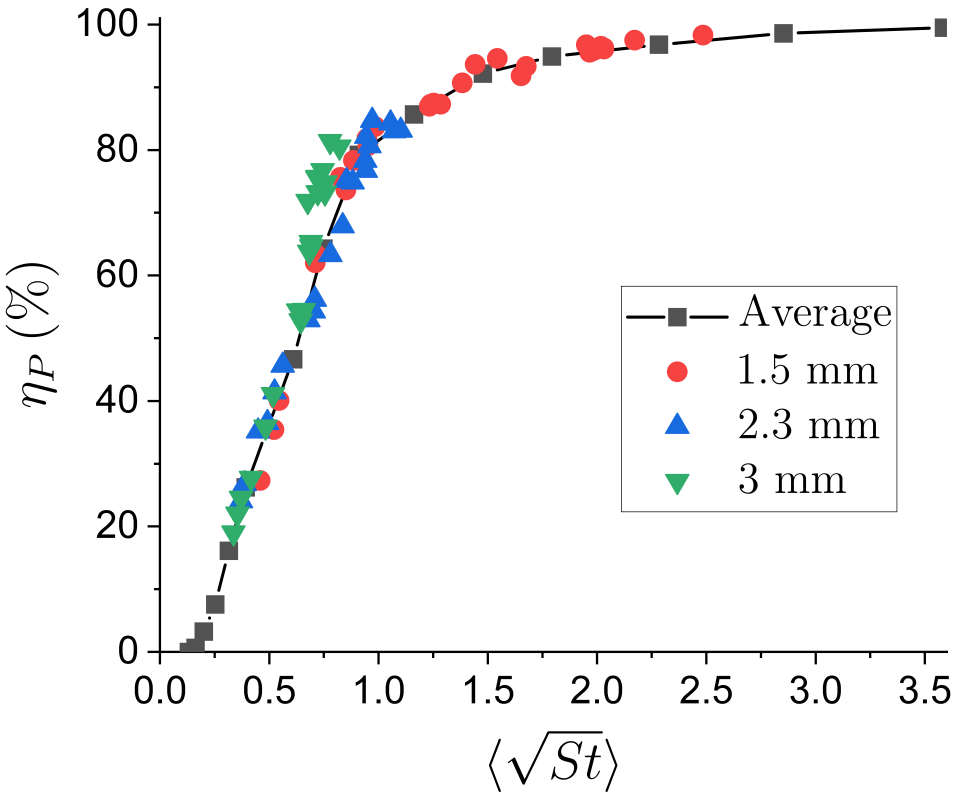

Figure 6.2: Predicted efficiencies as a function of $\langle\sqrt{St}\rangle$ for the average and individual distributions.

6.1.2 Olive Oil Droplet Efficiency Results

Efficiency experiments were performed and compared to the predictions. The procedure for these experiments is described in section 4.5, and important geometric parameters for the impactors are given in the table below. Across 223 trials, 80% of experiments had uncertainties for removal efficiency, trap efficiency, and wall losses less than or equal to 4%, 8%, and 8%, respectively. In some experiments, these uncertainties were as high as 7%, 16%, and 17%. The error bars for the experimental data are generated using the Student t-distribution with a 95% confidence interval and do not factor in the uncertainty in the efficiencies.

2R (mm)	TR	$D_T/2R$	S / 2R	T / 2R	Q_{air}(L/min)
1.5	0.77	2.7	1.5	2.2	1 - 17
2.3	0.69	2	1	1.5	2 - 20
3	1.50	2.7	1.5	1.1	3 - 30

Table 6.1: Trap impactor parameters for 2R = 1.5, 2.3, and 3 mm nozzles using olive oil droplets.

Figure 6.3 displays the experimental efficiencies compared to the average distribution predicted efficiency for values of the average square root of Stokes by mass between 0 and 3.2. The error bars are generated using a Student-t 95% confidence interval. Overall, the experimental removal efficiencies agree well with the predicted efficiency, demonstrating that the prediction model is viable. Similar to η_P, the removal efficiency, η_R (defined by Equation 4.5) exceeds 80% for $\langle\sqrt{St}\rangle_a = 1$. The maximum removal efficiency is 98% and is achieved with the 1.5 mm impactor for $\langle\sqrt{St}\rangle_a = 2.2$. The 2.3 and 3 mm impactors have maximum efficiencies of 91 and 83%, but are limited by their maximum $\langle\sqrt{St}\rangle_a$ of 1.1 and 0.8, respectively. Limitations in $\langle\sqrt{St}\rangle_a$ are due to the nozzle geometries being unable to increase the flow velocity as much as the 1.5 mm nozzle. Even though the air flow rates are greater than the flow rate in the 1.5 mm impactor, due to continuity, the flow speed cannot increase enough to result in larger $\langle\sqrt{St}\rangle$ for inlet pressures less than 1.5 psi. This limitation was highlighted in Figure 4.2 and is a design constraint for the impactor.

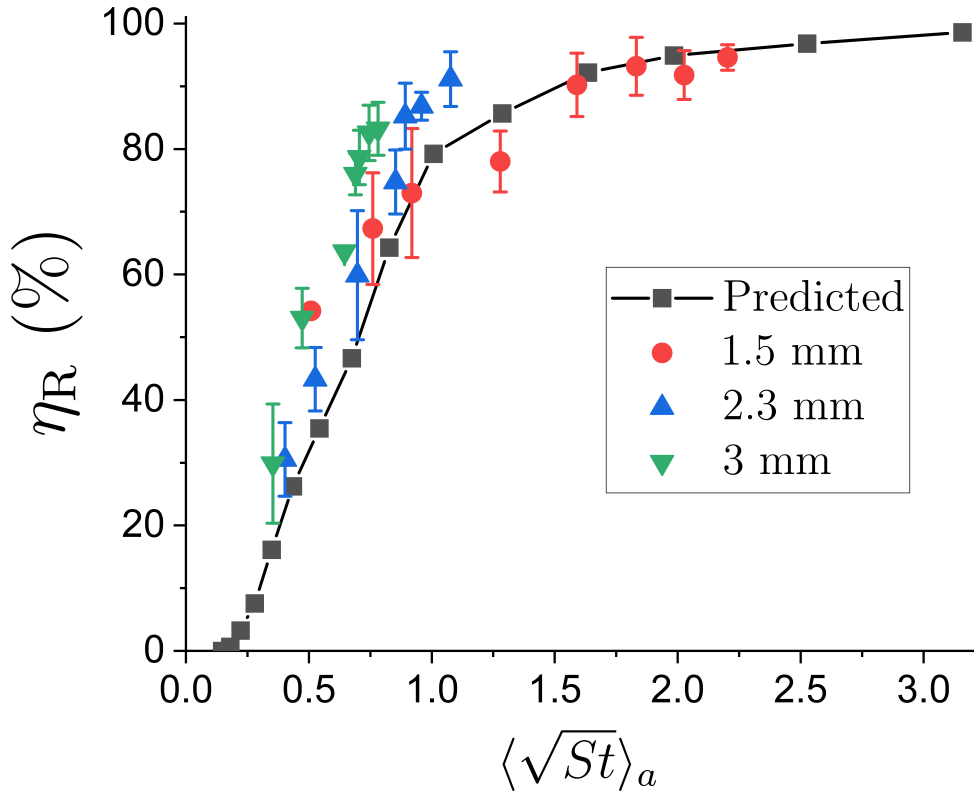

Figure 6.3: Comparison of the average predicted removal efficiency and the experimental removal efficiencies.

Next, the predicted (η_P), removal (η_R), and trap (η_{Trap}) efficiencies are compared for the three impactors, shown below in Figure 6.4. All removal and trap efficiencies agree well with the predictions, as the error bars overlap with the predicted values. The 1.5 mm impactor has the maximum trap efficiency of 90% at $\langle\sqrt{St}\rangle_a$ = 1.6. However, at a certain $\langle\sqrt{St}\rangle$, the trap and removal efficiencies begin to diverge. These results are unexpected: in principle, for increasing $\langle\sqrt{St}\rangle_a$ the particles are more likely to deviate from the streamlines and deposit into the trap. However, η_R is consistently similar to the predictions, but the trap efficiency begins to decrease, and therefore, the wall losses (W) increase. The wall losses for the three impactors as functions of $\langle\sqrt{St}\rangle$ are shown in Figure 6.4d. Figure 6.4d highlights that the magnitude of the wall losses is similar for all impactors with a maximum of 12%. As nozzle diameter increases, however, the increase in wall losses occurs for

lower values of $\langle\sqrt{St}\rangle$. This increase in wall losses is similar to that reported by Tsai and Cheng [15], where for decreasing trap diameters, more particles were seen to collect on the backside of the impactor nozzle.

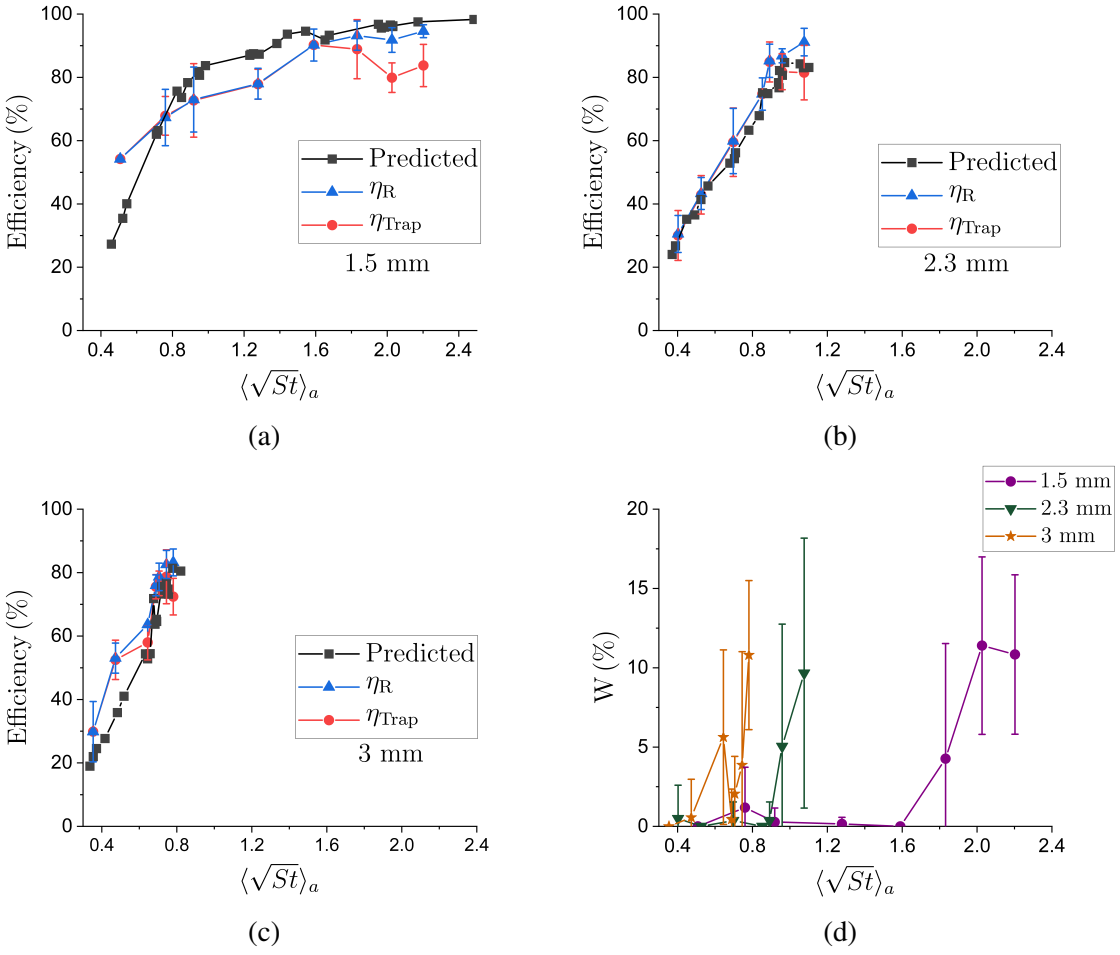

Figure 6.4: Comparison of predicted, removal, and trap efficiencies for the (a) 1.5 mm, (b), 2.3, (c) 3 mm impactors. (d) Wall Losses for impactors as functions of $\langle\sqrt{St}\rangle$.

We do not expect the decrease in trap efficiency to stem from particle-particle or particle-fluid interactions. From the experiments, the average volume fraction of oil droplets-to-air is on the order of 10^{-12}. A schematic modeling the particles in air as concentric spheres is shown in Figure 6.5, where r is the radius of the particle, and R is the particle-particle distance between the particle centers. By using the volume ratio of the sphere with radius R with the particle of radius r as the average volume fracation of oil droplets-to-air, the

particle-particle distance for the largest particles (10 μm) is on the order of 10^{-1}m, which is orders of magnitude larger than the size of the particles themselves. Therefore, we do not expect any interactions between the particles or any fluid disturbances caused by the particles to affect their neighbors. Instead, as the wall losses increase, the particles potentially enter and exit the trap for increasing St, or have their trajectories altered and never enter the trap. This could potentially be caused by the flow field generated by the trap at higher Reynolds numbers, which is a design criterion to be considered [85, 86].

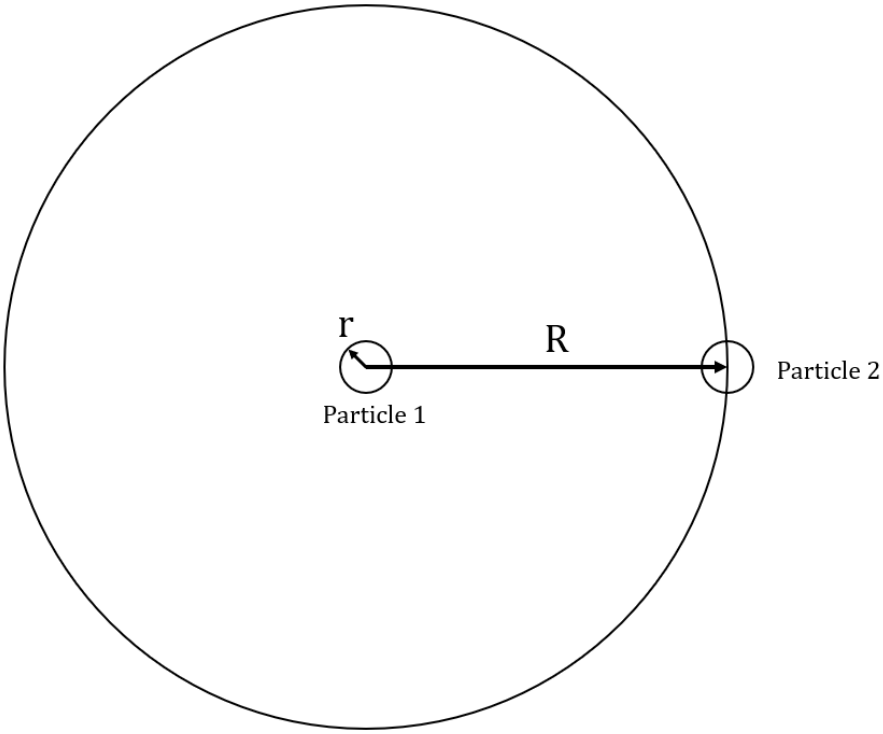

Figure 6.5: Schematic of interparticle distance.

6.1.3 Trap Efficiency and Trap Ratio

To investigate the influence of trap geometry on trap efficiency, multiple traps were designed and tested with the 1.5 mm nozzle. Trap geometry was discussed in Figure 4.3, where the pertinent geometric parameters are the trap diameter (D_T) and flat plate depth (H_1). The o-ring diameter (W) and thickness (H_2) are fixed. Seven different trap geometries were tested, and their geometries are given in the table below. T is the total trap depth and

is given by $H_1 + H_2$. Traps varied based on their trap width and depth. Wide traps were characterized as $D_T/2R = 3.2$, medium as $D_T/2R = 2.7$, and narrow as $D_T/2R = 2.0$. A deep trap was characterized as $T/2R = 3.7$, medium as $T/2R = 2.9$, and shallow as $T/2R = 2.2$. As a reminder, the trap ratio is the ratio of the difference in nozzle outlet diameter and trap diameter divided by the trap depth ($(D_T - 2R)/T$).

Design	TR	$D_T/2R$	$T/2R$	Trap Width	Trap Depth	$\eta_{Trap,Max}$ (%)	Marker
1	1.00	3.2	2.2	Wide	Shallow	94	■
2	0.77	2.7	2.2	Medium	Shallow	90	●
3	0.60	3.2	3.7	Wide	Deep	74	□
4	0.59	2.7	2.9	Medium	Medium	70	●
5	0.46	2.7	3.7	Medium	Deep	64	○
6	0.45	2.0	2.2	Narrow	Shallow	56	▲
7	0.27	2.0	3.7	Narrow	Deep	31	△

Table 6.2: Trap impactor parameters for 2R = 1.5 mm and S/2R = 1.5 with varying trap geometries.

Figure 6.6 shows η_{Trap} as a function of $\langle\sqrt{St}\rangle_a$ for all traps using the 1.5 mm nozzle. The red curve is the predicted efficiency for the 1.5 mm nozzle. Categorizing the geometries by TR displays a remarkable correlation with the trap efficiency. TR = 1.00 (wide and shallow trap), performs the best and has high agreement with the predictions, along with a maximum trap efficiency of 94%. Even at larger $\langle\sqrt{St}\rangle_a$, the trap efficiency mirrors the predicted values, which was not observed for the trap impactors considered previously. As TR decreases, the trap performance degrades. TR = 0.77 is similar to TR = 1.00 for $\langle\sqrt{St}\rangle_a < 2$ before its trap efficiency decreases from 90% to 80%. For $TR < 0.77$, the trap efficiencies are significantly less than η_P. The worst performance is seen for TR = 0.27 (narrow and deep trap), which has a maximum efficiency of a mere 31% for a predicted efficiency of 91%.

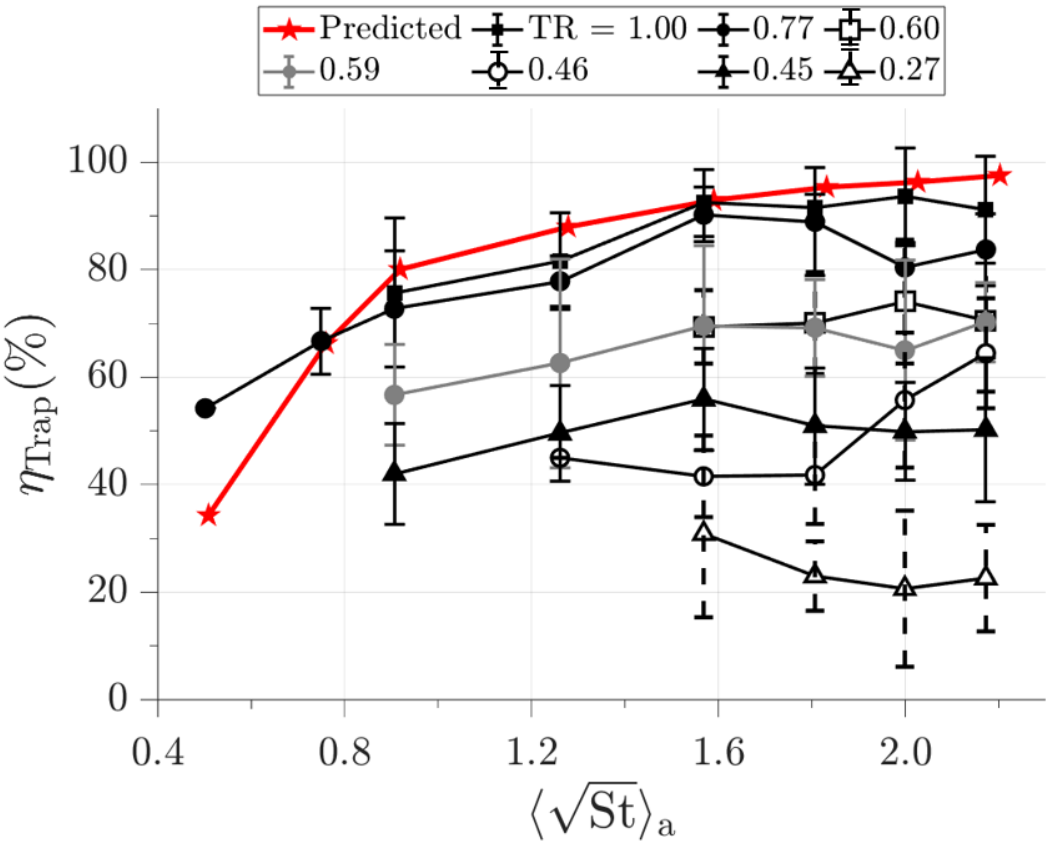

Figure 6.6: Trap efficiencies for various trap geometries using the 1.5 mm nozzle as functions of $\langle\sqrt{\mathrm{St}}\rangle_{\mathrm{a}}$.

The maximum values for the wall losses and trap efficiencies as functions of TR are shown in Figure 6.7a. As mentioned earlier, trap efficiency is maximized for increasing TR, and consequently, wall losses are reduced. Wall losses as functions of $\langle\sqrt{\mathrm{St}}\rangle_{\mathrm{a}}$ are shown in Figure 6.7b. Wall losses are minimal for TR = 1.00 with a maximum of only 5% for $\langle\sqrt{\mathrm{St}}\rangle_{\mathrm{a}} = 2.2$, and only a slight increase with increasing $\langle\sqrt{\mathrm{St}}\rangle_{\mathrm{a}}$. TR = 0.77 has similar performance with small increases in W with no significant wall losses until $\langle\sqrt{\mathrm{St}}\rangle_{\mathrm{a}} = 1.8$ and a maximum of 11%. Other geometries do not fare as well, such as TR = 0.45, which initially has W = 5% for $\langle\sqrt{\mathrm{St}}\rangle_{\mathrm{a}} = 0.8$, but gradually increases to a sustained maximum of W = 42% for $\langle\sqrt{\mathrm{St}}\rangle_{\mathrm{a}} \geq 1.8$. TR = 0.27 performs the worst and consistently has wall losses greater than 55% with a maximum of 73%. All traps have an increase in W for increasing $\langle\sqrt{\mathrm{St}}\rangle_{\mathrm{a}}$ except for TR = 0.46. TR = 0.46 experiences a dramatic decrease in W from 47%

to 26%, which is unexpected and could potentially be due to the flow field generated from this geometry.

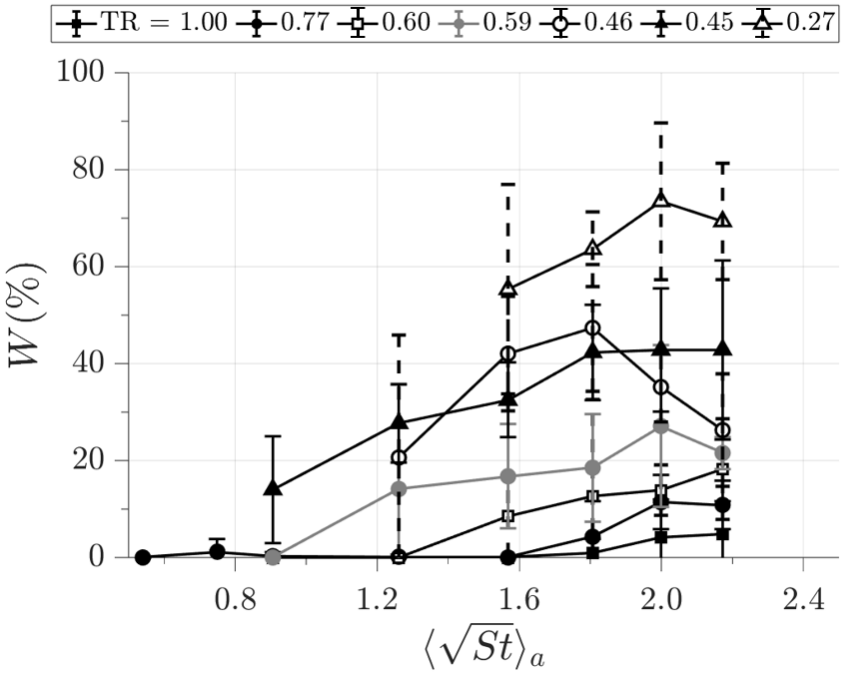

(a)

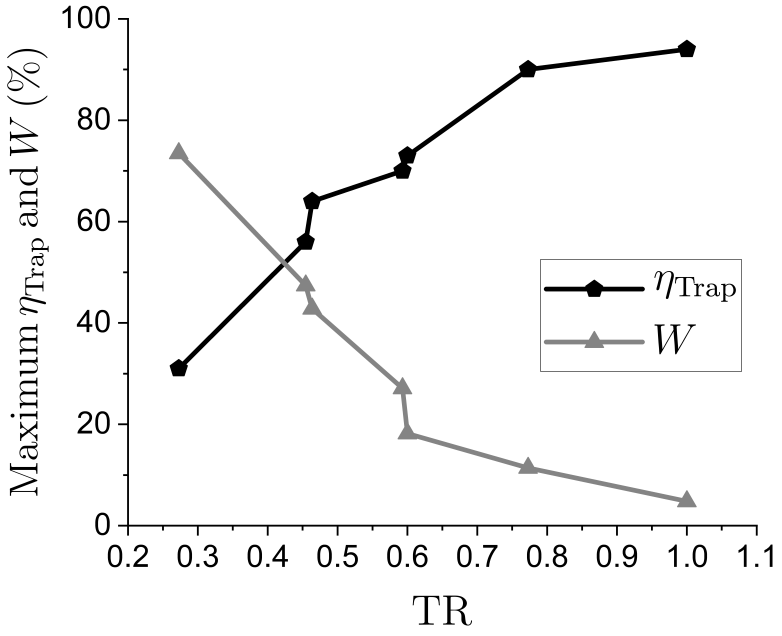

(b)

Figure 6.7: a) Wall losses for various trap geometries using the 1.5 mm nozzle as functions of $\langle\sqrt{\mathrm{St}}\rangle_{\mathrm{a}}$, b) Maximum trap efficiency and wall losses for varying TR.

The results discussed above highlight that to optimize trap efficiency, impactor geom-

etry needs to be considered. The nozzle outlet diameter (2R) should be minimized to increase $\langle\sqrt{\mathrm{St}}\rangle$. However, if 2R is made too small, consideration needs to be given to particles lost inside the nozzle and the potential changes in the distribution of particle sizes. From the nozzles tested, $\langle\sqrt{\mathrm{St}}\rangle = 1$ results in a predicted efficiency greater than 80%. After calculating the predicted efficiencies for the given particle size distribution and nozzle outlet diameter, the trap ratio (TR) should be maximized for enhanced trap efficiency while reducing wall losses. Figure 6.8 shows schematics of impactors with TR = 0.27, 0.45, 0.60, and 1.00 with their accompanying maximum trap efficiency. TR = 0.27 (narrow and deep) has a maximum efficiency of only 31%. To increase the efficiency, the trap can be made shallower, as shown by moving to TR = 0.45. A larger improvement can be made by instead increasing the trap diameter and moving to TR = 0.60. For peak performance, the trap is made shallower and wider for TR = 1.00 with a maximum trap efficiency of 94%. It should be noted that while increasing the trap ratio has been shown to improve trap efficiency, an infinitely large trap ratio produces a flat plate and defeats the purpose of the trap.

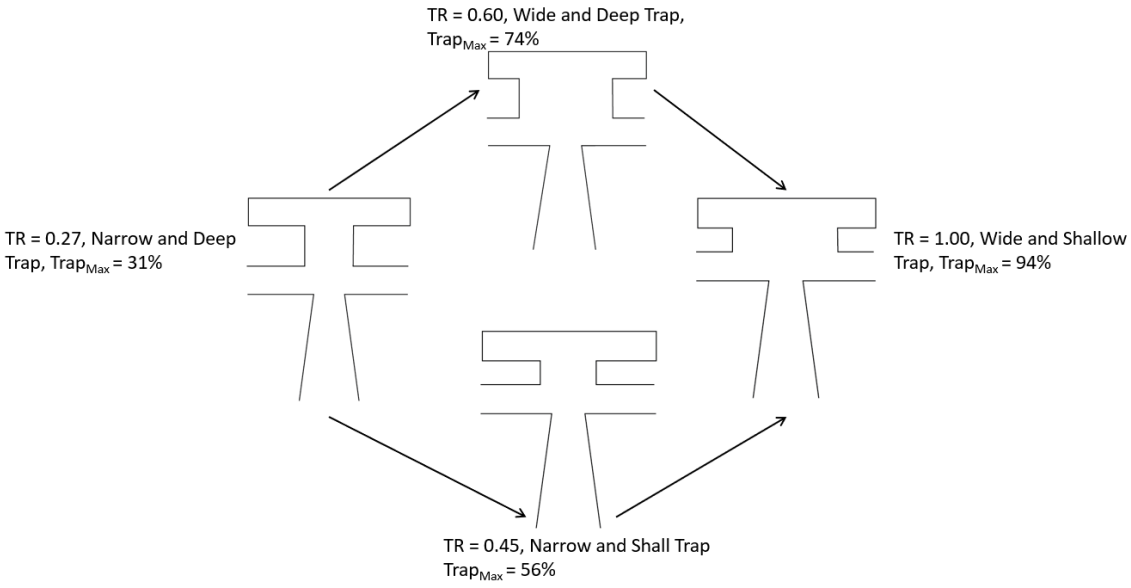

Figure 6.8: Schematics of trap impactors with different trap ratios and their maximum trap efficiencies.

Altering the trap ratio reveals that for similar $\langle\sqrt{\mathrm{St}}\rangle$, impactors can have a large vari-

ation in trap efficiency. This effect has not been studied in impactors and potentially is a consequence of the flow field generated by the trap. By studying the flow field, improved trap impactors can be developed and implemented to maximize particle capture.

Portions of this chapter are reproduced from my previously published article: White, Liam, Edward P. DeMauro, and German Drazer. ”The influence of geometry on particle capture efficiency in trap impactors.” Journal of Aerosol Science (2025): 106643.

CHAPTER 7
IMPACTOR FLOW FIELD EXPERIMENTAL INVESTIGATION

7.1 Introduction

There have been multiple studies, theoretically and numerically investigating the impactor flow field to determine efficiency. Marple and Liu used Hiemenz flow to model the impactor flow field to predict the efficiency of round and rectangular flat plate impactors [87]. Marple also used the numerical solution to the Navier-Stokes equation to solve for the flow field and particle trajectories for round and rectangular impactors with good agreement with experimental results [11, 72, 88, 89, 90]. However, numerical solutions are less reliable when turbulent effects become more prevalent with transitioning flows and more complex geometries [91]. In these instances, experiments to visualize the flow field are valuable to have a more complete understanding of the flow field.

Attempts to visualize impactor flow fields have been limited to the flat plate geometry. Marple and Liu [87] used a water tunnel with a plexiglass rectangular flat plate impactor and pH indicators to show the impactor streamlines for Re = 700 and 2,300. The experimental streamlines are in agreement with the theoretical predictions presented in the study, but are limited to laminar flow. Several studies have experimentally investigated the flow field of an impinging jet on a flat surface in the area of processor cooling [92, 93, 94, 95, 96, 97, 98, 99]. Van Hout *et al.* [93] performed particle image velocimetry (PIV) experiments to investigate the flow field of a round jet impinging on a flat surface for Re = 1,300, 6,620, and 12,354. The motivation was for cooling applications, but this flow field resembles that of the flat plate impactor. The results identify distinct counter-rotating vortex pairs formed on the edge of the jet shear layer due to the Kelvin-Helmholtz instability for all Re.As Re increases, the primary vortices break up into smaller vortices before impinging on the plate.

Shukla and Dewan [94] give a comprehensive review of studies investigating the flow field for impinging jets. Muarel and Solliec [95] also report vortices at the impingement region for turbulent plane jets (rectangular jets with large aspect ratios to represent a 2D geometry) with Re of 13,500 and 27,000 and increased turbulence near the wall. O'Donovan and Murray [96] show similar results using laser Doppler anemometry (LDA) for plane jets for Reynolds numbers between 10,000 and 30,000. Ashforth-Frost and Jambunathan [100] compared the developing velocity profiles of impinging fully developed and flat turbulent axisymmetric jets. They demonstrate that the potential core decreases from 4.8 to 4.5D for the fully developed to flat jet, and is attributed to the higher velocity gradient, which leads to increased entrainment.

For geometries similar to trap impactors, many studies on jets impinging on cavities are again found in the heat transfer literature [101, 102, 103, 104, 105]. Terekhov *et al.* [106] experimentally investigated the flow field of an axisymmetric jet impinging normally onto spherical cavities using PIV for Re = 12,000 and 28,000. The jet exits an 8.9 mm nozzle and impinges on cavities two nozzle diameters downstream (S/2R = 2) with a 46 mm diameter ($\mathrm{D_T}/2\mathrm{R} = 5.2$) with varying depths of 0.12, 0.26, and 0.5 times the diameter (T/2R = 0.01, 0.03, 0.06). When T/2R = 0.01, the flow resembles a jet impinging on a flat plate. For $\mathrm{T}/2\mathrm{R} > 0.01$, the flow makes a 180° turn and interacts with the incoming jet flow. They also discussed the existence of a toroidal vortex whose axis lies within the cavity when T/2R = 0.06, but moves upward and is approximately halfway between the nozzle exit plane and the cavity for T/2R = 0.03. Xie *et al.* [107] also performed PIV experiments for jets impinging on spherical dimples and noted the existence of toroidal vortices as well. They attribute the vortex formation to the flow deflection at the stagnation point and the centrifugal force exerted on the deflected flow inside the cavity.

These studies have investigated the flow field for geometries simpler than the trap impactors used in this dissertation. Although they identify certain flow features, such as the existence of the Kelvin-Helmholtz vortices at the shear layer and toroidal vortices near the

cavity, to truly understand the flow field for our trap impactors, our own experimental investigation needed to be performed. By studying the trap impactor flow fields, we could potentially find fluid structures that contribute to the decrease in trap efficiency at high Stokes numbers. Our flow field investigation explored two potential modes for decreased trap efficiency: particles that enter and exit the trap, and particles that deviate from their initial trajectories and never enter the trap.

7.2 Flow Field Investigation Experimental Setup

7.2.1 Dynamic Similarity

It would be ideal to study the impactors used in the efficiency experiments; however, the sizes of the impactors are not large enough to be compatible with the experimental techniques used throughout this dissertation. A high-speed camera was used to qualitatively measure the flow field, while a sCMOS camera and a hot wire anemometer were employed for quantitative measurements. Due to the gap between the end of the nozzle and the trap entrance for the 1.5 mm impactor only being 2.25 mm, the resolution required to resolve the region was not feasible. Also, the 1.5 mm outlet nozzle was comparable to the length of the hotwire probe and would not have a high enough spatial resolution. To combat these issues, larger impactors were modeled to maintain dynamical similarity with the original designs. Dynamic similarity is the concept where, if the dimensionless parameters of one flow are matched to another, then the two flows are comparable. To match the flow field of the original impactors to the larger models, the Reynolds numbers for the two must match.

Three trap impactors with 2R = 1.5 mm flow fields were investigated: TR = 0.27, 0.59, and 1.00. TR = 1.00 (wide and shallow trap) was chosen because it had the highest trap efficiency and closely resembled the predicted efficiency. This configuration is assumed to most resemble the flat plate impactor, which will be used as the control. TR = 0.27 (narrow and deep trap) had the worst efficiency and can potentially provide the most detail about what flow features potentially reduce trap efficiency. TR = 0.59 (medium width and depth)

had a reduced trap efficiency but not as poor of performance as TR = 0.27. This design could be a transition point between low and high trap efficiencies.

The larger impactors were again modeled in SolidWorks and printed with the FormLabs Form 3 SLA printer. One nozzle was used with the three interchangeable traps. The nozzle was not scaled to mimic the original 1.5 mm nozzle length due to size limitations. However, we were less concerned with the internal flow in the nozzle and were more focused on the outlet velocity and jet Reynolds number. The nozzle inlet diameter is 25.7 mm, the outlet is 16.9 mm, and the length is 55 mm. No spline was used here, like in the original models, as the taper is linear. We targeted Re = 1,000 - 20,000 as this was the range for the impactors used in the efficiency experiments. All dimensions for the trap models are scaled to the larger nozzle outlet diameter and are the same as in Table 6.2. The modeled traps included the impactor plate, o-ring, and trap backing so the traps could be printed as one piece. A flat plate model was also printed to compare with the trap flow fields. Pictures of the larger traps are shown in Figure 7.1.

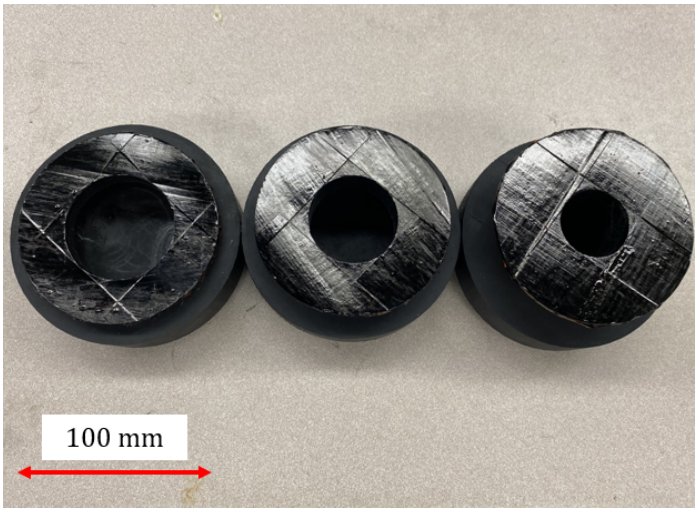

(a)

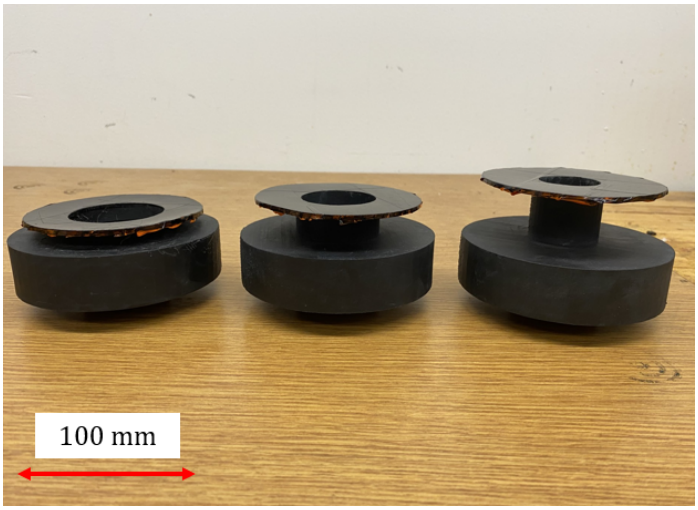

(b)

Figure 7.1: From left to right: TR = 1.00, 0.59, 0.27. a) Top view of larger traps, b) side view

7.3 Experimental Setup

7.3.1 Flow Conditioning

All of the following experiments will use the same flow conditioning apparatus. A picture of the flow conditioning setup is shown in Figure 7.2. A 60-gallon compressor with a pressure gauge compresses air to 30 psi. Downstream of the compressor are a gate valve and a pressure gauge to set and modulate the inlet air pressure to the impactor. A solenoid

valve is directly after the pressure gauge and is actuated by a solid-state relay connected to a variable power supply. After the solenoid valve is a mixing chamber with one inlet for the compressed air and another for smoke particles from a smoke machine used in flow visualization experiments. The mixing chamber outlet then connects to the inlet of the impactor. All components downstream of the compressor are secured to an optical table to prevent them from shifting. The impactor nozzle is secured to a stand on the table, and the flat plate or traps are held by a burette clamp. The clamp is fixed to a stand on two micrometers that can make fine adjustments in the lateral and longitudinal directions. The combination of the micrometers and the clamp allows for fine adjustments in all directions.

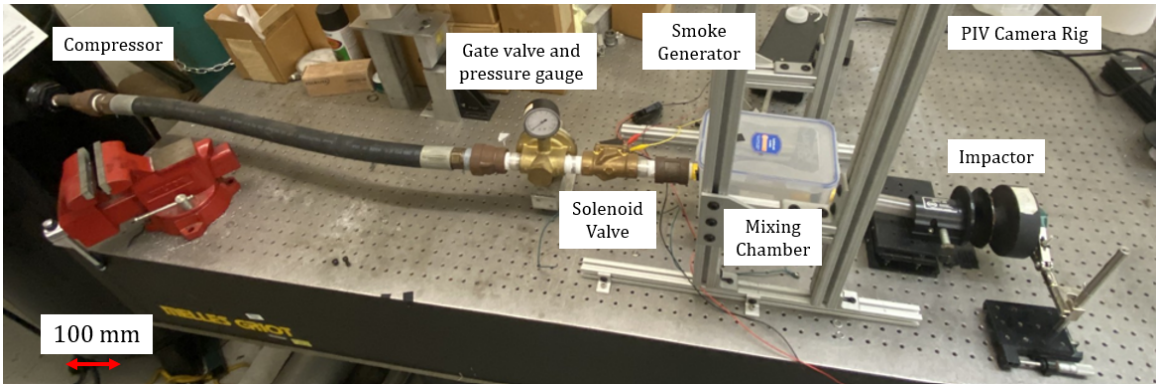

(a)

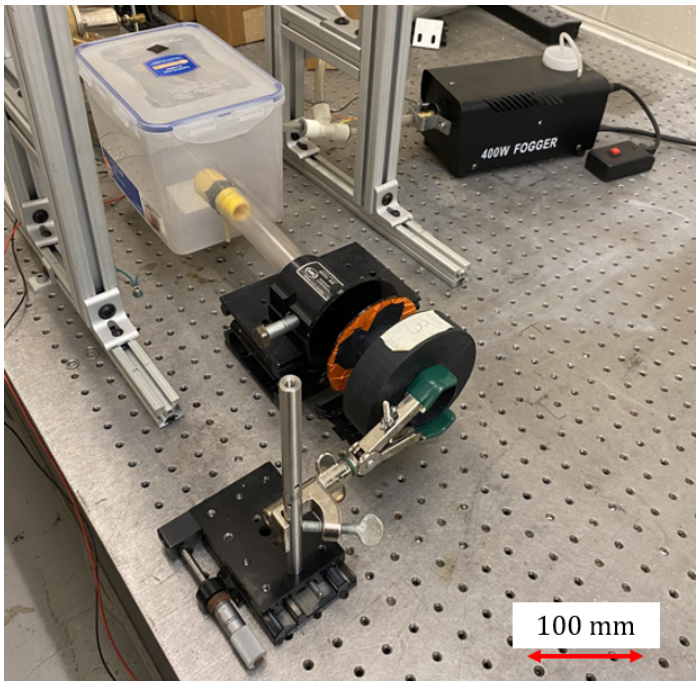

(b)

Figure 7.2: a) Picture of the experimental setup for the flow field investigation, b) Enhanced view of impactor, mixing chamber, and smoke generator. Note: The second micrometer for trap adjustment is not shown.

7.3.2 High-Speed Shadowgraphy Setup

Initial experiments used the principle of shadowgraphy, or backlit imaging, to record high-speed videos of the flow emanating from the impactor nozzle and interacting with the flat plate or the trap. Shadowgraphy is the experimental method where a light source is placed behind the flow, and a camera is placed opposite the light source. In these experiments,

a smoke machine generates smoke particles that seed the flow, and the light illuminates the smoke particles against a black background. In contrast to the efficiency experiments, where we wanted to maximize the particle Stokes numbers, for these experiments, we want to minimize the Stokes number. The smoke particles are assumed to have low enough Stokes numbers so they follow the streamlines and perfectly represent the flow field. A Photron Fastcam SA-Z high-speed camera was then used to capture thousands of images during each experiment. The high-speed camera used a frame rate of 3,000 frames per second and a shutter speed of 1/3,015 s^{-1}. Capturing images at 3,000 frames per second can record the flow as it is changing over time. For a frame rate of 3,000, the pixel array was 896 $\times$ 896, with a 12-bit monochromatic dynamic range. Typical cameras have frame rates between 24 and 60 frames per second and can miss important details because they are taking images with too long intervals between frames, or can blur and distort the images. However, with the high-speed camera, large-scale flow features can be recorded and tracked, such as the Kelvin-Helmholtz instability and vortices impinging on the flat plate. After recording the images, they can be replayed and analyzed to watch the flow evolve over time. The camera was placed on the optical table, about 500 mm away from the impactor. A Nikon Micro-NIKKOR 105 mm lens was used to focus the region between the end of the nozzle and the top of the trap, and the impactor midplane was in the center of the frame. To match S/2R for the smaller impactors, a gap of 25.4 mm was to be used. However, the gap was too small as smoke particles quickly filled the region and led to the images being oversaturated. A 40 mm gap was used instead because it allowed for more images to be recorded before becoming oversaturated. The shadowgraphy results are qualitative and intended to only visualize the flow field and reveal structures in the flow. The fluid dynamical structures discussed in the results section are assumed to be present for the 25.4 mm gap, and the flow field can still be analyzed and discussed. A picture of the setup is shown in Figure 7.3, and a picture of the field of view for the flat plate impactor with the coordinate axes is shown in Figure 7.4.

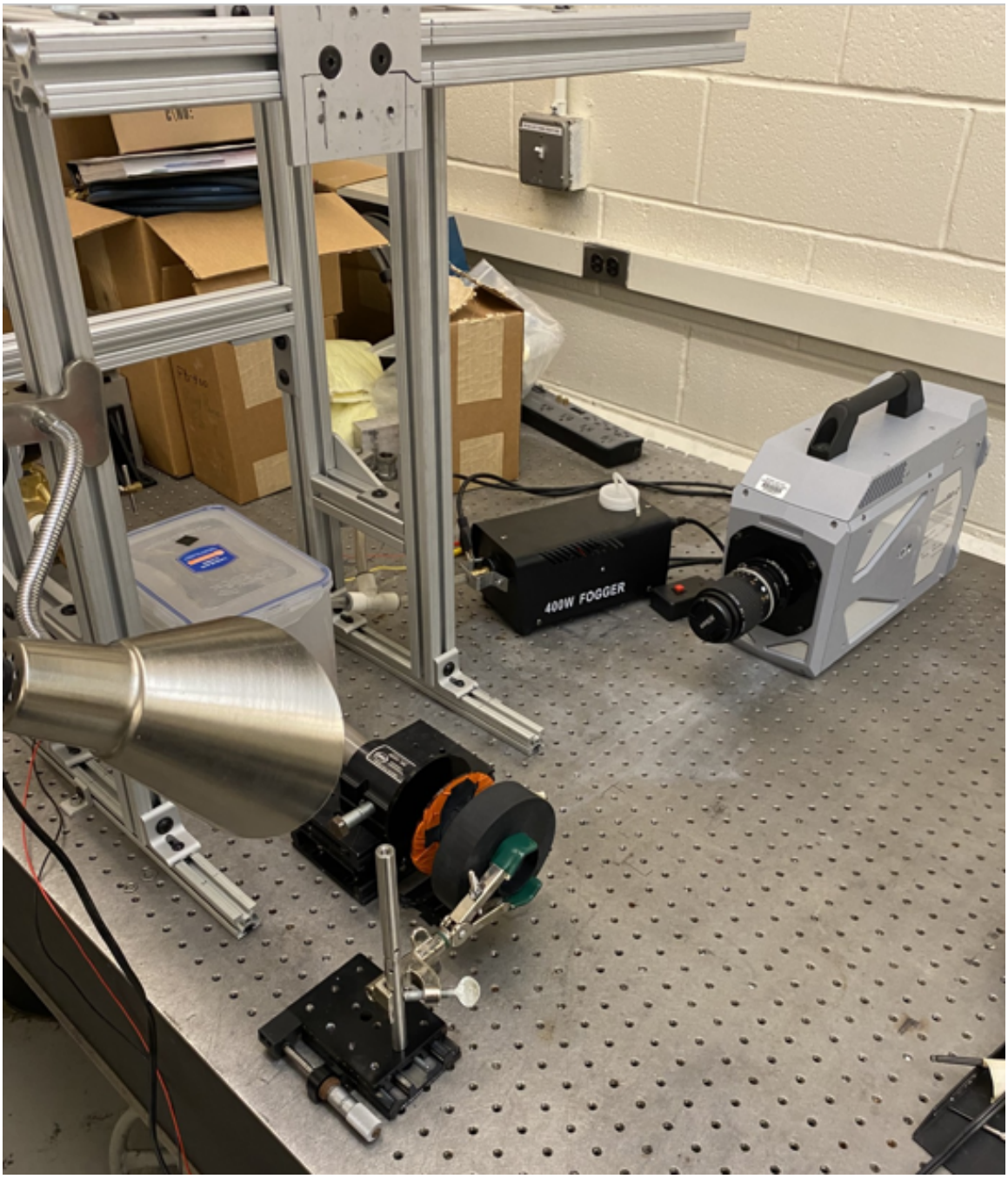

Figure 7.3: A picture of the shadowgraphy experimental setup.

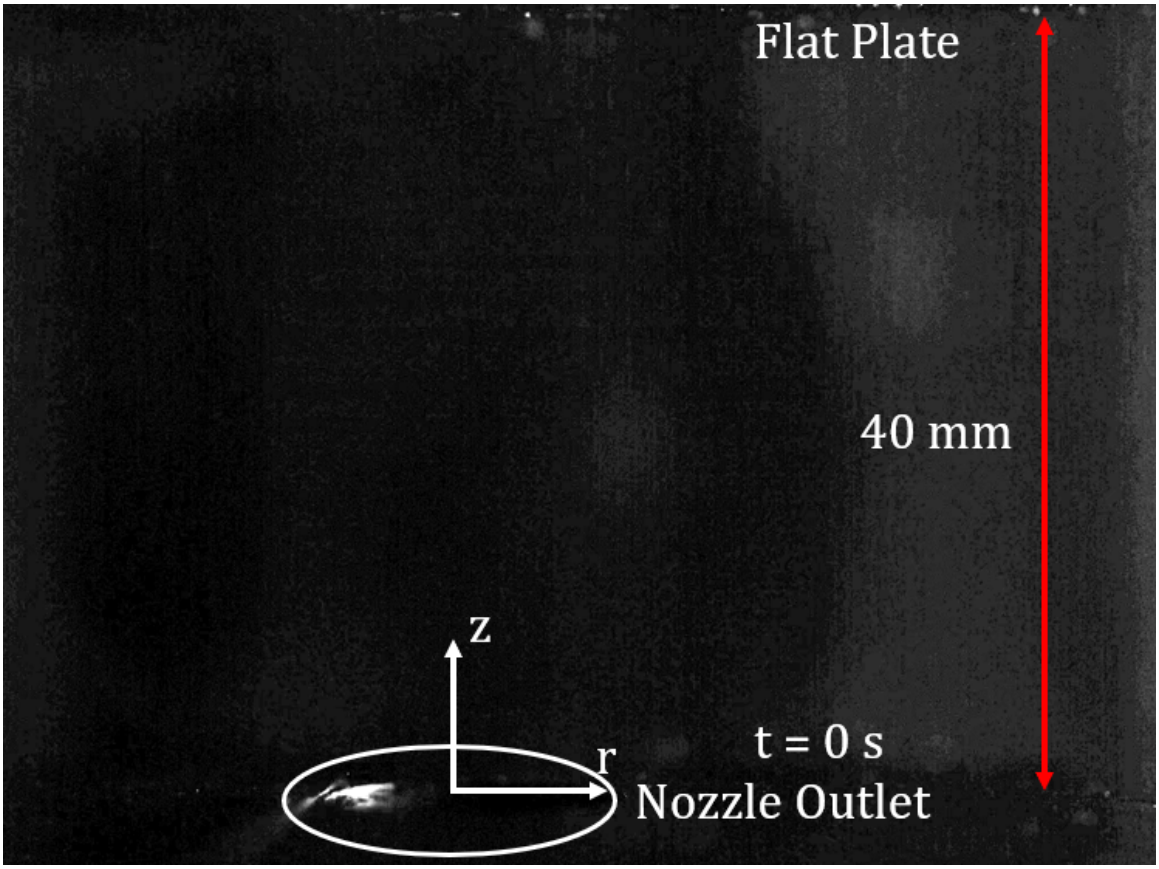

Figure 7.4: A picture of the flat plate impactor used for the shadowgraphy experiments.

The experimental procedure is as follows. First, the air compressor is turned on and set to 30 psi. Next, the gate valve is rotated to set the desired pressure at the pressure gauge. The mixing chamber is then primed with smoke particles. Next, the high-speed camera begins recording, and the solenoid valve is triggered to allow the compressed air to evacuate the mixing chamber, and the particle-seeded flow enters the nozzle. Images are recorded until there are too many smoke particles in the frame and the images become saturated, which is approximately 2 s.

7.3.3 2D PIV Setup

While the shadowgraphy experiments can visualize the flow, they do not easily provide quantitative results. The high-speed videos can show the existence of large-scale features in the flow, but they do not give the velocity at different points to fully reconstruct the flow

field. To reconstruct the flow field, particle image velocimetry (PIV) experiments were performed on the gap between the end of the nozzle and the flat plate or one of the traps. Similar to the shadowgraphy experiments, the flow will be seeded with smoke particles that are assumed to be perfectly advected. As the particles are transported, a laser pulses and illuminates the flow. The laser is in sync with a camera that will take images of the flow when the particles are visible. A schematic of the timing diagram is shown in Figure 7.5. The camera exposure square wave is shown on top in black, and the laser pulses are shown in green on the bottom. When the frames are exposed, denoted by the maximum of the black square wave, the frames will be dark until the laser is pulsed. Once the laser fires, the seed particles will be illuminated and recorded by the camera. The pulse duration is in the nanosecond range and effectively freezes the particles in place. This process repeats for the second pulse at a time Δt later. The time between the first pulses in the double-pulse sequence is determined by the laser repetition rate of 15 Hz. Frames 1 and 2 combine to form one image pair, and the runtime set by the control unit determines of the number of image pairs recorded during a trial.

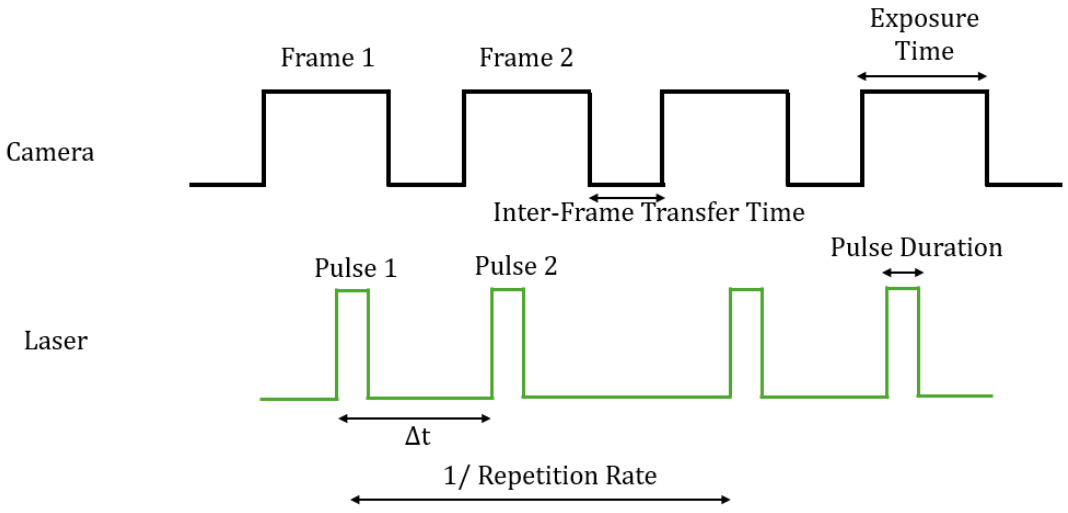

Figure 7.5: PIV timing diagram.

Two frames are necessary to calculate the predicted displacement of the particles. Each frame is subdivided into smaller interrogation windows, each with at least 10 particles, and

the cross-correlation for each window is performed. The cross-correlation is given below

$$\mathrm{C(dx,dy)} = \sum_{\mathrm{x=0,y=0}}^{\mathrm{x<n,y<n}} \mathrm{I_1(x,y)I_2(x+dx,y+dy)},\ -\frac{\mathrm{n}}{2} < \mathrm{dx,dy,} < \frac{\mathrm{n}}{2}, \tag{7.1}$$

where $\mathrm{I_1}$ and $\mathrm{I_2}$ are intensities of the first and second interrogation windows, x and y are the coordinates for the images, and dx and dy are the displacements between the windows. The peak of C (see Figure 7.6) is then the most probable particle displacement for the window, and dividing by $\Delta \mathrm{t}$ yields the local velocity vector. The quality of the correlation can be quantified by the peak ratio,

$$\mathrm{Q} = \frac{\mathrm{P_1 - min}}{\mathrm{P_2 - min}}, \tag{7.2}$$

where $\mathrm{P_1}$ and $\mathrm{P_2}$ are the peak heights of the first and second highest correlation peaks, respectively, and min is the lowest value of the correlation plane. A higher peak ratio corresponds to a stronger correlation to the highest peak compared to the others. A peak ratio below one generally indicates low confidence and may be excluded from the vector field. This process is repeated for each window to construct the velocity field [108, 109, 110, 111].

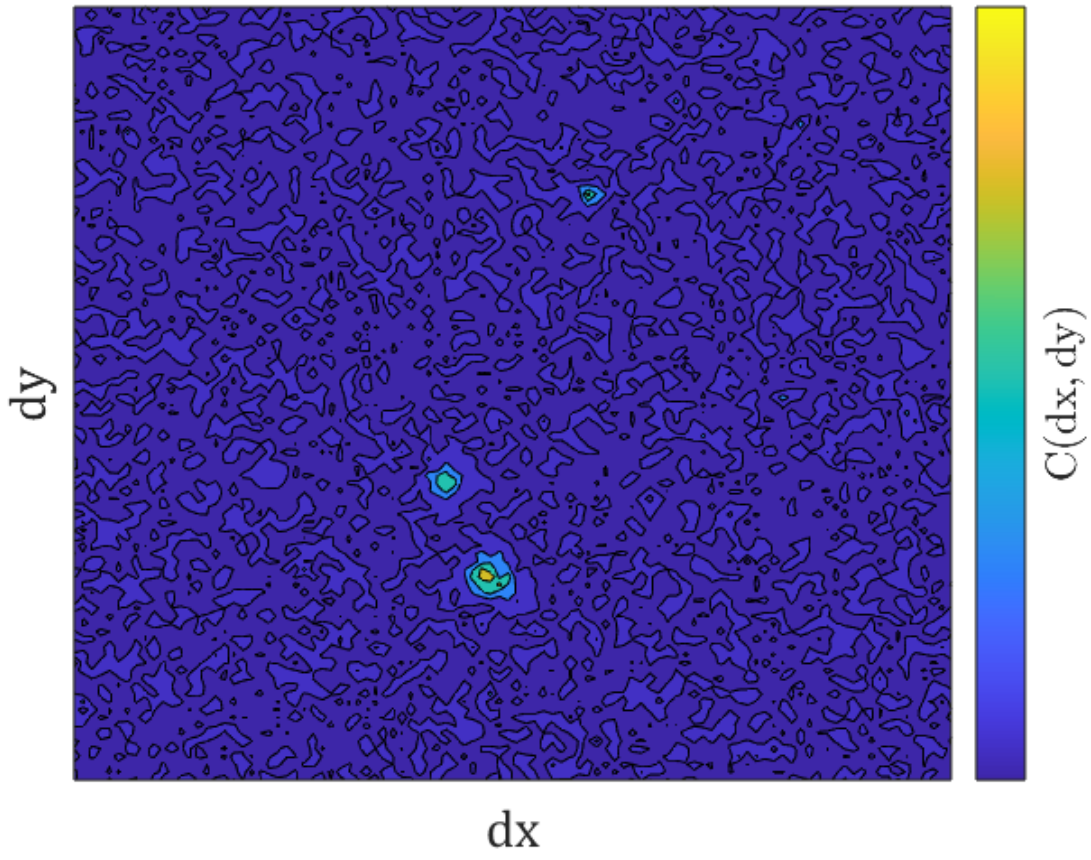

Figure 7.6: Example of cross-correlation, $\mathrm{R}(\mathrm{s})$, highlighting the peaks that corresponds to the most probable displacements of an interrogation window.

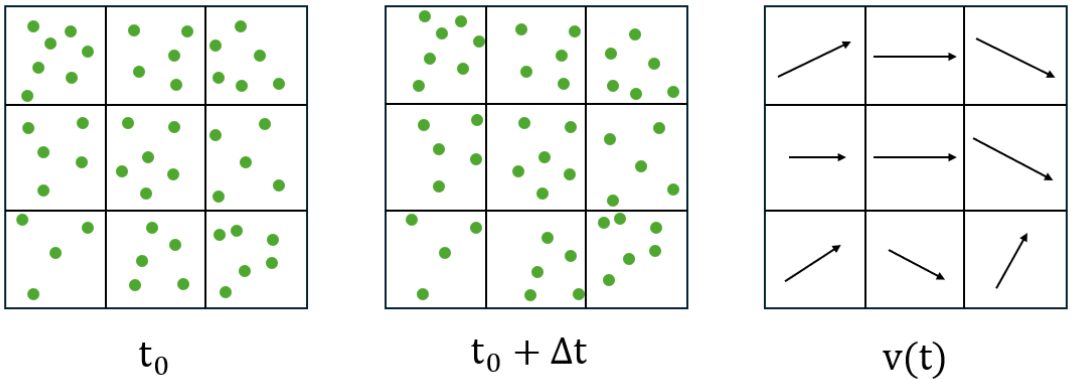

Figure 7.7: Schematic of an example flow field deduced by the cross-correlation of two PIV images.

A schematic of the PIV experimental setup can be seen below in Figure 7.8. The PIV

measurements were performed using a LaVision DaVis v8.4 system. A Quantel Evergreen 200 mJ/pulse, double-pulsed Nd:YAG laser with a 532 nm wavelength and repetition rate of 15 Hz illuminated the field of view. The laser beam was expanded using a cylindrical lens into a 1.5 mm-thick laser sheet at the midplane of the impactor.

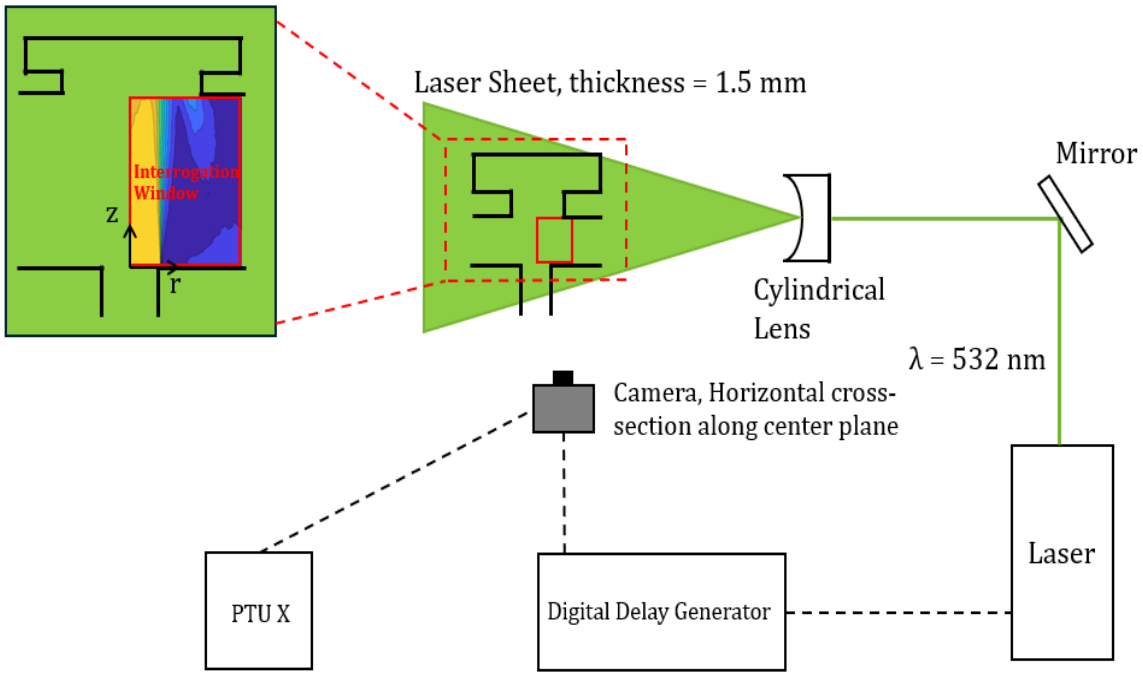

Figure 7.8: Schematic of the particle image velocimetry (PIV) experimental setup.

A LaVision Imager scientific complementary metal-oxide-semiconductor (sCMOS) camera equipped with a 200 mm Nikon NIKKOR lens with a resolution of 2560 x 2160 pixels, digitized to 16 bits, was mounted vertically above the impactor. Only one camera was needed to capture the axial and radial velocity components due to the axisymmetric flow field. A rig constructed of aluminum t-slot frames was assembled to secure the camera above the setup while allowing for easy lateral and longitudinal adjustments. To calibrate the camera, a mock particle trap was 3D-printed with a jig to hold a 58 mm x 58 mm calibration plate at the midplane of the trap. The traps could then be interchanged without the need for recalibration. The time delay, Δt, between laser pulses varied between 6 and 46 µs, depending on the average nozzle outlet velocity, to capture the appropriate particle

displacement with a Stanford Systems DG-535 digital delay generator. The digital delay generator also triggered a LaVision Programmable Timing Unit (PTU X) to capture the images at a frequency of 15 Hz. The flow could only be viewed in the gap between the end of the nozzle and the obstruction due to the cylindrical geometries of the traps. Curved surfaces can distort the light moving through the traps, and therefore, it was not possible to visualize the flow inside them. The left border of the interrogation window was aligned with the centerline of the flow field. To avoid laser reflections that add additional noise to the velocity vectors, the models were covered with vinyl tape and painted black. Also, a LaVision 532 +/- 10 nm optical filter was placed over the camera lens to reduce optical noise. However, some reflections were still present at the nozzle exit and the trap, and to remove these reflections, the top and bottom of the interrogation window were slightly offset from these areas.

The beginning of the procedure is similar to the shadowgraphy experiments, where the gate valve is set and the mixing chamber is primed with smoke particles. After priming the mixing chamber, the laser is turned on, the solenoid valve is opened, and the PTU X begins to capture images. For lower velocities, the images are captured directly after the solenoid valve is opened. However, for higher velocities, there is a delay between 1 and 3 s due to the smoke particle density being too high and oversaturating the first images. Waiting for a short period of time allows the smoke particle density to decrease, and the images are no longer oversaturated. For lower velocity experiments, 50 images were recorded per experiment, but only 30 were recorded at higher velocities. This is due to the high velocities expelling all of the smoke particles quickly, and only 30 images could be recorded during the runtime when the images were visible. In total, between 200 and 250 images were recorded for each trap configuration and jet velocity.

The workflow to construct the flow fields is as follows. First, the images for each test condition were appended. A single run could record between 30 to 50 images, and therefore, all of the trials for a test condition were appended to be analyzed together to

create the 200-250 image data set. Next, the average intensity of the first five images was removed from all images to create a baseline. Then, each intensity was multiplied by a constant of two to equally enhance all intensities, which allows for the velocity vectors to be calculated more easily. The images were then pre-processed by using a sliding background subtraction with a length of 10 pixels and a particle intensity normalization filter, also with a scale of 10 pixels. After pre-processing the images, a multi-pass algorithm started with two passes using a 64 x 64 pixel interrogation window with 50% overlap, followed by three passes using a 32 x 32 pixel window also with 50% overlap, with high accuracy enabled. The Standard I1$\times$I2 (via FFT, no zero-padding) cross-correlation algorithm was used to calculate the velocity vectors. Although a velocity vector is calculated for each window, not every vector is high quality. A minimum peak ratio of 1.1 was used to remove low-quality vectors. These removed vectors appear as white holes in the resultant velocity fields. The flow velocity uncertainty was calculated by DaVis as explained in [112] and had a maximum uncertainty of 0.2 m/s.

7.3.4 Hotwire Anemometry Setup

Although the PIV experiments are able to reconstruct the flow field, due to the frequency response of only 15 Hz, they cannot resolve higher frequency events in the flow, such as a convected vortex. The instantaneous images from the PIV experiments may show a vortex at different locations, however, it may not be the same vortex moving downstream due to the low temporal resolution of the system. To resolve temporal fluctuations in the flow, a Dantec Mini CTA 54T30 constant temperature hotwire anemometer was used to record the flow speed at different points across time. This is a single-wire probe that can record the velocity at a rate of 10 kHz, but due to the Nyquist criterion, it can only resolve a maximum frequency of 5 kHz, which is still orders of magnitude improvement over the PIV. A Wheatstone bridge circuit with closed-loop feedback to adjust the applied current to the sensor maintains the wire at a constant temperature. The hotwire was placed in the

flow field with its long axis perpendicular to the flow. The local fluid speed is calculated by the heat transfer rate from the cylindrical wire. The unsteady energy balance for the cylindrical wire is

$$\mathrm{mc_p}\frac{\partial \mathrm{T_s}}{\partial \mathrm{t}} = \dot{\mathrm{Q}}_\mathrm{e} - \dot{\mathrm{Q}}_\mathrm{f}, \tag{7.3}$$

where m is the wire mass, $\mathrm{c_p}$ is the wire specific heat at constant pressure, $\mathrm{T_s}$ is the wire temperature, $\dot{\mathrm{Q}}_\mathrm{e}$ is the heat transfer rate to the wire from the applied current, and $\dot{\mathrm{Q}}_\mathrm{f}$ is the heat transfer from the wire due to convection. The expressions for $\dot{\mathrm{Q}}_\mathrm{e}$ and $\dot{\mathrm{Q}}_\mathrm{f}$ are given below

$$\dot{\mathrm{Q}}_\mathrm{e} = \mathrm{I}^2\mathrm{R_s} \tag{7.4}$$

$$\dot{\mathrm{Q}}_\mathrm{f} = \mathrm{hA}(\mathrm{T_s} - \mathrm{T_f}), \tag{7.5}$$

where I is the current applied to the wire, $\mathrm{R_s}$ is the wire resistance, h is the heat transfer coefficient of the fluid, A is the surface area of the cylindrical wire, and $\mathrm{T_f}$ is the fluid temperature. Due to the hotwire probe being a constant temperature anemometer, the left-hand side of the energy balance is negligible, and the heat transfer rates to and from the wire are equal. To maintain a constant wire temperature ($\mathrm{T_s}$), the applied current to the wire changes with time, and results in an output voltage of the Wheatstone bridge, E. Lastly, King's law [113] gives the relationship between the output voltage and the fluid velocity, U, by

$$\mathrm{E}^2 = \mathrm{A} + \mathrm{BU}^\mathrm{n} \tag{7.6}$$

where A, B, and n are found through calibration by the manufacturer under a fixed sensor and fluid temperature condition. E is recorded by a National Instruments compactDAQ at a sampling rate of 25 kHz.

Without knowledge of the constants A, B, and n in Equation 7.6, the flow velocity

can be deduced from a calibration curve. A calibration curve was constructed using the setup from the water droplet efficiency tests outlined in section 4.2. A portion of nylon tubing with a 4 mm internal diameter was used as a nozzle with varying flow rates. The outlet velocity of a constant diameter tube with a known flow rate can be calculated from continuity (Equation 4.1). The probe was placed at the center of the tube at the outlet, and the output voltage was recorded for various flow rates. The corresponding calibration curve is shown below in Figure 7.9. By applying the equation from the line of best fit, the flow velocity can be deduced from the probe output (E). The hotwire was used to confirm the nozzle exit velocities for the PIV experiments.

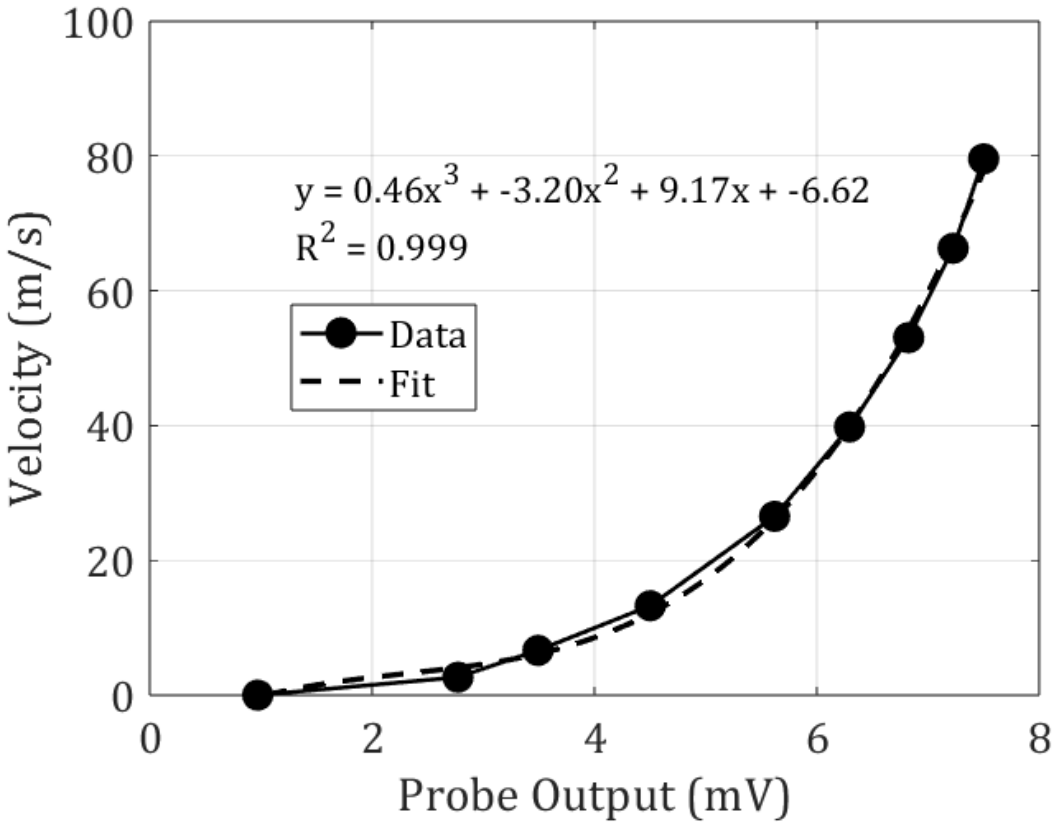

Figure 7.9: Calibration curve for the hotwire anemometer constructed using a 4 mm nozzle with varying outlet velocities.

As mentioned previously, the hotwire anemometer had a frequency response of 10 kHz, and due to the Nyquist criterion, a maximum signal of 5 kHz could be analyzed to avoid

aliasing. Although some hotwire anemometers have a frequency response up to 100 kHz, this probe is still an orders of magnitude improvement over the PIV setup. Placing the probe in the flow and recording over the duration of the runtime gives the point speed as a function of time. This time trace can then be used to analyze the turbulent intensity, power spectra, and other time dependent phenomena. A picture of the probe placed in the center of the gap is shown in Figure 7.10.

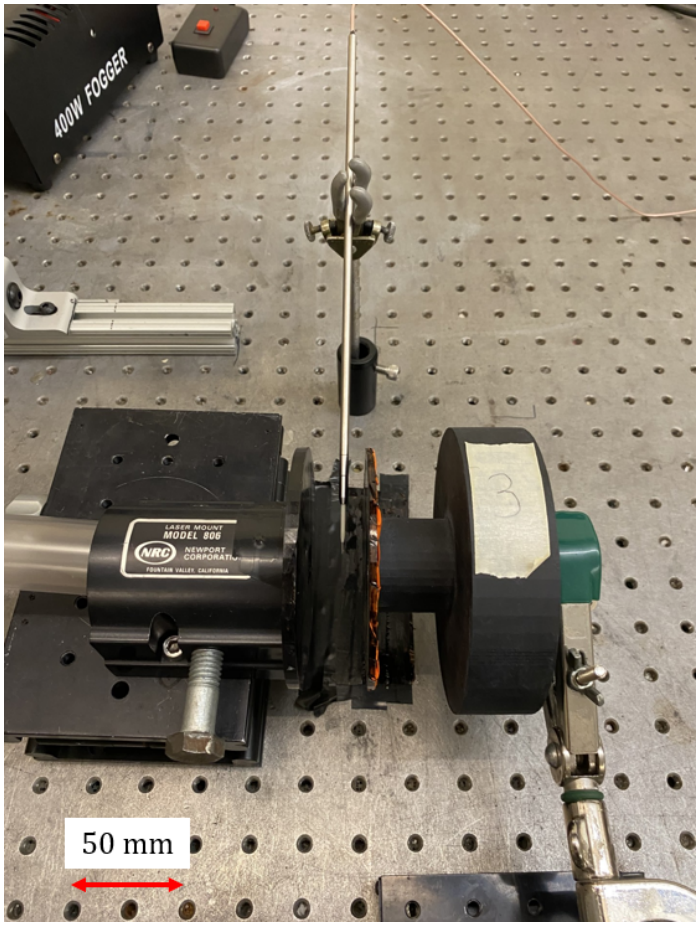

(a)

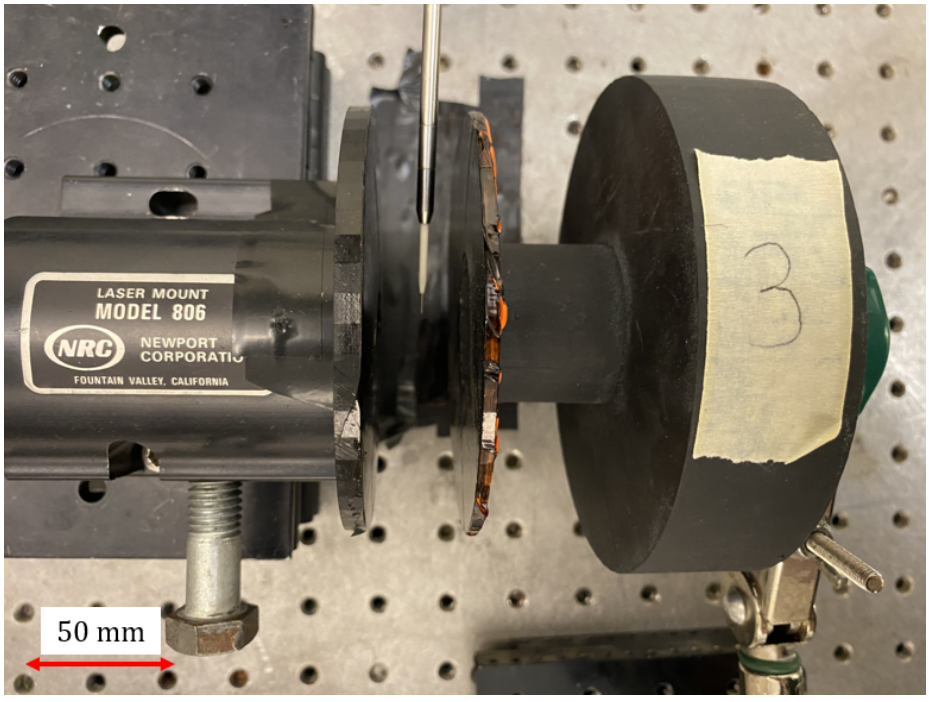

(b)

Figure 7.10: Images of the hotwire anemometer placed in the gap between the end of the nozzle and the TR = 0.27 trap.

CHAPTER 8
IMPACTOR FLOW FIELD EXPERIMENTAL RESULTS

8.1 High-Speed Shadowgraphy Results

The first shadowgraphy experiments were performed with the flat plate impactor with a 40 mm gap (S/2R = 2.4) and a Reynolds number of 800 using the jet centerline velocity at the nozzle exit as the characteristic velocity. The purpose of these experiments was to inspect the flow field of the jet emerging from the round nozzle and impinging on the flat plate. As mentioned previously, the geometry does not match the impactors used in subsection 6.1.3, but certain characteristics from the flows will be consistent with the other geometries. The frame rate for these experiments was 3000 frames per second, and the trials were recorded until the smoke particles oversaturated the field of view. Frames from the experiment between t = 0.0167 and 0.0817 s are shown below in Figure 8.1 with the flow moving from bottom to top.

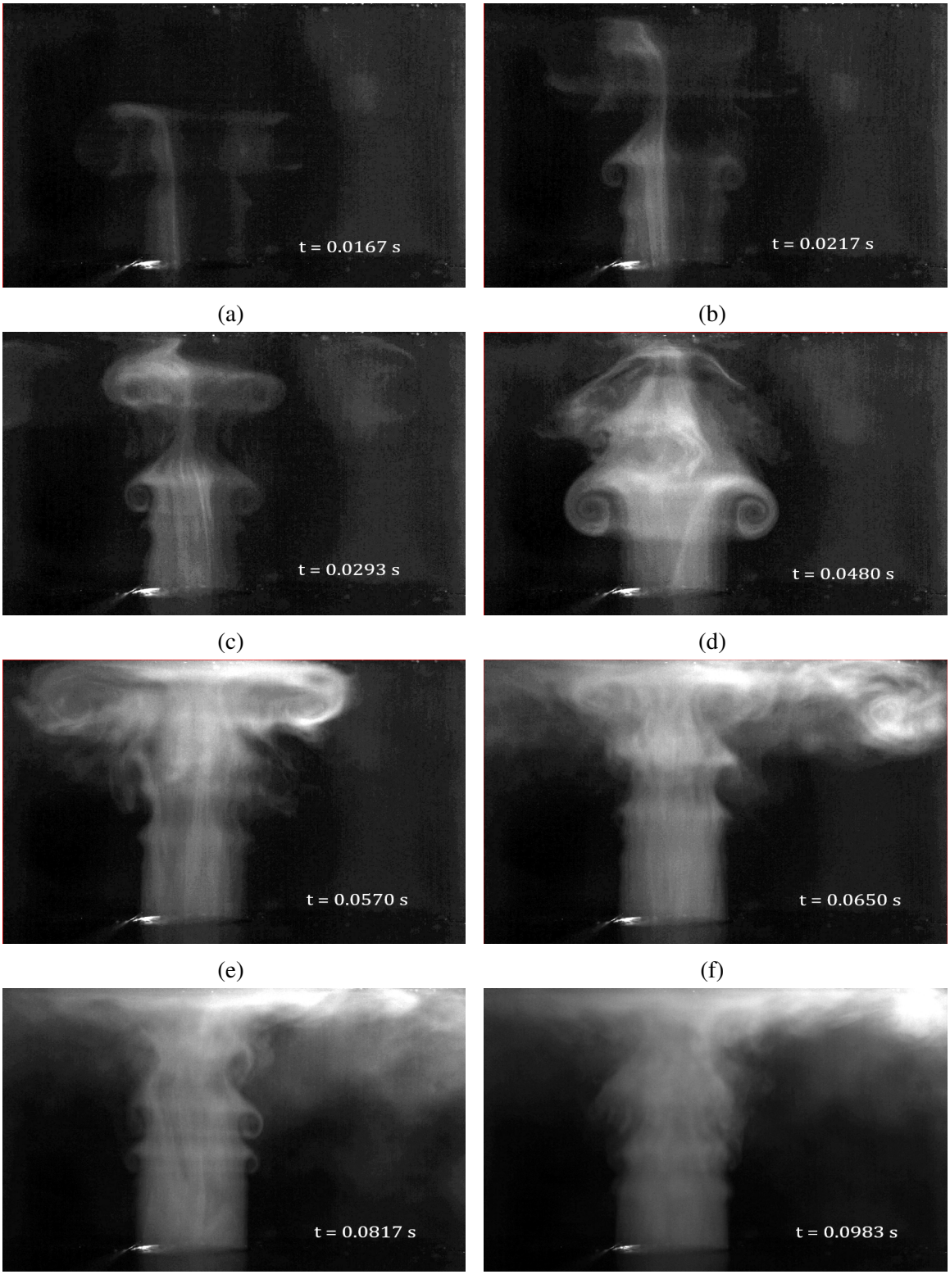

Figure 8.1: Shadowgraphy results for the flat plate impactor with Re = 800. a) Initial faint ring vortex is visible, b) Ring vortex impinges on flat plate, c) Clearer images of impinging vortex and another vortex convected downstream, d) Well-defined primary ring vortex at the nozzle outlet, e) Primary vortex impinges on flat plate, f) Ring vortex rolls up and separates from plate, g) Developed impinging flow and defined K-H vortices, h) Flow impinging on plate and smaller vortices are rolling up and moving outward.

As the first smoke particles emerge from the nozzle outlet (Figure 8.1a), there is a vortex roll-up that forms a faint ring vortex. In the next two images, vortices are seen impinging on the flat plate, and a smaller vortex can be seen near the halfway point of the gap. The vortices are generated due to the Kelvin-Helmholtz instability driven by the velocity gradient between the jet and the quiescent ambient air. The instability in the shear layer causes the fluid at the edge of the jet to roll up and form the vortex around the circumference of the jet [65, 114, 115, 116]. These vortices are periodic and are shown to form a coherent shape near halfway between the nozzle and the flat plate. Figure 8.1a-c show the startup transient of the emerging jet, and it is not until Figure 8.1d that the thicker, more defined flow emerges from the nozzle in the form of a larger ring vortex. After the ring vortex impinges on the plate, the defined impinging flow, typically characterized by potential flow, is seen. Here, the jet impinges normally on the flat plate, and the centerline comes to rest at the stagnation point. All fluid elements not lying on the centerline will move radially outward when interacting with the solid boundary due to the no-slip and no-penetration conditions. Figure 8.1f then shows the ring vortex has moved radially outward, rolled up, and separated from the plate. This action of the flow lifting up and away from the plate has been described in the literature as the wall jet after impingement [93, 105, 107]. Figure 8.1g shows that the initial vortex has moved out of frame as smaller vortices form along the jet mixing layer. The last image shows that secondary vortices have also impinged on the plate and then moved radially outward, similar to the primary ring vortex.

The experiments were repeated for the flat plate impactor with Re = 13,000, and the results are shown in Figure 8.2.

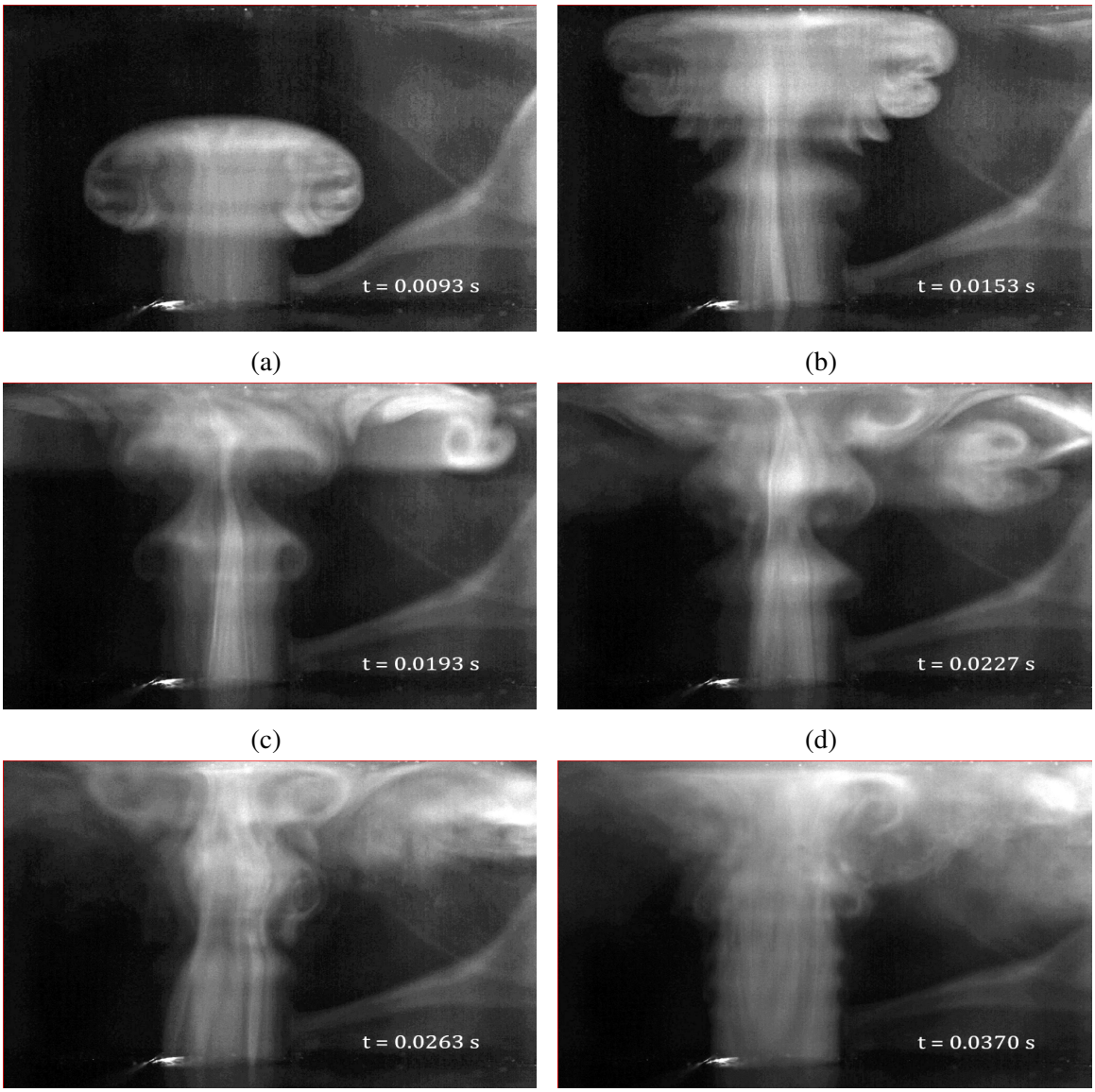

Figure 8.2: Shadowgraphy results for Re = 13,000, flat plate impactor. a) Primary vortex emerging from outlet, b) Primary ring vortex impinging on flat plate, c) Vortex rolling up and beginning to separate from plate and creating the wall jet, d) Vortex has separated from the plate and secondary vortices are seen forming, e) Secondary vortices impinging on plate, f) Smaller K-H vortices are seen forming around the circumference of the jet.

The overall behavior of the jet is similar to that of Re = 800. The slight differences appear in the onset of the Kelvin-Helmholtz instability. Figure 8.3 compares the Re = 800 jet at t = 0.0983 s with the Re = 13,000 jet at t = 0.0370 s.

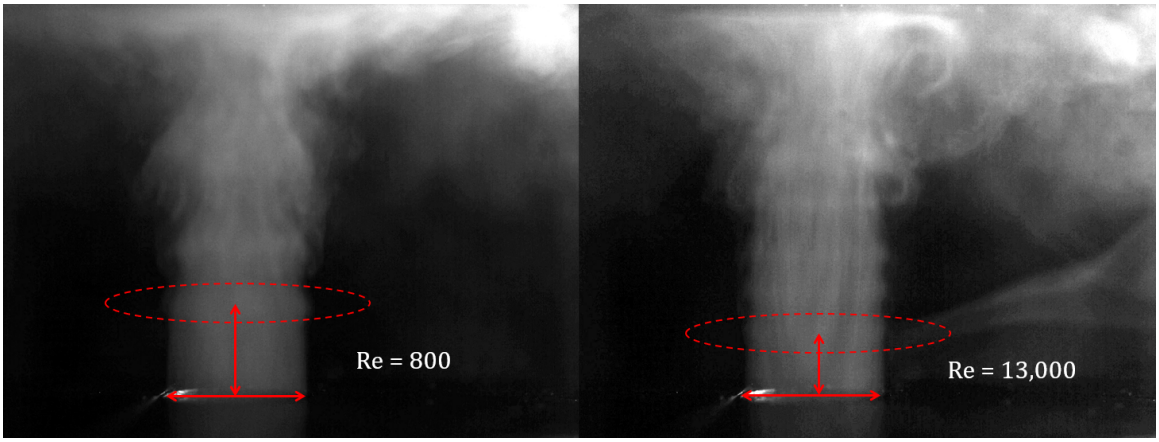

Figure 8.3: Comparison of the onset of the Kelvin-Helmholtz instabitlity for Re = 800 and Re = 13,000 flat plate impactors. The Re = 800 instability appears at $z/2R \approx 0.64$, whereas the instability appears at $z/2R \approx 0.46$ for Re = 13,000.

In these images, the inception of the K-H instability is visible along the edges of the jets. Comparing the locations using pixel analysis, the Re = 800 jet instability appears at $z/2R \approx 0.64$, whereas the instability Re = 13,000 appears at $z/2R \approx 0.46$. This is to be expected as the increase in Reynolds number increases the velocity shear and can cause the flow to become unstable at an earlier downstream location. Because the densities are constant between the jet and the ambient air, the shear layer can be modeled as a vortex sheet with strength $\gamma = U_2 - U_1$, where U_2 is the jet velocity and U_1 is the velocity of the stagnant air. The wave speed for the instability is then

$$c = \frac{U_2 + U_1}{2} \pm i\frac{U_2 - U_1}{2}. \tag{8.1}$$

For increasing values $U_2 - U_1$, the wave speed increases leading to stronger instabilities [65].

After recording the high-speed shadowgraphs for the flat plate impactor, which will act as our base flow case for comparison, the experiments were repeated for the TR = 0.27 trap impactor. This design has the smallest trap diameter, the deepest depth, and overall, the worst trap efficiency. Comparing the flow field to that of the flat plate could reveal potential mechanisms for the decrease in performance. Images for the TR = 0.27 impactor with Re

= 13,000 are shown in Figure 8.4. Re = 13,000 was chosen because the trap efficiency results were only 30% when the predicted efficiency was 90% for this Reynolds number. Figure 8.4a and b are similar to the flat plate result as the primary ring vortex moves towards the trap. In Figure 8.4c the jet enters the trap, but the ring vortex is stopped by the edge of the trap. The trap is wider than the jet, but the ring vortex extends radially past the edge of the trap and can only partially enter before coming to a stop. Figure 8.4d then shows the ring vortex mixing with the incoming jet. This phenomenon could prevent particles from entering the trap or alter their trajectories and reduce the trap efficiency. In Figure 8.4e, the jet then begins to distort due to its collision with the vortex, as seen by the skewed shape. In the next image (Figure 8.4f), the reverse flow emanating from the trap, which we will refer to as the wall jet, also distorts the incoming jet. Shortly after, due to the increased flow from the wall jet, the incoming jet becomes turbulent, characterized by regions of high mixing in the smoke particles, and could also alter particle trajectories. This was not seen for the flat plate results at the same Reynolds number, as the jet remained laminar into the impingement zone, and only after the vortices rolled up and separated would there be regions with mixing. Larger wall jets are periodically shed from the trap shown on the right side of Figure 8.4g. These wall jets then impinge on the back end of the nozzle shown in Figure 8.4h. In the efficiency experiments, traps with high wall losses were shown to have droplets at the end of the nozzle, which could potentially be caused by the jets impinging in this region.

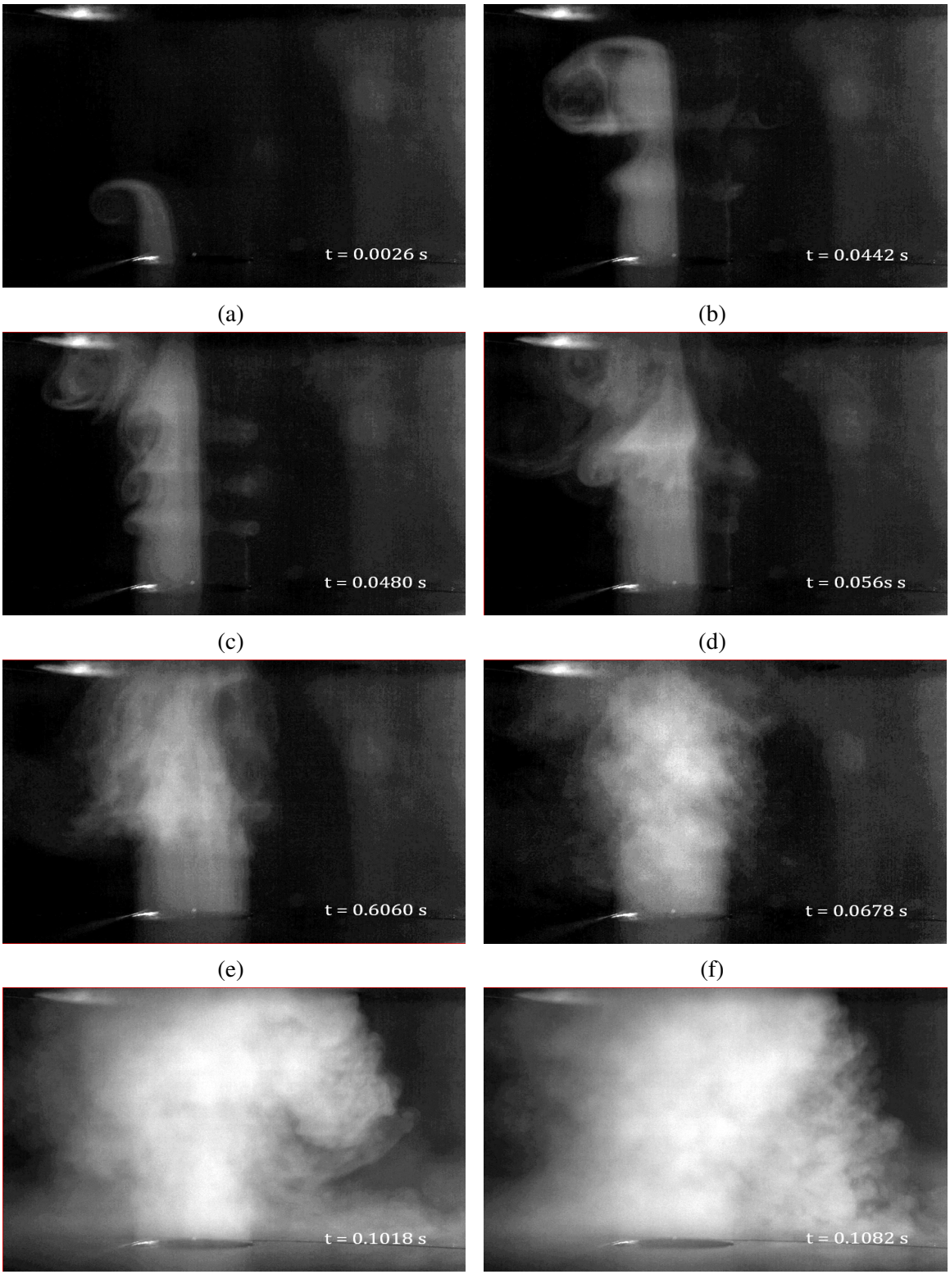

Figure 8.4: Shadowgraphy results for Re = 13,000, TR = 0.27 trap impactor. a) Jet emerges and the primary ring vortex is visible, b) Jet is about to enter the trap, c) Jet enters the trap but the ring vortex is stopped, d) Ring vortex interacts with the jet entering the trap, e) Reverse flow from the trap (wall jet) interferes with jet, f) Jet loses coherent shape and becomes turbulent, g) A large wall jet is ejected from the edge of the trap, h) Wall jet impinges on backside of the nozzle.

The high-speed shadowgraphs were able to visualize the jets exiting the nozzle and interacting with the flat plate and trap. These images revealed that both jets have a primary ring vortex and then secondary vortices due to the Kelvin-Helmholtz instability. As the jets interact with the respective obstruction, the flat impactor jet remains laminar into the impingement region, and only after the flow rolls up and separates at the plate does the flow have high mixing indicative of turbulence. However, the trap impactor jet becomes turbulent in the jet core due to the mixing of the wall jet and the primary jet. The effects of these phenomena will be further investigated with particle image velocimetry experiments, but qualitatively, we found evidence that jet mixing in the TR = 0.27 flow could be responsible for the poor trap efficiency.

8.2 2D PIV Results

2D PIV experiments were performed using the setup and procedure outlined in subsection 7.3.3. Four impactors were used: flat plate, TR = 1.00 (wide and shallow trap), TR = 0.59 (medium diameter and depth), and TR = 0.27 (narrow and deep) for Re = 2,000; 7,000; 10,000, and 17,000. The Reynolds number used the average nozzle outlet velocity as the characteristic velocity. Each impactor and Reynolds number combination used between 200 and 250 images, with the uncertainty calculated by DaVis as explained in [112]. The flow field results will be used to explain potential reasons for the trap efficiency (η_{Trap}) and wall losses (W) from the efficiency test results in subsection 6.1.3. The efficiency and wall losses results are replotted as functions of Reynolds number below in Figure 8.5. For the Reynolds numbers used in the PIV experiments, the corresponding predicted efficiency is between 66 and 96%, and the wall losses are assumed to be zero. TR = 1.00 had trap efficiencies between 76 and 94%, TR = 0.59 had efficiencies between 57 and 65%, and TR = 0.27 had efficiencies between 21 and 31%. The wall losses were between 0 and 5%, 0 and 27%, and 55 and 73% for TR = 1.00, 0.59, and 0.27, respectively.

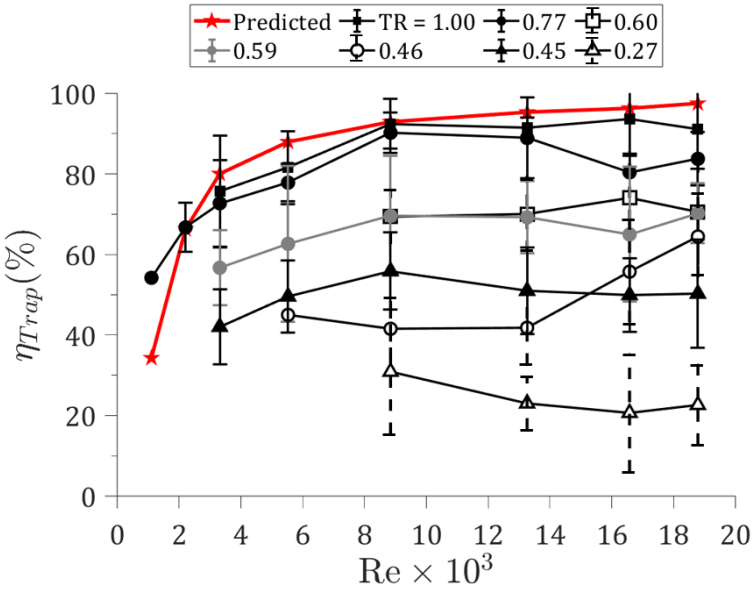

(a)

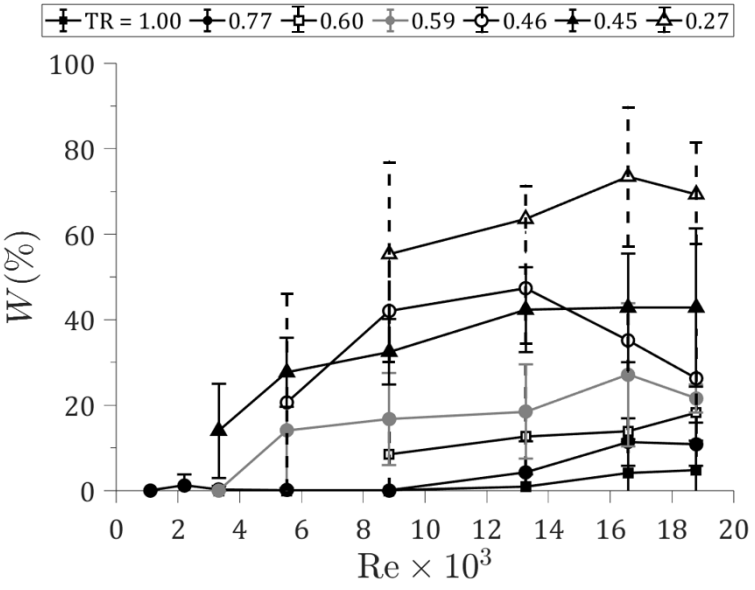

(b)

Figure 8.5: (a) Trap efficiency and (b) wall losses for trap impactors as functions of Reynolds number.

8.2.1 Flow Field

We first analyzed the time-averaged flow fields with overlaid streamlines. The time-averaged, or ensemble-averaged, quantities are the average values from the 200 - 250 images used per

nozzle and flow rate combination. A contour plot of the time-averaged flow field with overlaid streamlines for the flat plate impactor with Re = 2,000 is shown in Figure 8.6, with the flow moving from the bottom of the figure to the top. The left border of the contour plots is the impactor centerline, and the gap extends 3R axially to the beginning of the plate or trap. The maximum radial distance in view is 3.5R. All local velocity contours, V, are normalized by the maximum velocity, V_m, and are scaled from zero to unity by the colorbar. There are 135 and 160 vectors in the axial and radial directions, respectively, for a vector resolution of 5.3 vectors per mm.

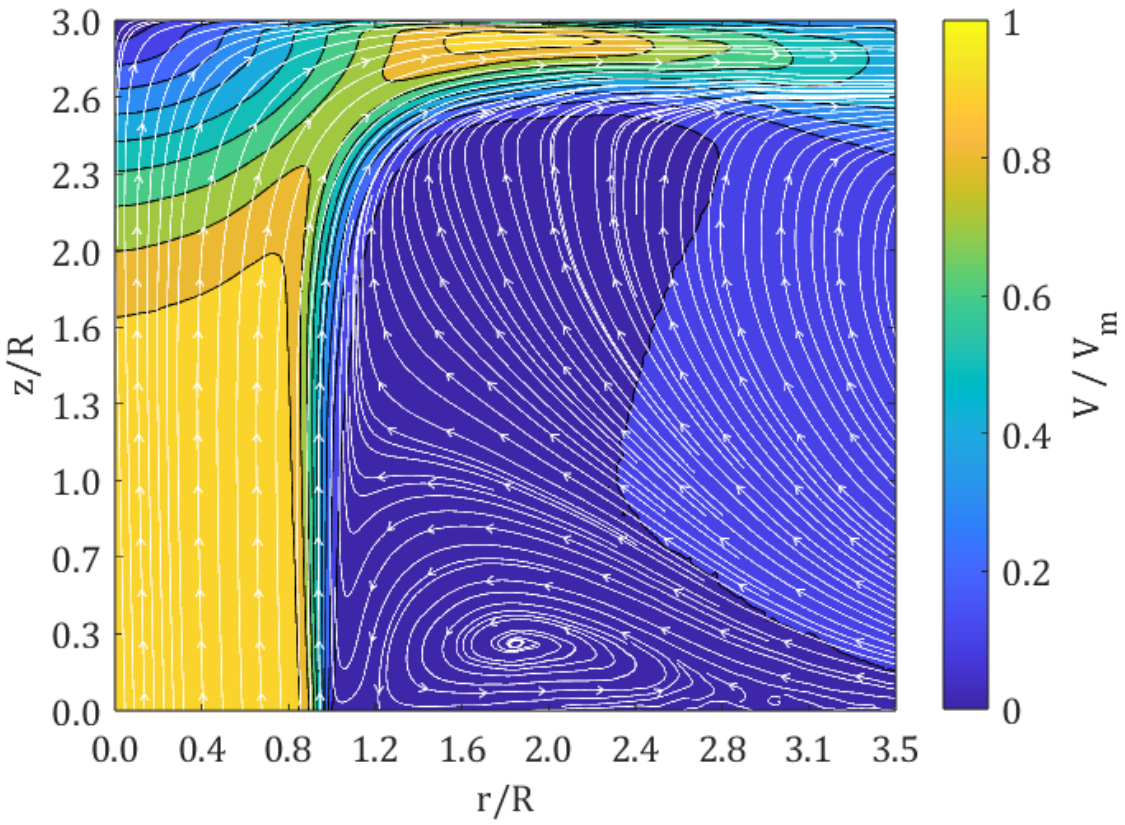

Figure 8.6: Flow field with overlaid streamlines for the flat plate impactor with Re = 2,000.

The flow exiting the nozzle at z/R = 0 and between r/R = 0 and 1.0 is almost uniform except for the thin shear layer due to the boundary layer formed in the nozzle. As the jet moves downstream, this shear layer broadens due to the velocity gradient between the jet and the stagnant air, slowing down the jet and increasing the velocity of the ambient air.

The streamlines, shown via the white arrows, indicate ambient air being pulled into the jet due to entrainment. Interestingly, near r/R = 1.8 and z/R = 0.3, a recirculation zone is created due to the entrained flow and the back end of the nozzle. Stagnant air is drawn to the shear layer and directed in the negative axial direction, likely due to the increasing shear along the jet closest to the nozzle exit. Portions of the entrained air will enter the jet, whereas others will instead be directed further in the negative axial direction and impinge upon the back end of the nozzle, as seen near z/R = 0 and r/R = 1.2. Fluid closer to the jet at the impinging point will get entrained, whereas fluid that is at a further radial distance away is directed along the surface until it separates and reverses direction.

As the jet encounters the plate, it begins to slow down near the impingement zone. The initial top-hat velocity profile decomposes into a W-shaped profile near the plate. This profile is due to the radial propagation of the adverse pressure gradient starting at the stagnation point. After the flow impacts the plate, near z/R = 3.0, it accelerates in the radial direction, now due to the favorable pressure gradient for increasing r/R, before decreasing near r/R = 2. The contour plots of the flow fields with overlaid streamlines for the flat plate impactor with Re = 2,000; 7,000; 10,000; and 17,000 are shown in the appendix in Figure A.1. There are no major differences in the contour plots, aside from the recirculation zone near the nozzle outlet disappearing at higher Reynolds numbers. This is potentially due to the higher shear at the edge of the jet, entraining more ambient air and preventing the flow from being redirected along the back of the nozzle.

The flow field contour plots for the TR = 1.00 impactor are shown in Figure 8.7 for Re = 2,000; 7,000; 10,000; and 17,000. Similar to the flat plate impactor, the flow field does not considerably change with Reynolds number; however, there are subtle differences. The fairly consistent flow field with Reynolds number is expected, as the trap efficiency for TR = 1.00 closely resembled the predicted efficiency. Unlike the flat plate impactor, the jet does not decrease in velocity in the axial direction due to the back of the trap being farther away than the flat plate. The pressure gradient established by the stagnation region

does not propagate into the gap, and the jet velocity is unaffected. The edge of the trap is located at r/R = 2.3, and for all Reynolds numbers, the wall jet is seen emanating from the trap. This reverse flow, combined with the incoming jet, creates a different recirculation zone between the edge of the trap and the jet that was referred to as a toroidal vortex by Terekhov *et al.* [106]. Although the recirculation zone was referred to as a vortex, vorticity contour plots for all impactors shown in the appendix in Figure A.2 - Figure A.4 highlight that although the streamlines show circular motion, the vorticity is nearly zero throughout the field and does not indicate the existence of a classical vortex. The recirculation zone, however, illustrates how the streamlines are altered by the existence of the trap. For all Reynolds numbers, the reverse flow impinges on the back end of the nozzle, similar to the shadowgraphs seen in the previous section. Although there is a secondary impinging flow on the back of the nozzle, TR = 1.00 did not experience high wall losses or droplets in this region, and therefore, the effects of the wall jet are potentially negligible.

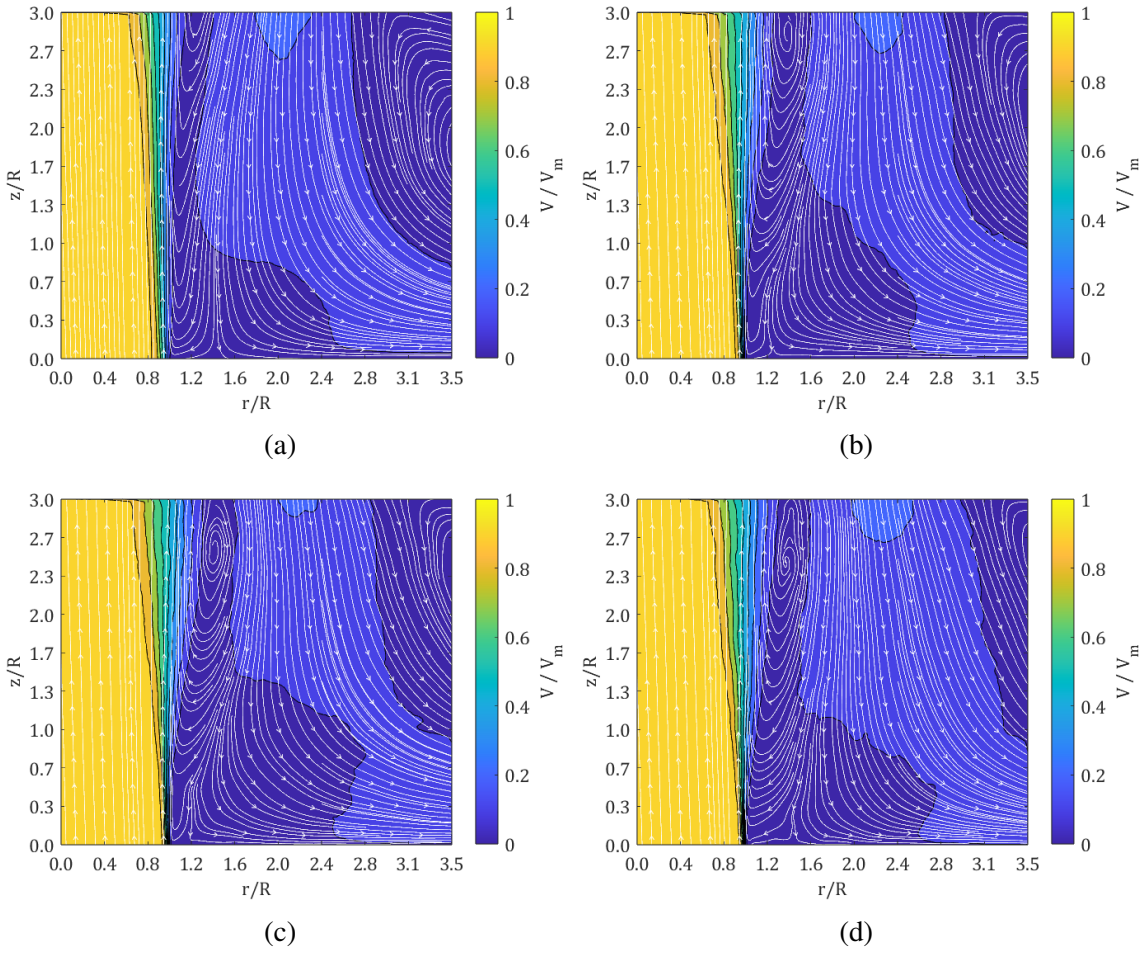

Figure 8.7: Experimental flow fields and streamlines for the TR = 1.00 impactor for a) Re = 2,000, b) Re = 7,000, c) Re = 10,000, d) Re = 17,000.

The flow fields for TR = 0.59 are shown in Figure 8.8. As Reynolds number increases, the flow field remains relatively unchanged and similar to TR = 1.00. One exception is the recirculation zone near the edge of the trap. For Re = 2,000, there are two zones with a saddle point between them near z/R = 1.5 and r/R = 1.2, but as Re increases, the saddle disappears and a distorted recirculation zone remains. Trap efficiency for the TR = 0.59 was constantly less than the predicted efficiency, as the maximum trap efficiency was 70%, with wall losses starting at 0 but increasing to 27%. As the Reynolds number increased, more particles began to deposit outside of the trap. The wall jet could be responsible for the lack of increasing efficiency expected at larger $\langle\sqrt{\mathrm{St}}\rangle_{\mathrm{a}}$. Potentially, the wall jet generated

by a narrower and deeper trap, compared to TR = 1.00, alters the flow field and may induce particles in the jet to deviate from their paths and alter their original trajectories. Fewer particles could be influenced when the recirculation is close to the trap, but as it distorts and moves closer to the jet, it may affect a larger fraction of particles and increase wall losses.

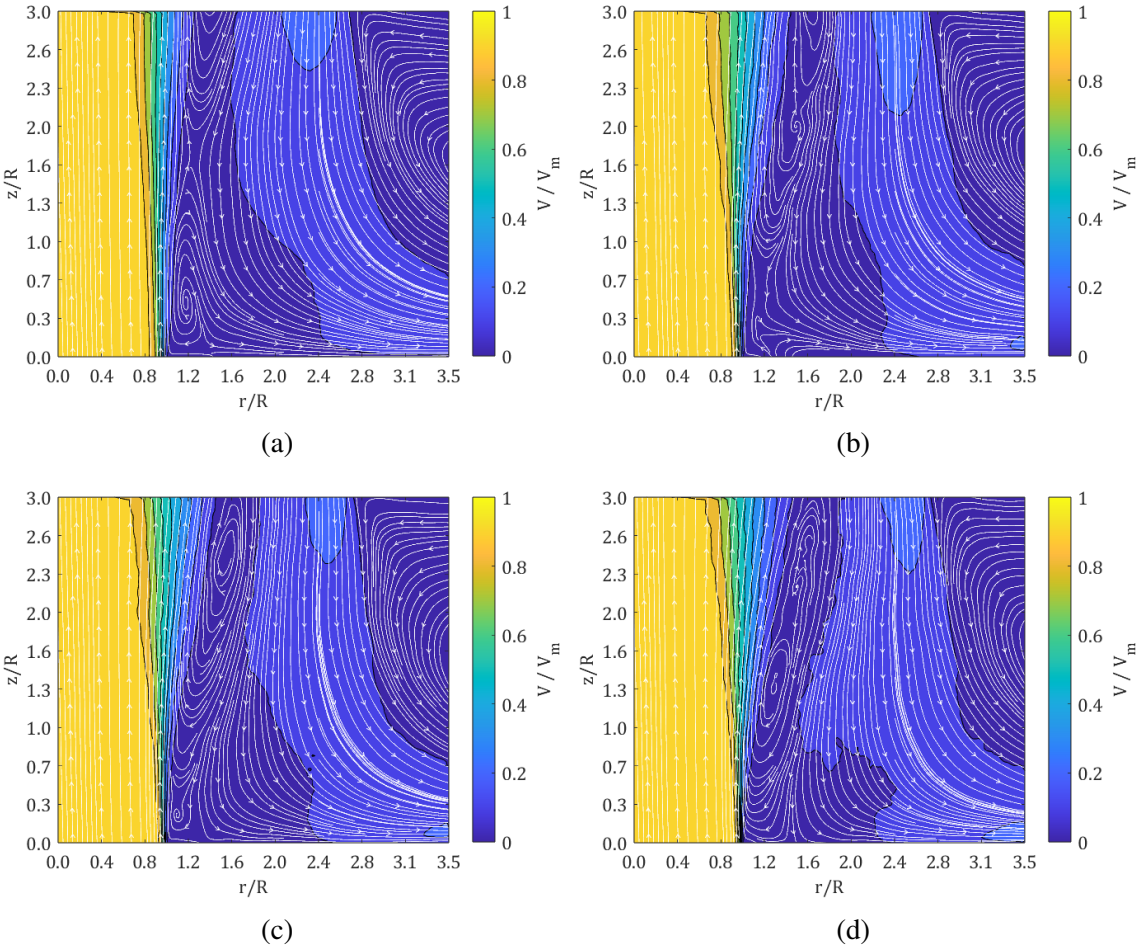

Figure 8.8: Experimental flow fields and streamlines for the TR = 0.59 impactor for a) Re = 2,000, b) Re = 7,000, c) Re = 10,000, d) Re = 17,000.

The most dramatic changes in the flow field occur for the TR = 0.27 impactor, which is not surprising as it had the worst trap efficiency of all the designs tested. An interesting result is unlike the previous trap impactors, the centerline velocity decreases downstream and worsens with increasing Reynolds number. TR = 1.00 and 0.59 did not have velocity

decays, as mentioned previously, due to the back of the trap being far away from the gap. However, TR = 0.27 decreases from 82 to 73% of maximum centerline velocity from Re = 2,000 to 17,000. This is highly unexpected as it has the deepest trap, and therefore, the solid boundary is the furthest away. The increased distance to the back of the trap would imply that the pressure gradient should have the weakest effect on the velocity profile in the gap, and the results should be similar to the other traps. The jet develops an M-shaped velocity profile near the entrance to the trap, which may be caused by an added adverse pressure gradient inside the trap. As particles are transported by the jet, if the velocity is decreasing well before the bottom of the trap, they will lose inertia and are more likely to stay attached to the streamlines. Due to the decreased inertia, the particles may enter the trap, but follow the streamlines and exit without depositing.

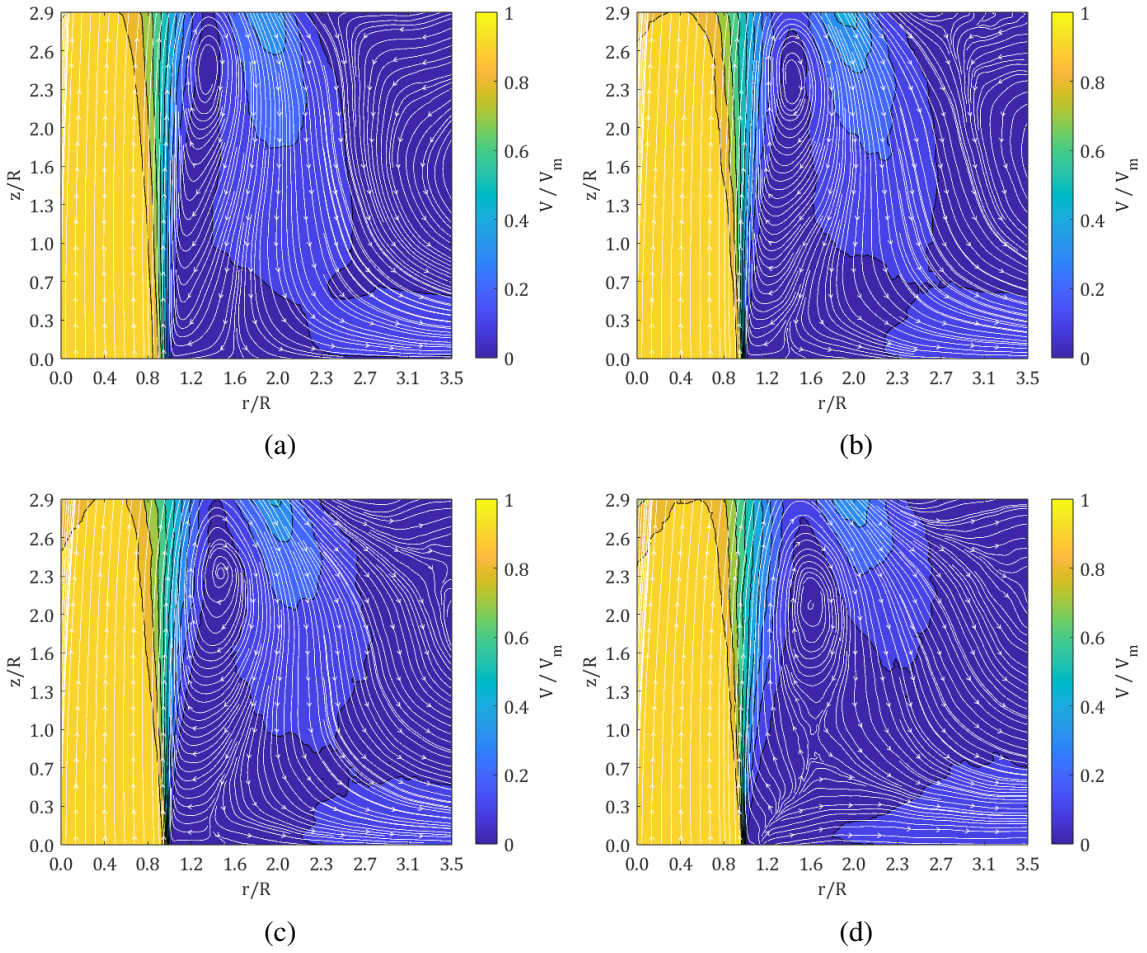

Figure 8.9: Experimental flow fields and streamlines for the TR = 0.27 impactor for a) Re = 2,000, b) Re = 7,000, c) Re = 10,000, d) Re = 17,000

A comparison of all trap impactor flow fields for Re = 17,000 is given below in Figure 8.10, and the axial velocity profiles normalized by the maximum velocity in the field at varying downstream locations are shown in Figure 8.11. For Re = 17,000, TR = 1.00 had a trap efficiency of 94%, whereas TR = 0.59 and TR = 0.27 had efficiencies of 65 and 21%, respectively. The most obvious difference in the time-averaged velocity fields stems from the centerline decay for TR = 0.27. While TR = 1.00 and 0.59 have velocities near the maximum at the entrance to the trap, TR = 0.27 has decreased to $0.73\mathrm{V_m}$. Another difference is that the contour plots show that for TR = 1.00 and 0.59, there appears to be a small separation between the edge of the jet entering the trap and the wall jet exiting the

trap. The recirculation zones then reside in the small separation between the incoming and wall jets. However, for TR = 0.27, which has the narrowest trap, there is no distinct end to the incoming jet and the exiting wall jet, potentially indicating that the two flows mix with each other more than the geometries with wider traps. TR = 0.27 and 0.59 have wall jets with larger velocity magnitudes than TR = 1.00, as indicated by the negative values in the velocity profiles at z/R = 2.7 and 2.9. TR = 0.27 and 0.59 both have minimum axial velocity components of -0.23V_m, whereas TR = 1.00 has a minimum of -0.21V_m. TR = 0.27 and 1.00 have symmetric wall jet profiles at z/R = 2.7 and 2.9, but TR = 0.59 has a profile that is slightly skewed further in the radial direction. This can potentially explain the tilted recirculation zone seen in the TR = 0.59 velocity contours. This tilt is potentially responsible for streamlines with larger positive radial components for TR = 0.59 and can direct particles to deviate from inside the jet compared to TR = 1.00. TR = 0.27 has a wider recirculation zone, and the streamlines inside the core of the jet and near the edge of the jet indicate larger radial components than TR = 1.00. The streamlines for TR = 0.59 and 0.27 demonstrate how efficiency can be lowered by causing particles to deviate from their initial trajectories.

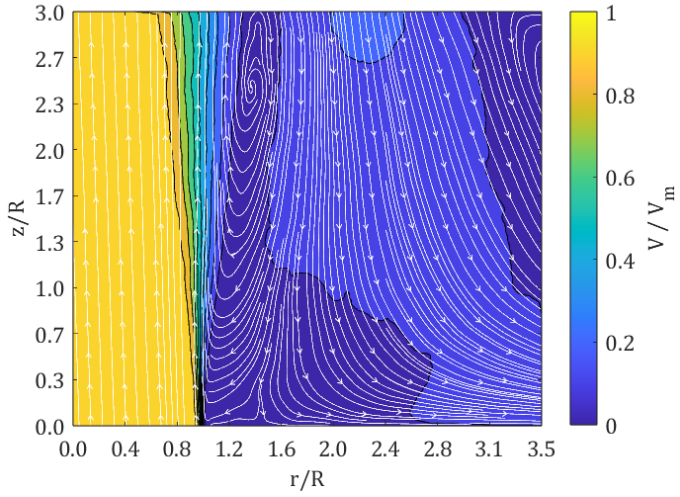

(a)

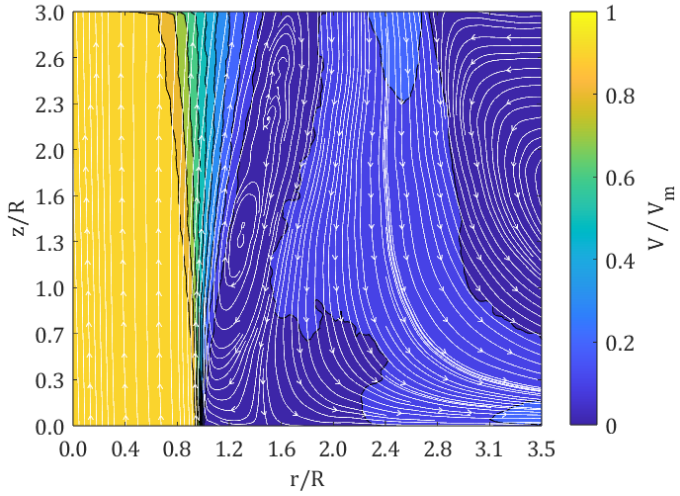

(b)

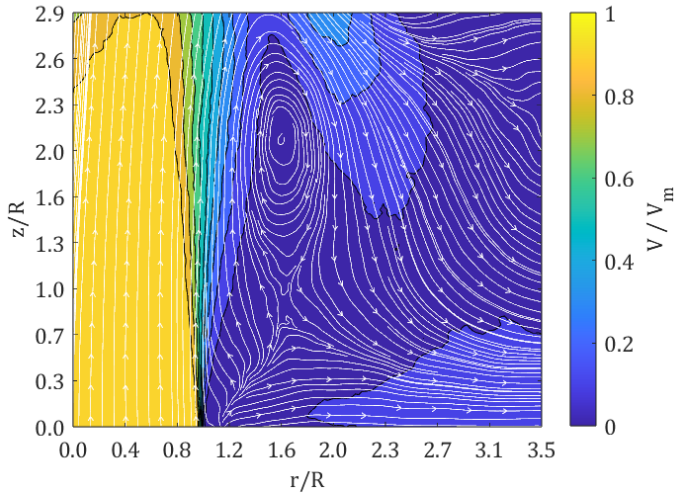

(c)

Figure 8.10: Flow fields and streamlines for for Re = 17,000 for a) TR = 1.00, b) TR = 0.59, c) TR = 0.27.

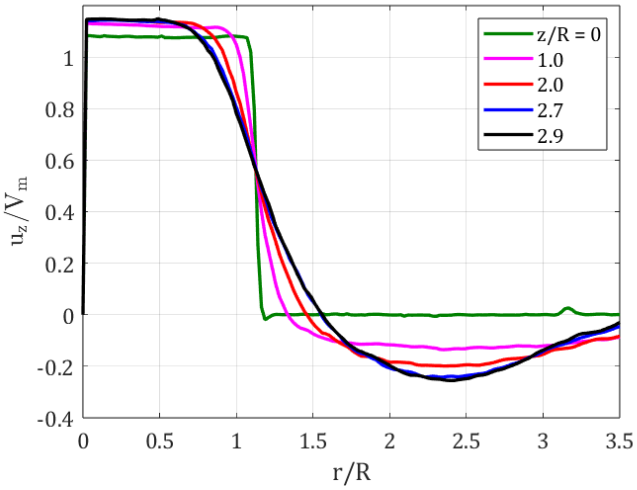

(a)

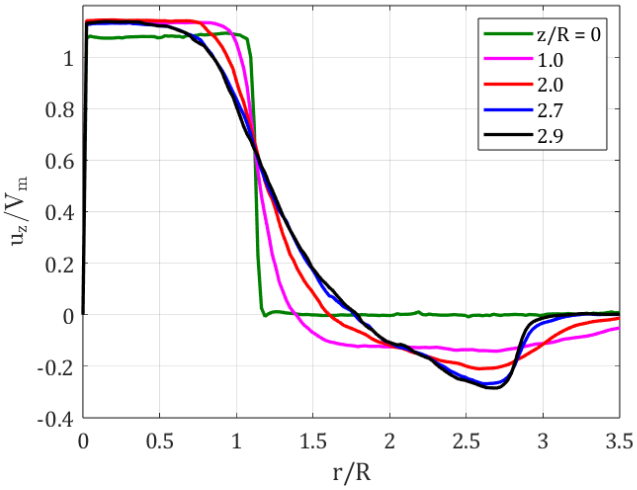

(b)

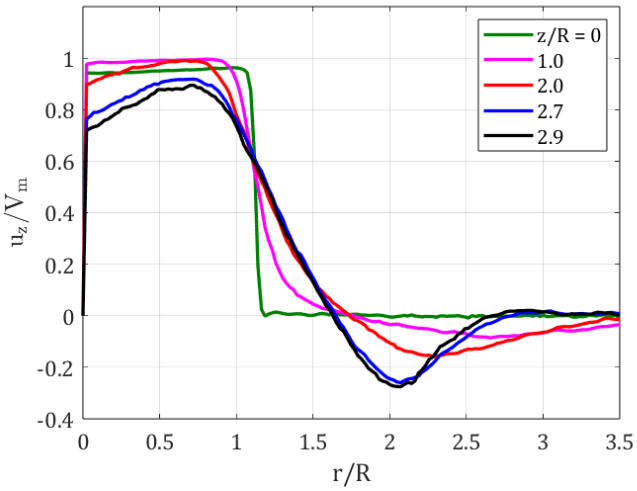

(c)

Figure 8.11: Axial velocity profiles for Re = 17,000 for a) TR = 1.00, b) TR = 0.59, c) TR = 0.27.

To further investigate the potential for altered particle trajectories, line plots of the radial velocities at r/R = 0.5 and 1.0 for all impactors and Re = 17,000 are shown below in Figure 8.12a and b, respectively. The velocities are normalized by the local total velocity, V, and are the percentage of the total velocity contributed by the axial component. $\mathrm{u_r}/\mathrm{V}$ for all impactors are shown as functions of axial distance z/R. The flat plate axial velocity, shown in green, is either zero or less than zero for z/R $<$ 1, but increases to a purely axial flow at z/R = 3 due to the no-penetration condition at the flat plate. Similarly, for r/R = 0.5, TR = 1.00 and 0.59 consistently have negative or nearly zero axial velocity components. This indicates that the flow is either moving slightly toward the centerline or straight towards the trap, which is conducive for capture. Conversely, TR = 0.27 initially has a negative radial component, but increases to a positive radial velocity downstream. Particles near r/R = 0.5 can then be influenced to move outward instead of remaining in the jet.

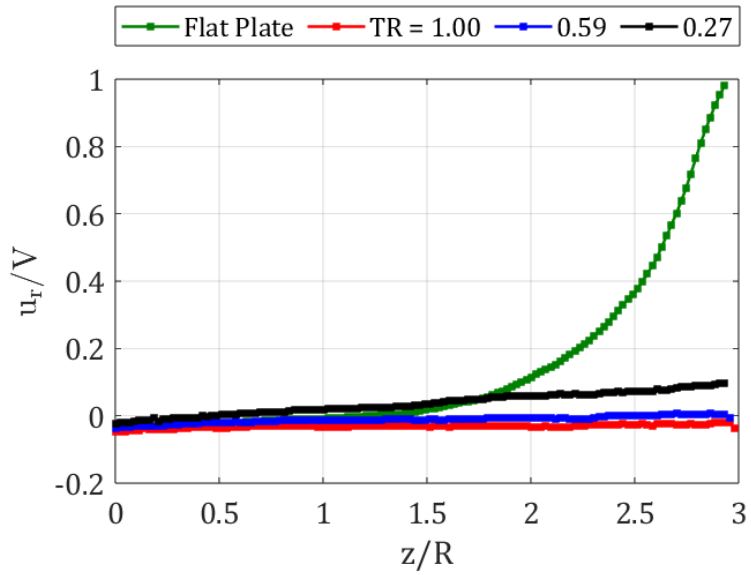

(a)

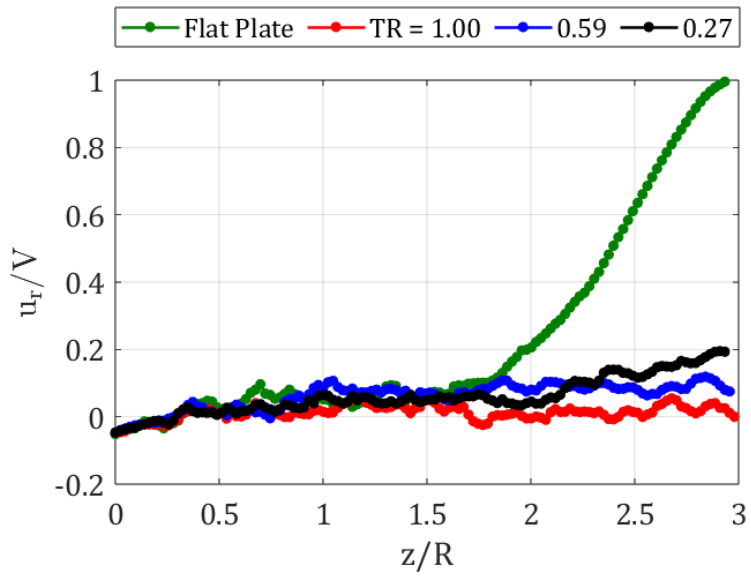

(b)

Figure 8.12: Plots of the radial velocities at a) r/R = 0.5 and b) r/R = 1 normalized by the local velocity as functions of z/R for Re = 17,000.

Examining r/R = 1.0, the trends are similar except the radial components have increased for TR = 0.59 and 0.27. For r/R = 0.5, TR = 0.59 had a maximum axial contribution of 1%, but for r/R = 1.0, the maximum contribution increased to 11%. Similarly, TR = 0.27 had an increase from 10% to 20%. The further the axial distance from the centerline, the

stronger the axial components of velocity become, while still being in the vicinity of the jet. TR = 1.00, has a maximum axial velocity of -0.02V, indicating that all of the flow is directed towards the centerline for r/R = 0.5, and only increases to 0.05V for r/R = 1, which is significantly less than the other designs. This discrepancy highlights that with decreasing trap ratio, the streamlines are directed more radially outward, and the flow moves toward the edges of the trap rather than the center.

Further emphasizing this point, plots of the radial velocity contributions are replotted as functions of z/(S + T) in Figure 8.13, which normalizes the axial distance by the total length the jet travels before impacting either the plate or the back of the trap. Using the flat plate as the control, the flow should gradually spread in the axial direction until it reaches the stagnation region and is converted to purely radial flow. However, for r/R = 0.5 and 1.0, TR = 0.27 immediately deviates from the flat plate and the other trap impactor profiles. TR = 0.27 spreads much quicker and reaches an axial contribution of 10% and 20% at only 29% of the jet distance for r/R = 0.5 and 1.0, respectively. The flat plate does not reach these radial contributions until nearly 70% downstream. TR = 1.00 is similar to the flat plate, but actually has a larger negative radial velocity, which could potentially increase capture efficiency, and TR = 0.59 has slightly larger radial contributions, but not nearly as large as TR = 0.27. Ignoring the obstacles and examining only the jets, this implies that TR = 0.27 has a much larger spread than the flat plate jet, and particles transported by TR = 0.27 could be much further from the centerline at z/(S + T) = 1. Consider the particles transported by the TR = 0.27 jet. Particles that start on the edge of the jet at r/R = 1.0 are influenced to move further towards the edge of the trap, and potentially never enter. Alternatively, particles starting at r/R = 0.5 are transported away from the centerline but may still enter the trap. However, the further away from the centerline they are as they approach the back of the trap, the larger the radial velocity component as they approach the solid surface (see Figure 8.6) and are induced to avoid the surface. If the particles are swept away, they could get transported out of the trap and decrease the trap efficiency.

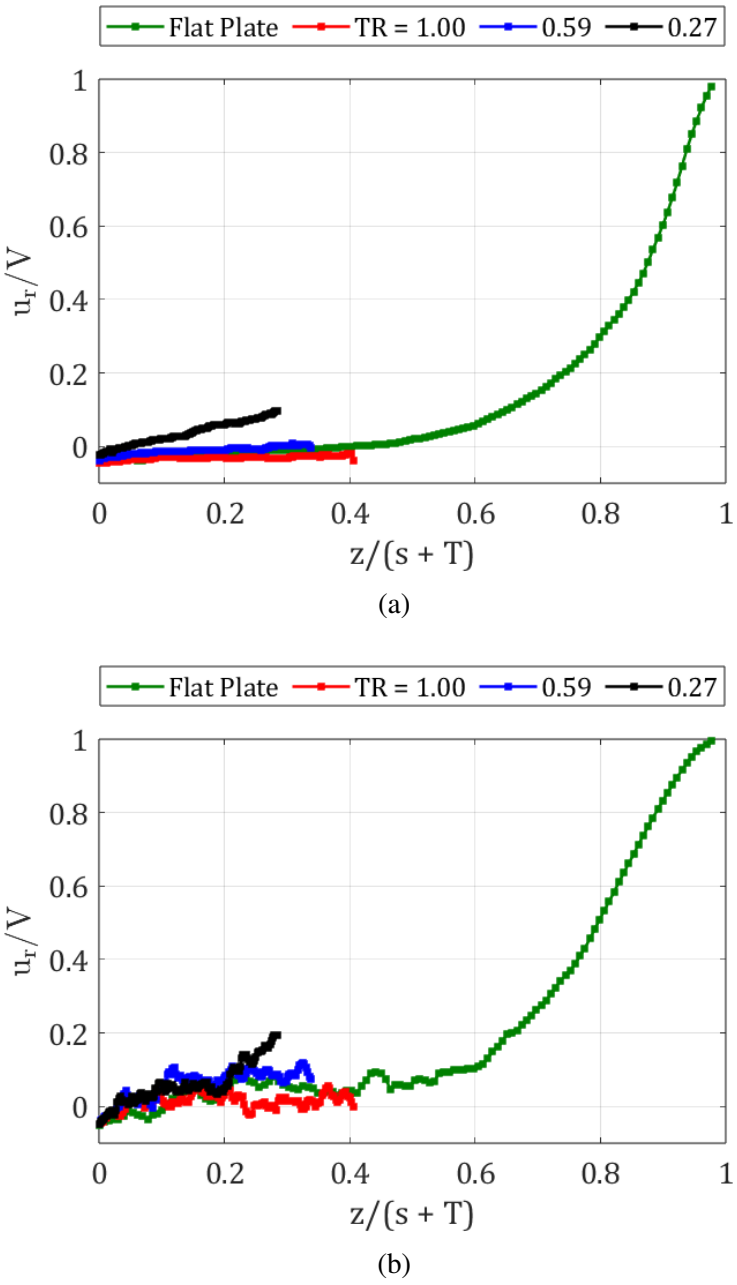

Figure 8.13: Plots of the radial velocities at a) r/R = 0.5 and b) r/R = 1 normalized by the local velocity as functions of z/(S + T).

Another mechanism preventing particle deposition upon entering the trap is due to the centerline velocity degradation. Figure 8.14 displays the normalized axial centerline velocities for all impactors and Reynolds numbers examined. The flat plate, TR = 1.00, and TR = 0.59 are not affected by the Reynolds number, and the flat plate centerline velocity

decays to 0 at the plate, whereas the trap impactors have maximum velocities through the gap. Decreases in velocity for the trap impactors at the edge of the window are potentially due to reflections and may have larger variations at the edge of the window. TR = 0.27 has a different behavior as the centerline velocity begins to decay near z/R = 1.5. The decrease in velocity at z/R = 2.9 then increases with Re, as Re = 17,000 is only 73% of the maximum.

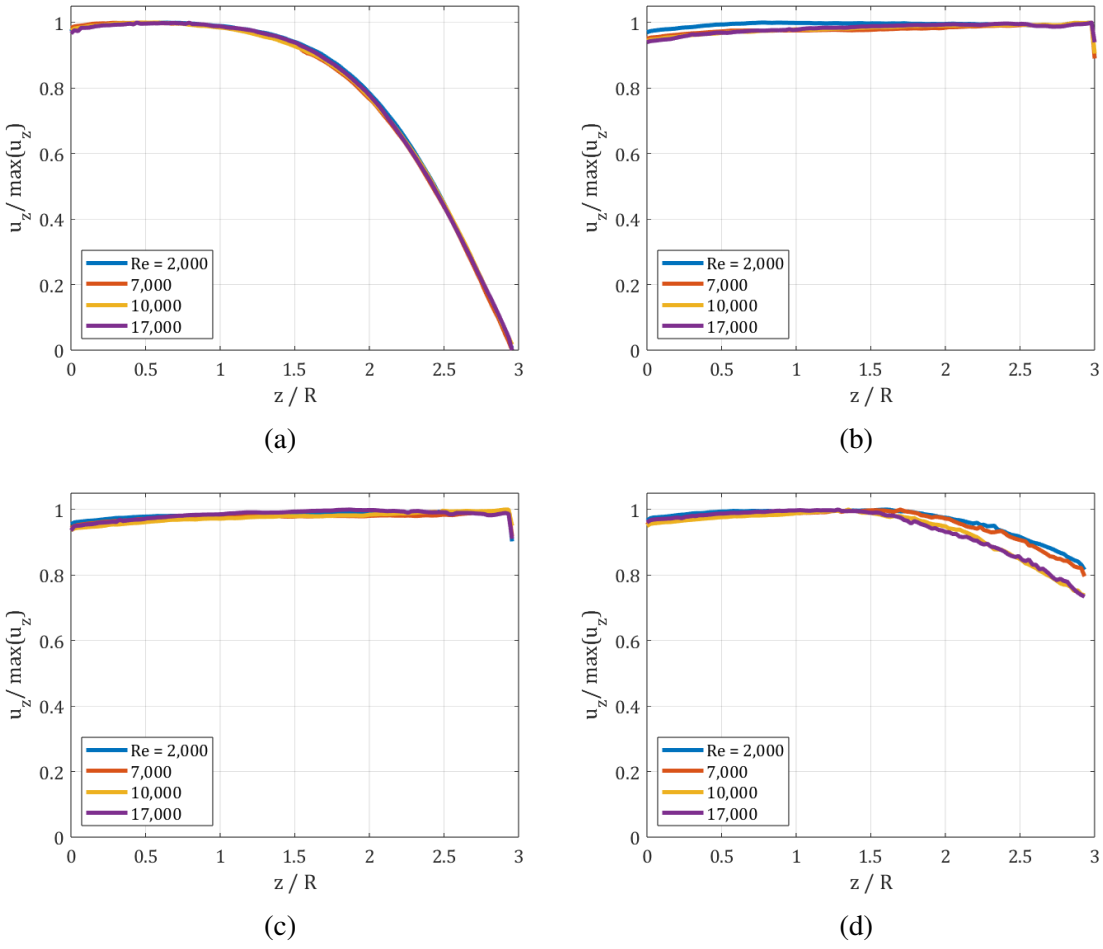

Figure 8.14: Centerline axial velocities as functions of axial distance for a) flat plate, b) TR = 1.00, c) TR = 0.59, d) TR = 0.27.

Similar to the radial velocities, the centerline axial velocities for Re = 17,000 are plotted as functions of z/(S + T) in Figure 8.15. TR = 1.00 and 0.59 match closely to the flat plate with centerline velocities near the maximum until 40% downstream. TR = 0.27 is markedly different and begins to decrease much earlier than the other jets. The presence of an adverse

pressure gradient inside the trap, slowing down the incoming jet, can prevent particles from reaching the bottom of the trap and instead getting redirected outward by the wall jet.

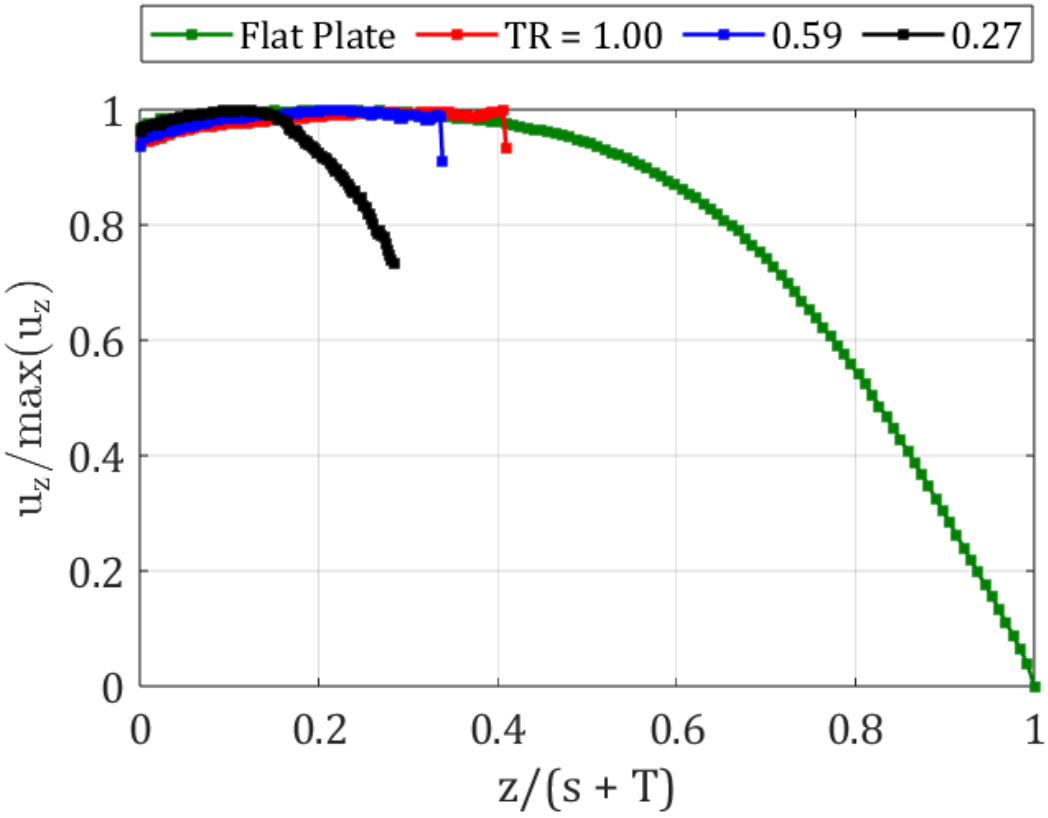

Figure 8.15: Re = 17,000 centerline axial velocities as functions of axial distance normalized by z/(S + T).

From analyzing the time-averaged flow fields and streamlines, we have shown that TR = 1.00 does not markedly change with Reynolds number, and its axial and radial velocity components in the gap are similar to the flat plate when scaled to the length of the jet. This is not surprising as the trap efficiency closely matched the predicted efficiency from a flat plate impactor. TR = 0.59 differed from the predicted efficiency, and this could be attributed to the radial velocity distribution being slightly larger than the flat plate impactor. A larger positive radial velocity component can influence the transported particles to move away from the center of the jet. If the radial distance of a particle is then larger than the radius of the trap, the particles are prevented from entering. TR = 0.27 had the worst

performance of the designs tested, with the trap efficiency only reaching a maximum of 30%. Poor performance is attributed to larger radial velocities than TR = 0.59, and also due to the degradation of the centerline velocity, which potentially prevents particles from penetrating deep enough into the trap to be collected.

8.2.2 Experimental Instantaneous Flow Fields

Thus far, we have analyzed the time-averaged PIV flow fields, but the instantaneous flow fields can be investigated as well to examine the time-varying flow characteristics. Instantaneous flow fields for the flat plate impactor for Re = 2,000 are shown in Figure 8.16. The contours, $\mathrm{V}/\mathrm{V_m}$, are the velocity normalized by the maximum velocity and are from 0 to unity. The time between the flow fields is 67 ms, which is determined by the PIV repetition rate of 15 Hz. The images have minor differences between them, indicating that the flow is relatively steady. There are subtle changes in the flow after the jet impinges on the plate near z/R $\geq$ 2.7. These changing structures are from the flow rolling up and separating from the plate, which are not steady phenomena. The flow fields for Re = 7,000, 10,000, and 17,000 are shown in Figure A.8, Figure A.9, and Figure A.10 in the appendix. Similar to Re = 2,000, there is little variation in time. The jet core structure remains constant, but there are slight variations along the edge of the jet due to the Kelvin-Helmholtz instability seen in section 8.1, and are more prevalent at higher Reynolds numbers.

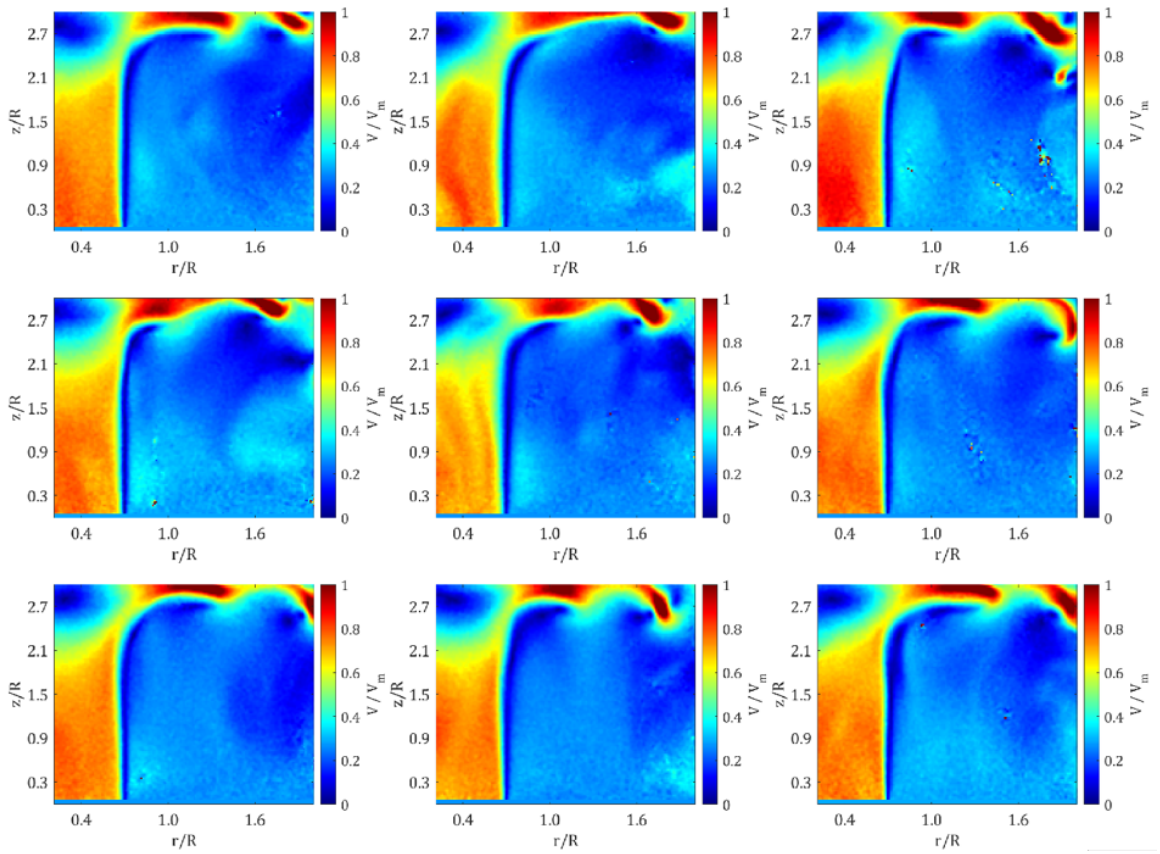

Figure 8.16: Instantaneous flow fields for Re = 2,000 flat plate impactor.

The instantaneous flow fields for TR = 1.00 for Re = 2,000 and 7,000 are shown in Figure 8.17 and Figure 8.18. Given in the appendix in Figure A.11 and Figure A.12 are the flow fields for Re = 7,000 and 17,000, and they are similar to Re = 7,000. For Re = 2,000, the instantaneous contours show little variation with time. Compared to the flat plate contours of the same Reynolds number, the jet edges have a slight curvature near z/R = 2.1. This appears to be due to the wall jet interacting with the incoming jet and can be seen by the light blue contours in the gap. For Re = 7,000, as the Reynolds number increases, the periphery of the jet develops eddies due to the Kelvin-Helmholtz instability starting near the nozzle outlet, which were seen in the shadowgraph images. These eddies are convected downstream and into the trap. The velocity of the wall jet increases with increasing Reynolds number, denoted by the green and yellow contours. The higher velocity wall jets cause the jet to become slightly distorted as seen in the bottom left contour in Figure 8.18

as the jet is slightly broken upon entering the trap compared to the other contours.

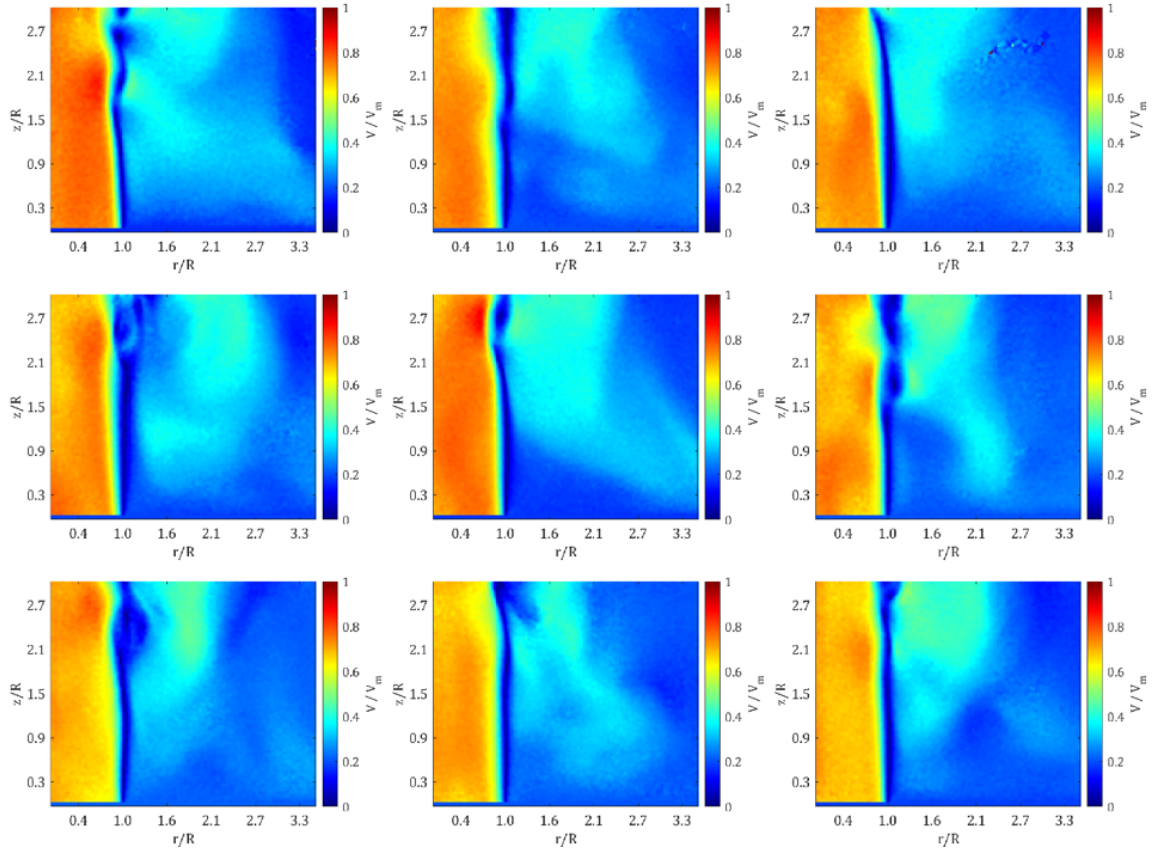

Figure 8.17: Instantaneous flow fields for TR = 1.00, Re = 2,000

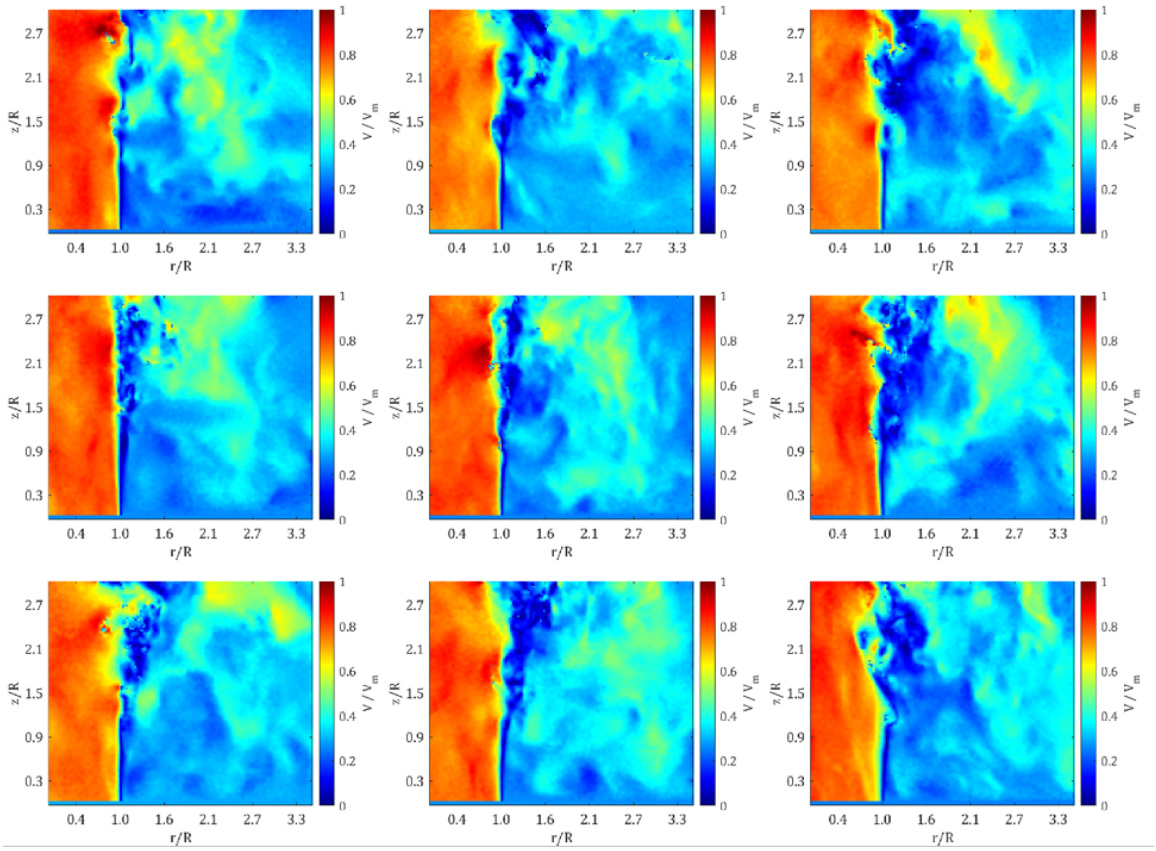

Figure 8.18: Instantaneous flow fields for TR = 1.00, Re = 7,000

The time-varying behavior for the TR = 0.59 design for Re 2,000 is similar to that of TR = 1.00 for the same Reynolds number shown in Figure 8.19. There is little variation across Reynolds number aside from slight distortions in the jet due to the wall jet. The contours for Re = 7,000 - 17,000 are given in Figure A.13, Figure A.14, and Figure A.15 in the appendix. In the top row of Figure 8.19, the jets are uniform with very little variation between the first three contours. However, in the first image of the second row, the plume exiting the trap interferes with the jet and induces a negative radial displacement of the jet near z/R = 1.5. Here, it can be seen that the reverse flow is making contact with the jet and causing the distortion. Although the incoming jets come in contact with the exiting wall jets, the incoming jet integrity is maintained as they are able to enter the trap without large variations in velocity. From the instantaneous velocity fields, particles transported by the jets close to the centerline should not be adversely affected. On the contrary, particles near

the edges of the jets can be altered due to the reverse flow.

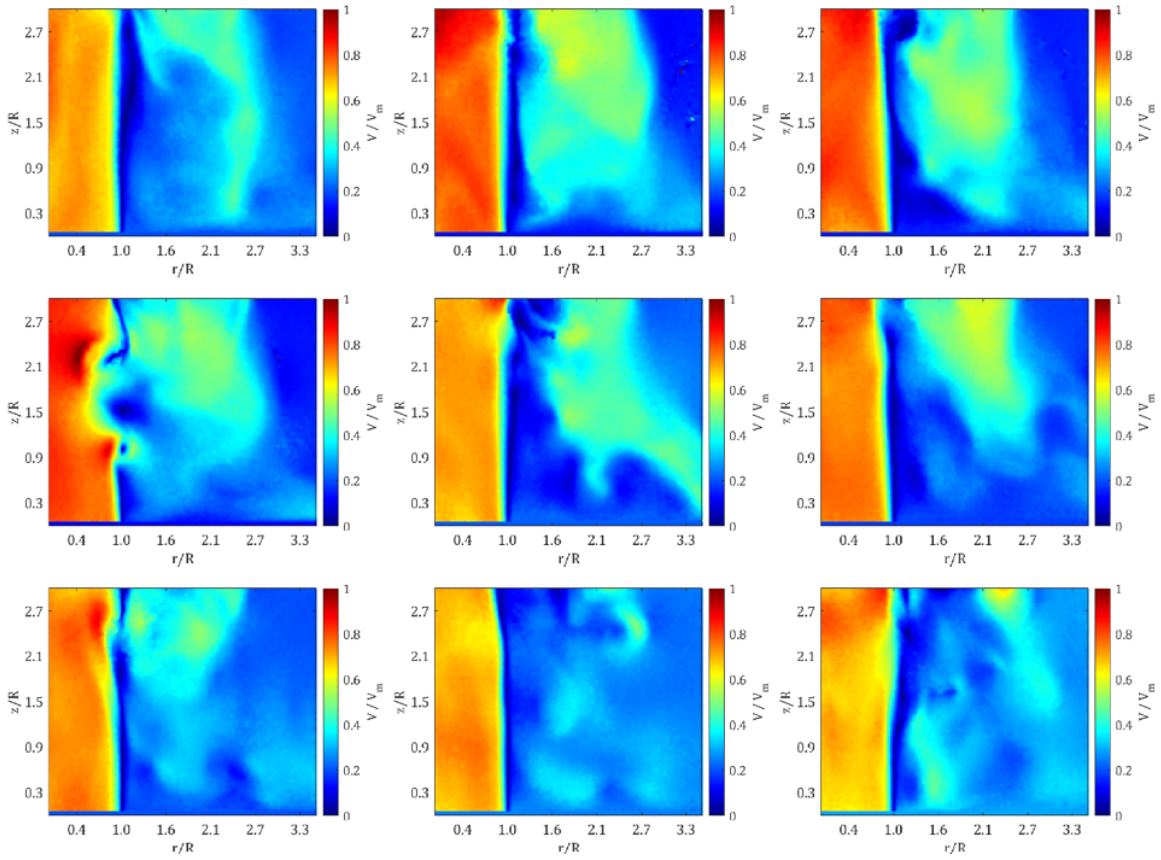

Figure 8.19: Instantaneous flow fields for TR = 0.59, Re = 2,000

The instantaneous flow fields discussed thus far have been fairly consistent for Reynolds numbers between 2,000 and 17,000. The presence of the trap and the wall jets causes the incoming jets to become slightly distorted and their velocities to vary, but on average, the jets remain intact. This trend fails for TR = 0.27, however, as the flow fields vary greatly in time, shown in Figure 8.20, Figure 8.21, Figure 8.22, and Figure 8.23 for Re = 2,000, 7,000, 10,000, and 17,000, respectively. The previous designs only displayed slight distortion with the jet maintaining its integrity; however, the jets for TR = 0.27 are broken up by the wall jets across all Reynolds numbers. For Re = 2,000, the wall jets are seen interfering with the jets near z/R = 2.1 - 2.9. This phenomenon is maximized in the bottom right contour, where the jet width almost decreases to zero near z/R = 2.3. The effect is enhanced at Re = 7,000, where the jet splits in the middle contour of the bottom row. Here,

there is a low velocity region, beginning at z/R = 2.1, where the wall jet has caused a split in the jet, but is restored in the next image, displaying that the jets have an oscillatory nature. This behavior is seen again in Re = 10,000 and 17,000, with the pulsatile wall jet causing the incoming jet to break down and split. This behavior is potentially due to the proximity of the edge of the trap to the edge of the jet. TR = 0.27 has the narrowest trap, and it was shown in the time-averaged velocity field in Figure 8.11 that there is no distinct distance between the incoming jet and the exiting reverse flow, like in the other designs. Because the wall jet is forced out of the trap and into the incoming jet, the breakdown of the incoming jet is inevitable. Unlike the previous designs, particles near the centerline are now susceptible to deviations in their trajectories. The flat plate and wider traps had steady centerline velocities with only the regions of the jet near r/R = 1 having distortions due to the K-H instability or with weaker interactions with the pulsatile plumes. In contrast, particles in the TR = 0.27 jets are exposed to an erratic flow field, even inside the jet, and their trajectories can be altered anywhere in the flow. It is due to this erratic behavior that potentially results in the dramatically reduced trap efficiency for this design, as particles have a much smaller chance of continuing along their original trajectories and depositing in the trap.

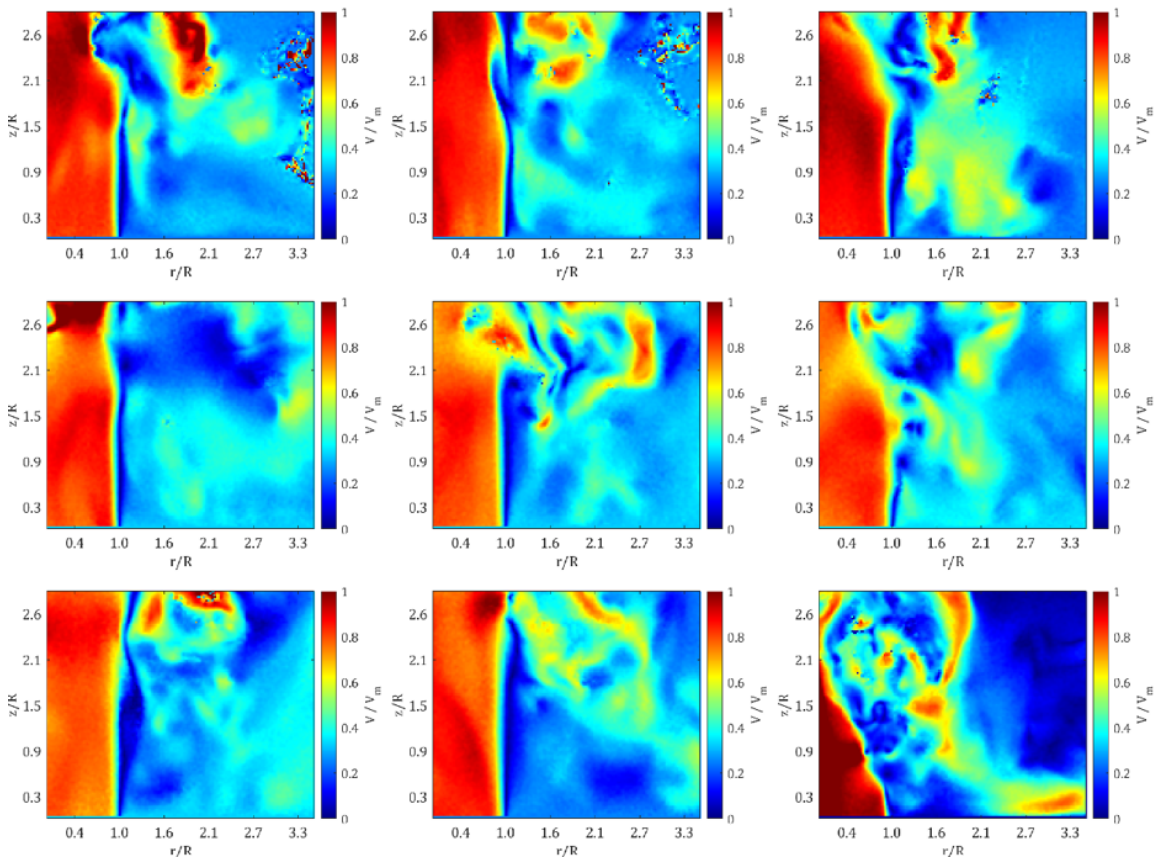

Figure 8.20: Instantaneous flow fields for TR = 0.27, Re = 2,000

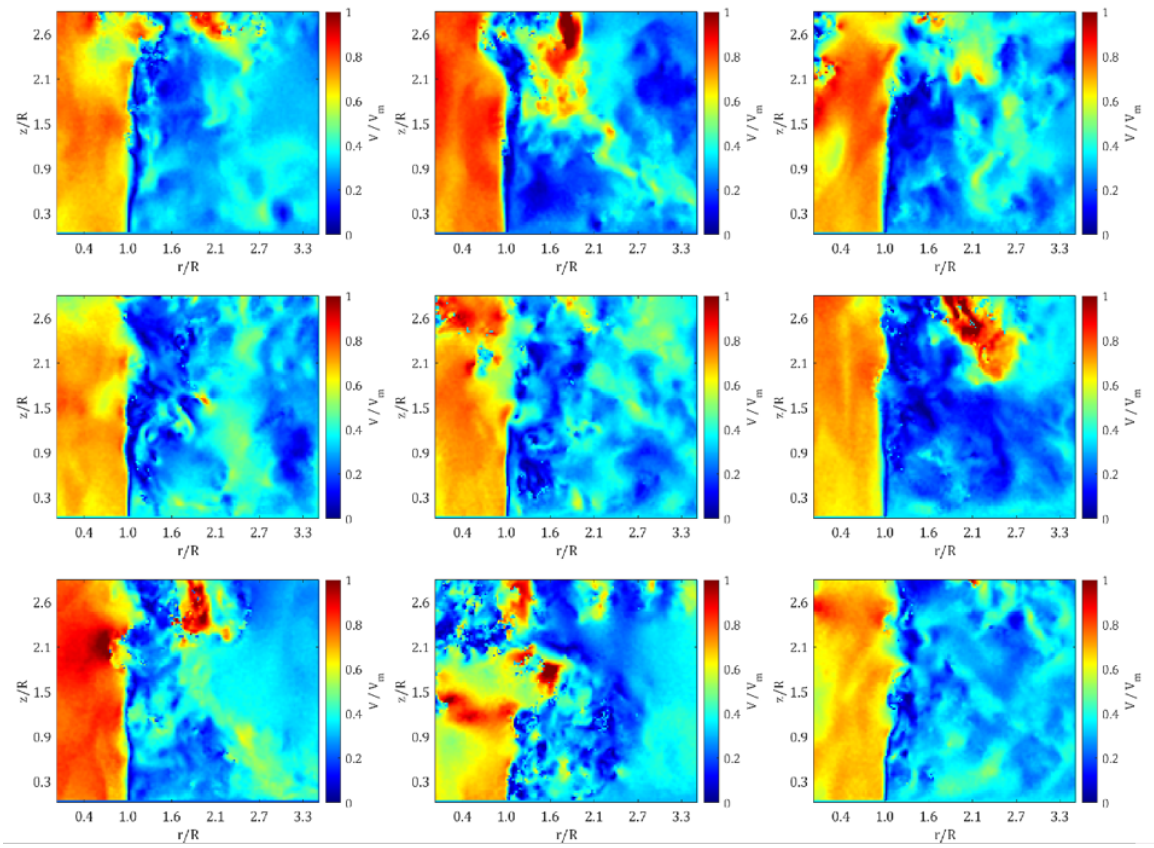

Figure 8.21: Instantaneous flow fields for TR = 0.27, Re = 7,000

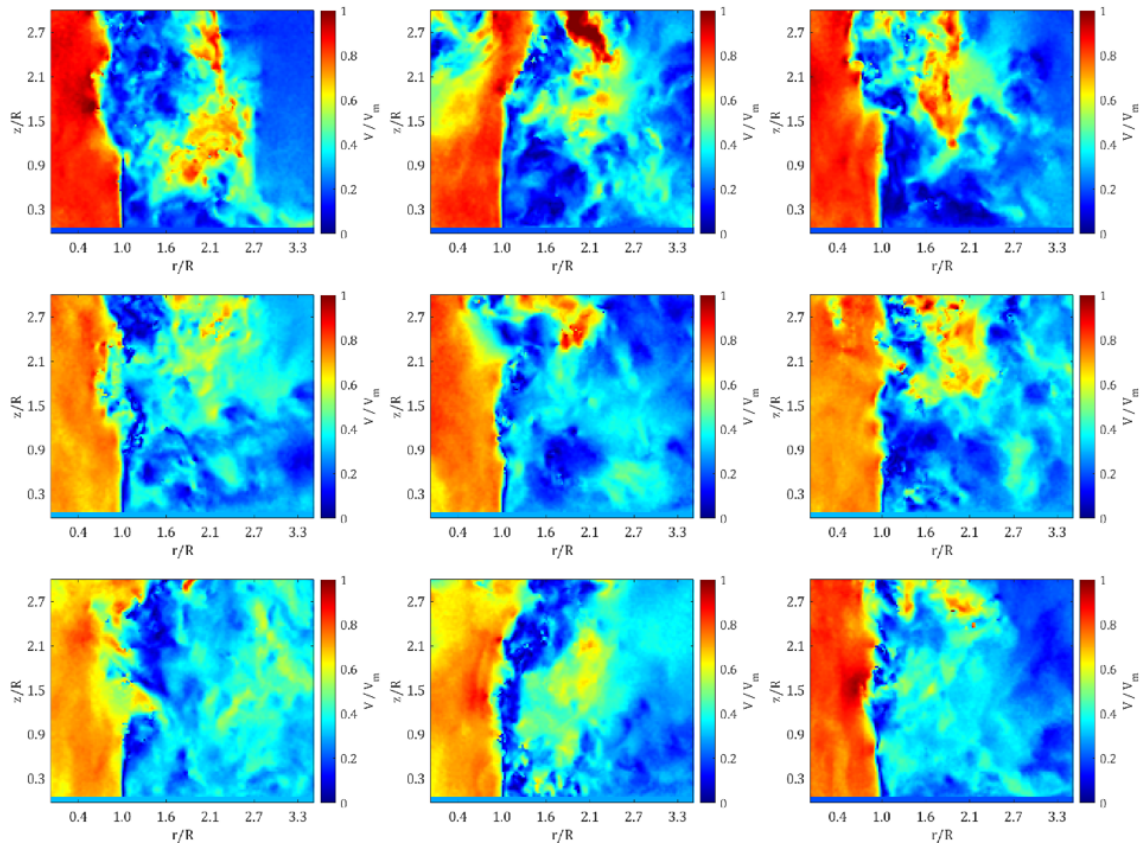

Figure 8.22: Instantaneous flow fields for TR = 0.27, Re = 10,000.

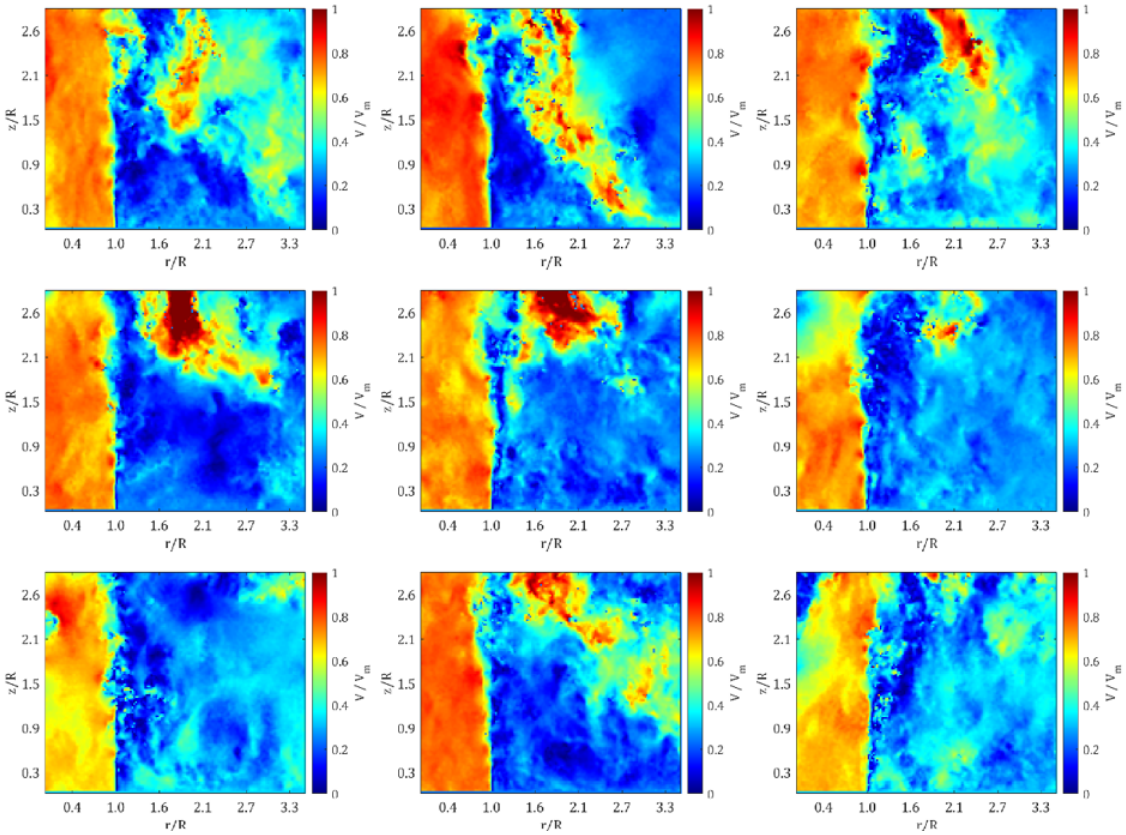

Figure 8.23: Instantaneous flow fields for TR = 0.27, Re = 17,000.

8.2.3 Reynolds-Averaged Navier-Stokes Equations

The erratic behavior seen in the instantaneous flow fields is driven by turbulence, which is an unpredictable and irregular variation in the flow [65]. To describe the time-varying quantities in the flow, we can use the Reynolds decomposition. Let Q be the ensemble average quantity, such as velocity, pressure, temperature, etc, and q be the fluctuations across individual realizations. The instantaneous quantities are then

$$\tilde{q} = Q + q. \tag{8.2}$$

We can then apply the Reynolds decomposition to the continuity equation and axisymmetric Navier-Stokes equations and take the time-average to produce the Reynolds-Averaged Navier-Stokes equations (RANS) shown below.

$$\overline{\frac{1}{r}\frac{\partial(r\tilde{u_r})}{\partial r}+\frac{\partial\tilde{u_z}}{\partial z}}=0 \tag{8.3}$$

$$\overline{\frac{\partial\tilde{u_r}}{\partial t}+\left(\tilde{u}\cdot\nabla\right)\tilde{u_r}}=\overline{-\frac{1}{\rho}\frac{\partial\tilde{p}}{\partial r}+\nu\left(\nabla^2\tilde{u_r}-\frac{\tilde{u_r}}{r^2}\right)} \tag{8.4}$$

$$\overline{\frac{\partial\tilde{u_z}}{\partial t}+\left(\tilde{\mathbf{u}}\cdot\nabla\right)\tilde{u_z}}=\overline{-\frac{\partial\rho}{\partial z}+\nu\nabla^2\tilde{u_z}}, \tag{8.5}$$

Simplifying Equation 8.3 results in the mean axisymmetric continuity equation,

$$\frac{1}{r}\frac{\partial(rU_r)}{\partial r}+\frac{\partial U_z}{\partial z}=0. \tag{8.6}$$

This result highlights that the mean flow is divergence-free, and applying this to Equation 8.3 shows that the turbulent fluctuations are also divergence-free.

The mean momentum equations in the radial and axial directions, respectively, are

$$\frac{\partial \mathrm{U_r}}{\partial \mathrm{t}}+\mathrm{U_r}\frac{\partial \mathrm{U_r}}{\partial \mathrm{r}}+\frac{\partial\overline{\mathrm{u_r}\mathrm{u_r}}}{\partial \mathrm{r}}+\mathrm{U_z}\frac{\partial \mathrm{U_r}}{\partial \mathrm{z}}+\frac{\partial\overline{\mathrm{u_z}\mathrm{u_r}}}{\partial \mathrm{z}}=-\frac{1}{\rho}\frac{\partial \mathrm{P}}{\partial \mathrm{r}}+\nu\left[\frac{1}{\mathrm{r}}\frac{\partial \mathrm{U_r}}{\partial \mathrm{r}}+\frac{\partial^2 \mathrm{U_r}}{\partial \mathrm{r}^2}+\frac{\partial^2 \mathrm{U_r}}{\partial \mathrm{z}^2}-\frac{\mathrm{U_r}}{\mathrm{r}^2}\right] \tag{8.7}$$

$$\frac{\partial \mathrm{U_z}}{\partial \mathrm{t}}+\mathrm{U_r}\frac{\partial \mathrm{U_z}}{\partial \mathrm{r}}+\frac{\partial\overline{\mathrm{u_z}\mathrm{u_r}}}{\partial \mathrm{r}}+\mathrm{U_z}\frac{\partial \mathrm{U_z}}{\partial \mathrm{z}}+\frac{\partial\overline{\mathrm{u_z}\mathrm{u_z}}}{\partial \mathrm{z}}=-\frac{1}{\rho}\frac{\partial \mathrm{P}}{\partial \mathrm{z}}+\nu\left[\frac{1}{\mathrm{r}}\frac{\partial \mathrm{U_z}}{\partial \mathrm{r}}+\frac{\partial^2 \mathrm{U_z}}{\partial \mathrm{r}^2}+\frac{\partial^2 \mathrm{U_z}}{\partial \mathrm{z}^2}\right]. \tag{8.8}$$

The time-average of the fluctuations is zero by definition, but the terms $\overline{\mathrm{u_r}\mathrm{u_r}}$, $\overline{\mathrm{u_z}\mathrm{u_z}}$, and $\overline{\mathrm{u_z}\mathrm{u_r}}$ are typically nonzero and when multiplied by the density, are the Reynolds stresses present in a turbulent flow. The Reynolds stresses create additional motion in the fluid, causing the unpredictable behavior in the flow, and the axisymmetric Reynolds stress tensor is then

$$\rho \begin{bmatrix} \overline{u_r u_r} & \overline{u_r u_z} \\ \overline{u_z u_r} & \overline{u_z u_z} \end{bmatrix}. \tag{8.9}$$

8.2.4 Experimental Reynolds Stresses Results

Similar to the impactor flow fields, contour plots can be generated for the different components of the Reynolds stress tensor. Figure 8.24 displays $\overline{u_z u_r}$ for the flat plate impactor across all Reynolds numbers normalized by the square of the maximum velocity. $\overline{u_z u_r}$ has contributions from the axial and radial velocity fluctuations and demonstrates the variation in both components of the flow. Across all Reynolds numbers, the magnitude of $\overline{u_z u_r}$ is near zero inside the jet and near the outlet, but the contours increase along the jet shear layer and near the impingement zone. This increase could be due to the vortices along the shear layer being distorted upon impact. As Reynolds number increases, the Reynolds stress along the shear layer increases closer to the nozzle outlet due to the increase in entrained air and the earlier formation of the K-H eddies. At the plate, where the flow begins to roll up and separate, the Reynolds stress becomes negative but with the largest magnitude, indicative of the most variation in the flow. For increasing Reynolds number, the Reynolds stress decreases in this region. This could be due to the impinged flow separating less at the plate for increased Re and the u_z fluctuations dominating less.

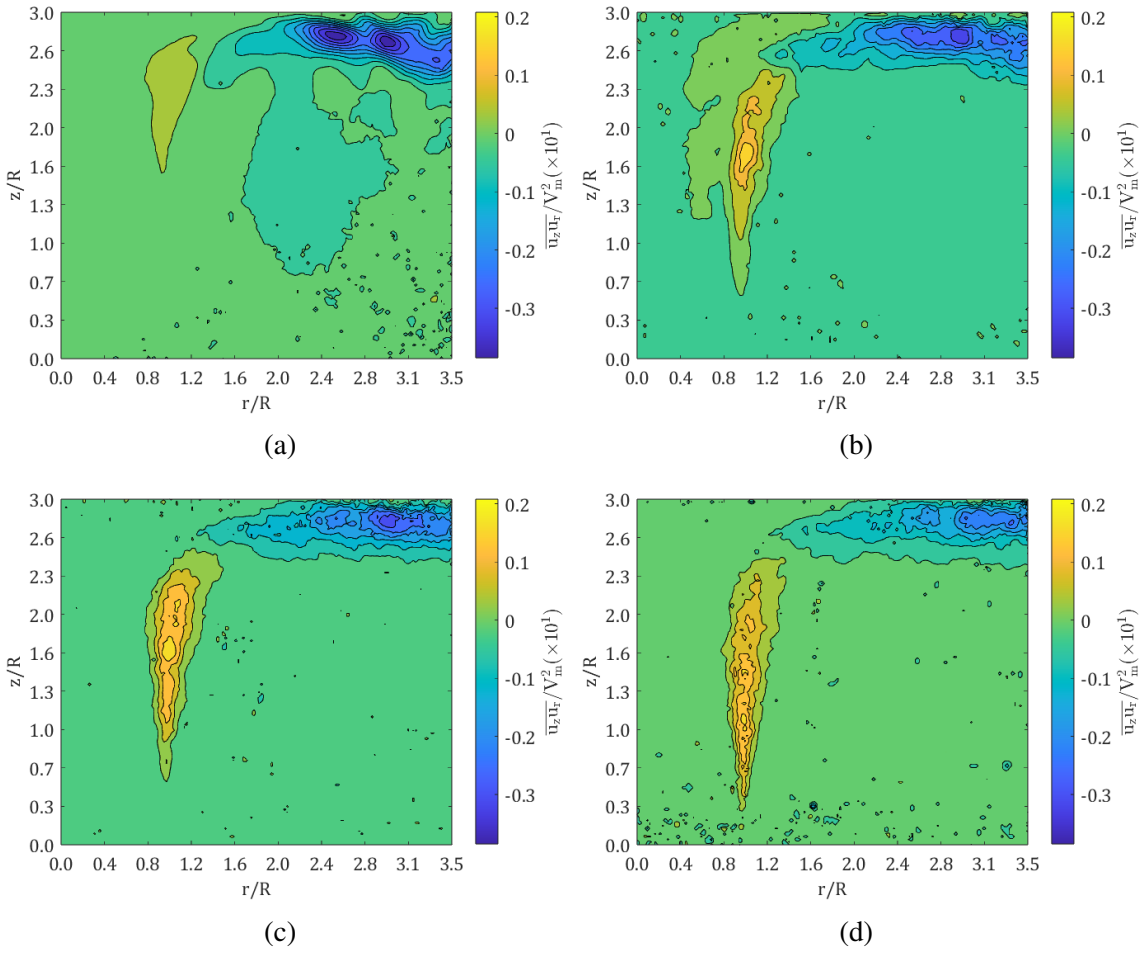

Figure 8.24: Contour plots of $\overline{u_z u_r}$ for the flat plate impactor for a) Re = 2,000, b) Re = 7,000, c) Re = 10,000, d) Re = 17,000.

Figure 8.25 compares $\overline{u_z u_r}$ for the different impactor designs for Re = 17,000. All other $\overline{u_z u_r}$ are shown in Figure A.5, Figure A.6, and Figure A.7 in the appendix. Similar to the flat plate impactor, all designs show increases in $\overline{u_z u_r}$ extending closer to the nozzle for increasing Reynolds number. Due to the wall jets, the edges of the traps show negative Reynolds stress, shown in light blue, from the pulsatile plumes. TR = 0.27 has the largest negative component of $\overline{u_r u_r}/V_m^2 \approx -0.3$. For all designs except TR = 0.27, the core of the jet has $\overline{u_z u_r}$ close to zero. However, TR = 0.27 has a large negative Reynolds stress component in the jet that increases in magnitude in the axial direction. This behavior is due to the fluctuations seen in the instantaneous contours, with the jet breaking up in certain

images.

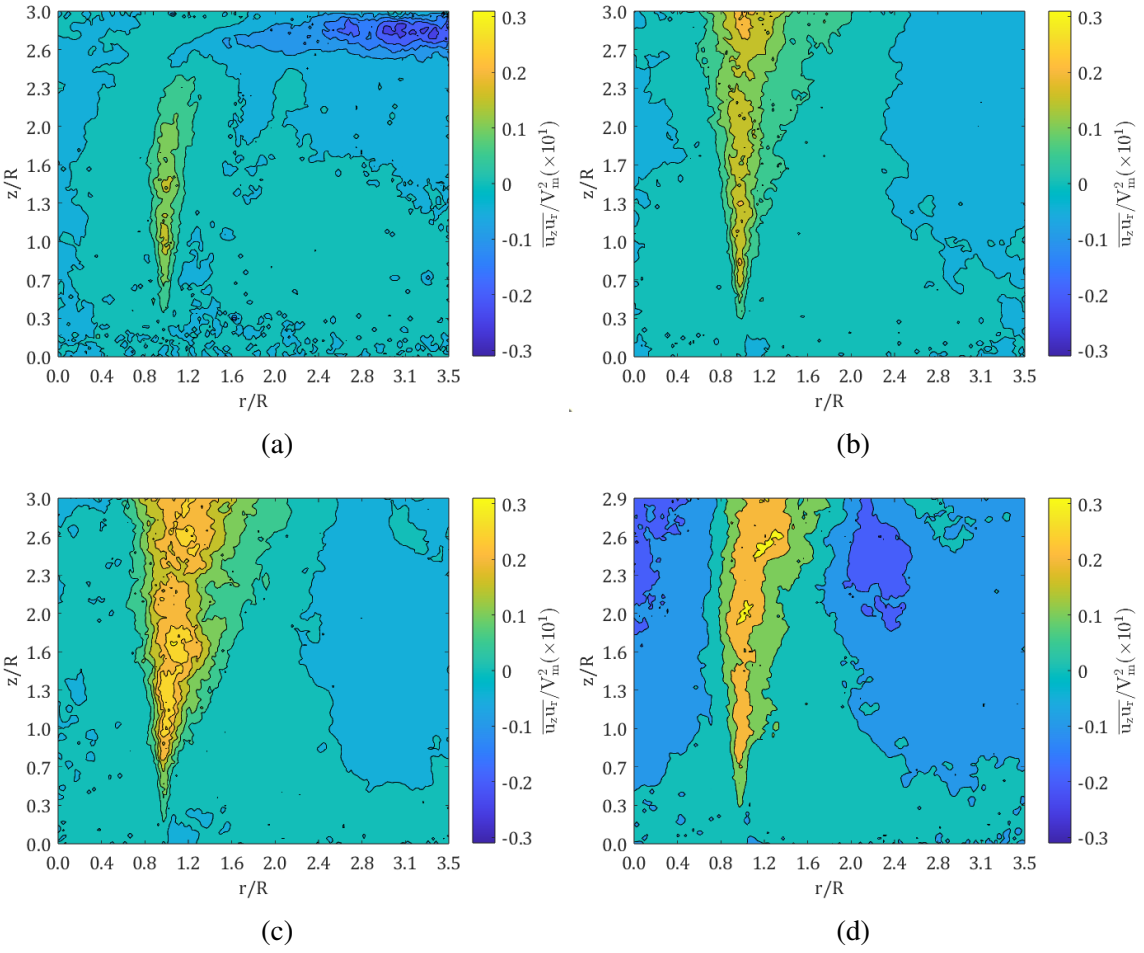

Figure 8.25: Contour plots of $\overline{u_z u_r}$ for Re = 17,000 for a) flat plate, b) TR = 1.00, c) TR = 0.59, d) TR = 0.27.

To isolate the fluctuations in the axial and radial directions, contours of $\overline{u_z u_z}$ and $\overline{u_r u_r}$ are shown for the four impactors with Re = 17,000 in Figure 8.26 and Figure 8.27, respectively. Examining $\overline{u_z u_z}$, the flat plate impactor has the least amount of velocity fluctuations compared to the other impactors. The only areas of nonzero $\overline{u_z u_z}$ for the flat plate impactor are along the shear layer and the wall jet. The trap impactors also have nonzero Reynolds stress along the shear layer, but at higher magnitudes, potentially due to the interaction between the jets and wall jets. TR = 0.27 has the largest $\overline{u_z u_z}$ component between the jet and end of the trap (r/R $\approx 1.2 - 2.0$) and larger variation in the gap than the other im-

pactors. Also, as seen in the $\overline{u_z u_r}$ contours, the jet core has a fluctuating axial velocity that worsens as the jet nears the trap. Inspecting the $\overline{u_r u_r}$ contours, the trends are similar, but the magnitudes of the Reynolds stresses are half that of the axial fluctuations. Compared to the $\overline{u_z u_z}$ contours, the flat plate impactor now has the highest $\overline{u_r u_r}$ in the wall jet, and this is the dominant component in the $\overline{u_z u_r}$ contours. Also, the jet core for TR = 0.27 is also nonzero in $\overline{u_r u_r}$, indicating that there is turbulent motion in both the axial and radial directions inside the jet.

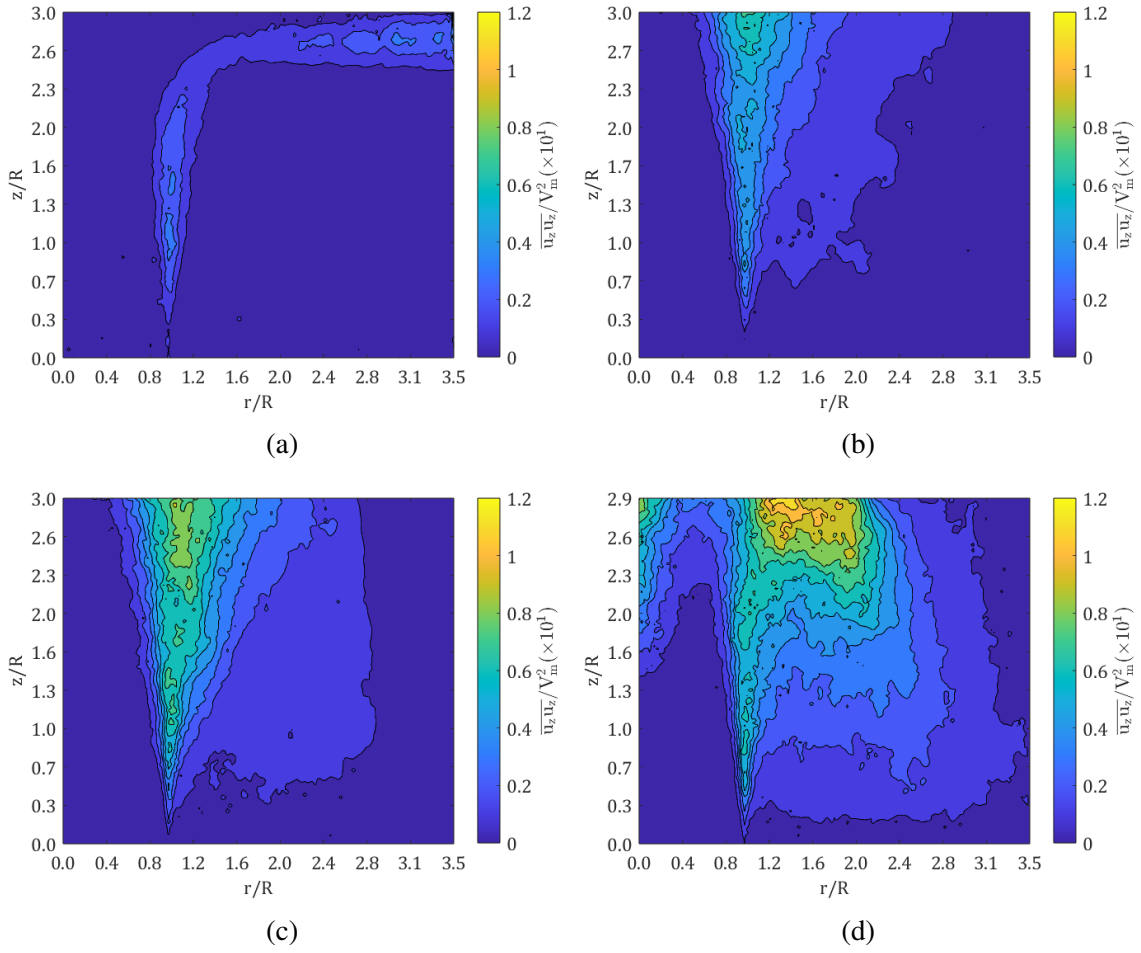

Figure 8.26: Contour plots of $\overline{u_z u_z}$ for Re = 17,000 for a) flat plate, b) TR = 1.00, c) TR = 0.59, d) TR = 0.27.

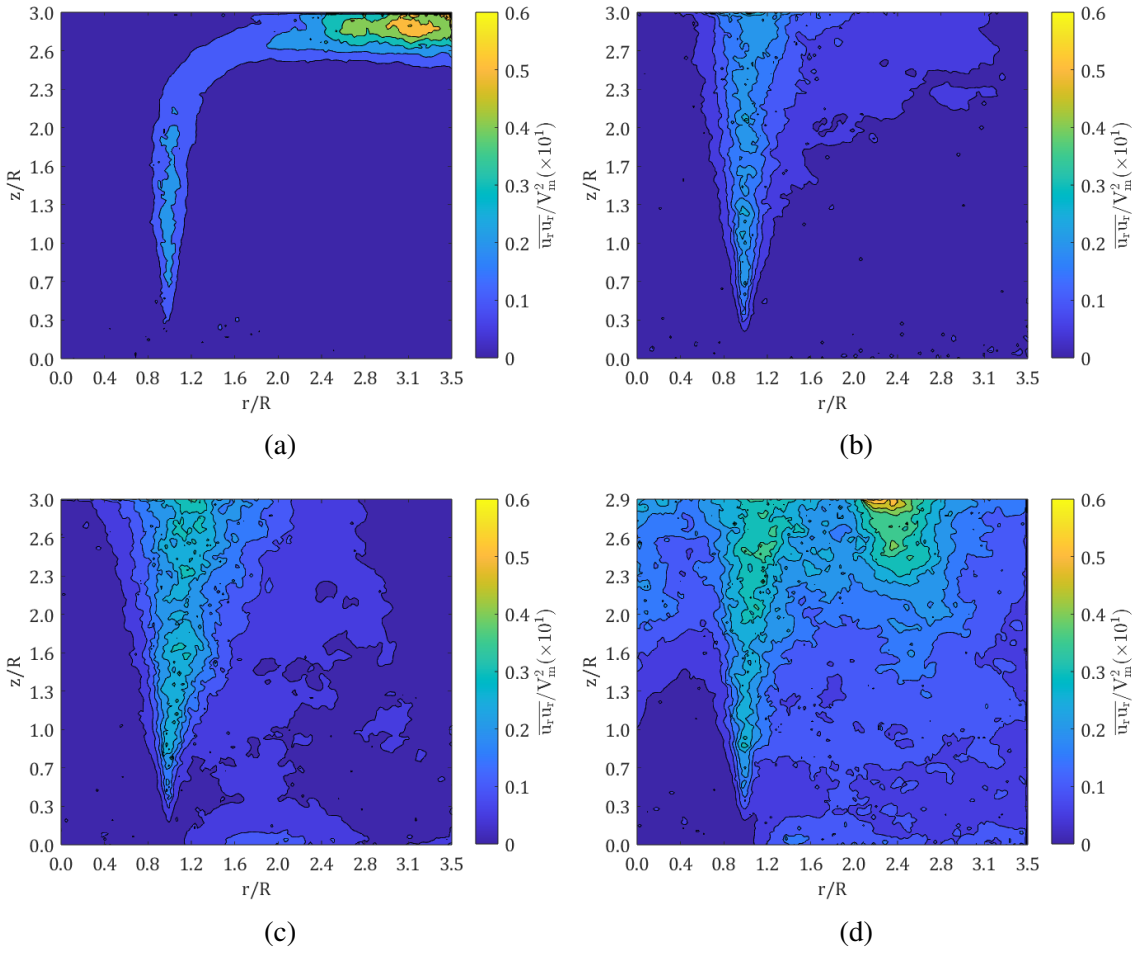

Figure 8.27: Contour plots of $\overline{u_r u_r}$ for Re = 17,000 for a) flat plate, b) TR = 1.00, c) TR = 0.59, d) TR = 0.27.

8.2.5 Experimental TKE Results

The Reynolds stress contours highlight the unpredictable and erratic behavior in the flow that can affect impactor efficiency. The overall effects of turbulence can be assessed by examining the turbulent kinetic energy,

$$k = \frac{1}{2}\left(\overline{u_r^2} + \overline{u_z^2}\right). \tag{8.10}$$

The turbulent kinetic energy is a measure of the strength of the fluctuations present in the flow, and again, the contours can be created. Turbulent kinetic energy contours normalized

by V_m^2 for the four impactors for Re = 17,000 are shown below in Figure 8.28. The TKE contours mimic the $\overline{u_z u_z}$ contours as the axial fluctuations were the dominant component.

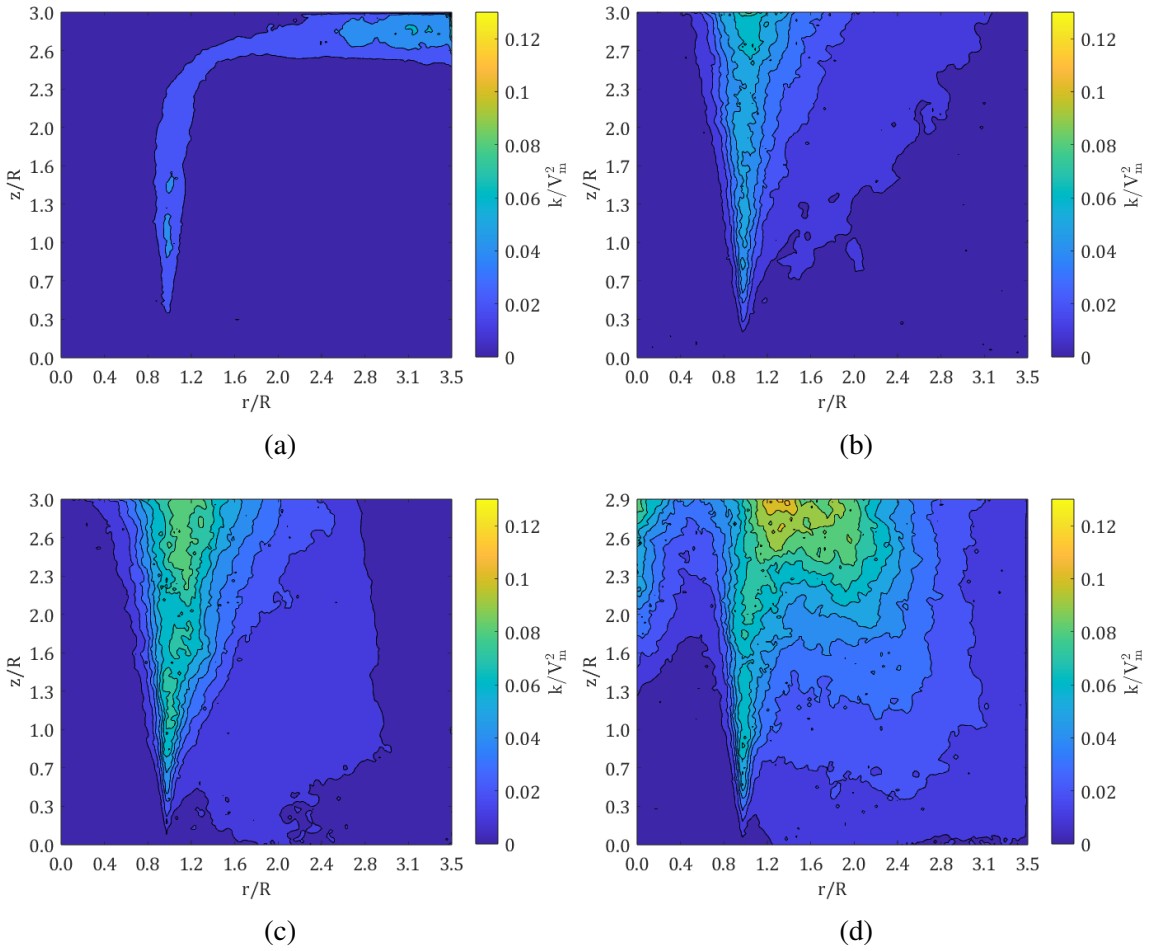

Figure 8.28: Contour plots of turbulent kinetic energy for Re = 17,000 for a) flat plate, b) TR = 1.00, c) TR = 0.59, d) TR = 0.27.

To assess how turbulence affects impactor efficiency, we analyzed the TKE profiles for Re = 17,000 at different downstream locations shown in Figure 8.29. At z/R = 1.0, the profiles are similar for $0 \leq z/R \leq 1.0$ as all designs have low normalized TKE inside of the jet, with TR = 0.27 having a slightly larger magnitude than the other designs. The TKE then sharply increases to a maximum at the shear layer. Past the shear layer, the flat plate has almost zero TKE, while the trap impactors have a slowly decreasing TKE that increases with decreasing trap ratio. Increasing the downstream location has little change on the flat

plate profiles as they continue to have low fluctuations inside the jet, but an increase in the shear layer. The only differences are due to the presence of the recirculation zone near the flat plate, causing the TKE to increase past the shear layer for z/R = 2.6 and 2.9. TR = 1.00 and 0.59 have small variations in downstream distance as the overall shape is similar to that of z/R = 1.0, but the peaks in the TKE profiles become broader and increase in magnitude. The most dramatic changes are seen for the TR = 0.27, where TKE increases inside the jet core with increasing downstream location. Inside the core, the TKE is highest along the centerline, and then decreases near r/R = 0.5, only to increase again at the shear layer, as seen in the other designs. There is a second peak near r/R = 2.0, which coincides with the edge of the trap, before gradually decreasing to nearly zero.

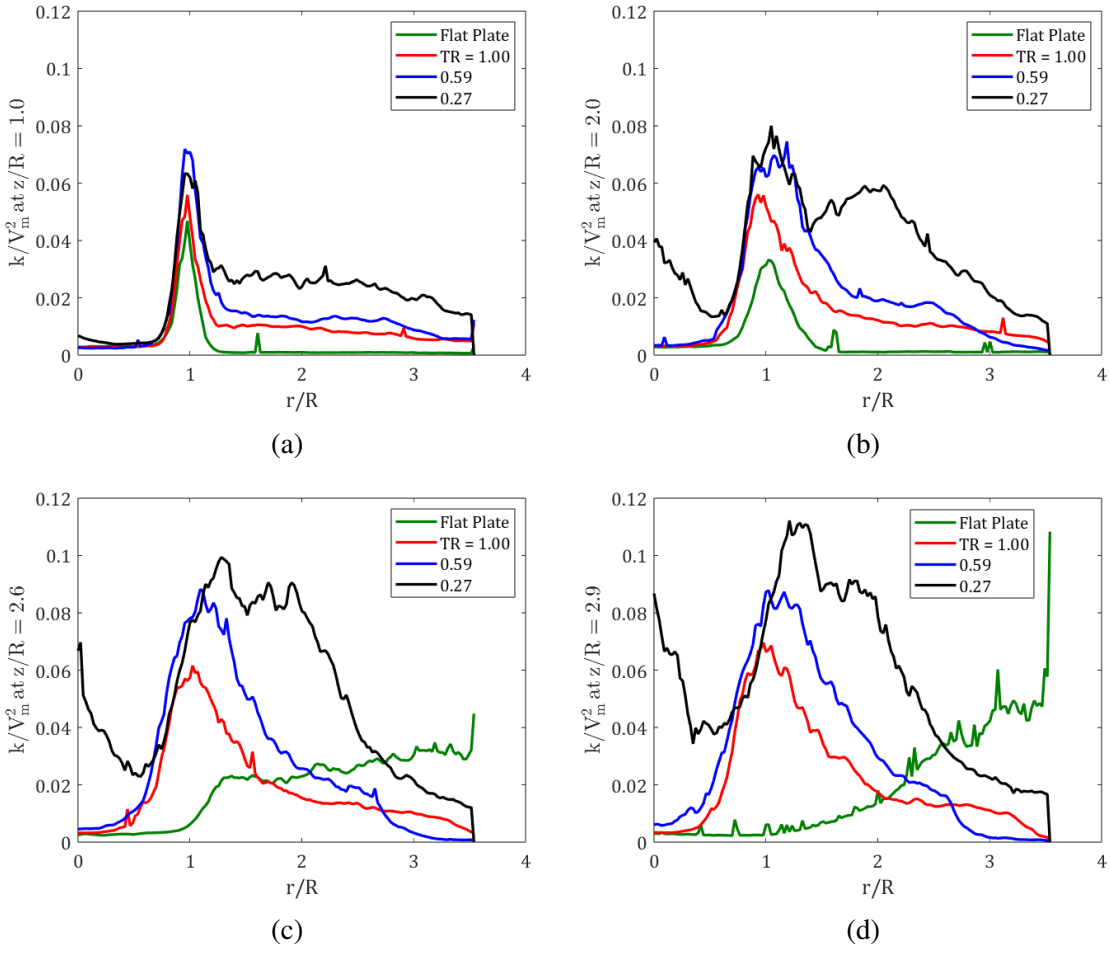

Figure 8.29: Comparison of Re = 17,000 normalized turbulent kinetic energy profiles at a) z/R = 1.0, b) z/R = 2.0, c) z/R = 2.6, d) z/R = 2.9.

By analyzing the turbulent fluctuations in the different impactor configurations, we have shown that increased fluctuations correlate with decreasing trap efficiency. The flat plate geometry is the control with the maximum efficiency and has the least amount of turbulence according to the contour plots and TKE profiles. TR = 1.0, the trap with the largest diameter and shallowest depth, most closely resembled the flat plate profiles. As the traps became narrower and deeper, the normalized TKE increased with TR = 0.27 (narrow and shallow), having a markedly different profile demonstrating turbulence inside the jet core. The increase in TKE is indicative of erratic and unpredictable behavior, which can explain the decrease in efficiency accompanied by an increase in turbulent fluctuations. As particles are exiting the nozzle, they may experience sudden changes in the flow and deviate from their initial trajectories, preventing them from entering the trap.

8.3 Hotwire Anemometry Results

Although the PIV results can provide quantitative information about the flow field, their time resolution was poor, as they were only able to resolve flow features at a maximum of 7.5 Hz. This low-frequency response is highlighted in the instantaneous velocity fields. While the instantaneous contours can reveal the expelled wall jets or eddies along the incoming jet, they cannot accurately show them developing with time because the time between images is too large. To accurately time-resolve these moving structures, we used a hotwire anemometer with a frequency response of 10 kHz, allowing us to resolve features with a 5 kHz frequency, a 667 times improvement over the PIV.

The hotwire was first placed in stagnant air to record the background noise as the negative control. A sampling rate of 25 kHz was used, and a digital lowpass IIR Butterworth filter of order 20 and a cutoff frequency of 2 kHz was applied to the data in MATLAB. The output voltage from the hotwire in stagnant air is shown in Figure 8.30 with the average value, $\overline{y}$, subtracted to emphasize the variation in the output signal. The original signal is in blue, and the filtered signal is in orange; the two overlap as the original signal demonstrates

very little activity at frequencies larger than the cutoff frequency of 2 kHz. As can be seen in the time trace, there is little variation in time in the ambient air.

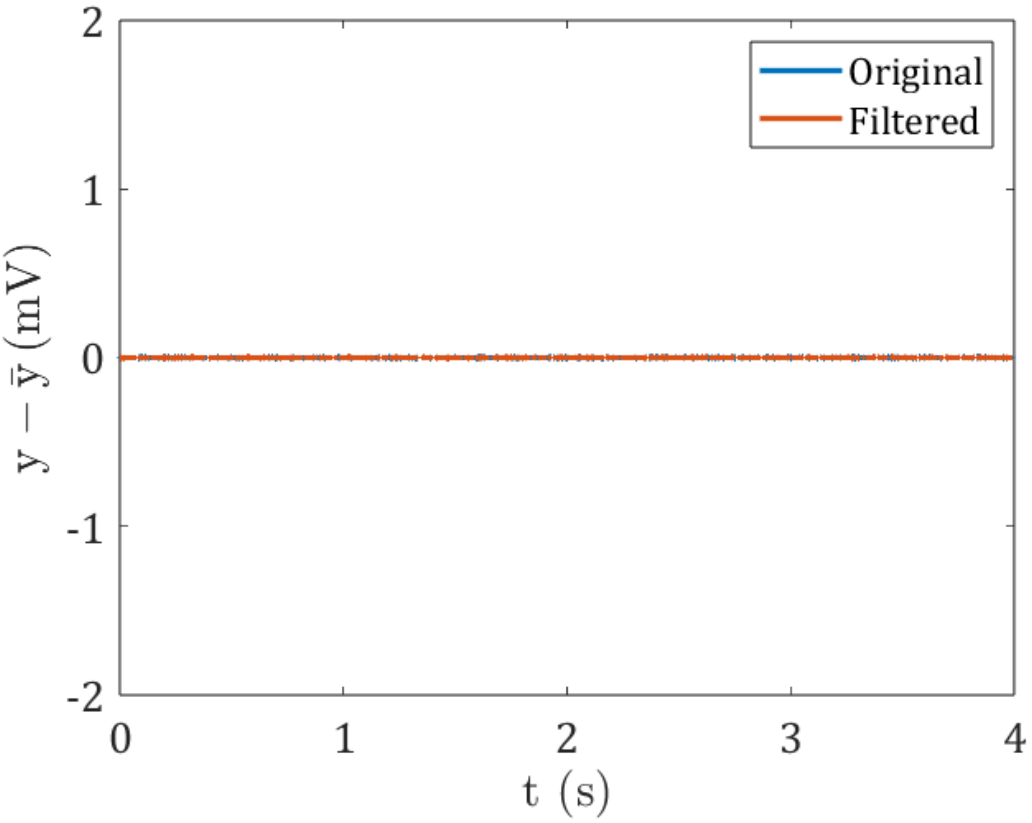

Figure 8.30: Voltage output of hotwire in ambient with the average value subtracted.

The power spectral density (PSD) was then calculated using Welch's method, averaged over four realizations, to analyze the frequency domain of the signal. The sampling window was half of the total length, with 50% overlap between windows, the number of Fast Fourier Transform (nFFT) points was the length of the window, and a resultant frequency density of 2.7 Hz/ bin was obtained. The PSD is shown in Figure 8.31 with peaks every 60 Hz. These peaks are due to the electromagnetic interference caused by the AC electrical signal and are not indicative of periodic perturbations present in the flow. In stagnant air, the filtered signal has very low magnitude (O(10^{-9})), and is constant, aside from the AC signal peaks, until $\approx$ 300 Hz when the signal begins to decrease due to the applied digital filter.

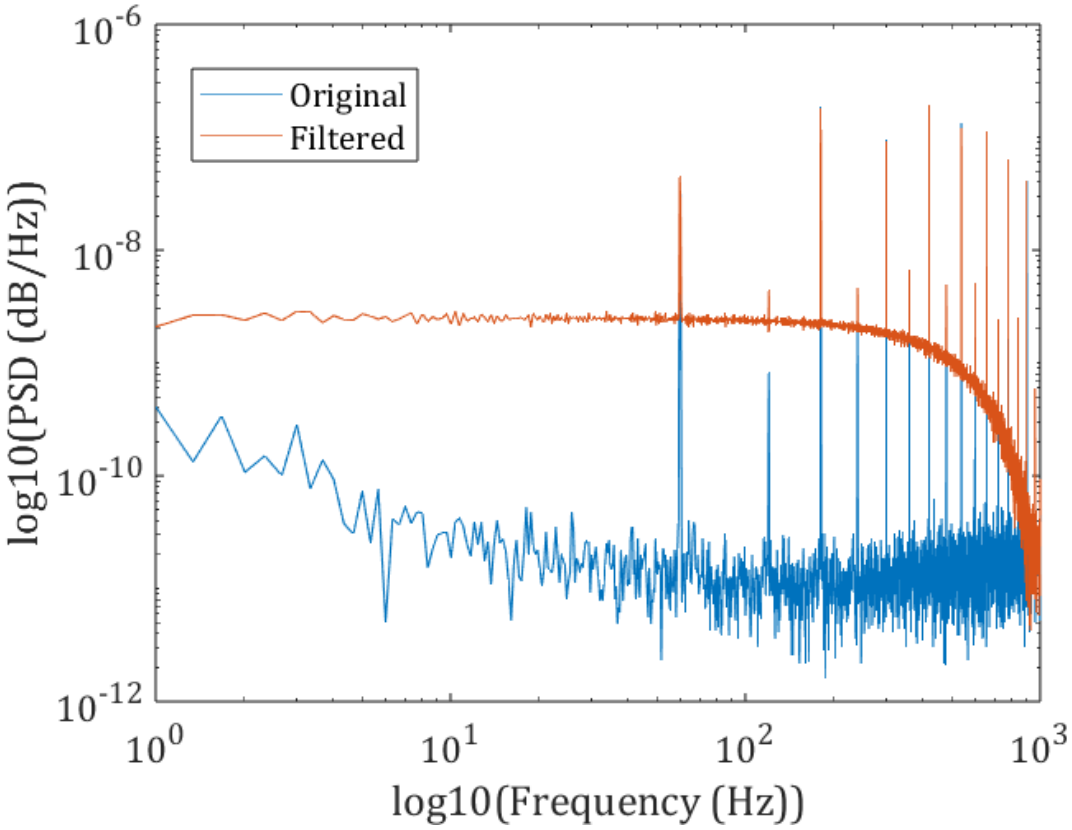

Figure 8.31: Power spectral density of probe in stagnant air.

The hotwire probe was then used with the TR = 0.27 impactor due to it having the largest turbulent fluctuations. The hotwire was placed at different locations inside the gap, and a schematic of the four probe placements at an axial distance z/R = 2.7 is shown in Figure 8.32. Location 1 is along the centerline (r/R = 0), 2 is near the nozzle radius (≈ r/R = 1.2), 3 is at the edge of the trap (r/R = 2), and 4 is at r/R = 3.0.

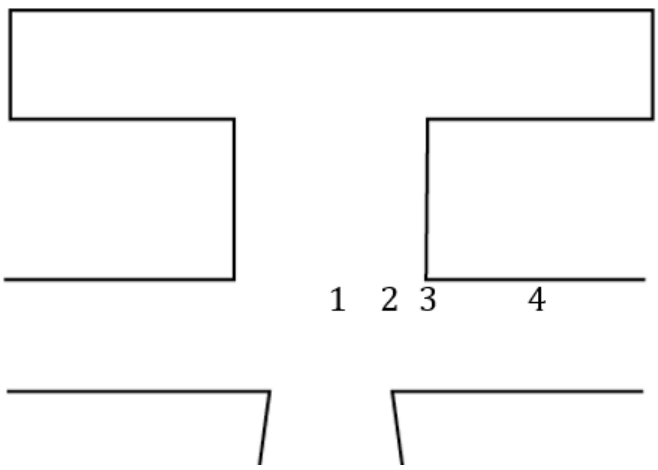

Figure 8.32: Schematic of the hotwire probe placement inside the TR = 0.27 gap.

The velocity time traces at the four locations are shown in Figure 8.33, the voltage output is converted to velocity using the calibration curve established in subsection 7.3.4. The average velocity is removed to analyze the fluctuations, and locations 1 - 3 have qualitatively similar behavior. Location 4 has notably less variation due to it being further removed from the centerline. The first position has larger negative fluctuations, demonstrating that there are more instances when the flow is erratically reduced compared to the average. This result is consistent with the instantaneous flow fields, where it was revealed that there are instances when the centerline velocity decreases due to the wall jet interfering with the incoming jet. Positions 2 and 3 have similar magnitudes in fluctuations to the centerline, but in the positive direction as the escaping wall jets increase the local velocity. Position 4 is at the edge of the PIV viewing window, and the instantaneous images show that the local velocity changes in time, but not as much as at the other locations, which is consistent with the PIV results.

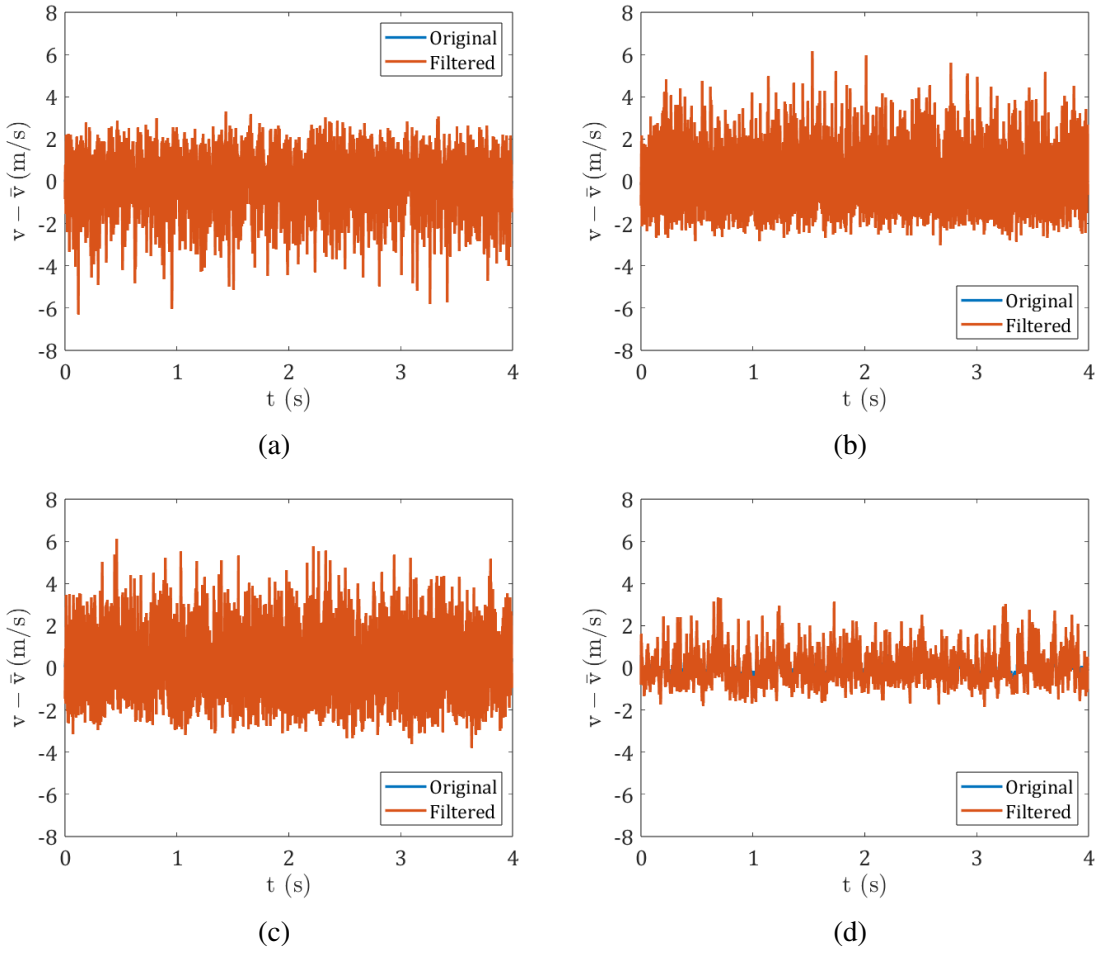

Figure 8.33: Comparison of Re = 17,000 velocity time traces for the TR = 0.27 impactor at the four different probe positions. a) r/R = 0, b) r/R ≈ 1.2, c) r/R = 2, d) r/R = 3.

The benefit of the increased frequency response of the hotwire is the ability to analyze the power spectrum of the velocity fluctuations. This was not practical with the PIV because the maximum frequency we could analyze was only 7.5 Hz. The averaged PSDs across three realizations for the four probe locations are given below in Figure 8.34 and are constructed using Welch's method with the window divided into four segments with 12.5% overlap and an nfft equal to the length of the window. At position 1 (centerline), there are three minor peaks at ≈ 20, 40, and 60 Hz; however, their magnitudes are only incrementally higher than the surrounding frequencies due to a low signal-to-noise ratio. The PSDs for r/R = 1 and 2 are similar, with neither showing significant peaks. A small peak is slightly

visible at 40 Hz at both locations, similar to the centerline. At these three locations, a peak in the PSD would indicate periodic behavior in the wall jet. Again, the magnitudes are not high, but the small peak at 40 Hz could be indicative of periodic shedding. At r/R = 3, there are again no strong peaks, but the overall shape of the distribution is different from the other three locations, as it immediately begins to roll off, indicative of purely broadband turbulence. Although the first three locations did not have strong evidence for the existence of a well-defined periodic behavior, they are still qualitatively different than the broadband turbulence of r/R = 3, potentially indicating the existence of periodic structures.

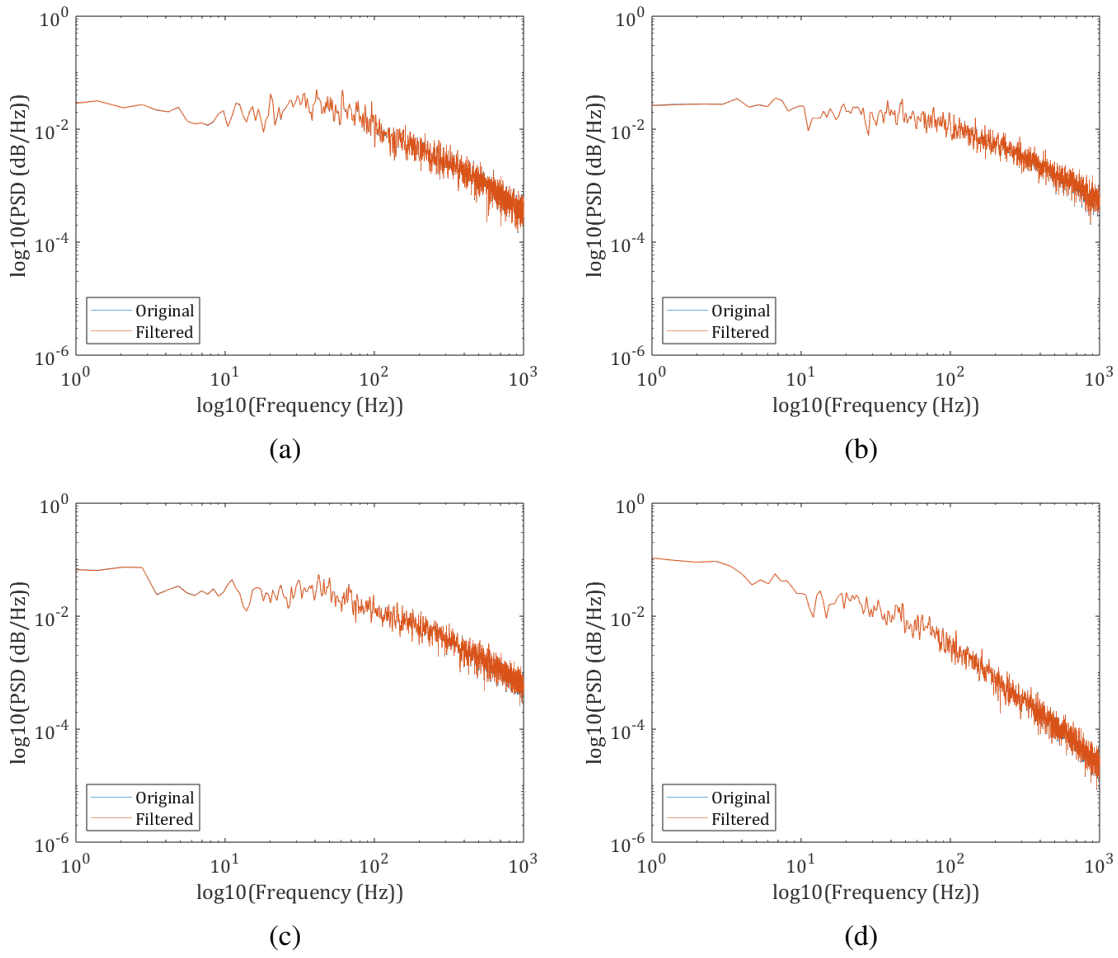

Figure 8.34: Power spectral densities for TR = 0.27 at a) Centerline, b) r/R = 1, c) r/R = 2, d) r/R = 6

Through shadowgraphy, PIV, and hotwire anemometry, we have been able to experi-

mentally analyze the flow in the impactor gap. Through these three methods, we were able to investigate the potential modes that reduce trap efficiency: particles deviating from their initial streamlines and particles losing momentum and being unable to impact inside the trap. Time-averaged flow fields and streamlines highlighted that the TR = 1.00 (wide and shallow trap) impactor had straight streamlines inside the jet that were similar to the flat plate impactor. However, TR = 0.59 (medium width and depth) and TR = 0.27 (narrow and deep) had streamlines that could induce particles to move away from the center of the jet. This phenomenon, coupled with the wall jets exiting the trap, could prevent particles from entering and reduce the trap efficiency that was seen in the efficiency plots. Analyzing the instantaneous flow fields revealed the erratic and turbulent behavior created by the narrow and deep trap. For this configuration, the plumes were shown to interfere and break up the incoming jet at a frequency between 20-60 Hz from the hotwire analysis. The effect of the wall jets could not only alter particle trajectories, but also decrease the momentum of the particles that are able to enter the trap, and render them unable to impact the trap surfaces. These experimental methods have been able to allowed us to correlate the decrease in trap efficiency with characteristics in the time-averaged and time-varying flow fields in the gap. However, to truly understand the different mechanisms that are decreasing trap efficiency, an investigation into the flow inside the trap needs to be performed.

CHAPTER 9
IMPACTOR FLOW FIELD NUMERICAL INVESTIGATION

9.1 Introduction

The experimental methods employed in chapter 8 have limited use when exploring the flow field inside the trap. The 3D-printed traps are opaque, and thus it is not possible to view the flow inside through shadowgraphy. If the traps were transparent, the high concentration of smoke particles in the trap would most likely oversaturate the images. Also, if transparent traps were used, particle image velocimetry would be difficult to perform due to the cylindrical geometry. The curved walls of the trap would refract the light at different angles, and the cameras would record distorted images. A calibration, or correction, would then have to be applied to the images to reconstruct them, but the flow field would need to be known *a priori*. A hotwire could be placed inside the trap; however, due to its limited spatial resolution, it is not feasible to map the entire flow field.

Due to these limitations in our experimental methods, numerical solutions were sought using the commercial software, ANSYS Fluent. The benefit of the numerical simulations is that they can predict the flow field for the entire impactor. After the flow field in the trap is constructed, we can then verify its validity by comparing the numerical results in the gap to our experimental data.

9.2 Numerical Setup

9.2.1 Simulation Domain

The TR = 1.00, 0.59, and 0.27 trap impactors were simulated with similar meshing schemes. The simulation domain included the nozzle interior, gap, and the trap, and can be seen below in Figure 9.1. Also shown in the schematics are the inlet, outlet, and axis of symmetry

for the axisymmetric flow field. The domain was then subdivided into eight sections to allow for different meshing strategies in regions where higher resolution was needed, such as in the jet core and near the edges of the trap. The subdivisions will be described in greater detail when discussing the mesh in the next subsection. Pertinent dimensions for dividing the simulation domain are $h_1, h_2, v_1,$ and v_2, and are given in Table 9.1.

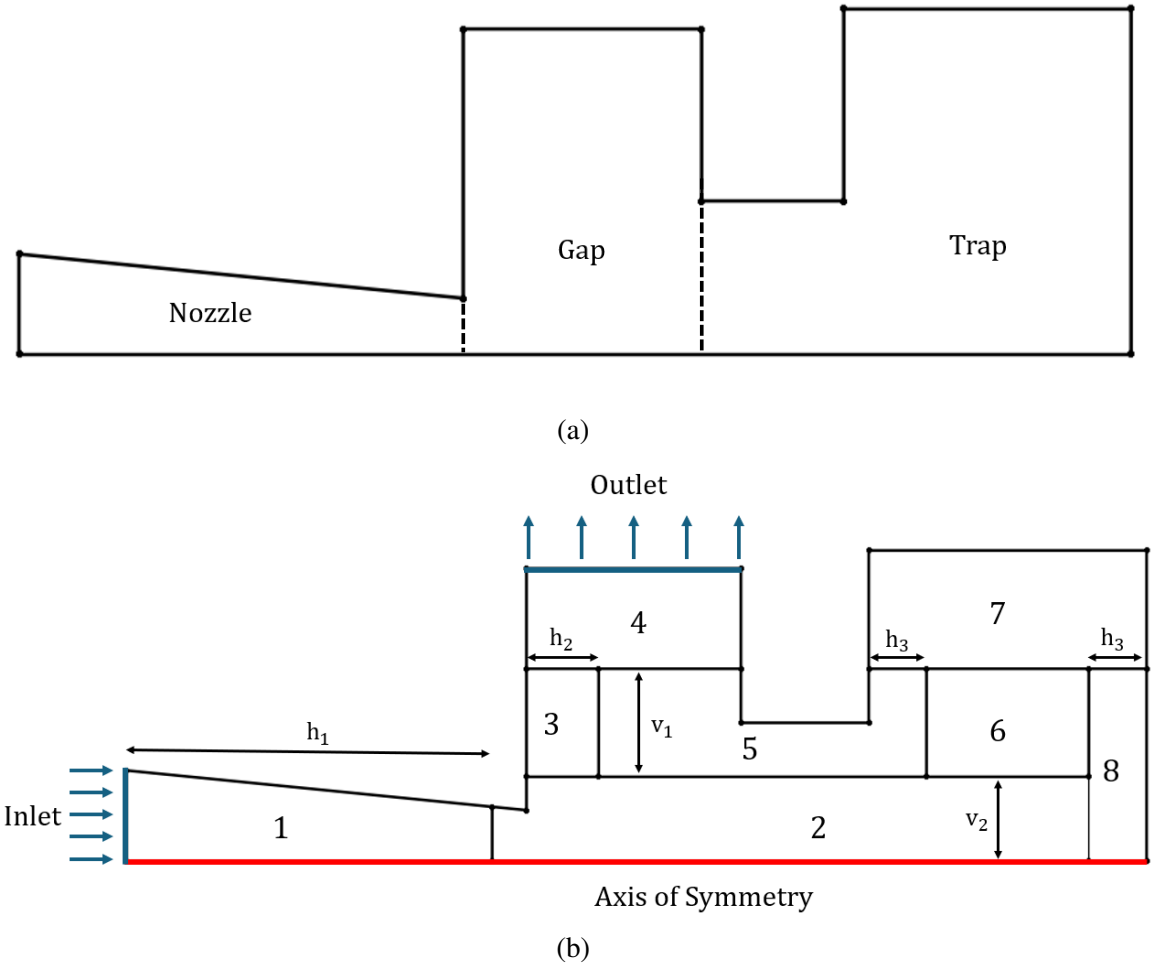

Figure 9.1: a) Schematic of simulation domain used in ANSYS Fluent, b) Domain is subdivided into eight sections with varying meshes. Not to scale.

Dimension	Length
h_1	5.64R
h_2	1.23R
h_3	0.59R
v_1	3.14R
v_2	1.41R

Table 9.1: Table of important dimensions for subdividing the simulation domain.

9.2.2 Mesh

The same meshing strategy was used for TR = 1.00 and 0.59. Face meshing and inflation layers were used for each domain subdivision. Zones 1 and 4 are considered low-priority zones and use face sizings of 4×10^{-4} m, with inflation layers with 8 smooth-transitioning layers. Zone 3 is of higher priority than 1 and 4 as the jet walls impinge in this region and used a face sizing of 3×10^{-4} with similar inflation layers. Zones 2, 5, 6, 7, and 8 are considered high-priority and all use a face sizing of 2×10^{-4} m with inflation layers with a 1×10^{-5} m first layer height and 8 smooth-transition layers, where applicable. We decided on a first layer thickness of 1×10^{-5} m by using the criterion of $y^+ = 1$. y^+ is the non-dimensional spacing in the viscous sublayer near the wall and is given by

$$y^+ = \frac{u_\tau \Delta y}{\nu}, \tag{9.1}$$

where y is the distance normal to the wall, u_τ is the friction velocity, and ν is the kinematic fluid viscosity [65, 114]. The friction velocity is given below,

$$u_\tau = \sqrt{\frac{\tau_w}{\rho}}, \tag{9.2}$$

where τ_w is the wall shear stress and ρ is the fluid density [65, 114]. τ_w is then given by,

$$\tau_w = \frac{1}{2} c_f \rho U^2, \tag{9.3}$$

where c_f is the skin friction coefficient at the wall and U is the freestream fluid velocity. For a turbulent boundary layer flow, c_f can be modeled as

$$c_f \approx \frac{0.027}{Re_x^{1/7}}, \tag{9.4}$$

where Re_x is the local Reynolds number along the wall [117]. As a first approximation, we assumed the local Reynolds number to be equal to the Reynolds number of the jet. Setting $y^+ = 1$, with U = 15 m/s and Re = 17,000, the resultant value was $\Delta y = 1.6 \times 10^{-5}$ m which we reduced to 1×10^{-5} m for increased accuracy. The total number of mesh elements for TR = 1.00 and 0.59 was 91,931 and 85,526, respectively. The meshing strategy details are shown in Table 9.2. The mesh for TR = 0.27 is nearly identical, except zone 4 used a face meshing of 5×10^{-4} m. The mesh for TR = 0.27 is shown below in Figure 9.2, and has a total of 84,234 elements.

Zone	**Face Meshing (m)**	**Inflation**
1	4×10^{-4}	Smooth transition, 8 layers
2	2×10^{-4}	First layer height = 1×10^{-5} m, 8 layers
3	3×10^{-4}	Smooth transition, 8 layers
4	4×10^{-4}	Smooth transition, 8 layers
5	2×10^{-4}	First layer height = 1×10^{-5} m, 8 layers
6	2×10^{-4}	NA
7	2×10^{-4}	First layer height = 1×10^{-5} m, 8 layers
8	2×10^{-4}	First layer height = 1×10^{-5} m, 8 layers

Table 9.2: Meshing strategy for TR = 1.00 and 0.59. TR = 0.27 is nearly identical except zone 4 used a face meshing of 5×10^{-4} m. TR = 1.00 used 91, 931 total elements, TR = 0.59 used 85, 526, and TR = 0.27 used 84,234.

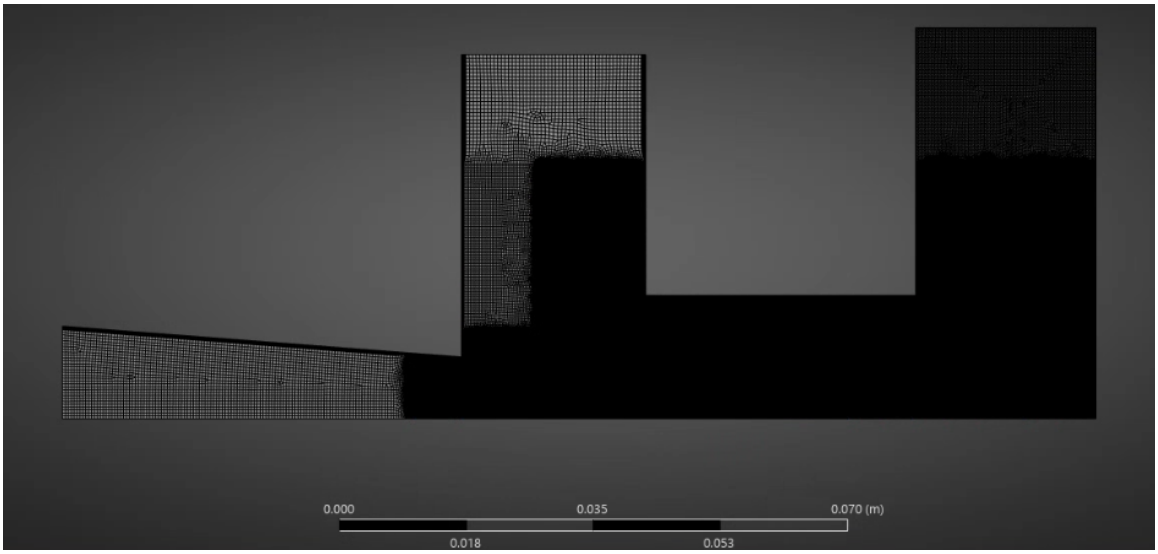

Figure 9.2: TR = 0.27 mesh applied in ANSYS Fluent.

9.3 Solution Methods

Only the flow fields similar to Re = 17,000 were simulated for the three trap impactors. We initially attempted to match the Reynolds numbers for the simulations with the PIV results, but due to the outlet velocity profile being sensitive to the converging nozzle geometry, we instead matched the nozzle outlet centerline velocity. We discuss the model validation in section 9.5.

For TR = 1.00, the steady-state k-ω RANS model was used, whereas the Detached Eddy Simulation (DES) model was used for the TR = 0.59 and 0.27 impactors. The instantaneous flow fields in subsection 8.2.2 highlighted that for TR = 1.00, the flow field did not noticeably change in time and was essentially quasi-steady, whereas TR = 0.59 and 0.27 were time-dependent. DES is inherently transient and can better predict the time-varying nature of the flow fields. We ran DES simulations for TR = 1.00, but the solution eventually approached the steady-state k-ω solution. The impactors had varying inlet pressures to match the centerline velocities of the Re = 17,000 impactors. TR = 1.00 used an inlet pressure of 185 Pa, TR = 0.59 used 180 Pa, and TR = 0.27 used 234 Pa. The differences in inlet pressure are due to the varying static pressures at the nozzle outlets for each configu-

ration. At the inlet, all models used a turbulence intensity of 5% and an intermittency of 1. TR = 1.00 and 0.59 used a turbulent viscosity ratio of 0.1, and TR = 0.27 used 0.01. For the outlet boundary condition, all had a pressure outlet condition of 0 Pa, with a turbulent intensity of 5%, a viscosity ratio of 1.0, and an intermittency of 1. Due to the outlet being multiple nozzle radii away from the trap, less importance was placed on the outlet boundary condition aside from the prescribed pressure. The initial condition for the transient solvers was set so that the flow started from rest.

As mentioned previously, the TR = 0.59 and 0.27 impactors used the Detached Eddy Simulation (DES) solver. DES is the preferred model in this instance due to the interaction between the fluid and the solid boundaries of the impactor, and is a combination of the Large Eddy Simulation and the RANS k-ω model near the boundary layer. The timestep for these simulations was selected using a Courant-Friedrichs-Lewy (CFL) number of 1. The CFL number is a dimensionless parameter that compares the distance the flow moves in one timestep to the mesh element size. A CFL number of 1 allows the flow to move through one element each timestep. The CFL number is

$$\mathrm{CFL} = \frac{\mathrm{u}\Delta\mathrm{t}}{\Delta\mathrm{x}}, \tag{9.5}$$

where u is the fluid velocity, Δx is the mesh element size, and Δt is the timestep. From the PIV data, the maximum velocity was 17 m/s, which will be used as u, and the typical mesh element size is 2×10^{-4} m in the jet. The resultant timestep for CFL of 1 is 1.2×10^{-5} s, but the simulations used a smaller timestep of 5×10^{-6} s as an added precaution. The transient simulations were run for a total computation time of 0.3, and data were recorded every 20 timesteps to analyze the time-dependent flow field.

9.4 Numerical Solution Verification

We needed to verify that the numerical solvers properly solved the Navier-Stokes equations. First, we analyzed the inlet and outlet velocity profiles in the nozzle shown in Figure 9.3. The inlet velocity profiles are as expected, with the maximum values near r/R = 0 and then decreasing near the nozzle walls. The velocities do not reach 0 m/s at the walls, as is expected due to the no-slip condition, due to the center of the mesh element closest to the wall being slightly removed from the wall itself. However, all three velocities for the different impactors are dramatically reduced near the wall and are tending towards zero. The outlet velocity profiles are similar to the outlet profiles noted by Ashforth *et al.* [100] for a converging nozzle, where the maximum velocity near r/R = 0.9 was attributed to the vena contracta phenomenon. The velocities at the nozzle exit wall are shown to reduce to near zero, and this is due to the refined mesh at the nozzle outlet.

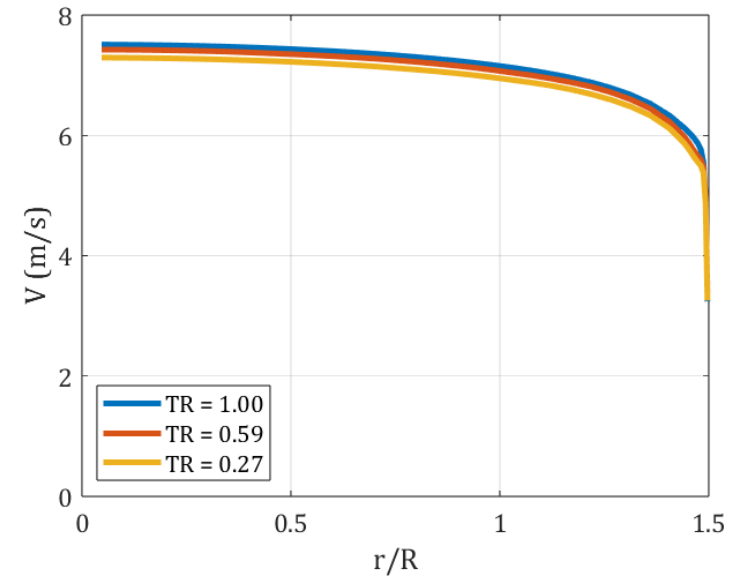

(a)

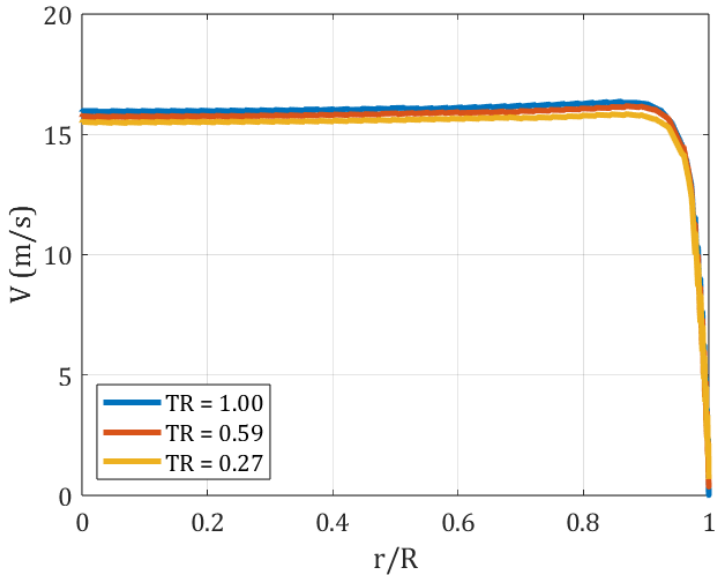

(b)

Figure 9.3: Velocity profiles for the a) nozzle inlet, b) nozzle outlet.

We next verified that the mass flow rate into and out of the domain was conserved. This was done in Fluent by using the built-in mass flow rate surface integrals function, and the mass flow rate percent error is shown below in Figure 9.4. The percent error is on the order of 10^{-4} and confirms that the mass flow rate is conserved.

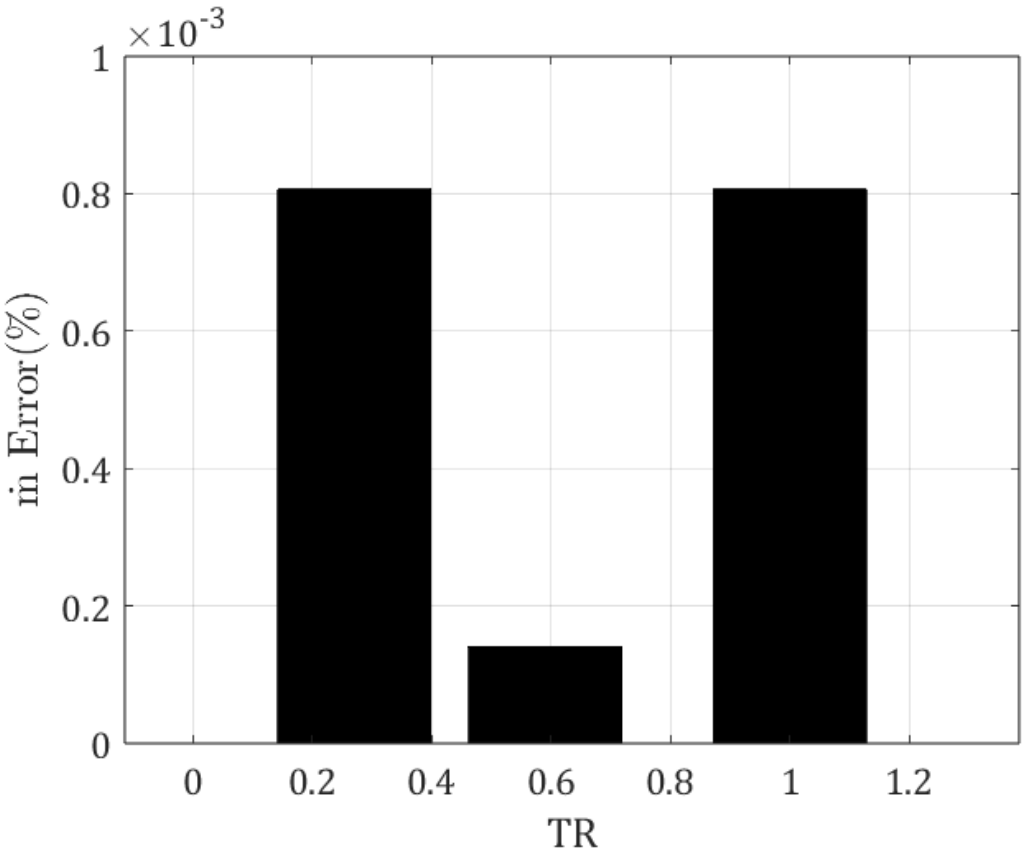

Figure 9.4: Percent error of mass flow rate through the domain for the various impactors.

Lastly, we calculated the momentum flux and compared it to the net forces exerted on the nozzle to assess momentum conservation. A schematic used for the momentum conservation is shown in Figure 9.5.

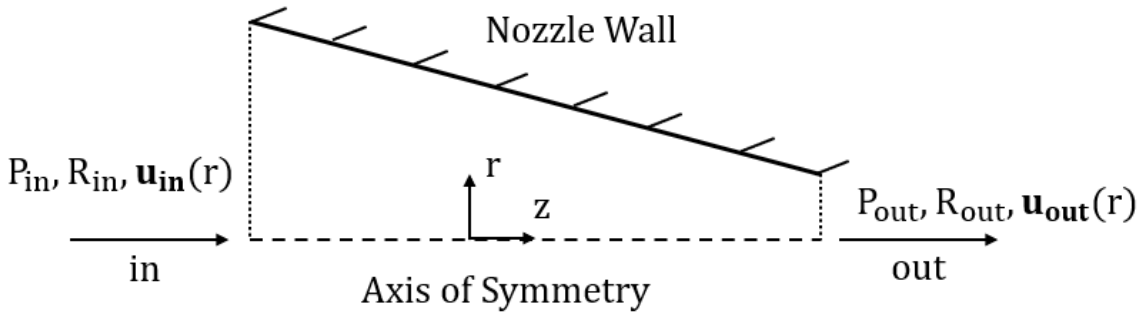

Figure 9.5: Schematic for conservation of momentum through the nozzle.

A control volume was used surrounding the nozzle to encompass the nozzle inlet and outlet and the nozzle walls. Conservation of momentum for a control volume states that the sum of the forces applied to the control volume is equal to the net momentum flux through the volume. The conservation of momentum can then be decomposed into the axial and radial directions. The sum of forces in the axial direction is given as

$$\begin{aligned}\sum \mathrm{F_z} = &\int_0^{\mathrm{R_{in}}} \mathrm{P_{in}(r)}\, 2\pi \mathrm{r}\, \mathrm{dr} - \int_0^{\mathrm{R_{out}}} \mathrm{P_{out}(r)}\, 2\pi \mathrm{r}\, \mathrm{dr} \\ &+ \int_0^{\mathrm{R_{in}}} \rho\, \overline{\mathrm{u'^2_{in,\,z}(r)}}\, 2\pi \mathrm{r}\, \mathrm{dr} - \int_0^{\mathrm{R_{out}}} \rho\, \overline{\mathrm{u'^2_{out,\,z}(r)}}\, 2\pi \mathrm{r}\, \mathrm{dr} \\ &- \mathrm{F_{wall,\,z}}. \end{aligned} \tag{9.6}$$

The first term is the pressure applied to the control volume inlet, the second is the pressure applied to the outlet, the third and fourth terms are the Reynolds stress contributions at the inlet and outlet, respectively, and the fifth term is the force of the walls acting on the control volume. The wall forces are in the negative axial direction due to Newton's third law. As the flow moves through the nozzle, it will impart a force on the walls in the

positive axial direction, and therefore, the opposite reaction applied to the control volume that encompasses the fluid will be in the negative axial direction. Equating the sum of forces and the momentum flux in the axial direction results in

$$\sum \mathrm{F_z} = \int_0^{\mathrm{R_{out}}} \rho \mathrm{u}^2_{\mathrm{out,\,z}}(\mathrm{r}) 2\pi \mathrm{r}\, \mathrm{dr} - \int_0^{\mathrm{R_{in}}} \rho \mathrm{u}^2_{\mathrm{in,\,z}}(\mathrm{r}) 2\pi \mathrm{r}\, \mathrm{dr}, \tag{9.7}$$

where the first term is momentum flux out of the control volume and the second is the momentum flux into the control volume. Similarly, the sum of forces in the radial direction is

$$\begin{aligned} \sum \mathrm{F_r} = &\int_0^{\mathrm{R_{in}}} \rho\, \overline{\mathrm{u}'_{\mathrm{in,\,r}}(\mathrm{r}) \mathrm{u}'_{\mathrm{in,\,z}}(\mathrm{r})}\, 2\pi \mathrm{r}\, \mathrm{dr} - \int_0^{\mathrm{R_{out}}} \rho\, \overline{\mathrm{u}'_{\mathrm{out,\,r}}(\mathrm{r}) \mathrm{u}'_{\mathrm{out,\,z}}(\mathrm{r})}\, 2\pi \mathrm{r}\, \mathrm{dr} \\ &- \mathrm{F_{wall,\,r}}, \end{aligned} \tag{9.8}$$

where there is no pressure force contributions due to the inlet and outlet surface normals being orthogonal to the radial direction, and the normal Reynolds stresses are replaced with the shear stresses for the same reason. Then, equating the radial forces and the momentum flux in the radial direction results in

$$\sum \mathrm{F_r} = \int_0^{\mathrm{R_{out}}} \rho \mathrm{u}_{\mathrm{out,\,r}}(\mathrm{r}) \mathrm{u}_{\mathrm{out,\,z}}(\mathrm{r}) 2\pi \mathrm{r}\, \mathrm{dr} - \int_0^{\mathrm{R_{in}}} \rho \mathrm{u}_{\mathrm{in,\,r}}(\mathrm{r}) \mathrm{u}_{\mathrm{in,\,z}}(\mathrm{r}) 2\pi \mathrm{r}\, \mathrm{dr}. \tag{9.9}$$

Figure 9.6a shows the percent error in the axial wall forces, $\mathrm{F_{wall,\,z}}$, from the control volume analysis with the wall forces calculated by ANSYS. The percent errors are near 2% for all three nozzles, which are nearly negligible. Figure 9.6b shows the wall forces in the radial direction. Due to the axisymmetric flow field, the nozzle wall forces in the radial direction are zero. The resultant forces calculated by the momentum balance are all on the order of 10^{-3}, which are also nearly negligible.

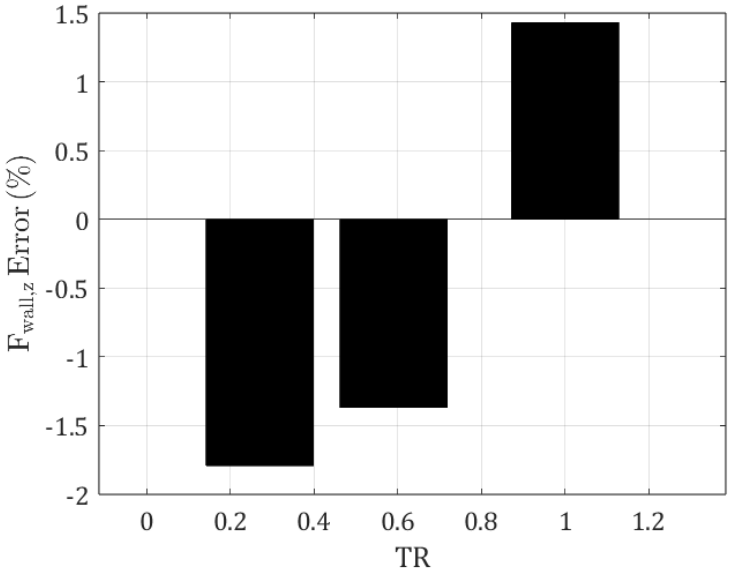

(a)

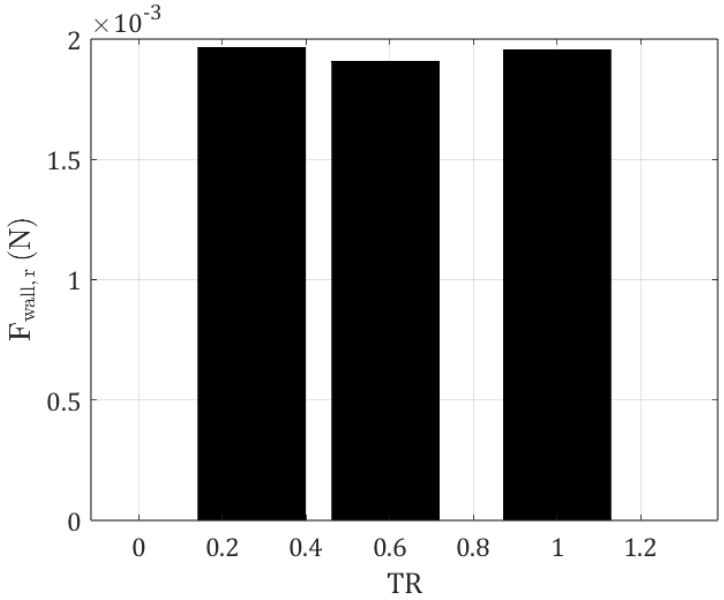

(b)

Figure 9.6: a) Percent error in the axial wall forces calculated by momentum conservation compared to the wall forces calculated by ANSYS, b) Resultant radial wall force from momentum conservation.

By analyzing the nozzle inlet and outlet velocity profiles, mass conservation, and momentum conservation with minimal discrepancies in the results, we can verify that the numerical solution is accurate.

9.5 Numerical Model Validation

9.5.1 Flow Fields

After verifying that the numerical solutions have accurately solved the Navier-Stokes equations, we need to validate the simulations with the experimental results. The previous section was to confirm that there were no errors in the numerical calculations used to simulate the flow. However, this does not mean that the simulated results are the proper solutions to the flows we are attempting to recreate. For example, the model may be solved correctly, but the input conditions do not properly represent the flow in the impactor, and we are not solving the correct equations. To validate the numerical results, we compared the simulations to the PIV data in the gap. The time-averaged flow fields for the TR = 1.00, 0.59, and 0.27 simulations compared to their PIV counterparts are shown in Figure 9.7, Figure 9.8, and Figure 9.9, respectively, with the numerical solutions on the left, and the PIV results on the right. Overall, the numerical contours match well with the experimental results. TR = 1.00 and 0.59 show the flow exiting the nozzle and entering the gap without a significant change in the jet core velocity, as expected. For TR = 0.27, the numerical solution accurately predicts the jet velocity decay, and the contours also show the M-shaped velocity profile seen in the PIV data.

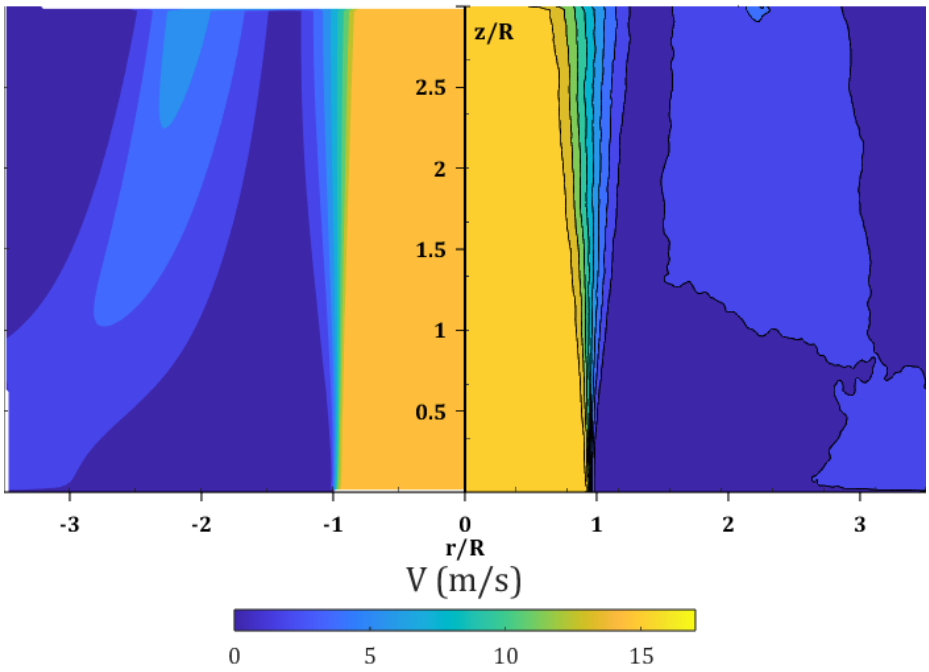

Figure 9.7: TR = 1.00 comparison of velocity contours in the gap for Re = 17,000.

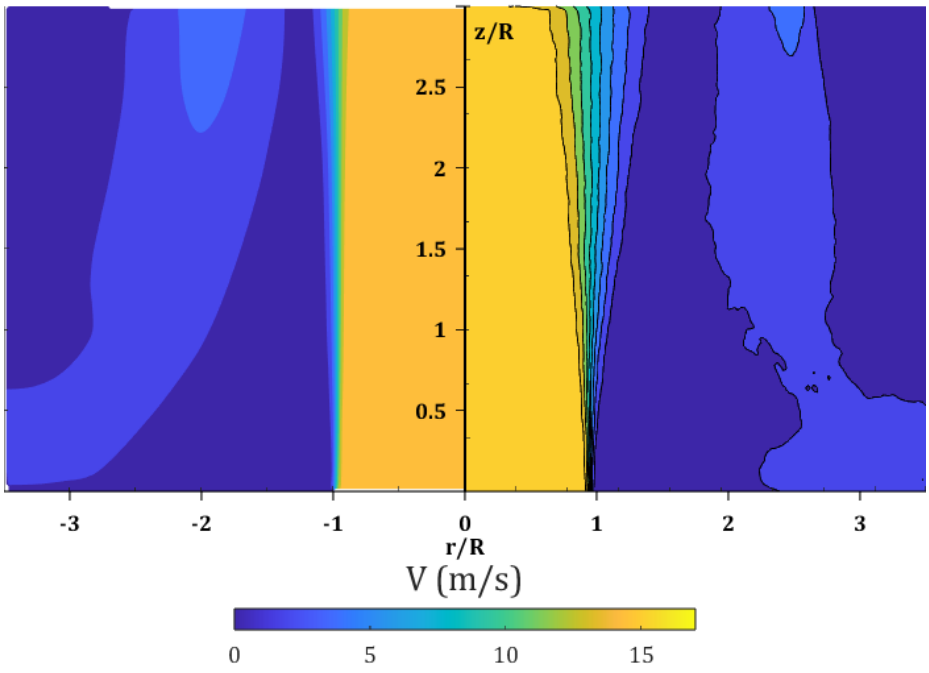

Figure 9.8: TR = 0.59 comparison of velocity contours in the gap for Re = 17,000.

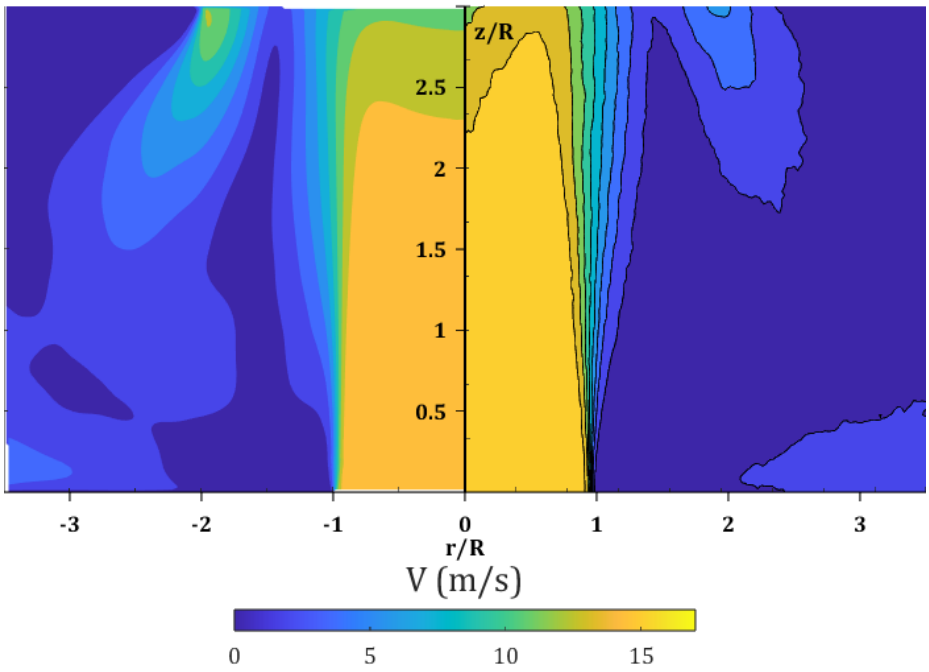

Figure 9.9: TR = 0.27 comparison of velocity contours in the gap for Re = 17,000.

We can further analyze the flow fields by examining the velocity profiles at downstream locations z/R = 0.1, 1.0, 2.0, and 2.9 as functions of r/R. The profiles for TR = 1.00, 0.59, and 0.27 are given in Figure 9.10, Figure 9.11, and Figure 9.12, respectively.

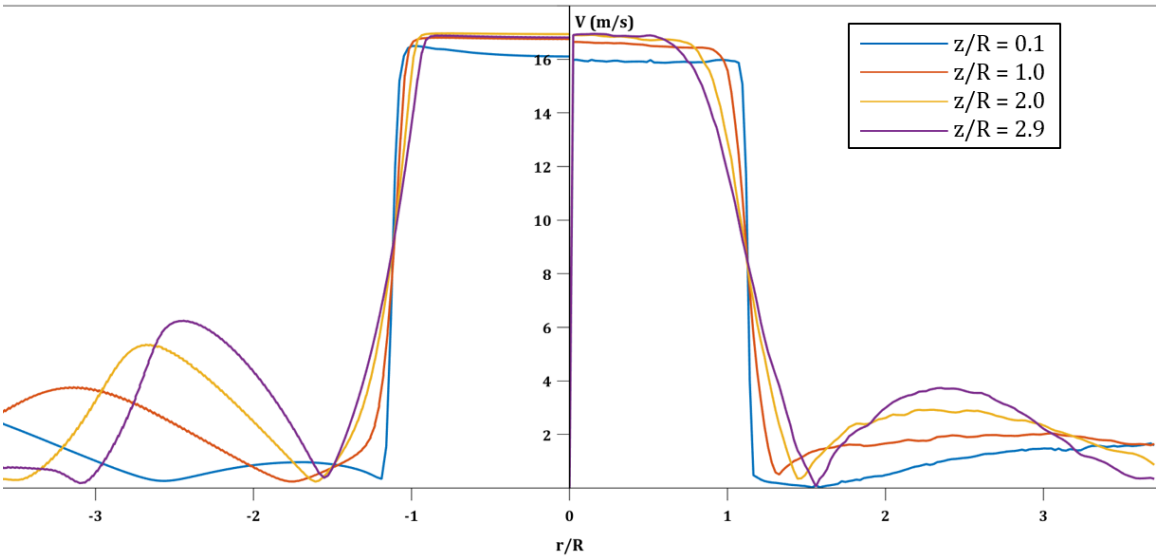

Figure 9.10: TR = 1.00 comparison of velocity profiles for r/R = 0, 1, 2. and 2.9. Numerical results are on the left, and experimental results are on the right.

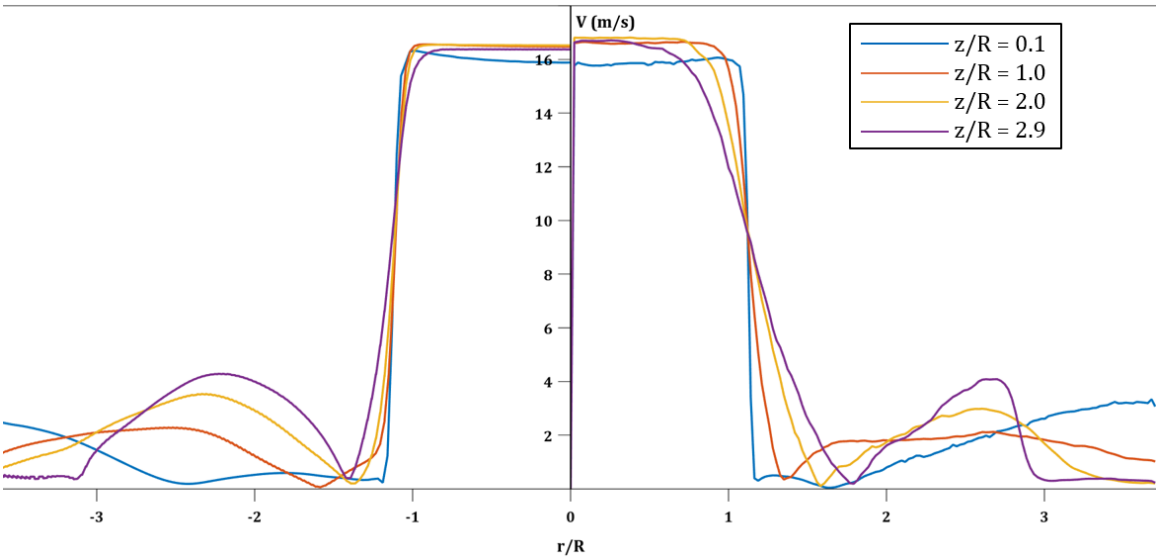

Figure 9.11: TR = 0.59 comparison of velocity profiles for r/R = 0, 1, 2. and 2.9. Numerical results are on the left, and experimental results are on the right.

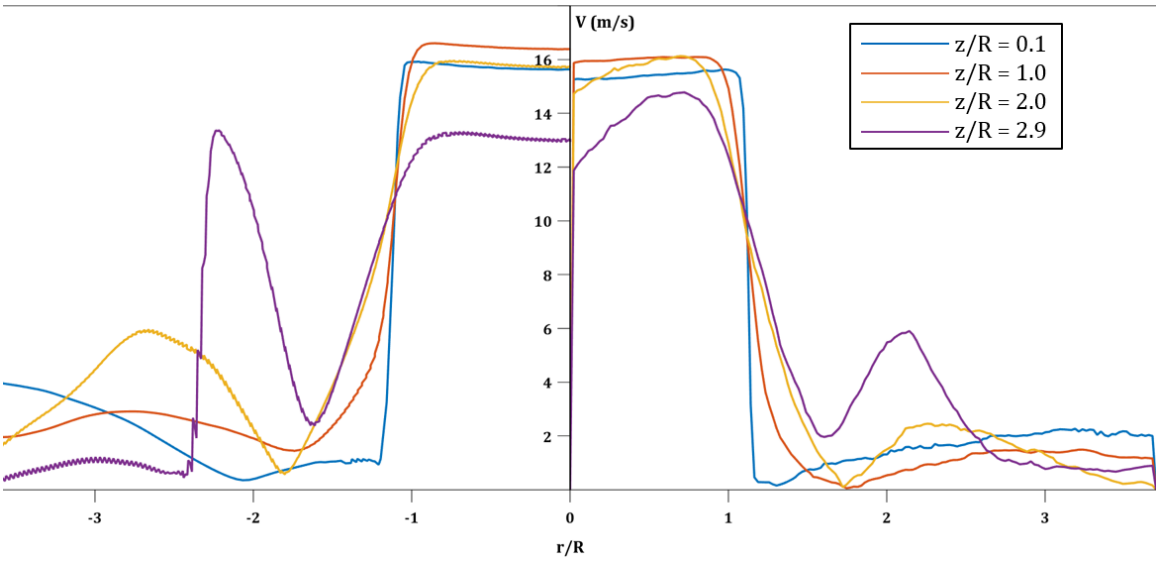

Figure 9.12: TR = 0.27 comparison of velocity profiles for r/R = 0, 1, 2. and 2.9. Numerical results are on the left, and experimental results are on the right.

The velocity profiles for TR = 1.00 show good agreement as they are similar in shape. A difference between the results, however, is that the simulations predict larger velocity wall jets seen in $\mathrm{r}/\mathrm{R} < 1.5$. This result is seen throughout all of the simulation results. Another common discrepancy is that the simulations underpredict the broadening of the shear layer, as evidenced by the profiles having a sharper transition as the velocity decreases from the

maximum near $|\mathrm{r}/\mathrm{R}| = 1$. The velocity profiles for TR = 0.59 are very similar to TR = 0.27, again with small differences in the shear layer broadening and slight overpredictions in the reverse flow magnitudes. The simulations for TR = 0.27 accurately predict the decrease in centerline velocity, but the M-shaped velocity profile is not as dramatic as it is in the PIV results. Also, as mentioned earlier, the wall jet velocity is significantly larger in the simulations than in the experiments, as the velocity magnitude at the edge of the trap is 14 m/s compared to only 6 m/s from the experiments.

The axial centerline velocity for the simulated TR = 1.00 impactor is shown in Figure 9.13. The numerical solutions are in black, and the experimental results are in red, with error bars generated using the largest error in the PIV vector field. As mentioned previously, we initially attempted to match the Reynolds numbers for the simulations and experiments, but the shape of the velocity profile at the outlet affected the average velocity and subsequently the Reynolds number. The length of the nozzle is not large enough to create a fully-developed pipe flow, and the velocity profile will have a broader shape, as seen in Figure 9.10. We instead matched the outlet centerline velocities. Figure 9.13 shows that the numerical and experimental centerline velocities overlap at each location in the gap, which gives credence to the accuracy of the numerical solution with the experimental data. The centerline velocities for TR = 0.59 and 0.27 are shown in Figure 9.14 and Figure 9.15, respectively, do not agree as well with the PIV data, but are still similar in shape. TR = 0.59 is within the uncertainty bounds for z/R < 1.5, but begins to decrease downstream, whereas the centerline velocity from the PIV continues to increase. Overall, however, the profiles and magnitudes are similar and demonstrate good agreement. The centerline velocity for TR = 0.27 is consistently greater than the PIV data suggests. However, the shape is similar as the deceleration as the jet nears the trap is similar to the experimental data.

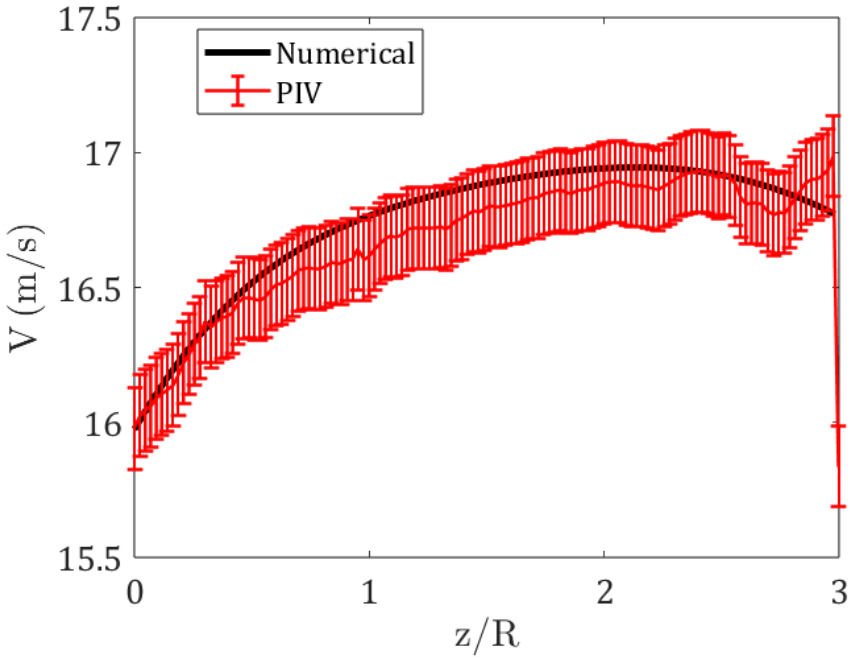

Figure 9.13: Comparison of centerline velocities inside the impactor gap for TR = 1.00.

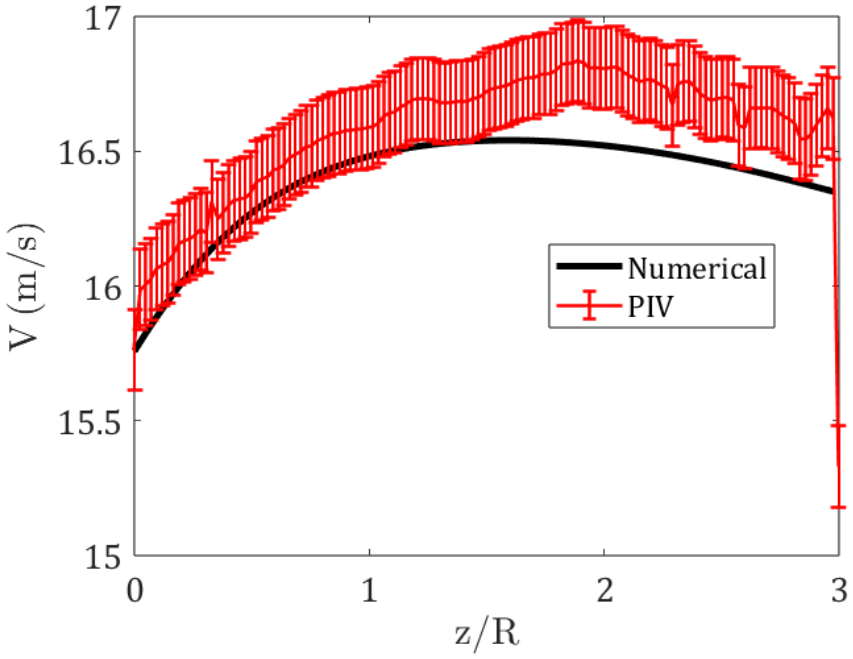

Figure 9.14: Comparison of centerline velocities in the gap of the TR = 0.59 impactor.

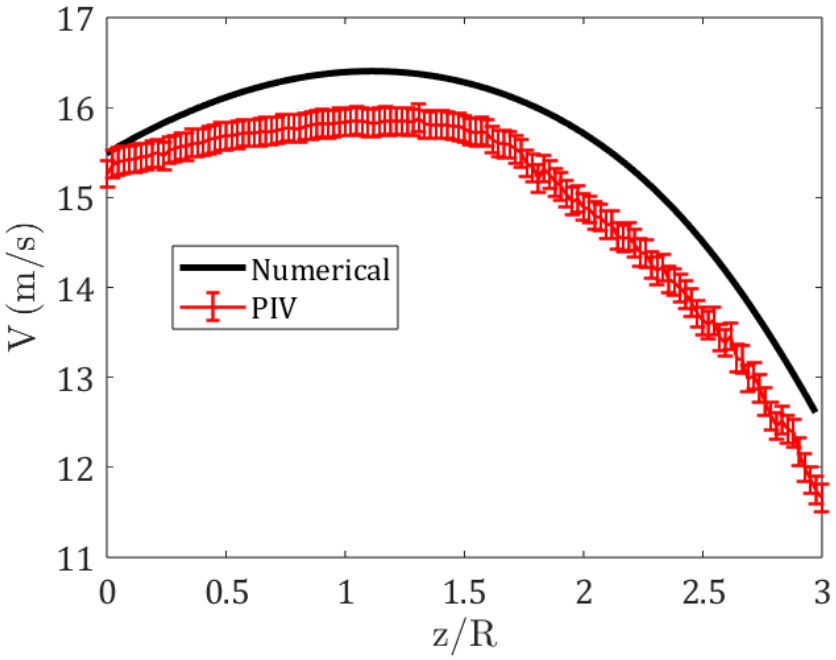

Figure 9.15: Centerline velocities for the DES and PIV results inside the gap for TR = 0.27.

9.5.2 Turbulent Kinetic Energy

Next, we analyzed the time-averaged TKE fields shown in Figure 9.16, Figure 9.17, and Figure 9.18. TR = 1.00 has fairly good agreement as the contour plots are similar. Two differences in the TKE contours are that the PIV results demonstrate higher TKE along the shear layer and less along the back of the nozzle due to the impinging reverse flow.

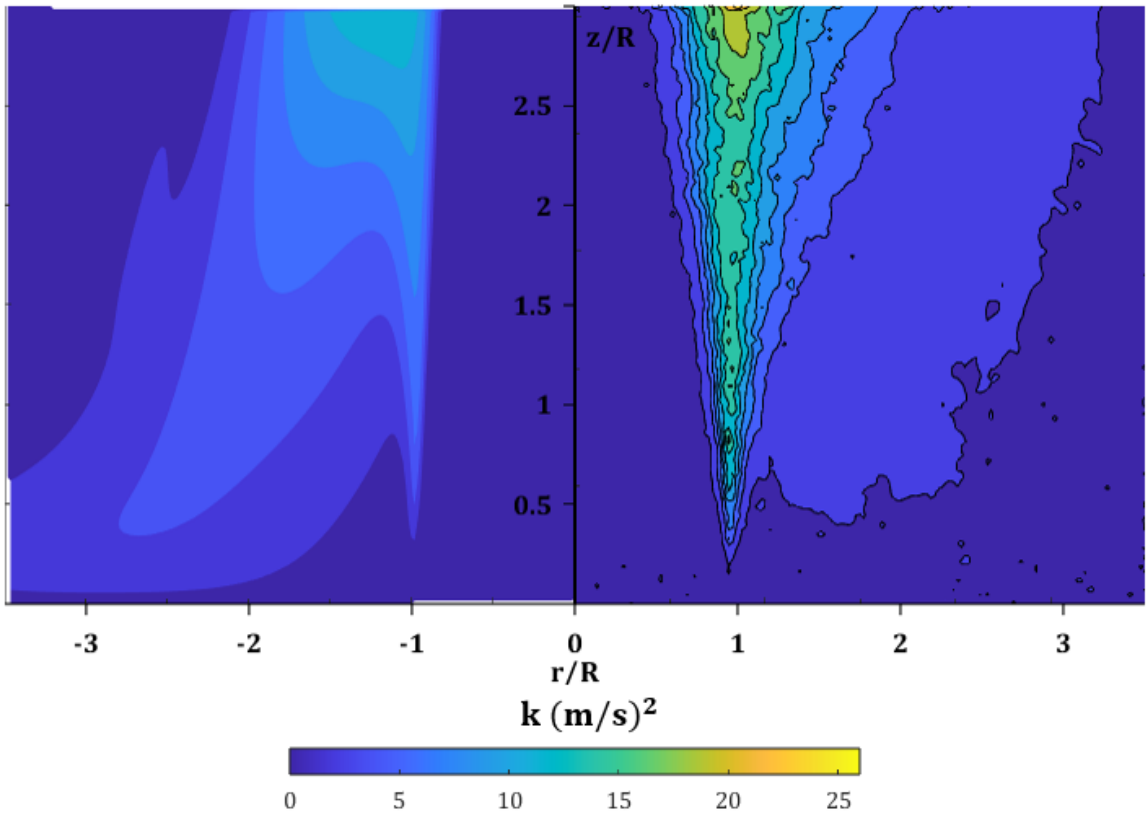

Figure 9.16: TKE contour comparison for the TR = 1.00 impactor. Numerical results are on the left and PIV on the right.

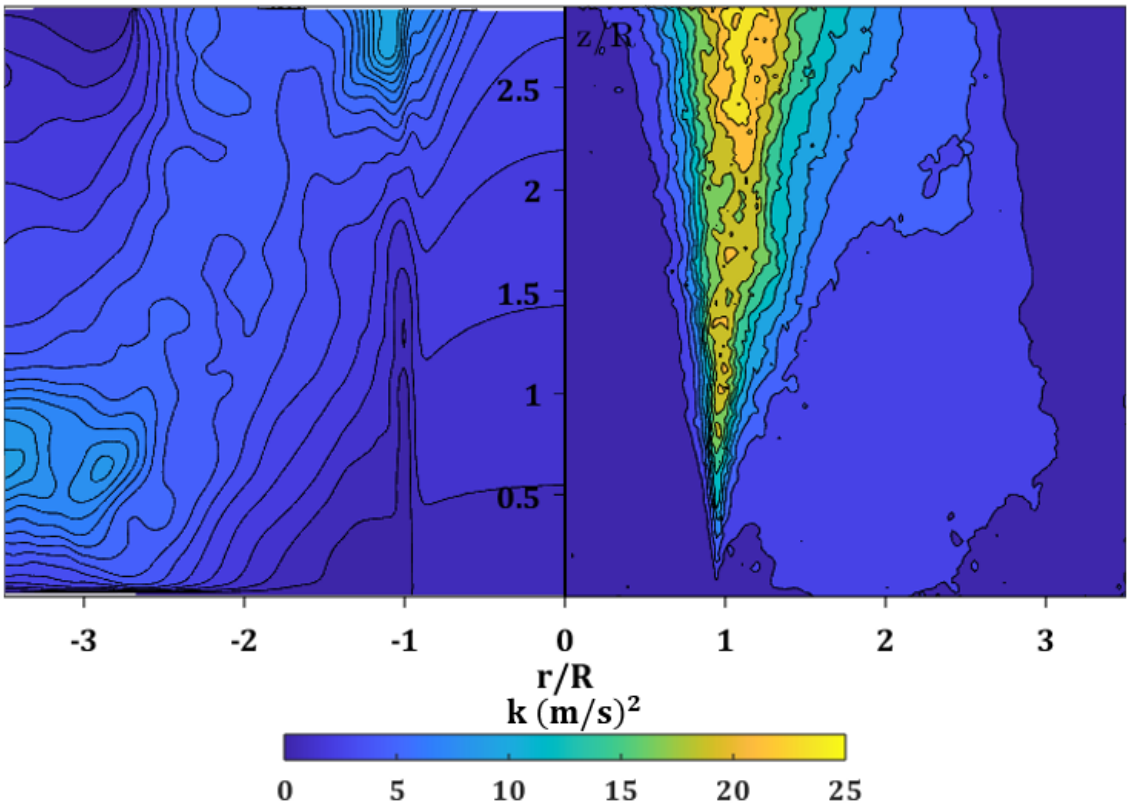

Figure 9.17: TKE contour comparison for the TR = 0.59 impactor. Numerical results are on the left and PIV on the right.

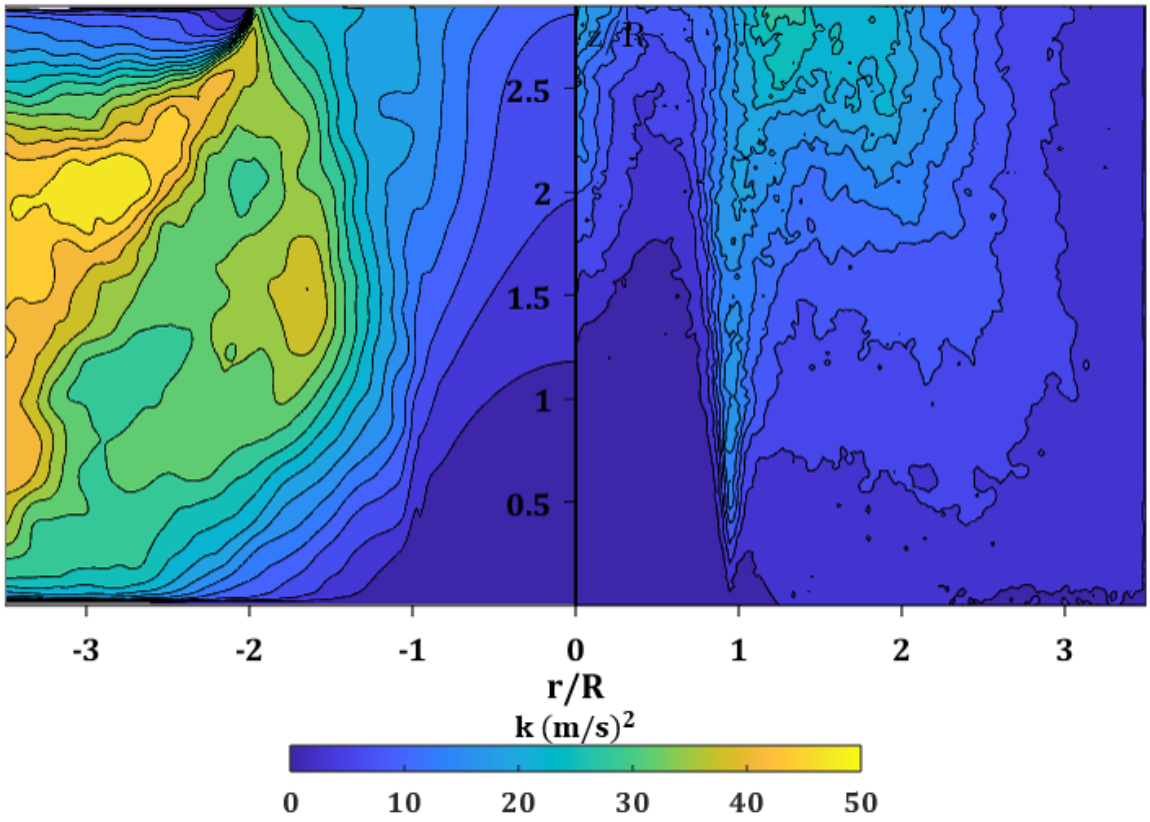

Figure 9.18: TKE contour comparison for the TR = 0.27 impactor. Numerical results are on the left and PIV on the right.

Unlike the k-ω model used for TR = 1.00, the DES model does not calculate the time-averaged turbulent kinetic energy. To calculate the time-averaged TKE, the Reynolds decomposition was used and calculated similarly to the PIV for each time instance and location in the flow. The TKE contours for TR = 0.59 are not in as good agreement with the PIV results as for TR = 1.00. Similar to TR = 1.00, the simulations underpredict the TKE along the shear layer. Also, the PIV results show very little TKE or changes inside the jet, yet the simulations predict slight increases downstream of the nozzle. These slight increases in TKE can be seen in the line plots below in Figure 9.20 along r/R = 0. The TKE only increases from $\approx 1 - 4\,(\mathrm{m/s})^2$, but it is nearly 4 times larger than the TKE along the centerline from the PIV. The line plots also reveal strange behavior in the simulated TKE. There is a decrease in fluctuations at r/R = -1 for z/R = 0.1 and 1.0, whereas the TKE has a relative maximum along the shear layer in the PIV and also in the simulations at z/R = 2.0

and 2.9. Overall, the turbulent kinetic energy for TR = 0.59 predicted by the simulations does not fare well with the experimental data.

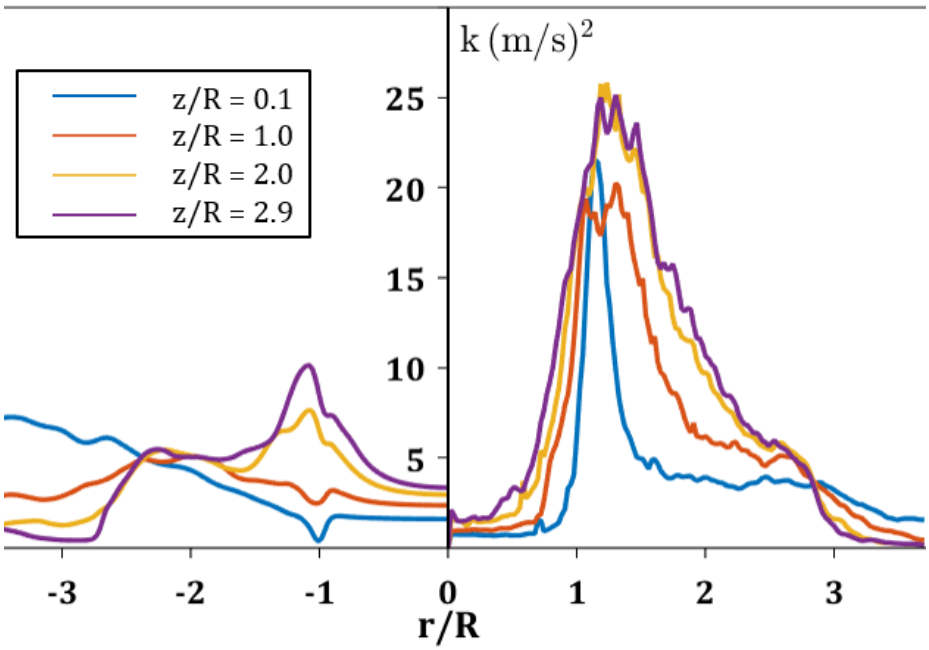

Figure 9.19: TKE line profiles at different downstream locations for TR = 0.59. Numerical results are on the left and PIV on the right.

The TR = 0.27 TKE contours comparison is shown in Figure 9.18, and unlike the contours for the previous impactors, the simulations predict much larger TKE than the PIV. The contours of the time-averaged flow fields revealed differences in the velocity magnitudes near the trap. These differences are further emphasized when examining the turbulent kinetic energy, as the predictions are far greater than the experimental results. The TKE is maximized in the region of the gap where the wall jet exits the trap. This region of high TKE is shown in the contour plots for r/R $<$ -2. The combination of the larger TKE and higher velocity magnitude at the edge of the trap shown in Figure 9.9 highlights that simulations are expecting larger velocity fluctuations and contributions from the wall jets for this design. Although the TKE is larger in the gap for this design, the simulations underpredict the velocity fluctuations in the jet core. This is demonstrated by the TKE line profiles at z/R = 0.1, 1, 2.0, and 2.9 shown in Figure 9.20. Along r/R = 0, the numerical result on the left

is similar to the PIV at z/R = 0.1, but the TKE does not increase as much downstream as is expected. Velocity fluctuations are still present in the core, and as the TKE increases from r/R = 0 to 1.0, the values are similar along the shear layer. From analyzing the TKE results, it is clear that the simulations bias the velocity fluctuations at the edge of the trap. The PIV demonstrated that the TKE along the centerline was similar in magnitude to that at the trap edge. However, the simulations have much higher TKE near the trap and in the gap compared to inside the jet, and at magnitudes exceeding the PIV results. The differences in the turbulent kinetic energy fields, therefore, require further efforts to improve their accuracy.

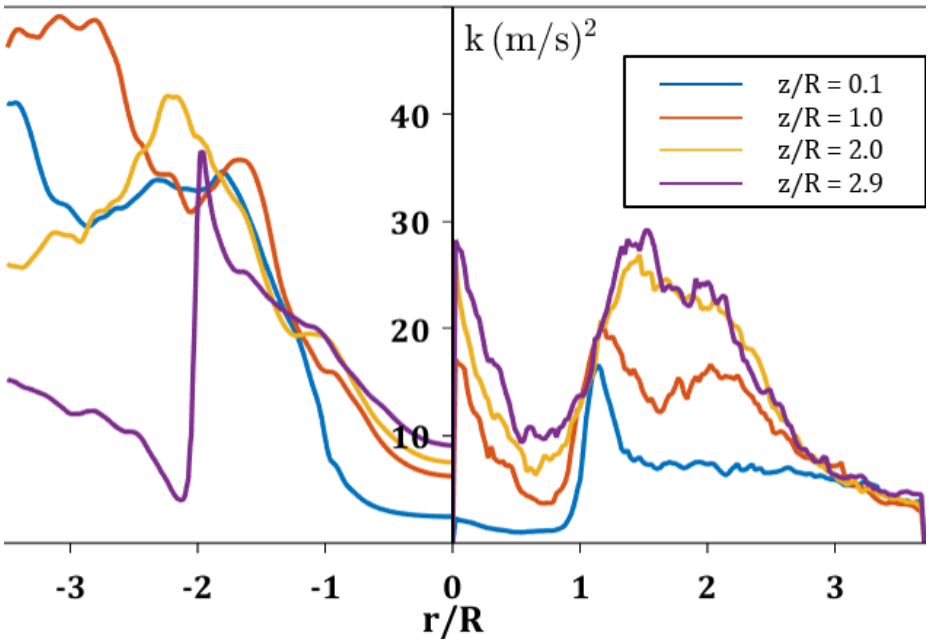

Figure 9.20: TKE line profiles at different downstream locations for TR = 0.27. Numerical results are on the left and PIV on the right.

9.5.3 Velocity Time Traces

We can also plot the time traces of the flow field at different points in the flow as we did with the hotwire anemometer. The time traces at the downstream position of z/R = 2.7 at the centerline and the edge of the trap (positions 1 and 3 in Figure 8.32) are shown in Figure 9.21 and Figure 9.22.

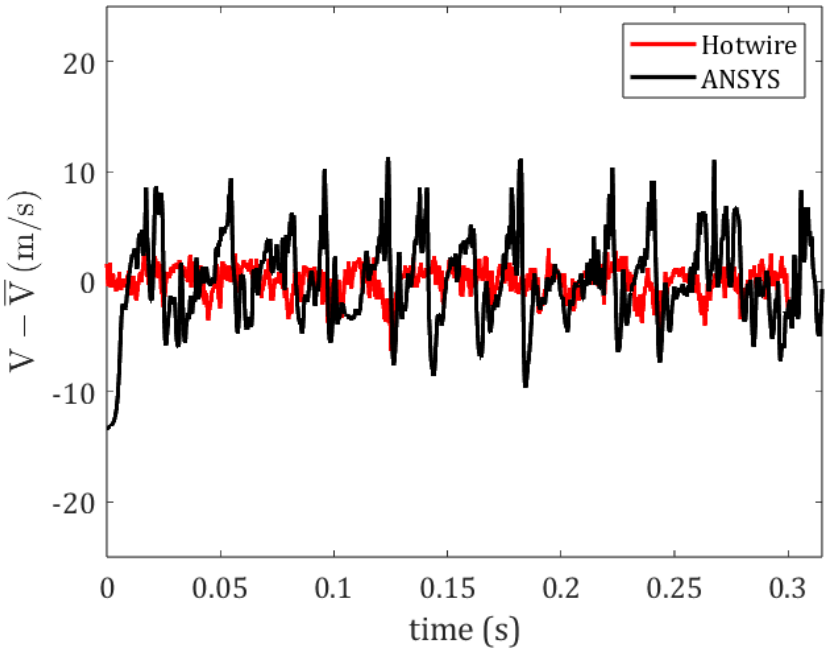

Figure 9.21: Velocity time trace from DES along impactor centerline at the downstream location z/R = 2.7.

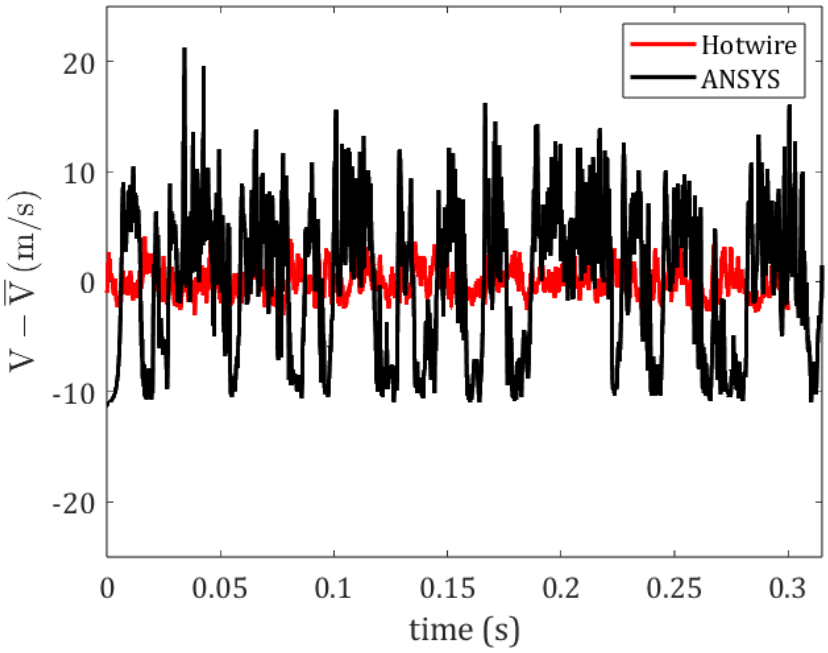

Figure 9.22: Velocity time trace from DES at the edge of the trap at the downstream location z/R = 2.7.

The sample time for the numerical time trace is only between 0 and 0.3s due to the 5×10^{-6} timestep used in the simulations. We recorded the data from ANSYS every 20 timesteps for an effective sampling rate of 10 kHz. In the time trace comparisons, again, the numerical solutions overpredict the magnitude of the velocity fluctuations compared to the experimental results. However, we can still analyze the periodic behaviors in the flow by comparing the power spectral densities as shown in Figure 9.23 and Figure 9.24 for the centerline and the edge of the trap, respectively. The frequency resolutions for the hotwire and simulation PSDs were 0.7 and 6.4 Hz, respectively, as the hotwire results had a much larger sample size.

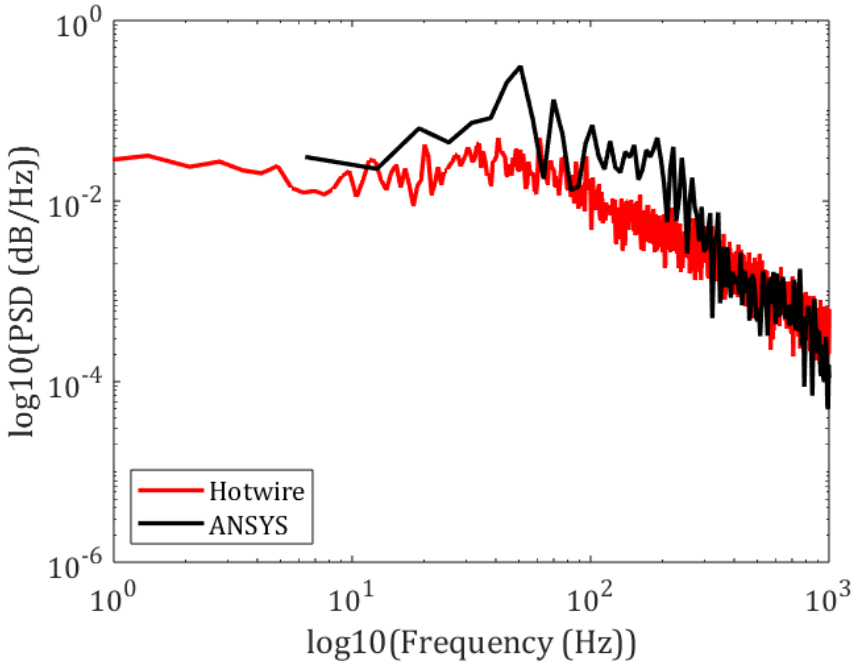

Figure 9.23: Comparison of the power spectral density predicted by the simulations and recorded by the hotwire anemometer along the impactor centerline at z/R = 2.7.

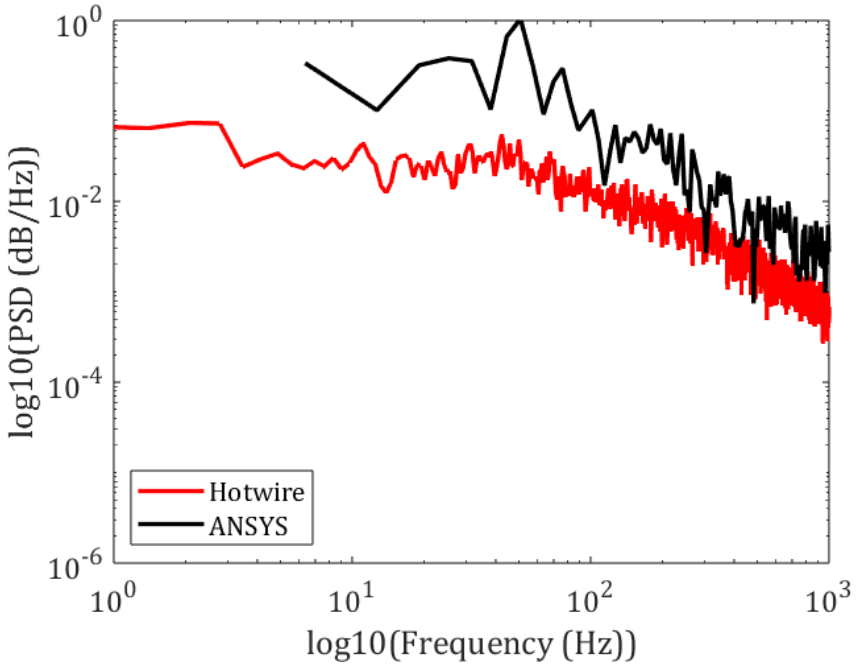

Figure 9.24: Comparison of the power spectral density predicted by the simulations and recorded by the hotwire anemometer at the edge of the trap at the downstream location z/R = 2.7.

In section 8.3, we stated that the power spectral density plots revealed slight peaks around 20, 40, and 60 Hz along the jet centerline and the edge of the trap, but needed to be treated with caution due to the low signal-to-noise ratio. However, the ANSYS simulations also reveal peaks in the PSD at 51 Hz, and smaller secondary peaks at 70 and 76 Hz for the centerline and trap edge, respectively. The magnitudes of the simulation PSDs are larger due to the larger amplitudes in the fluctuations, but the presence of the peaks in the spectrum coinciding with the hotwire provides further evidence that the wall jet may have a pulsatile behavior around 50 Hz.

9.5.4 TR = 0.27 Model Tuning

To improve the agreement between the simulated and experimental results, the inlet turbulent viscosity ratio, β was parametrized for the TR = 0.27 impactor. Turbulent viscosity ratios of 0.001, 0.01 (shown previously), 0.1, and 0.2 were used because we wanted to

improve the shear layer agreement between the simulations and experiments. The simulations and experiments had large disagreements in the velocity magnitude of the wall jets at the edges of the trap. We hypothesized that the wall jet magnitude could be reduced if the jet entering the trap resembled the experimental jet and set out to improve the jet shear layer thickness. The shear layer thickness, δ, was defined as the radial location where the jet velocity was 20% of the maximum flow field velocity. The jet shear layer thicknesses are normalized by the nozzle out radius, R, and are shown in Figure 9.25. The shear layer thickness most resembled the experiments for β = 0.01, where the thicknesses are equal at z/R $\approx$ 1.3. However, for z/R $>$ 1.6, the experimental shear layer continues to increase downstream, whereas the simulations predict a constant thickness. Increasing β to 0.1 and 0.2 did not improve the shear layer thickness agreement as anticipated, as the shear layers deviated more for these viscosity ratios compared to β = 0.01. Reducing the viscosity ratio to 0.001 had better agreement for $1 \leq z/R \leq 1.4$, as the simulated and experimental results overlapped. However, the numerical shear layer reached a constant value of 1.12 at z/R = 1.4 and began to deviate from the experimental results. An interesting result was that although the numerical and experimental nozzle outlet velocity profiles are similar, as shown in Figure 9.12, the predicted initial normalized shear layer thickness is 0.89, whereas the experimental results demonstrate a normalized thickness of 0.96. The initial numerical shear layer thicknesses do not change with increasing inlet turbulent viscosity ratio.

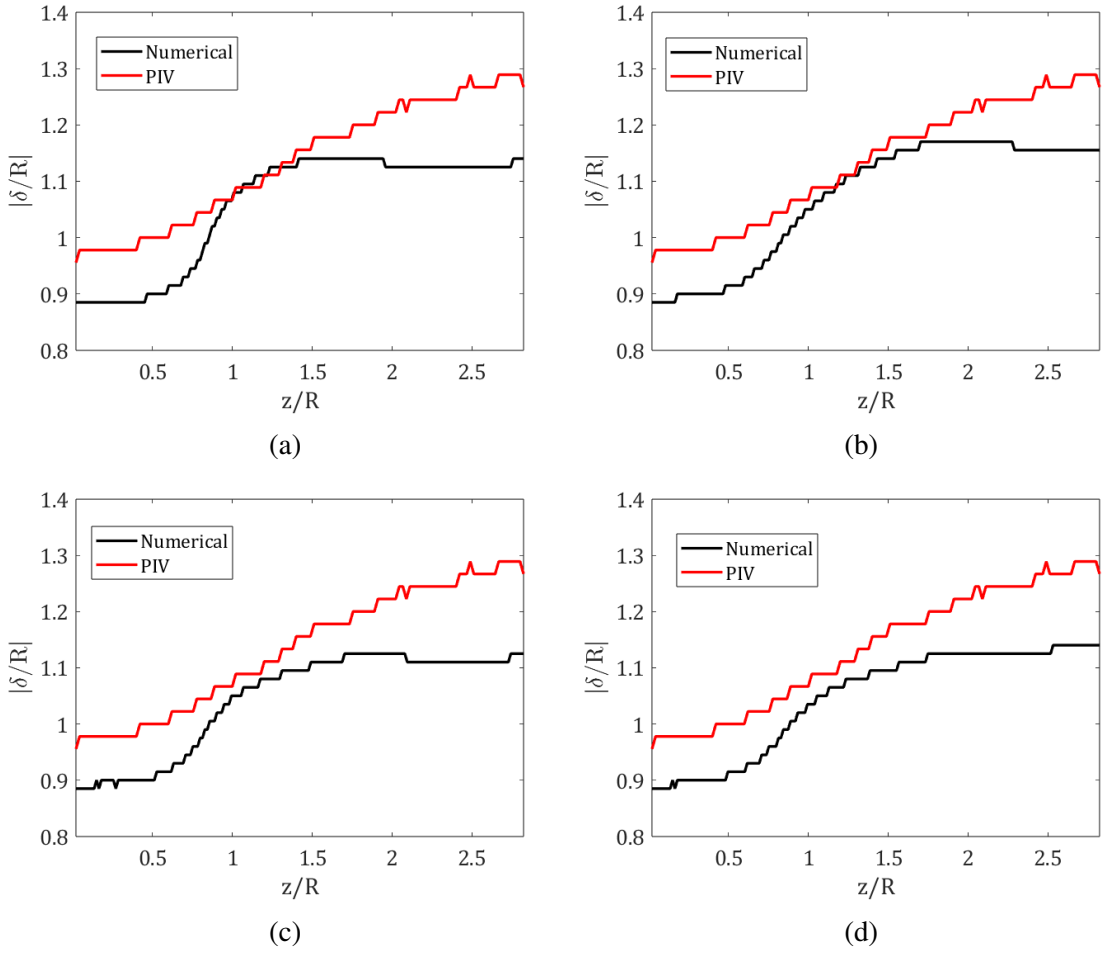

Figure 9.25: Normalized layer thicknesses for TR = 0.27 with turbulent viscosity ratios of a) 0.001, b) 0.01, b) 0.1, c) 0.2.

Centerline velocities for the varying β values are also shown in Figure 9.26. β = 0.001 improves upon the centerline velocity as it is nearer to the PIV results for all z/R. Increasing β also improved the centerline velocity agreement, albeit less than β = 0.001. However, as the PIV centerline velocity begins to decrease near z/R = 1.5, β = 0.1 and 0.2 start to deviate, and our original model,β = 0.01, tends closer towards the experimental values. At the edge of the gap (z/R = 3), β = 0.1 has the lowest centerline velocity of 12.7 m/s. These results highlighted that although β = 0.001 did not drastically improve the shear layer thickness, it did improve the centerline velocity profile. Increasing the turbulent viscosity ratio improved the centerline comparison near the nozzle, but deviated near the trap.

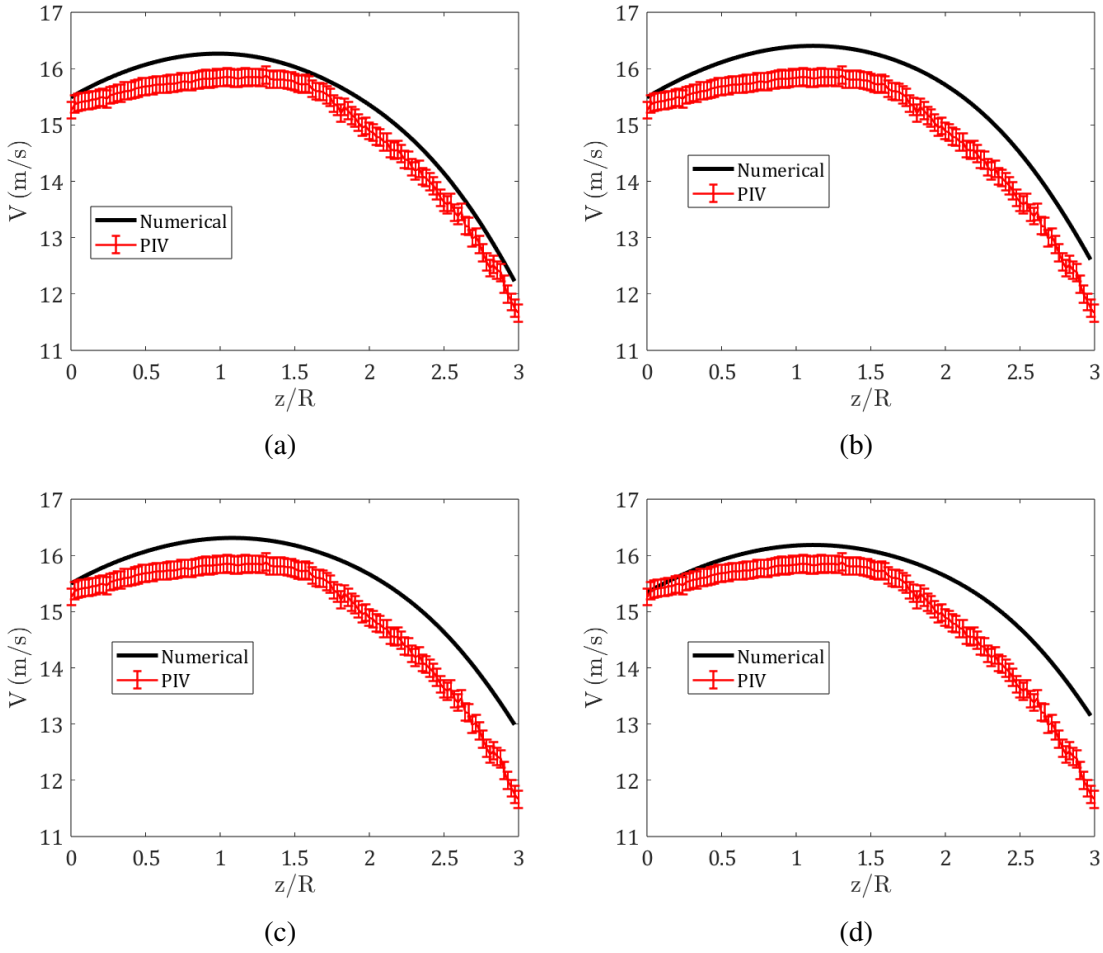

Figure 9.26: Centerline velocities for TR = 0.27 with turbulent viscosity ratios of a) 0.001, b) 0.01, c) 0.1, d) 0.2.

The time-averaged flow fields for the various viscosity ratios are shown below in Figure 9.27. The mismatch in the wall jet velocities is still seen in the simulations, even for the turbulent viscosity ratio 0.001 case, which was an improvement upon the original viscosity ratio of 0.01.

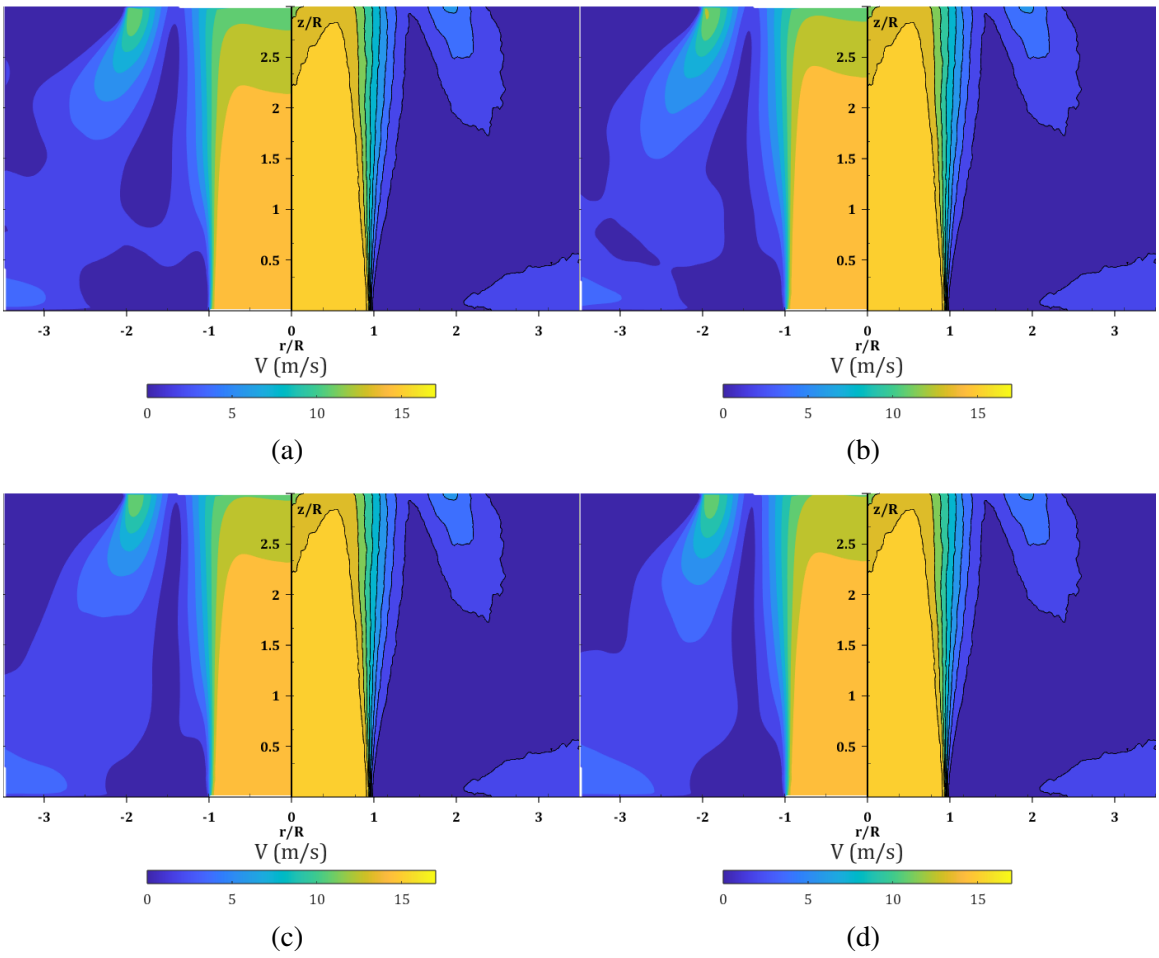

Figure 9.27: Time-averaged flow fields for TR = 0.27 with turbulent viscosity ratios of a) 0.001, b) 0.01, c) 0.1, d) 0.2.

Ultimately, altering the turbulent viscosity ratio did not have an impactful effect on the impactor flow fields. The main deviation between the simulations and the experiments is that the predicted wall jet velocity is far greater than the experimental results, and altering the turbulent viscosity ratio did little to decrease the wall jet velocity. The simulations tend to diverge from the experimental results as the jets approach the trap. The model could be improved by increasing the dissipation in the trap to reduce the wall jet velocity. Ultimately, future work to improve the agreement between the simulations and the experiments would be to first match the velocity profile at the outlet, and then tune the model parameters. Although the numerical models need to be refined, the numerical results still have good

agreement with the experiments and can be analyzed.

9.6 Numerical Results

The simulated time-averaged flow fields for the TR = 1.00, 0.59, and 0.27 impactors are given in Figure 9.28, Figure 9.29, and Figure 9.30, respectively. The flow fields in the nozzles are similar for all impactors as the flow accelerates due to the reduced cross-sectional area. A boundary layer develops along the nozzle walls, but the nozzle is not long enough for the flow to become fully developed. As the flow exits the nozzle, it is nearly a uniform velocity, except for the existence of the thin shear layer near the nozzle walls.

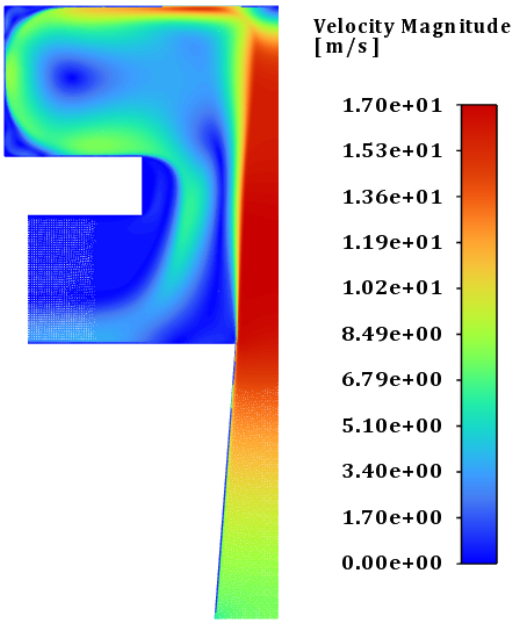

Figure 9.28: Flow field for the TR = 1.00 impactor with an inlet pressure of 185 Pa using the steady k-ω model.

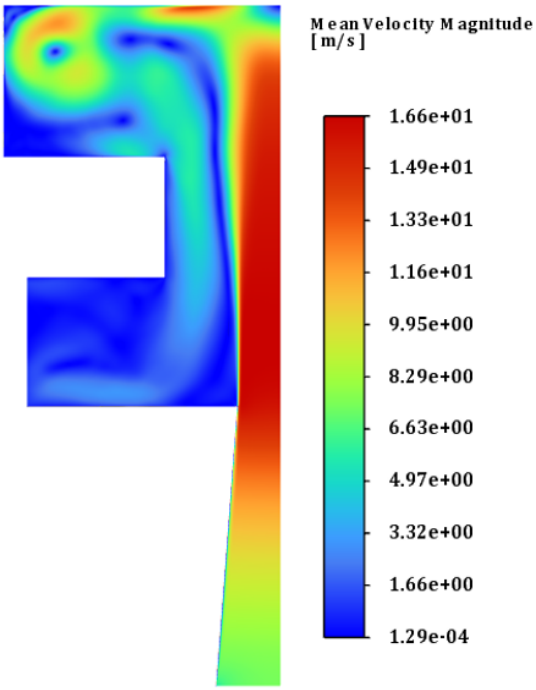

Figure 9.29: Time-averaged flow field for TR = 0.59 impactor with an inlet pressure of 180 Pa using the DES model.

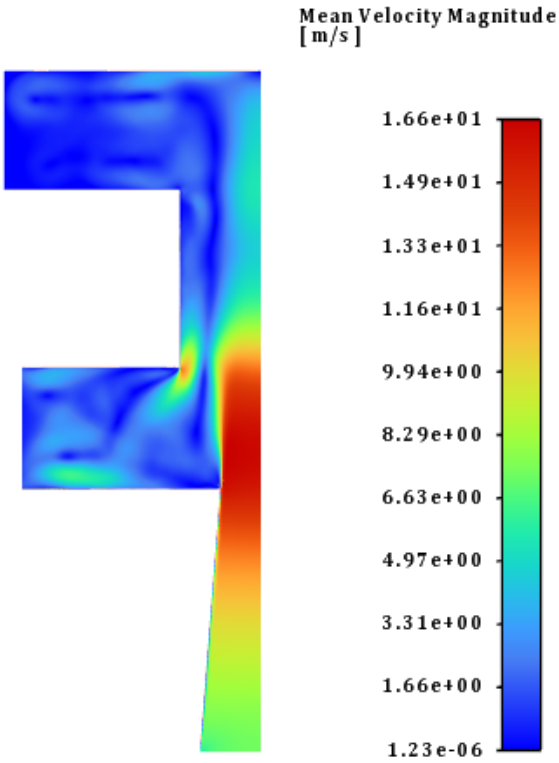

Figure 9.30: Time-averaged flow field for TR = 0.27 impactor with an inlet pressure of 234 Pa using the DES model.

After exiting the nozzle, the flow fields for TR = 1.00 and 0.59 are very similar as the jets enter the trap and begin to decelerate near the impingement zone. TR = 0.27 is markedly different, however, as the flow decelerates much earlier, and the velocity contours show a heavily reduced velocity inside the trap. TR = 0.27 also had a much faster wall jet compared to the other geometries at the edge of the trap. The flow inside the TR = 1.00 trap is clean as it is attached to the trap walls, although it separates from the wall before exiting and does not reattach to the surface. TR = 0.59 exits cleanly as well, but has a recirculation zone that is unseen in the other geometries.

Streamlines beginning at the nozzle inlet were generated for the three designs to show the paths the injected particles may follow as they move through the impactor. The streamlines for TR = 1.00 are for the time-averaged flow field and are shown in Figure 9.31. For TR = 0.59 and 0.27, the streamlines are generated for the flow field at t = 0.3s. The average

streamlines for the DES results may not be representative of the true time-dependent flow field, as the time-varying structures may be masked. TR = 1.00 shows that the streamlines are not greatly affected by the trap. The streamlines resemble impinging flow as the jet impacts the back of the trap. Then, as the flow spreads along the surfaces of the trap, it is attached to the walls as it reverses direction and begins to exit. As the flow exits the trap, it separates from the wall, as was seen in the velocity contour. As the flow separates from the wall, it approaches the incoming jet, but does not make contact. Curiously, the incoming jet appears to slightly expand in this region, as the streamlines move in the positive radial direction, before contracting further downstream. This result is interesting as particles in this region could potentially alter their trajectories, which was one of our proposed mechanisms for decreased trap efficiency. However, due to the trap efficiency agreeing well with the predicted efficiency for TR = 1.00, it is unlikely that this slight expansion has a large effect on trajectories and efficiency. This result also highlights that the large trap opening for TR = 1.00 allows the incoming jet to maintain its shape as the wall jet can exit the trap without mixing with the incoming flow.

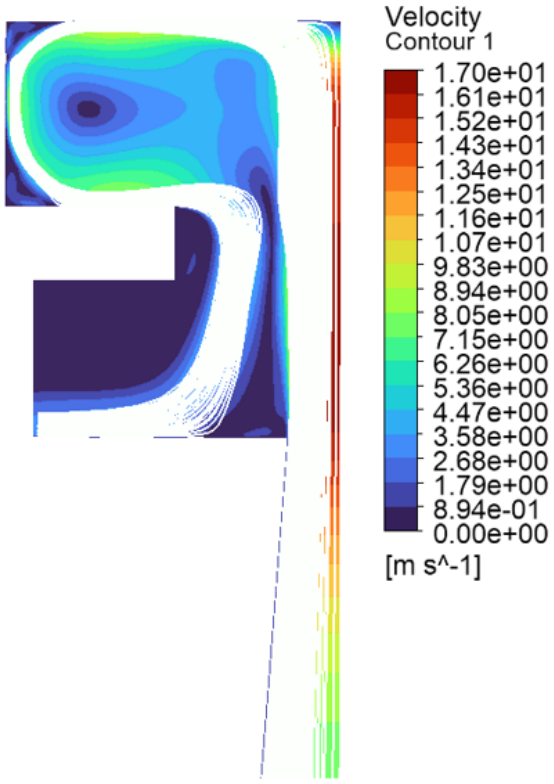

Figure 9.31: Numerical streamlines beginning at the nozzle inlet for TR = 1.00 and Re = 17,000.

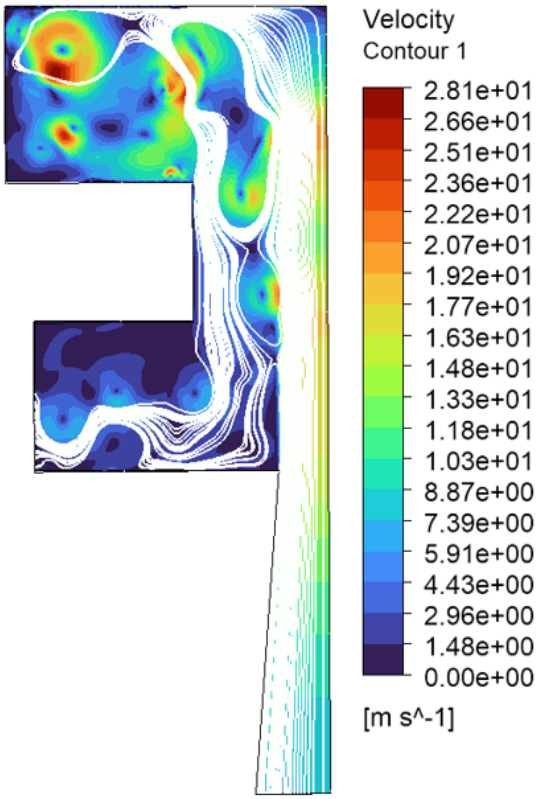

Figure 9.32: Instantaneous streamlines for t = 0.3s from TR = 0.59 DES results.

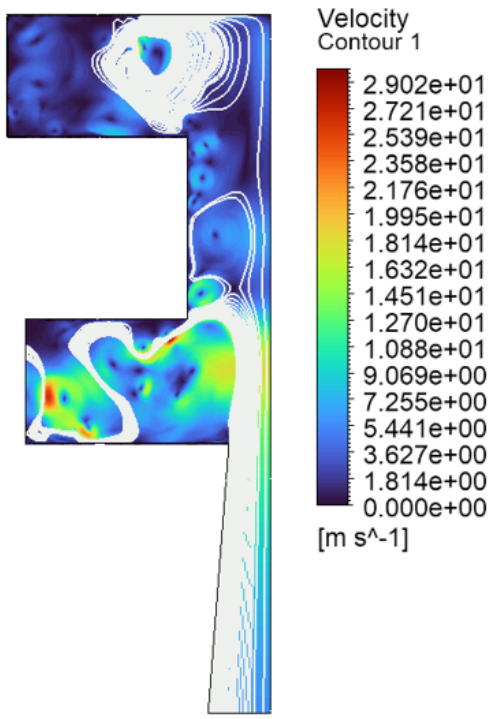

Figure 9.33: Instantaneous streamlines for t = 0.3s from TR = 0.27 DES results.

The edge of the trap for TR = 1.00 is located at r/R = 3.2, whereas TR = 0.59 is at r/R = 2.7, and 2.0 for TR = 0.27. The effect of the reduced trap diameter is seen by the streamlines of the flow exiting the trap mixing with the incoming jet for TR = 0.59. Some of the streamlines near the edge of the jet are shown to mix with the exiting flow without reaching the back of the trap. Particles along the edge of the jet can then be induced to move out of the trap without depositing, and reduce the trap efficiency. Conversely, particles that are concentrated more towards the centerline of the jet are able to penetrate into the trap, but the flow in this region is not nearly as clean as TR = 1.00, due to the presence of the recirculation zone that could also affect the particles in the trap. TR = 0.59 had a reduced trap efficiency of $\approx 65\%$ for Re $\approx 17,000$, and this could be explained by potentially 35% of the particles being concentrated in regions that are forced out by the reverse flow and are unable to penetrate to the back of the trap.

This effect is even more pronounced in the TR = 0.27 streamlines, as many of the streamlines do not penetrate into the back of the trap. TR = 0.27 had the worst trap effi-

ciency at a mere 30%, and the streamlines corroborate the poor efficiency results. Compared to TR = 0.59, a much larger fraction of the streamlines, and therefore a larger fraction of particles, are removed from the trap before impacting. Another interesting result from the TR = 0.27 streamlines at t = 0.3s is that most of the streamlines do not enter the trap at all before being redirected, which was our second proposed mechanism of efficiency reduction. The combination of the two mechanisms present in the TR = 0.27 streamlines agrees well with this design, which has the worst trap efficiency. Interestingly, the streamlines that enter the back of the trap are caught in a recirculation zone at t = 0.3s. The time-averaged flow fields did not show recirculation zones, which highlights that they are a transient phenomenon.

To quantify which streamlines for TR = 0.27 could result in particles not impacting inside the trap, the downstream locations where the streamlines terminate were calculated at different time instances in MATLAB. Streamlines terminate when the local velocity is close to zero or when the streamlines are directed out of the domain. Streamlines at four different time instances are shown below in Figure 9.34. In this orientation, the flow moves from left to right, and 95 streamlines are initiated at the nozzle outlet between $-1 \leq \mathrm{r/R} \leq 0$ and at z/R = 0. 95 streamlines were used as this was the maximum number of streamlines that could be generated at the outlet. The red numbers seen in the figures are labels placed on the streamlines to identify them. In the left column of Figure 9.34, none of the streamlines penetrate into the wider portion of the trap before coming to rest and terminating, or exiting the simulation domain. This is potentially due to the wall jet creating a temporary stagnation region in the flow, as seen in the TR = 0.27 instantaneous velocity contours. The location where every streamline terminates is shown in Figure 9.35, where the grey horizontal line at z/R = 16 is considered deep enough into the trap where particles transported by the streamlines are captured. In the top right plot, only streamlines beginning near r/R = -1 and 0, respectively, do not reach the back of the trap. The missing values in Figure 9.35 are for streamlines that cross the centerline and are no longer in the simulation domain.

These instances are treated as penetrating deep enough into the trap to be captured. The bottom right contour in Figure 9.34, and the corresponding bottom right plot in Figure 9.35 demonstrate that streamlines emanating between r/R = 0 and -0.75 penetrate into the trap, whereas those starting further from the centerline are caught in the recirculation zone and are prevented from entering.

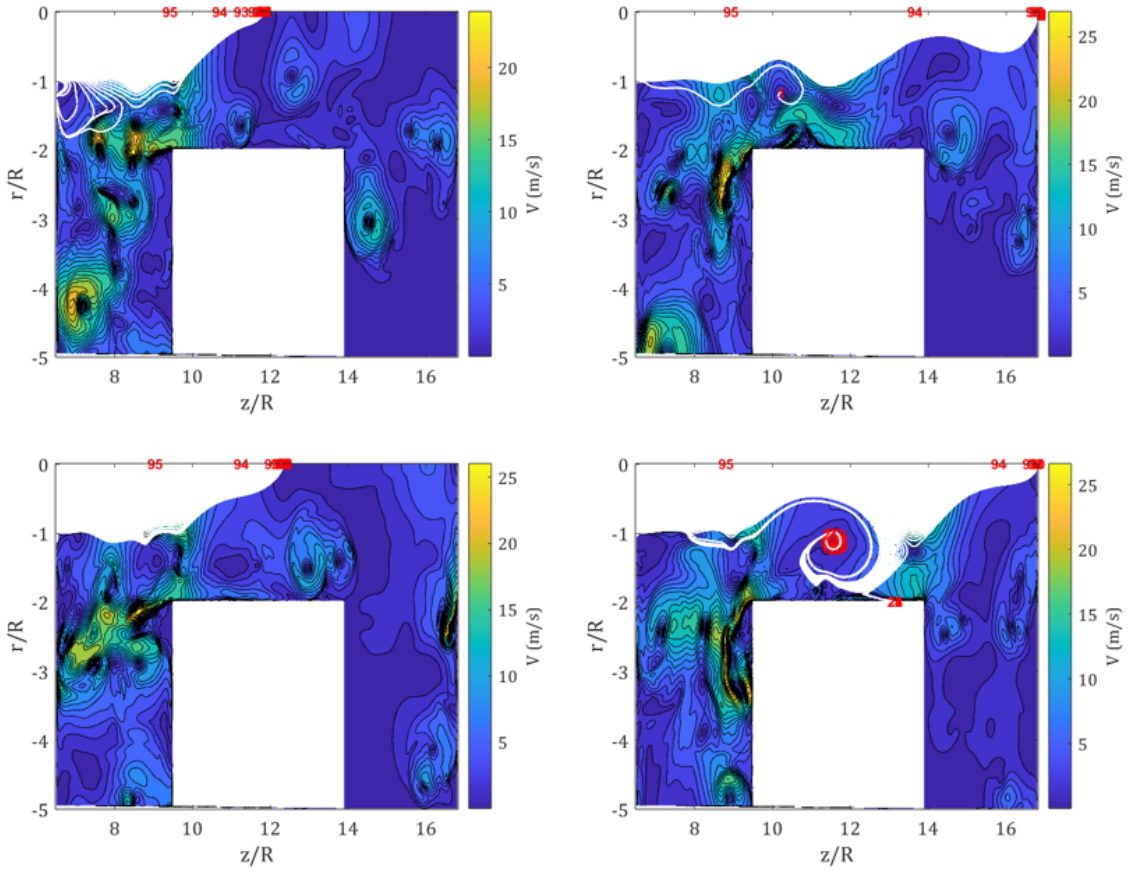

Figure 9.34: Streamlines for four different instances of the TR = 0.27 numerical flow field. The streamlines are initiated between $-1 \leq \mathrm{r/R} \leq 0$ and at z/R = 0. The flow moves from left to right.

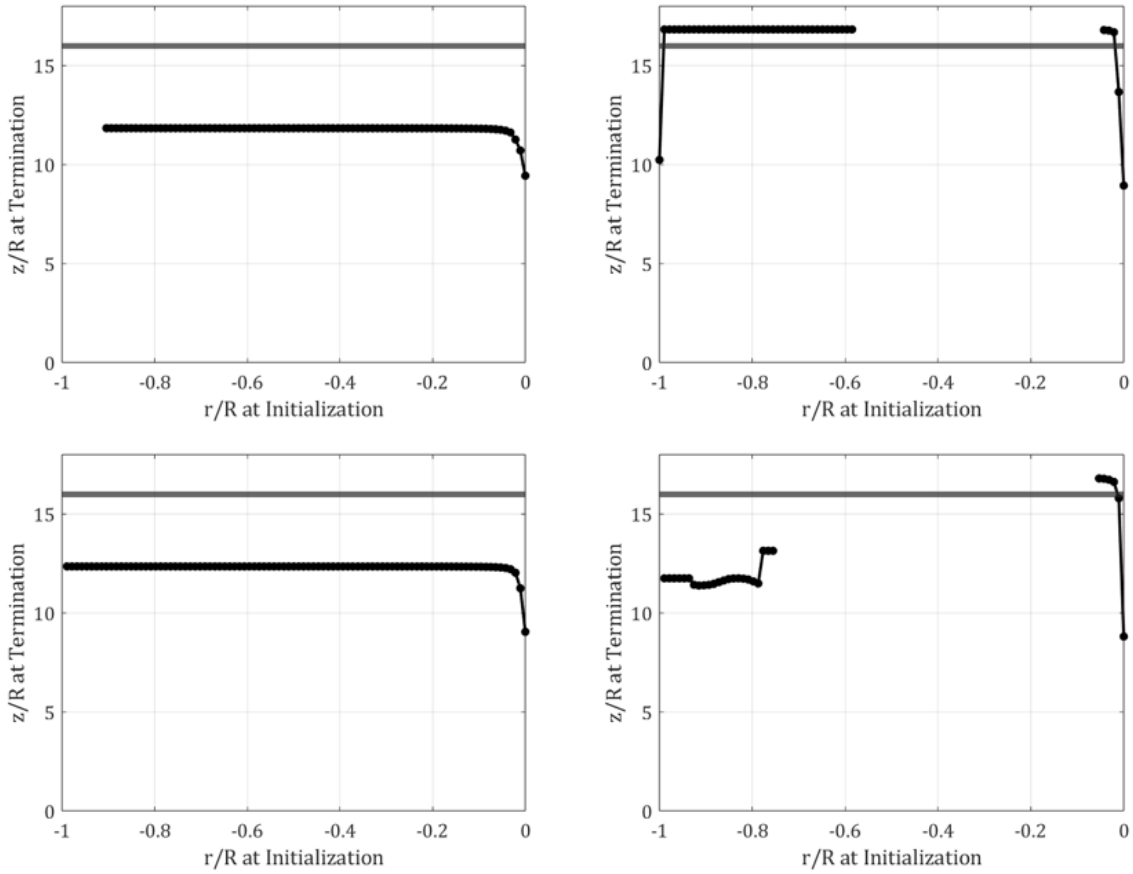

Figure 9.35: Locations of terminating streamlines for the streamlines shown in Figure 9.34.

To quantify the effects of the streamlines on trap efficiency, we calculated the percentage of the nozzle outlet area that has streamlines that penetrate into the back of the trap. Assuming the nozzle exit velocity profile is uniform, the percentage of the total flow rate through the nozzle that reaches the back of the trap is equal to the area ratio of the nozzle outlet containing penetrating streamlines. For example, if the location of the last streamline that penetrates into the back of the trap is r/R = 0.75, and all streamlines beginning at r/R $>$ 0.75 are terminated early, then the percentage of the nozzle area that has penetrating streamlines, and the resultant trap efficiency, is $0.75^2 = 0.5625$ as shown in Figure 9.36. Figure 9.36 represents a frontal view of the nozzle exit, and the green area indicates radial starting locations where particles are captured, and the red area indicates the starting locations where particles are not captured due to the streamline termination. If the nozzle

outlet flow is uniform and the particles are uniformly distributed, then the percentage of the nozzle area with penetrating streamlines represents the trap efficiency. The percentage of penetrating streamlines for various sample rates is shown in Figure 9.37. The transient simulations used a timestep of 5×10^{-6} s, and the sampling interval is then a multiple of the timestep. The sampling interval is used to increase or decrease the number of samples used to calculate the average penetration percentage. For intervals between 5×10^{-5} and 2.5×10^{-3} s, the penetration rate is between 40 and 43%. This trap efficiency is similar to the measured trap efficiency near 30% for TR = 0.27.

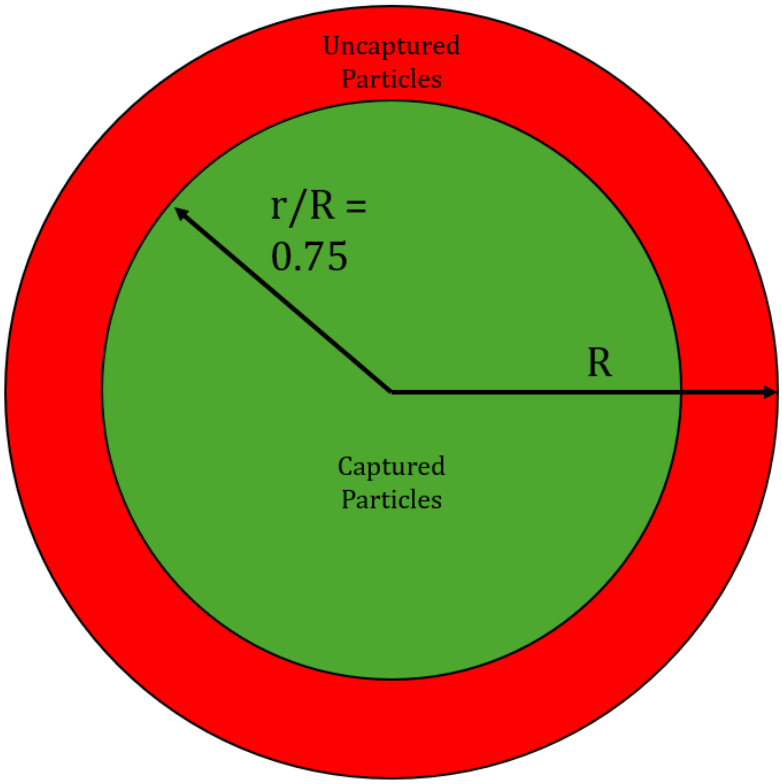

Figure 9.36: Schematic of radial locations where particles are captured due to streamline termination. The area in green indicates the radial starting location for captured particles, and the red area denotes the starting locations for missed particles.

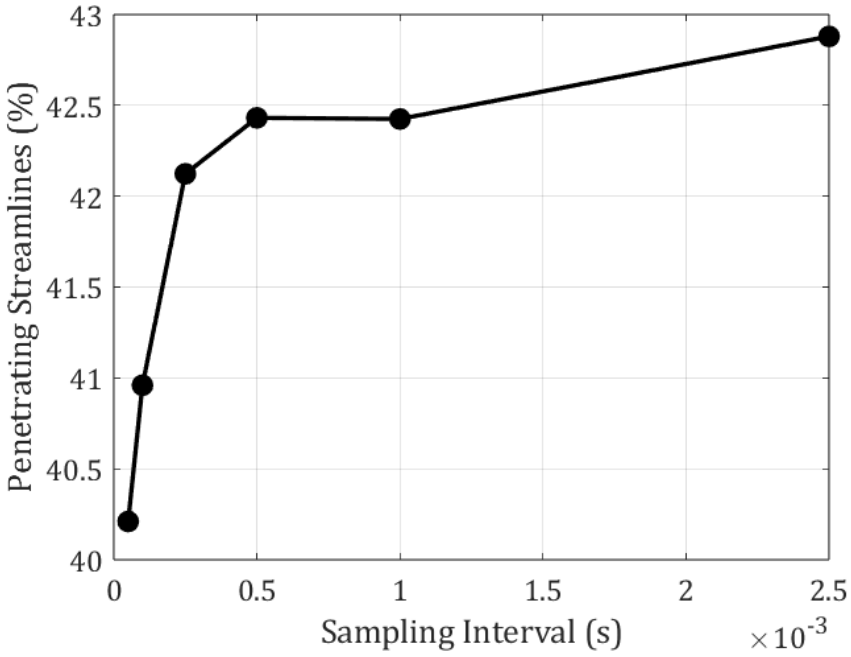

Figure 9.37: Percentage of the total area of the nozzle outlet for the TR = 0.27 impactor that has streamlines that penetrate into the back of the trap for varying sample rates.

The same analysis was applied to the TR = 0.59 impactor, and the percentage of penetrating streamlines as a function of the sampling interval is shown in Figure 9.38. The trend is the opposite of TR = 0.27, as the penetrating streamlines percentage decreases with increasing sample interval time, but the range is still small between 71 and 73%. These results have high agreement with the trap efficiency percentage of $\approx 65\%$ for Re $\approx$ 17,000.

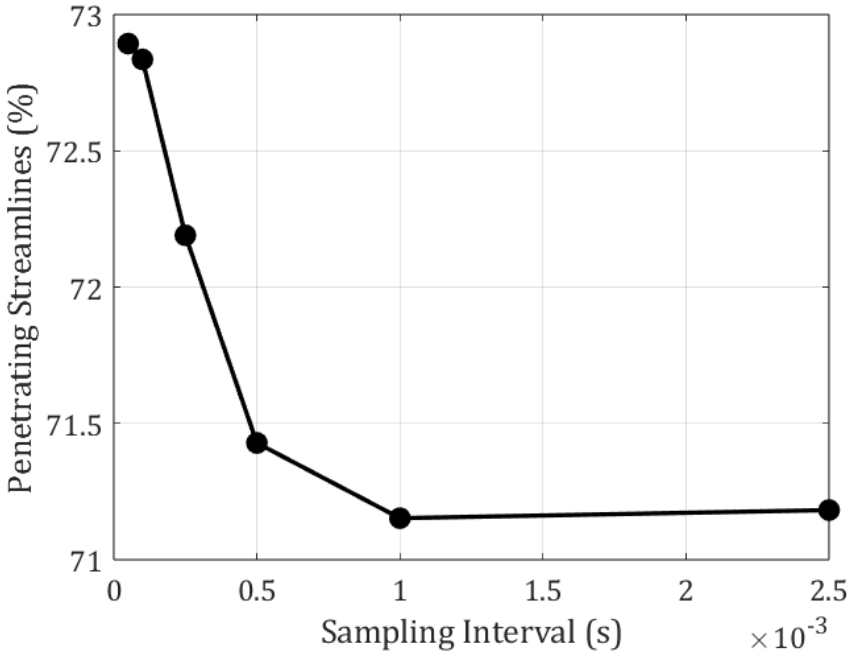

Figure 9.38: Percentage of the total area of the nozzle outlet for the TR = 0.59 impactor that has streamlines that penetrate into the back of the trap for varying sample rates.

9.7 Conclusion

In this chapter, we have simulated the flow field for the trap impactors in order to develop an understanding of the flow in the trap that could not be analyzed experimentally. As with all simulations, we had to validate the results by comparing them with our experimental data. Although the simulations calculated results for the entire impactor flow field, we could only compare the results in the impactor gap, as that was where we had the experimental data. The time-averaged flow fields fared well for all designs, with only slight differences being the reverse flow magnitude being larger in the simulations for TR = 0.27 and the TR = 0.27 simulations underpredicting the M-shaped velocity profile. The turbulent kinetic energy fields were then compared, and larger discrepancies arose for TR = 0.59 and 0.27. TR = 0.59 underpredicted the turbulent kinetic energy along the shear layer and overpredicted the TKE inside the jet. TR = 0.27 overpredicted the TKE in the gap due to the flow out of the trap. We then compared velocity time traces at the probe locations used with the hotwire

anemometer and compared the power spectral densities. The simulations and experiments both had peaks near 50 Hz, providing evidence that the reverse flow could have a coherent pulsatile behavior. Tuning the model by altering the turbulent viscosity ratio did little to improve the time-averaged flow field agreement between the simulations and experiments.

The numerical solutions provided us with insight into the paths particles may take as they approach and enter the trap by calculating the flow field and streamlines. TR = 1.00 had clean flow into and out of the trap, as the flow was shown to behave like impinging flow at the back of the trap, and then exited the trap without disturbing the incoming jet. These results were consistent with the TR = 1.00 trap efficiency having a very high trap efficiency. The flow fields were not as clean for the other geometries as both showed streamlines reversing direction and exiting the trap before reaching the back. We then quantified the effect of the streamlines on trap efficiency by calculating the percentage of streamlines that reached the back of the trap as a proxy for trap efficiency for TR = 0.59 and 0.27. Both demonstrated good agreement with the efficiency results. The percentage of penetrating streamlines for TR = 0.59 was $\approx$ 70% and the measured efficiency was $\approx$ 65%, and were 40% and 30% for TR = 0.27, respectively.

Overall, the simulations have provided us with an idea of the flow inside the traps and how they might affect efficiency. These results are promising and agree with the efficiency results, but it is clear that the models need to be refined to better resemble the experimental flow field data.

CHAPTER 10
EFFICIENCY REDUCTION AND DESIGN RECOMMENDATIONS

10.1 Efficiency Reduction Mechanisms

By analyzing the experimental and numerical flow field results, we can hypothesize two potential mechanisms responsible for the decrease in trap efficiency. It was shown in the experimental turbulent kinetic energy fields (see Figure 8.28) that an increase in TKE was correlated with a decrease in trap efficiency. The simulations revealed that the streamlines entering and exiting the trap (see Figure 9.31, Figure 9.32, and Figure 9.33) became more distorted with a decreasing trap ratio, potentially contributing to an increase in TKE. This increase in TKE can be attributed to the interaction between the incoming jet and the exiting wall jet. It was shown in the numerical flow fields that when the wall jet begins to exit the trap, it separates from the corner of the trap entrance channel. For TR = 1.00, the trap opening clearance was large enough so that the wall jet was able to exit the trap without mixing with the incoming jet. However, as the trap opening clearance is reduced, the wall jet can potentially separate from the corner and mix with the incoming jet, increasing the turbulent kinetic energy and reducing efficiency. The simulated time-averaged flow field for TR = 0.27, shown in Figure 9.30, revealed that the velocity is minimal inside the trap and is potentially unlikely to separate off the trap edge and mix with the incoming jet. Instead, another potential mechanism is that, as the trap opening clearance is reduced further, there is an increase in shear between the edge of the jet and the trap wall. The increase in the velocity gradient can strengthen the Kelvin-Helmholtz instability and cause the jet to break up upon entering the trap. The trap ratio is also a function of the total trap depth, T, and a larger trap depth has a longer confined region between the jet and the trap wall that can sustain the instability. The two proposed mechanisms are illustrated in Figure 10.1, where

Δ represents the distance between the edge of the jet and the trap wall, and the red arrows represent the exiting wall jet.

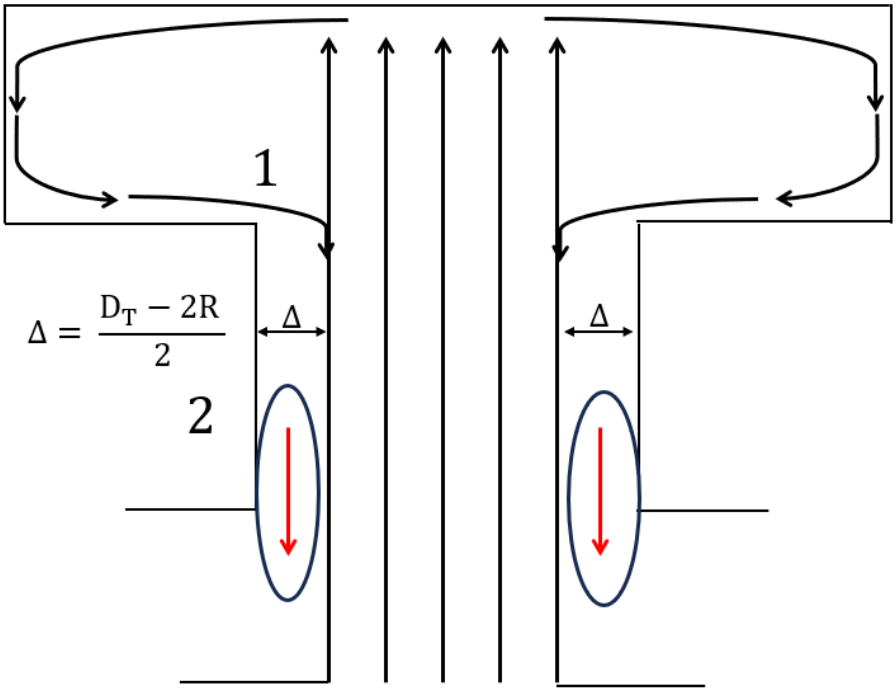

Figure 10.1: Efficiency reduction is hypothesized to be from two potential mechanisms. The first hypothesis is that a decreased trap opening clearance results in the separating wall jet mixing with the incoming jet. The second is that the increase in shear in the region between the incoming jet and the trap wall can strengthen the Kelvin-Helmholtz instability and break the jet up upon entering the trap.

10.2 Design Recommendations

By removing the interaction between the incoming jet and the wall jet, we can propose the optimal trap impactor design for the breathalyzer as shown in Figure 10.2. The optimal trap design removes the trap entrance channel and reduces the trap depth, T, while still maintaining a small cavity. By removing the entrance channel, the wall jet cannot separate from the trap corner and mix with the incoming jet. Next, the trap diameter is maximized to influence the impinging flow to spread out in the radial direction away from the incoming flow. Lastly, the trap edges are rounded to prevent flow separation and to guide the flow to smoothly exit the trap. These design recommendations bring the trap geometry closer to a

flat plate, but the need for a shallow cavity still exists to house the nanowell sensor.

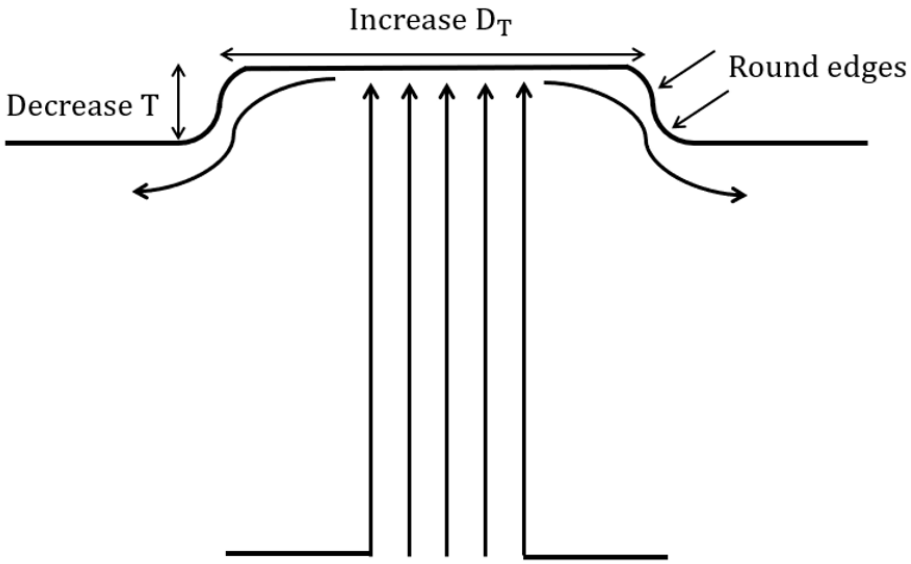

Figure 10.2: The proposed optimal trap design prevents the wall jet and incoming jet from mixing by reducing the trap ratio. This is done by reducing the trap depth and increasing the trap diameter. Another recommendation is rounding the trap corners to influence the flow to stay attached to the surfaces and exit smoothly.

CHAPTER 11
CONCLUSION AND FUTURE WORK

This dissertation demonstrated that a breathalyzer inspired by a particle trap impactor has the potential to be an effective device for detecting respiratory illnesses. First, experiments were performed to characterize the performance of a label-free nanowell-based impedance sensor used to detect antigen-antibody binding events. We demonstrated that the SARS-CoV-2 spike protein in artificial saliva added to the nanowell sensor coated with SARS-CoV-2 antibodies in 0.18X PBS buffer had a limit of detection of 0.2 ng/mL (1.5 pM, 0.05 significance level) with a less than 10-minute detection time. An added benefit is the small volume of samples needed for detection, with only 3 μL of buffered antigen needing to be added to the sensor. After quantifying the limit of detection, we performed specificity experiments to determine if the sensor could distinguish between the target antigen and a different spike protein. MERS-CoV spike proteins were injected into the sensor prepared with SARS-CoV-2 antibodies, and the device did not detect a binding event, demonstrating that the device can distinguish between SARS-CoV-2 and MERS-CoV spike proteins. Compared to other biosensors, our device has a positive combination of high sensitivity, low detection times, portability, and requires little sample preparation, making it a strong sensing platform.

After verifying the feasibility of the sensor, we focused on the protein delivery mechanism. The benchtop sensor characterization experiments introduced the sample via pipette; however, the end users will blow through the breathalyzer to deliver the viral particle-carrying water droplets. To increase the probability of detecting the virus, we needed to maximize the efficiency with which droplets delivered by the breathalyzer nozzle impacted the sensor. We performed efficiency experiments with water droplets as the test aerosols for three impactors with nozzle outlet diameters of 1.5, 2.3, and 3 mm. From inertial impaction

theory, the impactor efficiency increases to 100% with increasing Stokes number (St). We found that efficiency increased with Stokes number, but eventually began to decrease for varying Stokes numbers, depending on the nozzle diameter. The decrease in efficiency was better correlated with Reynolds number (Re), where each impactor efficiency decreased near Re = 14,000. We hypothesized that this decrease in efficiency was potentially not a flaw in the impactor but instead the water droplets evaporating during the experiments, and the Stokes number was decreasing.

To remove evaporative effects, we used olive oil droplets instead, which would have constant diameters throughout the efficiency experiments. A drawback of using olive oil droplets was that the atomization process resulted in a polydisperse distribution with unknown statistics. To characterize the particle size distribution, we used an optical particle sizer for various nozzle and flow rate combinations. We found that the particle size distribution was fairly consistent irrespective of flow rate or nozzle. The distribution, however, was polydisperse, whereas most impactor studies use monodisperse particles to isolate the Stokes number as only a function of velocity. To address this difference, we introduced the average Stokes number by mass, $\langle\sqrt{\mathrm{St}}\rangle$, which was a single statistic to characterize the polydisperse particle size distribution. We then proposed a model to predict the impactor efficiency as a function of $\langle\sqrt{\mathrm{St}}\rangle$ by assuming particles with an individual Stokes number greater than 0.5 are perfectly removed from the flow. After performing efficiency experiments for the 1.5, 2.3, and 3 mm nozzles with olive oil droplets as the test aerosols, the predicted and experimental efficiencies showed strong agreement, verifying that our predicted model was valid. Also, the efficiency exceeded 80% when $\langle\sqrt{\mathrm{St}}\rangle \geq 0.8$ and the maximum efficiencies for the 1.5, 2.3, and 3 mm impactors were 98, 91, and 83%, respectively. There were two interesting results from these experiments. The first was that the 1.5 mm nozzle was able to reach higher $\langle\sqrt{\mathrm{St}}\rangle$ and efficiency due to it having the smallest outlet diameter, and could maximize the Stokes number for the same particle size distribution. This highlights that smaller nozzles can result in higher efficiencies, with a lower bound on

nozzle diameter needing consideration. The other interesting result was the trap efficiency, which was the percentage of particles that were removed from the flow that were deposited in the trap, and still slightly decreased at higher Stokes numbers. These losses were found in droplets landing on top of the impactor plate but not inside the trap or on the back end of the nozzle. We hypothesized that these losses could be due to the trap geometry.

To examine the effects of the trap geometry, we used the 1.5 mm nozzle with seven different trap designs characterized by the trap ratio (TR), which compares the difference in nozzle and trap diameter to the trap depth. We found that the largest trap ratio of 1.00 (wide trap width and shallow depth) resulted in the largest trap efficiency and showed high agreement with the predicted efficiency with no degradation at higher Stokes numbers. The maximum trap efficiency was 94% at $\langle\sqrt{\mathrm{St}}\rangle$ = 2.0. The worst efficiency was seen for the lowest trap ratio of 0.27 (narrow width and deep depth), and it only had a maximum trap efficiency of 30% for predicted efficiencies near 100%. The overall trend was shown to be that an increasing trap ratio resulted in increasing trap efficiency.

The trap geometry clearly had an effect on the impactor performance, but it had not been thoroughly investigated in the literature. To understand what was causing the poor efficiency at high Stokes numbers, we investigated the flow field of the TR = 1.00, 0.59, and 0.27 impactors to see if there were flow features that affected efficiency. We hypothesized that two potential mechanisms for decreased efficiency were: 1) particles may deviate from their initial trajectories and not enter the trap, and 2) particles may enter the trap but lose inertia and exit without depositing. We examined the flow by performing high-speed shadowgraphy, particle image velocimetry (PIV), and hotwire anemometry experiments with larger impactor models. The shadowgraphs were qualitative, high-speed images taken to reveal the structures in the flow, and we saw evidence of a ring vortex as the jet first emerges from the nozzle, the Kelvin-Helmholtz instability along the jet shear layer, as well as the flow impinging on a flat plate and rolling up and separating. The most interesting result, however, was seeing the ring vortex being prevented from entering the TR = 0.27 trap, and

eventually the wall jet emanating out of the trap interfering with the incoming jet. This gave us reason to believe that the wall jet was potentially responsible for the decrease in efficiency.

We then performed the particle image velocimetry experiments to quantify the time-averaged flow field in the gaps of the three impactors, along with the flat plate impactor as a control. We found that the largest discrepancy between the flow fields had to do with the degradation of the centerline velocity for the TR = 0.27 geometry, which was highly unexpected, as the back of the trap was furthest away for this design. This reduction in velocity decreases the particle velocities as they enter the trap, lowers their Stokes numbers, and prevents them from impacting on the back of the trap. We also examined the turbulent kinetic energy (TKE) for the three designs and found that increasing TKE was correlated with worse performance. TR = 1.00 and 0.59 had minimal TKE in the core of the jet, but had increasing amounts at the shear layer and in the regions of the gap where the wall jet was expelled from the trap, with TR = 0.59 having higher TKE than TR = 1.00. TR = 0.27, however, had higher TKE, not only in the gap, but also in the core of the jet. Analyzing the instantaneous flow fields from the PIV results highlighted that TR = 0.27 had multiple instances of the wall jet interfering with the jet and breaking up the jet structure as it neared the trap. There were images where the collision of the incoming jet and wall jet resulted in near-zero velocities along the centerline, and these interactions could potentially alter particle trajectories, leading to decreased efficiency. TR = 0.59 was also shown to have interacting jets, but not to the degree that was seen for TR = 0.27. TR = 1.00 had a very steady flow field with only the shear layer showing time dependence due to the Kelvin-Helmholtz instability. Hotwire anemometer experiments were performed to further analyze the time-dependent nature of the flow, as its frequency response of 5 kHz was orders of magnitude faster than the PIV. The hotwire probe was placed at the downstream location of z/R = 2.9 and radial locations of r/R = 0, 1.2, 2.0, and 3.0. The power spectrum distribution (PSD) for r/R = 0, 1.2, and 2.0 for TR = 0.27 showed a very small peak near 20, 40, and 60

Hz, which could be indicative of the wall jet shedding frequency. However, the signal-to-noise ratio was low for these experiments, and the results should be interpreted carefully.

The drawback of the experimental methods employed to study the flow is that they are limited to the gap, and we are missing vital information about the flow in the trap. Because we could not perform experiments analyzing the trap, we simulated the impactor flow fields using ANSYS Fluent. The steady-state k-ω model was used for TR = 1.00, whereas the transient Detached Eddy Simulation (DES) solver was used for TR = 0.59 and 0.27. As with all simulations, the results must be taken with caution, as the numerical and experimental results had some discrepancies. The TR = 1.00 simulations had high agreement with the PIV data but overpredicted the velocity of the wall jets out of the trap. This was common among all of the simulations, with the difference in velocity increasing with TR. Also, the simulations underpredicted the presence of turbulence for TR = 0.59, but overpredicted it for TR = 0.27. The time-average flow fields for the transient simulations were similar to the experiments, but the velocity fluctuations require further refinement, and therefore, conclusions drawn from the simulations must be treated with caution. The numerical results for TR = 1.00 agreed well with the PIV results, and the flow field inside the gap was clean, as there was no interference between the reverse flow and the incoming jet. This was expected as TR = 1.00 had a very high trap efficiency. TR = 0.59 and 0.27 had more complicated flows in the trap, as the wall jet was shown to separate from the trap walls and mix with the incoming jet. When plotting the streamlines for TR = 0.59, it was shown that some of the streamlines near the edge of the jet would reverse direction before reaching the larger section of the trap. Particles transported along these streamlines would potentially enter and exit the trap without depositing. This effect was exacerbated for TR = 0.27, as more streamlines closer to the centerline would not penetrate deep enough into the trap, and therefore, a larger percentage of particles could be lost. The gap flow fields confirm our hypotheses about the decrease in efficiency and the worsening performance with decreasing trap ratio.

From analyzing the experimental and numerical flow fields, we hypothesized two potential mechanisms that decrease trap efficiency. As the trap opening clearance is decreased, the separating wall jet can mix with the incoming jet. This mixing can break the jet structure, increase the turbulent kinetic energy, and alter particle trajectories. Another mechanism is reducing the trap opening clearance increases the shear along the edge of the jet and can cause the jet structure to break apart upon entering the trap. A long trap entrance channel can sustain the instability, and therefore, reducing the trap opening clearance and reducing the trap depth can maintain the jet structure. This resulted in the optimal trap geometry resembling a flat plate with a shallow trap and rounding the trap edges to prevent wall jet separation.

There are still areas that require further investigation, such as the simulations, which can be improved upon to have closer agreement with the experimental data by reducing the wall jet velocities exiting the trap. The main area of future work is integrating the nanowell sensor into the impactor. In this dissertation, we have treated the two areas of the project separately, but for this technology to become a viable medical device, we need to integrate the two sectors. Preliminary experiments were performed where we aerosolized the Washington strain of the SARS-CoV-2 virus (WA1) in a Level 2 biosafety cabinet. The sensor was secured to the back of the flat plate and was incorporated into the trap. We were able to monitor the impedance after the virus was delivered, just as we did with the benchtop experiments, but the results were inconsistent, and a proper titration curve could not be constructed, as shown in Figure A.16 and Figure A.17. More experiments could be performed to potentially remedy the repeatability issues, and it remains an area for future work. Along with integrating the sensor into the impactor, the flow field and efficiency experiments have shown that a larger trap ratio (TR) improved trap efficiency. When integrating the sensor into the impactor plate, we will want to implement our design recommendations. Although this design was not tested, a potential alternative design would be to embed the PDMS well with the sensor into the impactor plate instead of securing

it behind. This design would resemble the optimal design and could be highly effective. Finally, another area of future work is the viability of the device with even smaller volumes. In the benchtop experiments, we supplied the sensor with 3 μL of antigen-laden PBS. This is multiple orders of magnitude greater than the volume of water droplets a human will expel when blowing into the breathalyzer. The sensor has demonstrated that it can detect very low concentrations on the order of pM, but this also needs to be researched with total lower sample volumes to have a proper understanding of how the device will behave in the user environment.

REFERENCES

[1] W. C. Hinds and Y. Zhu, *Aerosol technology: properties, behavior, and measurement of airborne particles*. John Wiley & Sons, 2022.

[2] U.S. Environmental Protection Agency, *AQI Basics*, Accessed: 2025-07-22, n.d.

[3] U.S. Environmental Protection Agency, "Technical Assistance Document for the Reporting of Daily Air Quality," U.S. Environmental Protection Agency, Office of Air Quality Planning and Standards, Research Triangle Park, NC, Technical Assistance Document EPA-454/B-13-001, May 2024, Accessed: 2025-07-22.

[4] S. S. Amaral, J. A. de Carvalho Jr, M. A. M. Costa, and C. Pinheiro, "An overview of particulate matter measurement instruments," *Atmosphere*, vol. 6, no. 9, pp. 1327–1345, 2015.

[5] V. A. Marple and K. Willeke, "Impactor design," *Atmospheric Environment (1967)*, vol. 10, no. 10, pp. 891–896, 1976.

[6] J. P. Mitchell and M. W. Nagel, "Cascade impactors for the size characterization of aerosols from medical inhalers: Their uses and limitations," *Journal of Aerosol Medicine*, vol. 16, no. 4, pp. 341–377, 2003.

[7] V. A. Marple and K. Willeke, "Inertial impactors: Theory, design and use," *Fine Particles: Aerosol Generation, Measurement, Sampling, and Analysis*, pp. 412–446, 1976.

[8] J. M. Macher, "Positive-hole correction of multiple-jet impactors for collecting viable microorganisms," *American Industrial Hygiene Association Journal*, vol. 50, no. 11, pp. 561–568, 1989.

[9] V. A. Marple, "History of impactors—the first 110 years," *Aerosol Science and Technology*, vol. 38, no. 3, pp. 247–292, 2004.

[10] K. May, "The cascade impactor: An instrument for sampling coarse aerosols," *Journal of Scientific instruments*, vol. 22, no. 10, p. 187, 1945.

[11] T. Mercer and R. Stafford, "Impaction from round jets," *Annals of Occupational Hygiene*, vol. 12, no. 1, pp. 41–48, 1969.

[12] K. May, "Aerosol impaction jets," *Journal of Aerosol Science*, vol. 6, no. 6, pp. 403–411, 1975.

[13] C.-H. Huang, C.-J. Tsai, and T.-S. Shih, "Particle collection efficiency of an inertial impactor with porous metal substrates," *Journal of Aerosol Science*, vol. 32, no. 9, pp. 1035–1044, 2001.

[14] V. A. Marple, K. L. Rubow, W. Turner, J. D. Spengler, *et al.*, "Low flow rate sharp cut impactors for indoor air sampling: Design and calibration," *Japca*, vol. 37, no. 11, pp. 1303–1307, 1987.

[15] C.-J. Tsai and Y.-H. Cheng, "Solid particle collection characteristics on impaction surfaces of different designs," *Aerosol Science and Technology*, vol. 23, no. 1, pp. 96–106, 1995.

[16] T. M. Peters, R. W. Vanderpool, and R. W. Wiener, "Design and calibration of the epa pm2. 5 well impactor ninety-six (wins)," *Aerosol Science & Technology*, vol. 34, no. 5, pp. 389–397, 2001.

[17] T.-C. Le and C.-J. Tsai, "Inertial impaction technique for the classification of particulate matters and nanoparticles: A review," *KONA Powder and Particle Journal*, vol. 38, pp. 42–63, 2021.

[18] A. Rao and K. Whitby, "Non-ideal collection characteristics of inertial impactors—i. single-stage impactors and solid particles," *Journal of Aerosol Science*, vol. 9, no. 2, pp. 77–86, 1978.

[19] S. Stern, H. Zeller, and A. Schekman, "Collection efficiency of jet impactors at reduced pressures," *Industrial & Engineering Chemistry Fundamentals*, vol. 1, no. 4, pp. 273–277, 1962.

[20] R. Mitchell and J. Pilcher, "Improved cascade impactor for measuring aerosol particle sizes," *Industrial & Engineering Chemistry*, vol. 51, no. 9, pp. 1039–1042, 1959.

[21] W. E. Ranz and J. Wong, "Impaction of dust and smoke particles on surface and body collectors.," *Industrial & Engineering Chemistry*, vol. 44, no. 6, pp. 1371–1381, 1952.

[22] P. Biswas and R. C. Flagan, "The particle trap impactor," *Journal of Aerosol Science*, vol. 19, no. 1, pp. 113–121, 1988.

[23] D. Ivnitski, I. Abdel-Hamid, P. Atanasov, and E. Wilkins, "Biosensors for detection of pathogenic bacteria," *Biosensors and Bioelectronics*, vol. 14, no. 7, pp. 599–624, 1999.

[24] J. H. Luong, C. A. Groom, and K. B. Male, "The potential role of biosensors in the food and drink industries," *Biosensors and Bioelectronics*, vol. 6, no. 7, pp. 547–554, 1991.

[25] M. Alvarez-Icaza and U. Bilitewski, "Mass production of biosensors," *Analytical Chemistry*, vol. 65, no. 11, 525A–533A, 1993.

[26] C. L. Morgan, D. J. Newman, and C. Price, "Immunosensors: Technology and opportunities in laboratory medicine," *Clinical Chemistry*, vol. 42, no. 2, pp. 193–209, 1996.

[27] Z. Meng *et al.*, "A label-free nanowell-based impedance sensor for ten-minute sars-cov-2 detection," *Sensors & Diagnostics*, 2025.

[28] Y. Lei, W. Chen, and A. Mulchandani, "Microbial biosensors," *Analytica Chimica Acta*, vol. 568, no. 1-2, pp. 200–210, 2006.

[29] Q. Liu, S. Yan, M. Zhang, C. Wang, and D. Xing, "Air sampling and atp bioluminescence for quantitative detection of airborne microbes," *Talanta*, p. 126 025, 2024.

[30] J. S. West and R. Kimber, "Innovations in air sampling to detect plant pathogens," *Annals of Applied Biology*, vol. 166, no. 1, pp. 4–17, 2015.

[31] World Health Organization, *COVID-19 deaths dashboard*, Accessed: 22 July 2025, 2025.

[32] C. C. Wang *et al.*, "Airborne transmission of respiratory viruses," *Science*, vol. 373, no. 6558, eabd9149, 2021.

[33] G. Johnson *et al.*, "Modality of human expired aerosol size distributions," *Journal of aerosol science*, vol. 42, no. 12, pp. 839–851, 2011.

[34] B. Bake, P. Larsson, G. Ljungkvist, E. Ljungström, and A.-C. Olin, "Exhaled particles and small airways," *Respiratory research*, vol. 20, pp. 1–14, 2019.

[35] B. Patterson and R. Wood, "Is cough really necessary for tb transmission?" *Tuberculosis*, vol. 117, pp. 31–35, 2019.

[36] W. Chen, N. Zhang, J. Wei, H.-L. Yen, and Y. Li, "Short-range airborne route dominates exposure of respiratory infection during close contact," *Building and Environment*, vol. 176, p. 106 859, 2020.

[37] K. P. Fennelly, "Particle sizes of infectious aerosols: Implications for infection control," *The lancet respiratory medicine*, vol. 8, no. 9, pp. 914–924, 2020.

[38] D. K. Milton, M. P. Fabian, B. J. Cowling, M. L. Grantham, and J. J. McDevitt, "Influenza virus aerosols in human exhaled breath: Particle size, culturability, and effect of surgical masks," *PLoS pathogens*, vol. 9, no. 3, e1003205, 2013.

[39] J. Gralton, E. R. Tovey, M.-L. McLaws, and W. D. Rawlinson, "Respiratory virus rna is detectable in airborne and droplet particles," *Journal of medical virology*, vol. 85, no. 12, pp. 2151–2159, 2013.

[40] P. Fabian *et al.*, "Influenza virus in human exhaled breath: An observational study," *PloS one*, vol. 3, no. 7, e2691, 2008.

[41] J. Yan *et al.*, "Infectious virus in exhaled breath of symptomatic seasonal influenza cases from a college community," *Proceedings of the National Academy of Sciences*, vol. 115, no. 5, pp. 1081–1086, 2018.

[42] N. H. Leung *et al.*, "Respiratory virus shedding in exhaled breath and efficacy of face masks," *Nature medicine*, vol. 26, no. 5, pp. 676–680, 2020.

[43] R. S. Papineni and F. S. Rosenthal, "The size distribution of droplets in the exhaled breath of healthy human subjects," *Journal of Aerosol Medicine*, vol. 10, no. 2, pp. 105–116, 1997.

[44] G. Bagheri *et al.*, "Size, concentration, and origin of human exhaled particles and their dependence on human factors with implications on infection transmission," *Journal of Aerosol Science*, vol. 168, p. 106 102, 2023.

[45] H. Liu *et al.*, "Development of a sers-based lateral flow immunoassay for rapid and ultra-sensitive detection of anti-sars-cov-2 igm/igg in clinical samples," *Sensors and Actuators B: Chemical*, vol. 329, p. 129 196, 2021.

[46] O. Filchakova, D. Dossym, A. Ilyas, T. Kuanysheva, A. Abdizhamil, and R. Bukasov, "Review of covid-19 testing and diagnostic methods," *Talanta*, vol. 244, p. 123 409, 2022.

[47] G. Rong, Y. Zheng, Y. Chen, Y. Zhang, P. Zhu, and M. Sawan, "Covid-19 diagnostic methods and detection techniques," *Encyclopedia of sensors and biosensors*, p. 17, 2023.

[48] O. Vandenberg, D. Martiny, O. Rochas, A. van Belkum, and Z. Kozlakidis, "Considerations for diagnostic covid-19 tests," *Nature Reviews Microbiology*, vol. 19, no. 3, pp. 171–183, 2021.

[49] T. Pinheiro *et al.*, "Based biosensors for covid-19: A review of innovative tools for controlling the pandemic," *ACS omega*, vol. 6, no. 44, pp. 29 268–29 290, 2021.

[50] S. K. Patel, J. Surve, J. Parmar, K. Ahmed, F. M. Bui, and F. A. Al-Zahrani, "Recent advances in biosensors for detection of covid-19 and other viruses," *IEEE reviews in biomedical engineering*, vol. 16, pp. 22–37, 2022.

[51] A. Wasfi, F. Awwad, N. Qamhieh, B. Al Murshidi, A. R. Palakkott, and J. G. Gelovani, "Real-time covid-19 detection via graphite oxide-based field-effect transistor biosensors decorated with pt/pd nanoparticles," *Scientific reports*, vol. 12, no. 1, p. 18 155, 2022.

[52] I. Irkham, A. U. Ibrahim, C. W. Nwekwo, F. Al-Turjman, and Y. W. Hartati, "Current technologies for detection of covid-19: Biosensors, artificial intelligence and internet of medical things (iomt)," *Sensors*, vol. 23, no. 1, p. 426, 2022.

[53] P. L. Truong, Y. Yin, D. Lee, and S. H. Ko, "Advancement in covid-19 detection using nanomaterial-based biosensors," in *Exploration*, Wiley Online Library, vol. 3, 2023, p. 20 210 232.

[54] M. Tayyab *et al.*, "A portable analog front-end system for label-free sensing of proteins using nanowell array impedance sensors," *Scientific reports*, vol. 12, no. 1, p. 20 119, 2022.

[55] N. Song *et al.*, "A microwell-based impedance sensor on an insertable microneedle for real-time in vivo cytokine detection," *Microsystems & Nanoengineering*, vol. 7, no. 1, p. 96, 2021.

[56] P. Xie, N. Song, W. Shen, M. Allen, and M. Javanmard, "A ten-minute, single step, label-free, sample-to-answer assay for qualitative detection of cytokines in serum at femtomolar levels," *Biomedical Microdevices*, vol. 22, pp. 1–9, 2020.

[57] H. Raji, P. Xie, S. R. Mahmoodi, and M. Javanmard, "Wireless power-up and readout of label-free electronic detection of protein biomarkers," in *25th International Conference on Miniaturized Systems for Chemistry and Life Sciences, MicroTAS 2021*, Chemical and Biological Microsystems Society, 2021, pp. 823–824.

[58] M. Kokabi, J. Sui, N. Gandotra, A. Pournadali Khamseh, C. Scharfe, and M. Javanmard, "Nucleic acid quantification by multi-frequency impedance cytometry and machine learning," *Biosensors*, vol. 13, no. 3, p. 316, 2023.

[59] S. R. Mahmoodi *et al.*, "Single-step label-free nanowell immunoassay accurately quantifies serum stress hormones within minutes," *Science Advances*, vol. 7, no. 27, eabf4401, 2021.

[60] Abbott Laboratories, *BinaxNOW COVID-19 Ag Card Home Test – Instructions for Use*, https://www.fda.gov/media/141570/download, Emergency Use Authorization document, 2020.

[61] Abbott Laboratories, *Panbio™ COVID-19 Ag Rapid Test Device (Nasal, Asymptomatic Use) – Instructions for Use*, https://dam.abbott.com/en-gb/panbio/120007883-v1-Panbio-COVID-19-Ag-Nasal-AsymptomaticSe.pdf, Document number: 120007883-v1, 2021.

[62] C. Lei, J. Yang, J. Hu, and X. Sun, "On the calculation of tcid50 for quantitation of virus infectivity," *Virologica Sinica*, vol. 36, no. 1, pp. 141–144, 2021.

[63] N. R. Pollock *et al.*, "Correlation of sars-cov-2 nucleocapsid antigen and rna concentrations in nasopharyngeal samples from children and adults using an ultrasensitive and quantitative antigen assay," *Journal of Clinical Microbiology*, vol. 59, no. 4, pp. 10–1128, 2021.

[64] N. Petrosillo, G. Viceconte, O. Ergonul, G. Ippolito, and E. Petersen, "Covid-19, sars and mers: Are they closely related?" *Clinical microbiology and infection*, vol. 26, no. 6, pp. 729–734, 2020.

[65] P. K. Kundu, I. M. Cohen, D. R. Dowling, and J. Capecelatro, *Fluid mechanics*. Elsevier, 2024.

[66] R. J. Smyth, K. R. Chapman, and A. S. Rebuck, "Maximal inspiratory and expiratory pressures in adolescents: Normal values," *Chest*, vol. 86, no. 4, pp. 568–572, 1984.

[67] D. W. Cox, M. M. Verheggen, S. M. Stick, and G. L. Hall, "Characterization of maximal respiratory pressures in healthy children," *Respiration*, vol. 84, no. 6, pp. 485–491, 2012.

[68] E. Mansour *et al.*, "Measurement of temperature and relative humidity in exhaled breath," *Sensors and actuators B: Chemical*, vol. 304, p. 127 371, 2020.

[69] S. Jennings, "The mean free path in air," *Journal of Aerosol Science*, vol. 19, no. 2, pp. 159–166, 1988.

[70] L. G. Leal, *Advanced transport phenomena: fluid mechanics and convective transport processes*. Cambridge university press, 2007, vol. 7.

[71] V. A. Marple, "Fundamental study of inertial impactors," Ph.D. dissertation, Dec. 1970.

[72] V. A. Marple and B. Y. Liu, "Characteristics of laminar jet impactors," *Environmental Science & Technology*, vol. 8, no. 7, pp. 648–654, 1974.

[73] S. Grinshpun *et al.*, "Collection of airborne spores by circular single-stage impactors with small jet-to-plate distance," *Journal of Aerosol Science*, vol. 36, no. 5-6, pp. 575–591, 2005.

[74] D. Kim, K. Lee, and Y. Kim, "Characterization of a particle trap impactor," *Journal of Aerosol Science*, vol. 37, no. 8, pp. 1016–1023, 2006.

[75] M. Chang, S. Kim, and C. Sioutas, "Experimental studies on particle impaction and bounce: Effects of substrate design and material," *Atmospheric Environment*, vol. 33, no. 15, pp. 2313–2322, 1999.

[76] L. White, E. P. DeMauro, and G. Drazer, "The influence of geometry on particle capture efficiency in trap impactors," *Journal of Aerosol Science*, p. 106 643, 2025.

[77] Y. A. Cengel, M. A. Boles, and M. Kanoğlu, *Thermodynamics: An Engineering Approach*, 9th ed. New York: McGraw-Hill Education, 2019, ISBN: 9781260048667.

[78] Engineers Edge, *Fluid properties - viscosity, density, specific weight*, https://www.engineersedge.com/fluid_flow/fluid_data.htm, Accessed: 2025-04-14, 2000.

[79] L. Li *et al.*, "Optimization of nozzle geometry for virtual impaction across more than one decade in particle size," *Journal of Aerosol Science*, vol. 184, p. 106 516, 2025.

[80] S. M. Eilts, T. Tamadate, M. E. Relling, I. A. Marabella, C. J. Hogan Jr, and B. A. Olson, "Virtual impaction in compressible flows with pressure recovery," *Journal of Aerosol Science*, vol. 167, p. 106 076, 2023.

[81] J. F. De La Mora and P. Riesco-Chueca, "Aerodynamic focusing of particles in a carrier gas," *Journal of Fluid Mechanics*, vol. 195, pp. 1–21, 1988.

[82] S. Fuerstenau, A. Gomez, and J. F. de la Mora, "Visualization of aerodynamically focused subsonic aerosol jets," *Journal of aerosol science*, vol. 25, no. 1, pp. 165–173, 1994.

[83] S. Anand and Y. Mayya, "Size distribution of virus laden droplets from expiratory ejecta of infected subjects," *Scientific reports*, vol. 10, no. 1, p. 21 174, 2020.

[84] M. Alsved *et al.*, "Exhaled respiratory particles during singing and talking," *Aerosol Science and Technology*, vol. 54, no. 11, pp. 1245–1248, 2020.

[85] A. C. Karapiperis, "Numerical simulation of the inertial trap impactor under the influence of evaporation," M.S. thesis, Rutgers The State University of New Jersey, School of Graduate Studies, 2024.

[86] M. J. Nayak, "A parametric study on the structures of the trap impactor," M.S. thesis, Rutgers The State University of New Jersey, School of Graduate Studies, 2025.

[87] V. A. Marple and B. Y. Liu, "On fluid flow and aerosol impaction in inertial impactors," *Journal of colloid and interface science*, vol. 53, no. 1, pp. 31–34, 1975.

[88] V. A. Marple, *A fundamental study of inertial impactors*. University of Minnesota, 1970.

[89] T. Mercer and H. Chow, "Impaction from rectangular jets," *Journal of Colloid and Interface Science*, vol. 27, no. 1, pp. 75–83, 1968.

[90] D. J. Rader and V. A. Marple, "Effect of ultra-stokesian drag and particle interception on impaction characteristics," *Aerosol Science and Technology*, vol. 4, no. 2, pp. 141–156, 1985.

[91] C. D. Argyropoulos and N. Markatos, "Recent advances on the numerical modelling of turbulent flows," *Applied Mathematical Modelling*, vol. 39, no. 2, pp. 693–732, 2015.

[92] C.-M. Ho and N. S. Nosseir, "Dynamics of an impinging jet. part 1. the feedback phenomenon," *Journal of Fluid Mechanics*, vol. 105, pp. 119–142, 1981.

[93] R. Van Hout, V. Rinsky, and Y. Grobman, "Experimental study of a round jet impinging on a flat surface: Flow field and vortex characteristics in the wall jet," *International Journal of Heat and Fluid Flow*, vol. 70, pp. 41–58, 2018.

[94] A. K. Shukla and A. Dewan, "Flow and thermal characteristics of jet impingement: Comprehensive review," *Int. J. Heat Technol*, vol. 35, no. 1, pp. 153–166, 2017.

[95] S. Maurel and C. Solliec, "A turbulent plane jet impinging nearby and far from a flat plate," *Experiments in Fluids*, vol. 31, no. 6, pp. 687–696, 2001.

[96] T. S. O'Donovan and D. B. Murray, "Jet impingement heat transfer–part ii: A temporal investigation of heat transfer and local fluid velocities," *International Journal of Heat and Mass Transfer*, vol. 50, no. 17-18, pp. 3302–3314, 2007.

[97] D. Cooper, D. Jackson, B. E. Launder, and G. Liao, "Impinging jet studies for turbulence model assessment—i. flow-field experiments," *International Journal of Heat and Mass Transfer*, vol. 36, no. 10, pp. 2675–2684, 1993.

[98] K. Nishino, M. Samada, K. Kasuya, and K. Torii, "Turbulence statistics in the stagnation region of an axisymmetric impinging jet flow," *International Journal of Heat and Fluid Flow*, vol. 17, no. 3, pp. 193–201, 1996.

[99] S. V. Alekseenko, A. V. Bilsky, V. M. Dulin, and D. M. Markovich, "Experimental study of an impinging jet with different swirl rates," *International Journal of Heat and Fluid Flow*, vol. 28, no. 6, pp. 1340–1359, 2007.

[100] S. Ashforth-Frost and K. Jambunathan, "Effect of nozzle geometry and semi-confinement on the potential core of a turbulent axisymmetric free jet," *International Communications in Heat and Mass Transfer*, vol. 23, no. 2, pp. 155–162, 1996.

[101] C. Cornaro, A. Fleischer, and R. J. Goldstein, "Flow visualization of a round jet impinging on cylindrical surfaces," *Experimental Thermal and Fluid Science*, vol. 20, no. 2, pp. 66–78, 1999.

[102] D. Lee, Y. Chung, and S. Won, "Technical note the effect of concave surface curvature on heat transfer from a fully developed round impinging jet," *International Journal of Heat and Mass Transfer*, vol. 42, no. 13, pp. 2489–2497, 1999.

[103] V. Terekhov, V. Barsanov, S. Kalinina, and Y. M. Mshvidobadze, "Experimental study of flow structure and heat transfer under a jet flow past a spherical-cavity obstacle," *Journal of Engineering Physics and Thermophysics*, vol. 79, pp. 657–665, 2006.

[104] R. Van Hout, V. Rinsky, N. Sasson, C. Hershcovich, M. Tshuva, and Y. Grobman, "Axisymmetric jet impingement on a dimpled surface: Effect of impingement location on flow field characteristics," *International Journal of Heat and Fluid Flow*, vol. 74, pp. 53–64, 2018.

[105] R. Van Hout, V. Rinsky, C. Hershcovich, and Y. Grobman, "Outer shear layer characteristics of a radially expanding wall jet on smooth and dimpled surfaces," *International Journal of Heat and Fluid Flow*, vol. 72, pp. 304–316, 2018.

[106] V. Terekhov, S. Kalinina, Y. M. Mshvidobadze, and K. Sharov, "Impingement of an impact jet onto a spherical cavity. flow structure and heat transfer," *International Journal of Heat and Mass Transfer*, vol. 52, no. 11-12, pp. 2498–2506, 2009.

[107] Y. Xie, P. Li, J. Lan, and D. Zhang, "Flow and heat transfer characteristics of single jet impinging on dimpled surface," *Journal of heat transfer*, vol. 135, no. 5, p. 052 201, 2013.

[108] R. J. Adrian and J. Westerweel, *Particle image velocimetry*. Cambridge university press, 2011.

[109] M. Raffel, C. E. Willert, F. Scarano, C. J. Kähler, S. T. Wereley, and J. Kompenhans, *Particle image velocimetry: a practical guide*. springer, 2018.

[110] K. Hinsch, "Particle image velocimetry," in *Speckle Metrology*, CRC Press, 2020, pp. 235–324.

[111] J. Westerweel, "Digital particle image velocimetry: Theory and application.," 1995.

[112] B. Wieneke, "Piv uncertainty quantification from correlation statistics," *Measurement Science and Technology*, vol. 26, no. 7, p. 074 002, 2015.

[113] R. S. Figliola and D. E. Beasley, "Theory and design for mechanical measurements," *Measurement Science and Technology*, vol. 12, no. 10, pp. 1743–1743, 2001.

[114] H. K. Versteeg, *An introduction to computational fluid dynamics the finite volume method, 2/E*. Pearson Education India, 2007.

[115] A. Yule, "Large-scale structure in the mixing layer of a round jet," *Journal of Fluid Mechanics*, vol. 89, no. 3, pp. 413–432, 1978.

[116] A. Michalke, "Vortex formation in a free boundary layer according to stability theory," *Journal of Fluid Mechanics*, vol. 22, no. 2, pp. 371–383, 1965.

[117] F. M. White *et al.*, *Fluid mechanics*, 2011.

Appendices

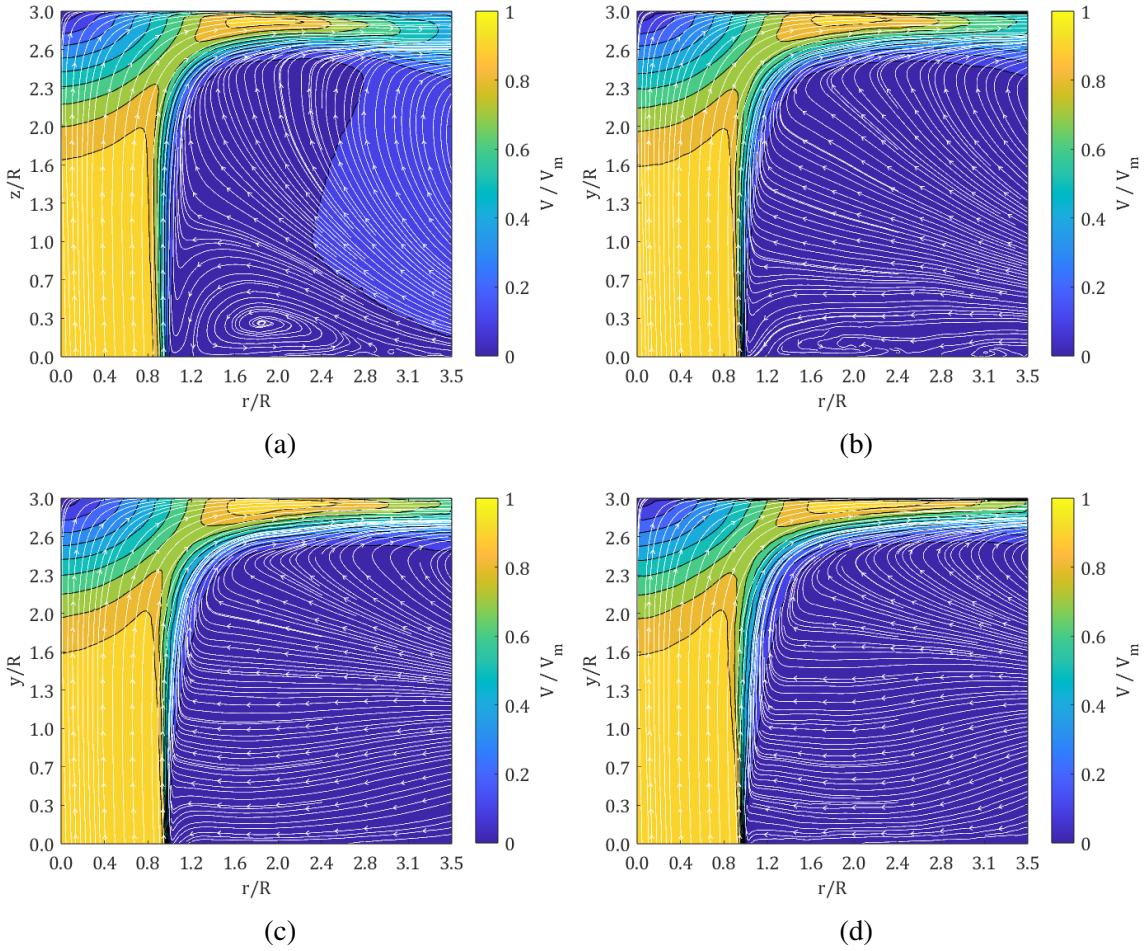

Figure A.1: Experimental flow fields and streamlines for the flat plate impactor for a) Re = 2,000, b) Re = 7,000, c) Re = 10,000, d) Re = 17,000.

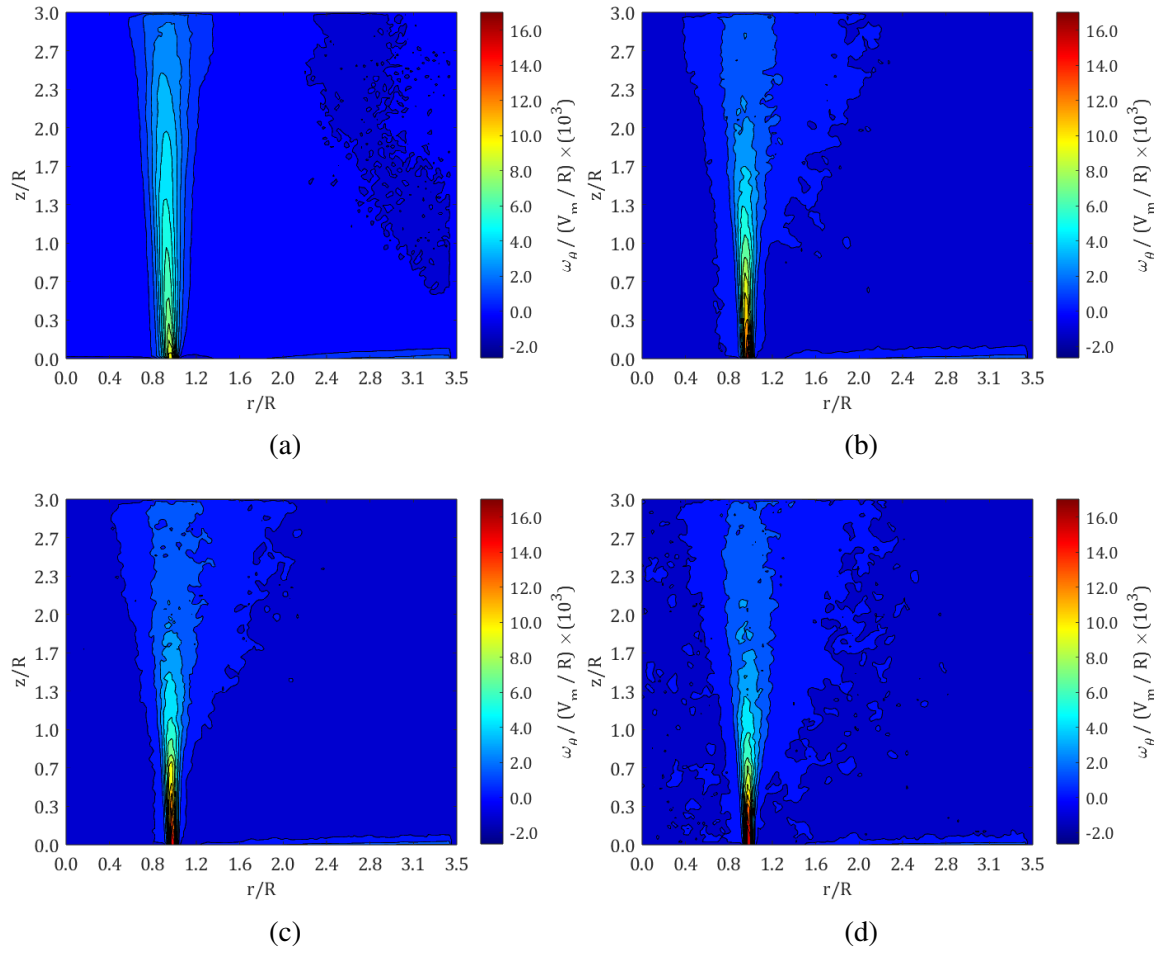

Figure A.2: Experimental vorticity contour plots for TR = 1.00 for a) Re = 2,000, b) Re = 7,000, c) Re = 10,000, d) Re = 17,000

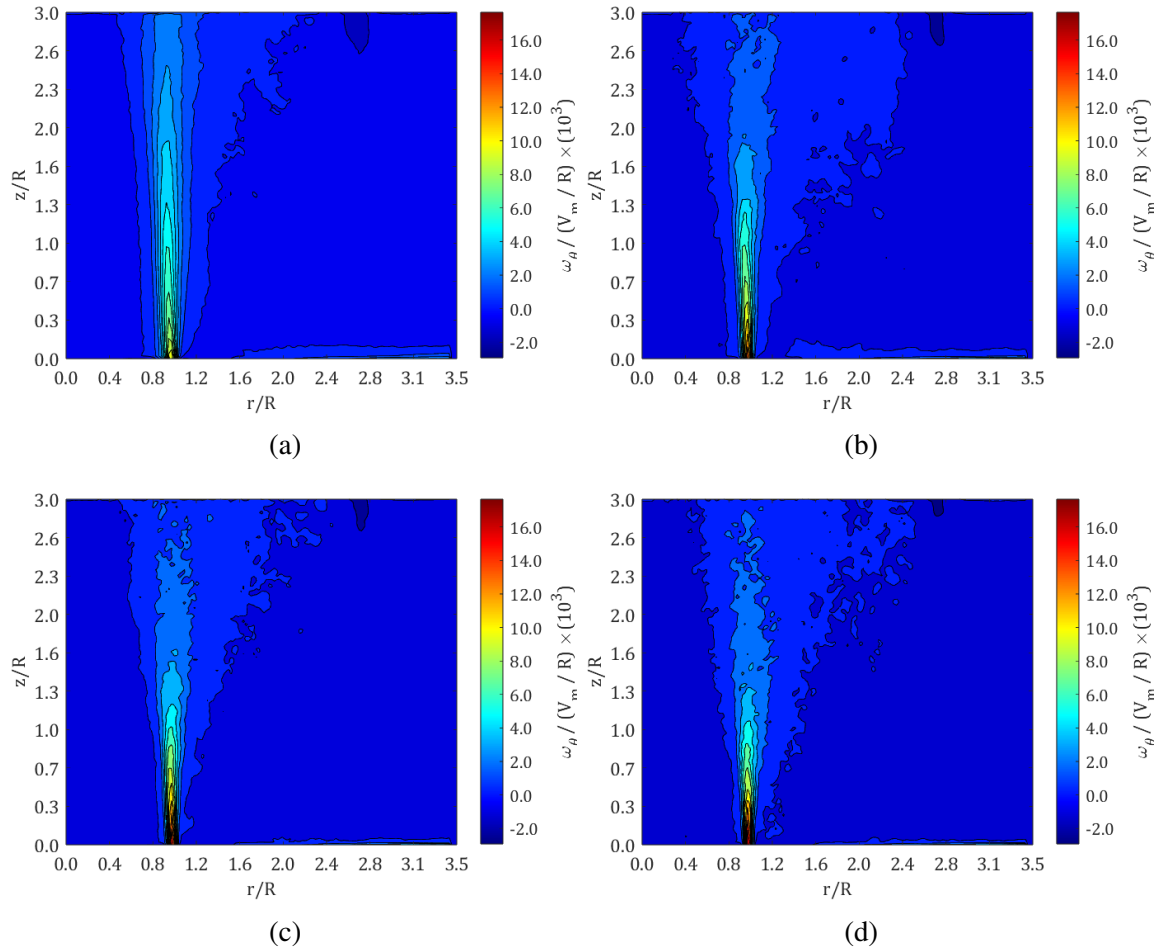

Figure A.3: Experimental vorticity contour plots for TR = 0.59 for a) Re = 2,000, b) Re = 7,000, c) Re = 10,000, d) Re = 17,000

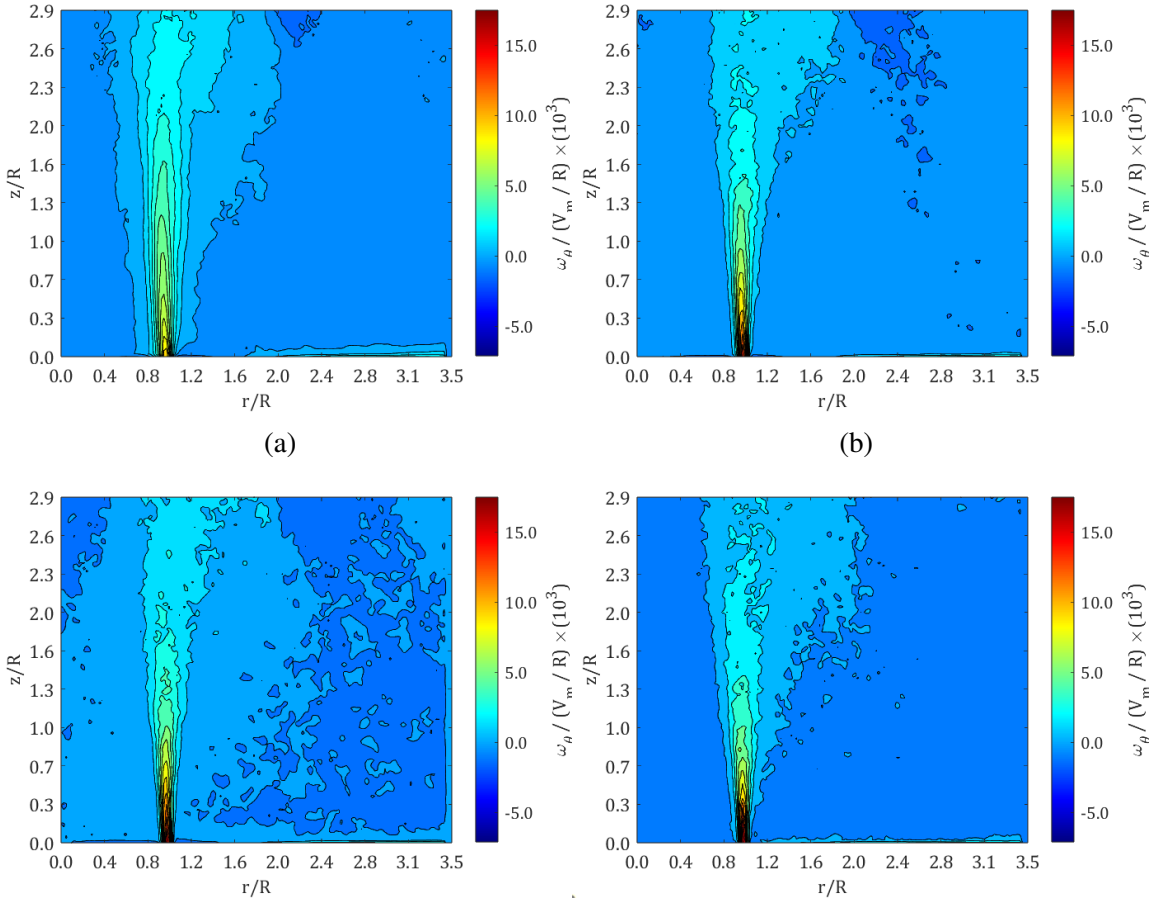

Figure A.4: Experimental vorticity contour plots for TR = 0.27 for a) Re = 2,000, b) Re = 7,000, c) Re = 10,000, d) Re = 17,000

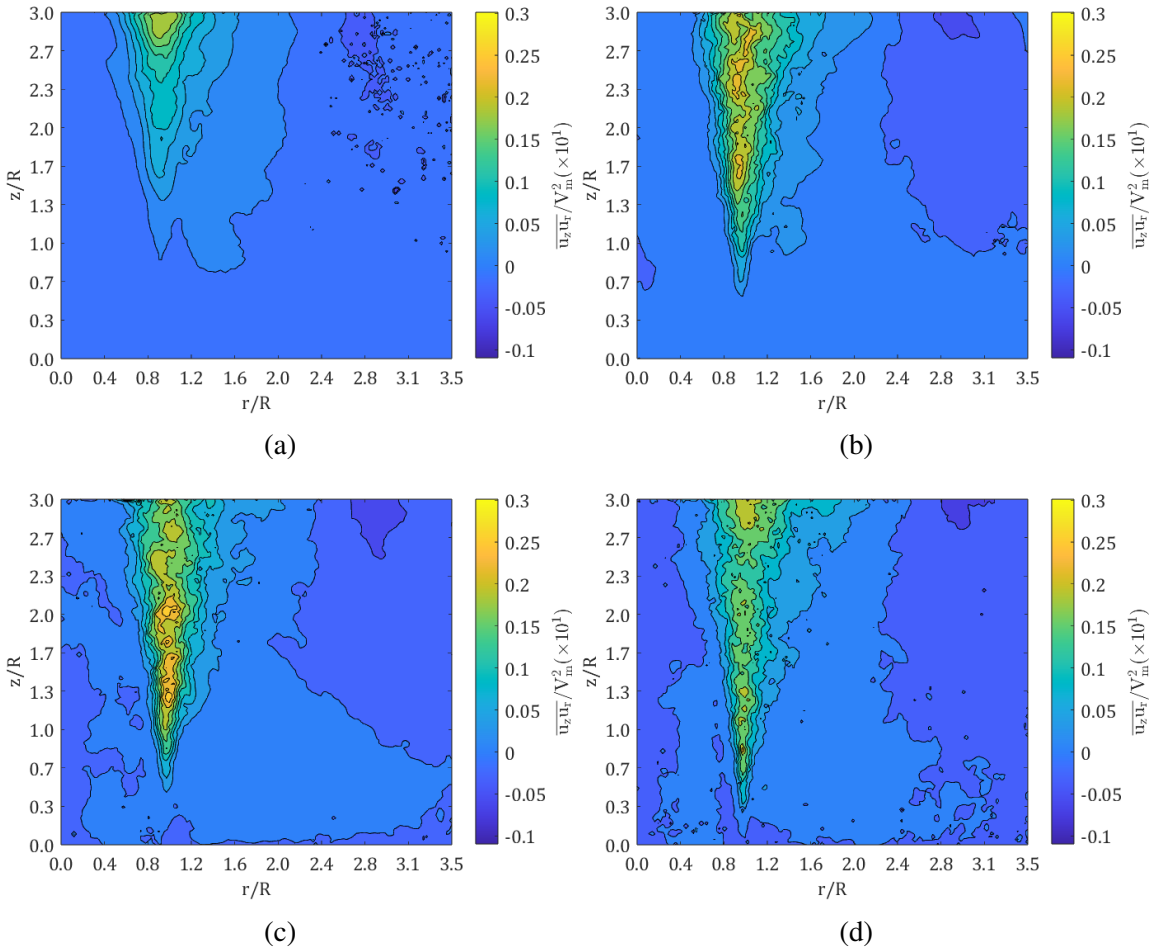

Figure A.5: Contour plots of $\overline{u_z u_r}$ for TR = 1.00 for a) Re = 2,000, b) Re = 7,000, c) Re = 10,000, d) Re = 17,000.

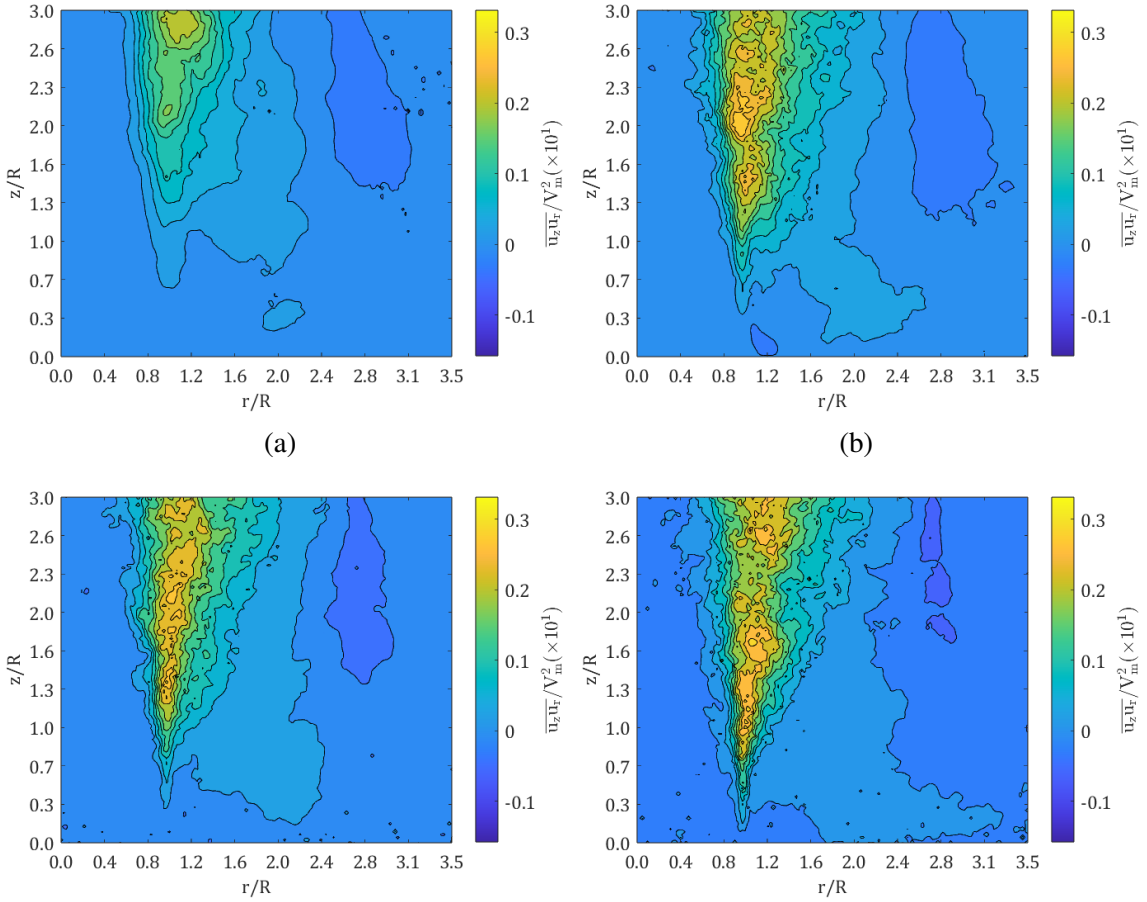

Figure A.6: Contour plots of $\overline{u_z u_r}$ for TR = 0.59 for a) Re = 2,000, b) Re = 7,000, c) Re = 10,000, d) Re = 17,000.

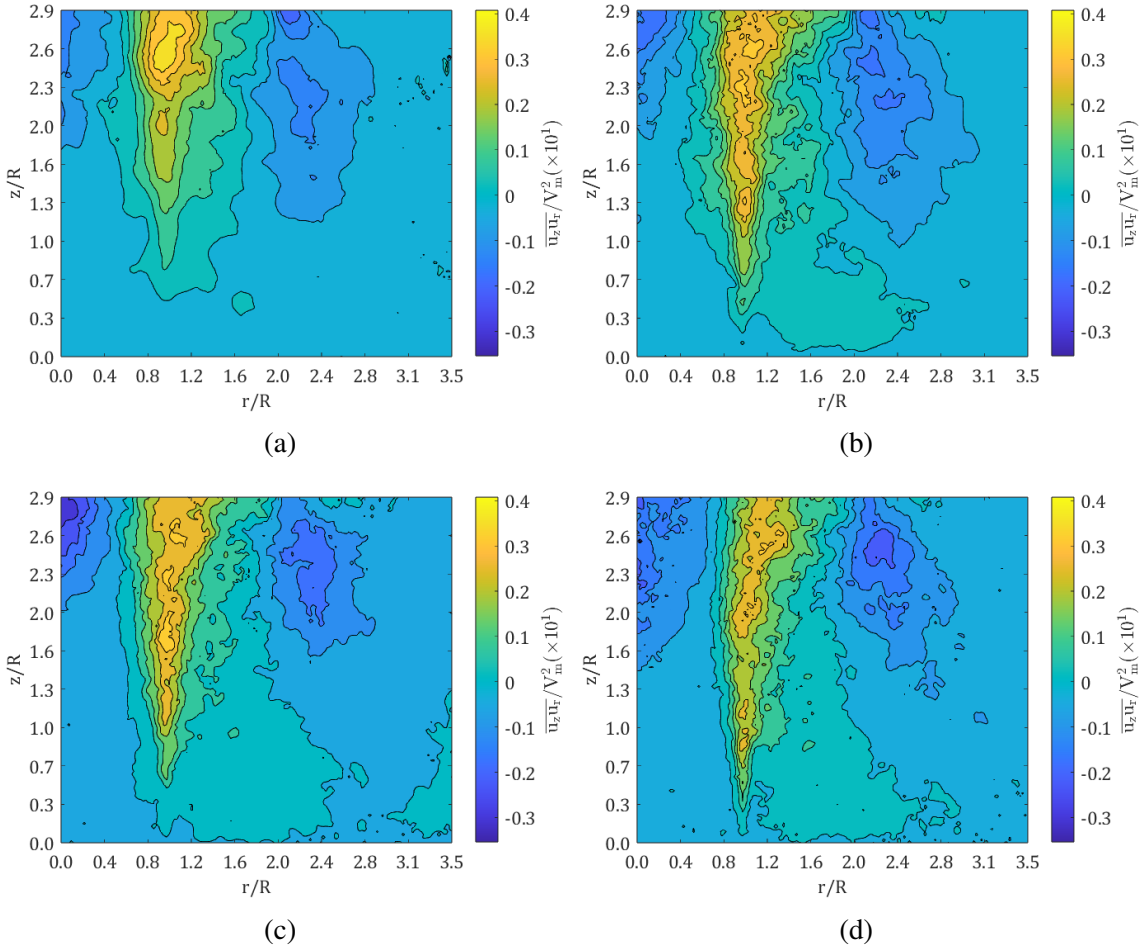

Figure A.7: Contour plots of $\overline{u_z u_r}$ for TR = 0.27 for a) Re = 2,000, b) Re = 7,000, c) Re = 10,000, d) Re = 17,000.

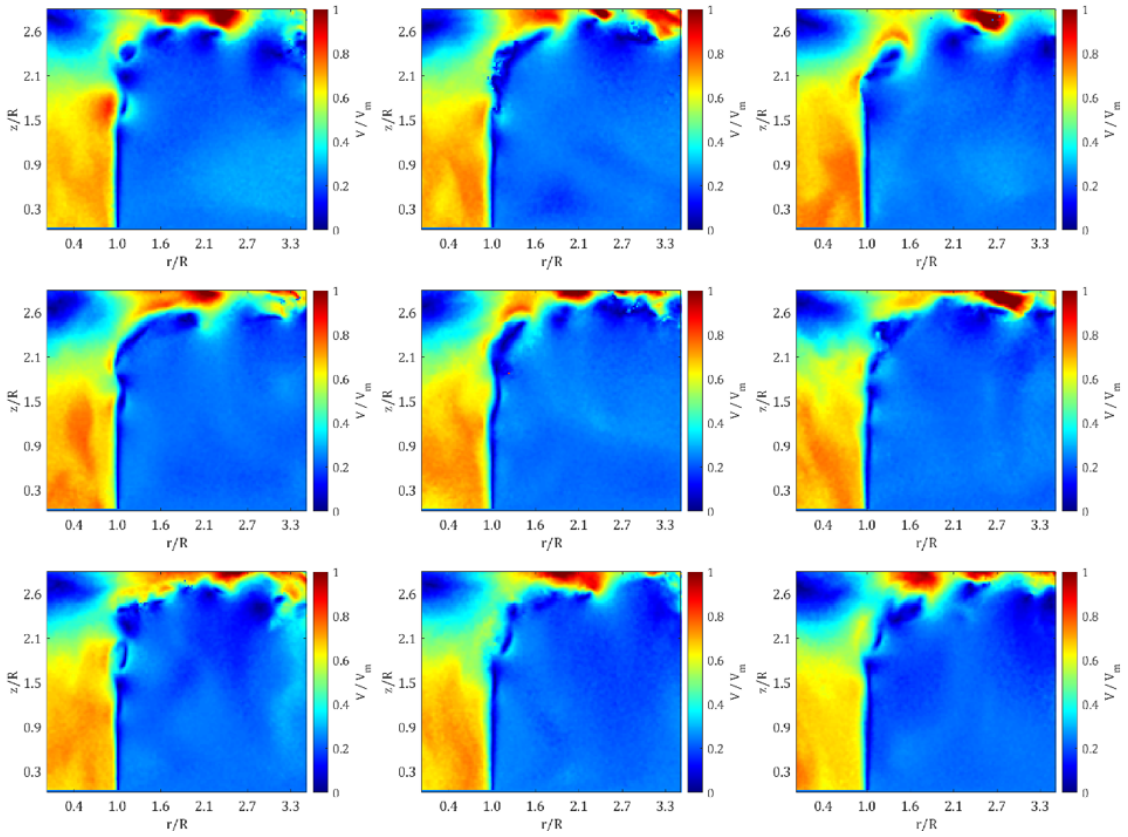

Figure A.8: Instantaneous flow fields for Re = 7,000 flat plate impactor.

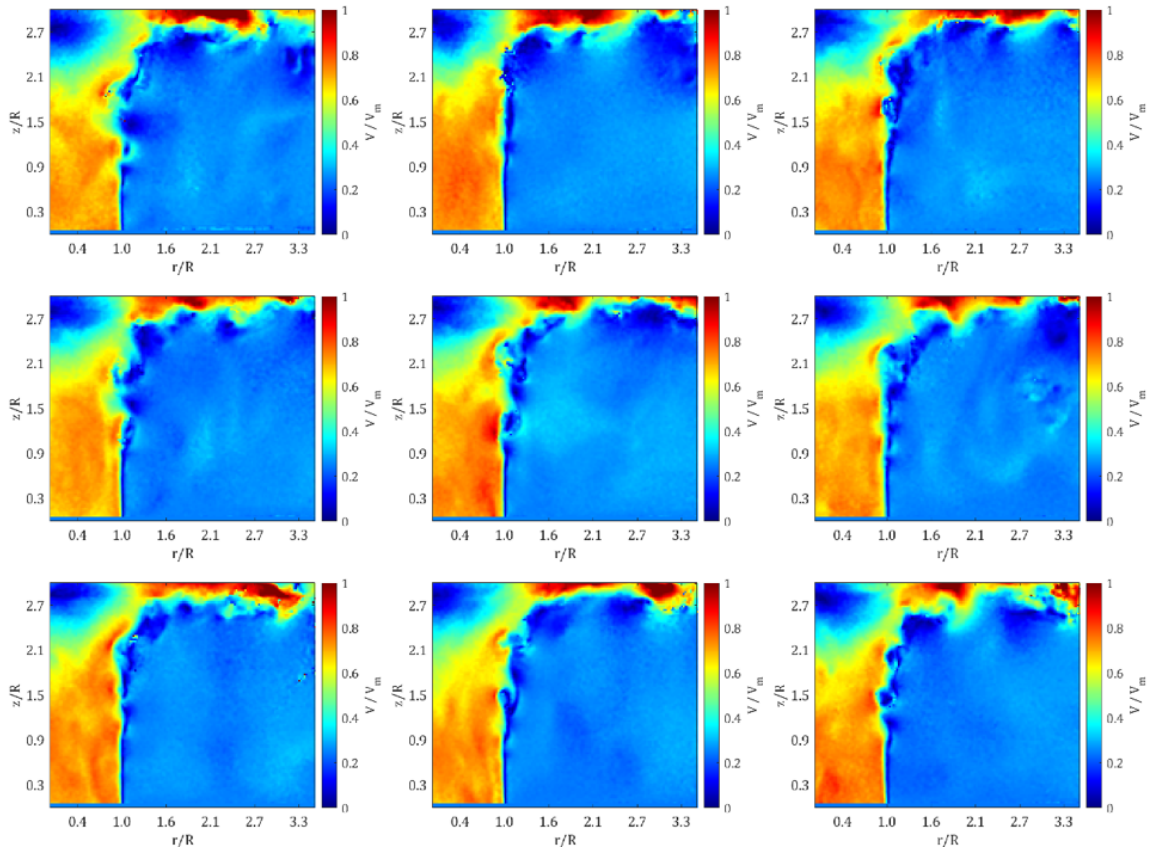

Figure A.9: Instantaneous flow fields for Re = 10,000 flat plate impactor.

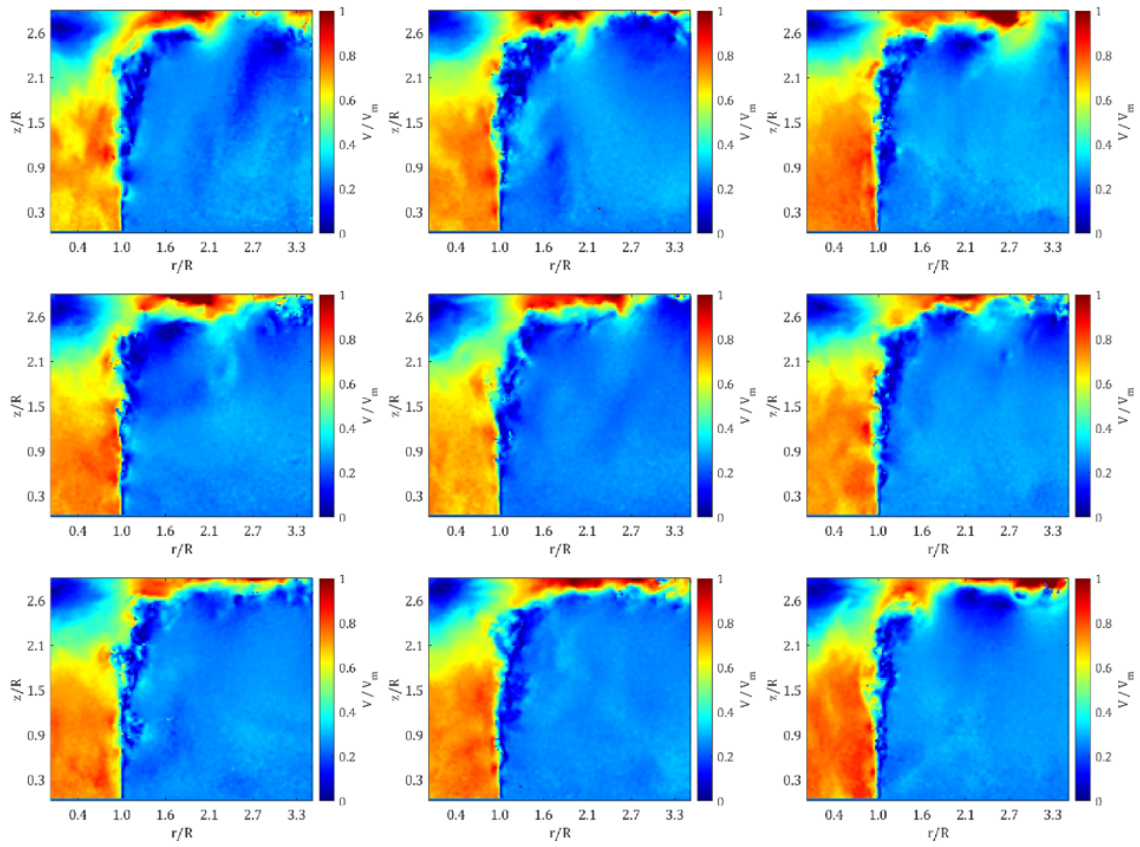

Figure A.10: Instantaneous flow fields for Re = 17,000 flat plate impactor.

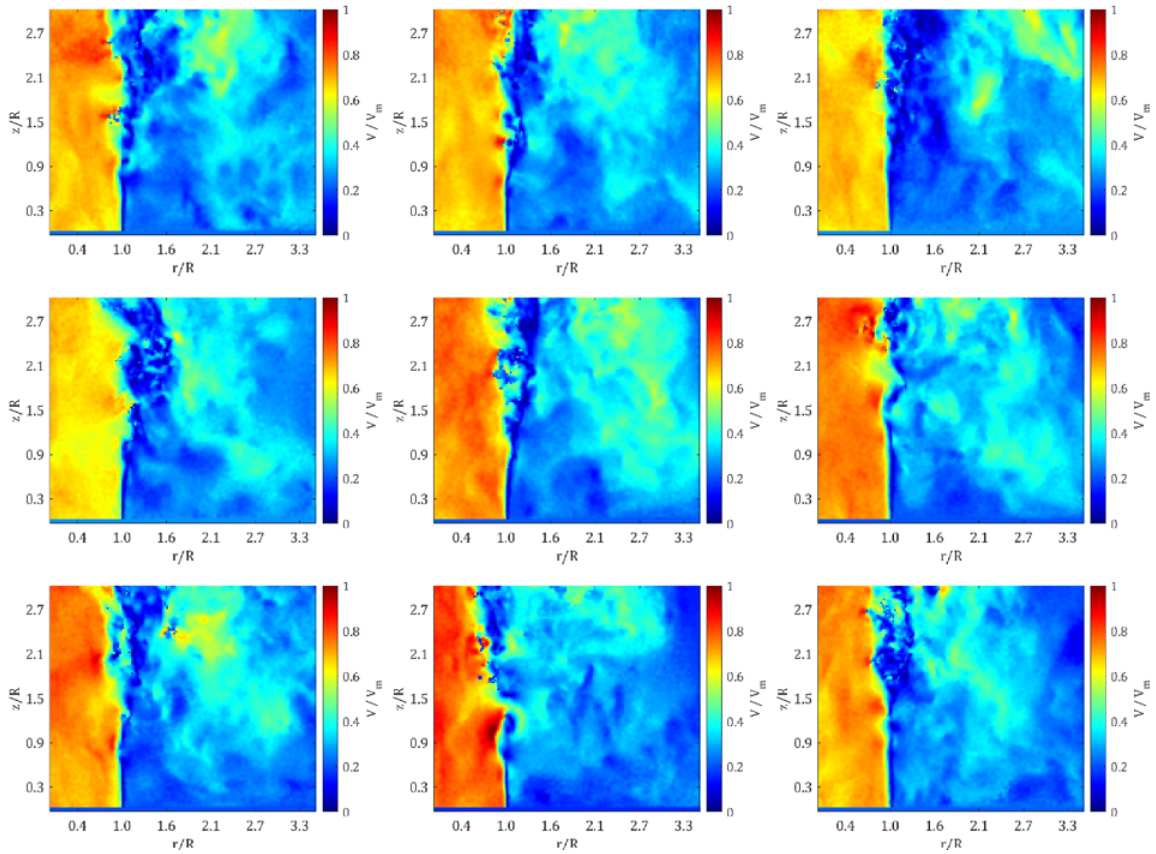

Figure A.11: Instantaneous flow fields for TR = 1.00, Re = 10,000.

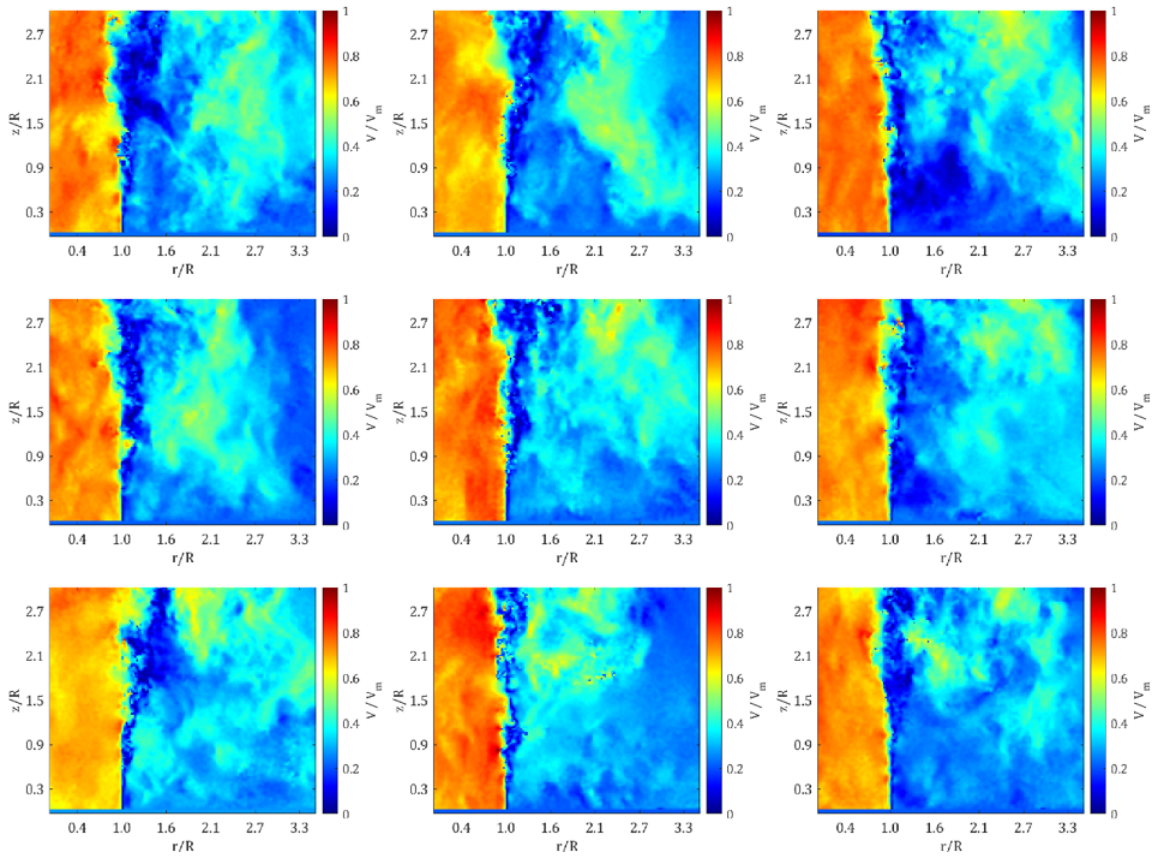

Figure A.12: Instantaneous flow fields for TR = 1.00, Re = 17,000.

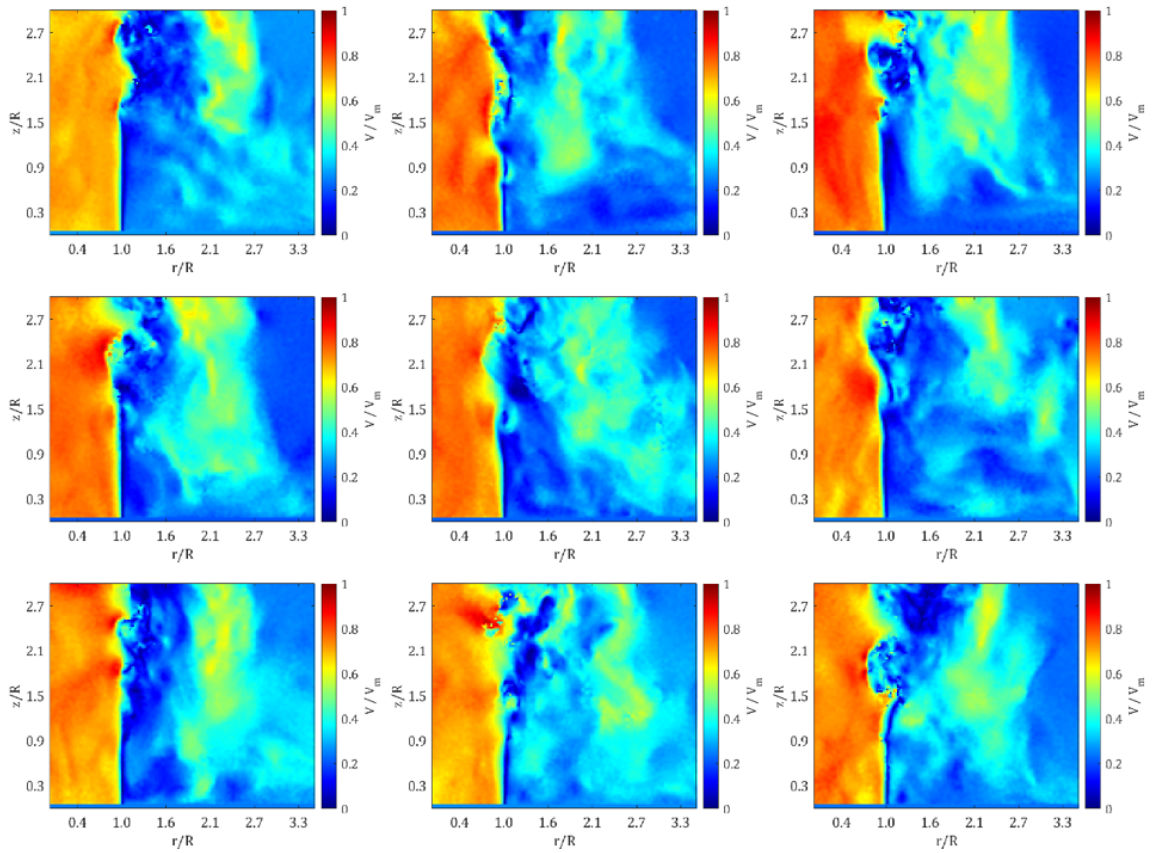

Figure A.13: Instantaneous flow fields for TR = 0.59, Re = 7,000

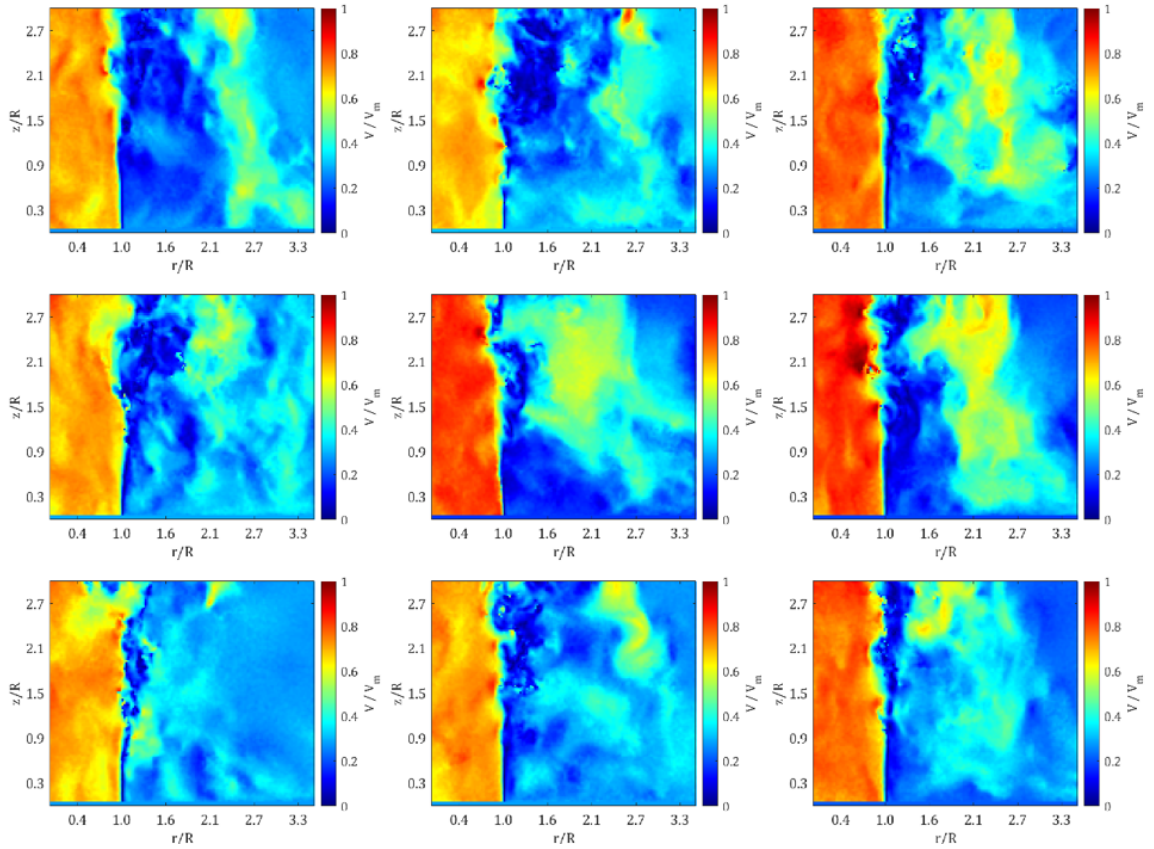

Figure A.14: Instantaneous flow fields for TR = 0.59, Re = 10,000.

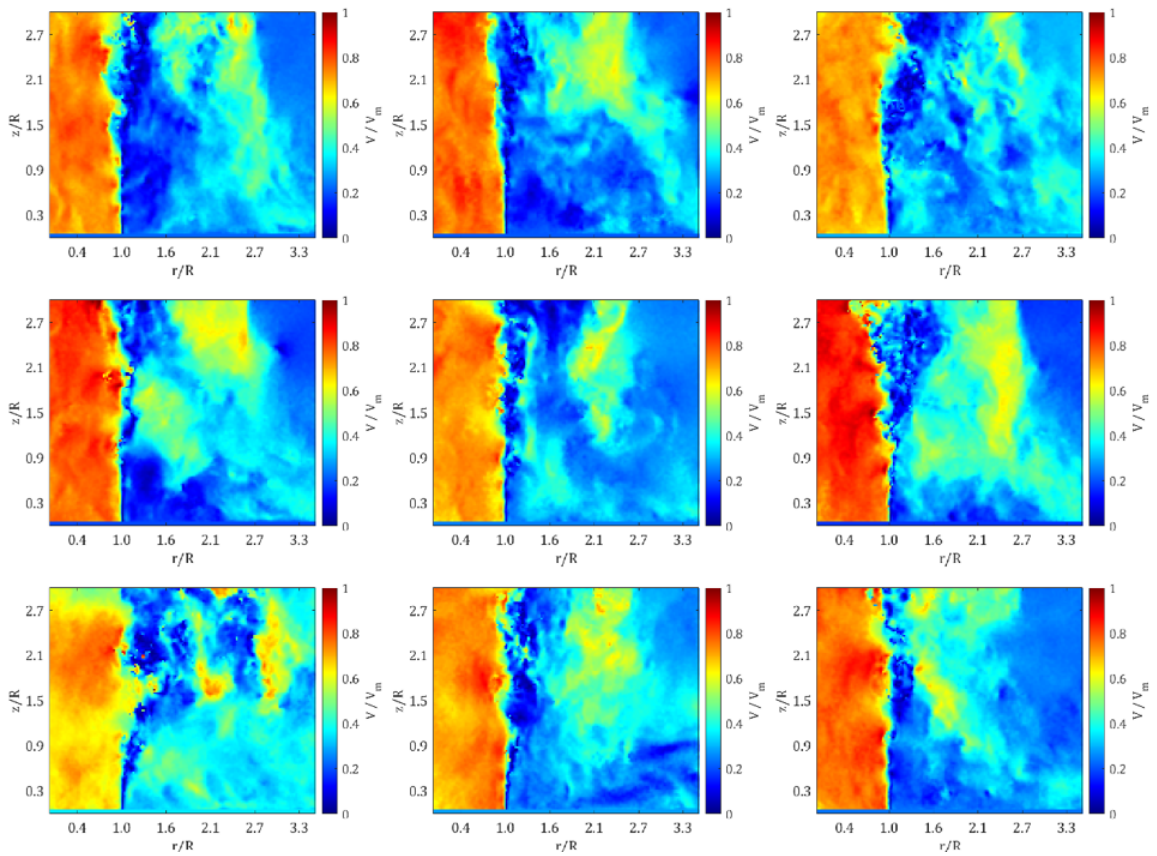

Figure A.15: Instantaneous flow fields for TR = 0.59, Re = 17,000.

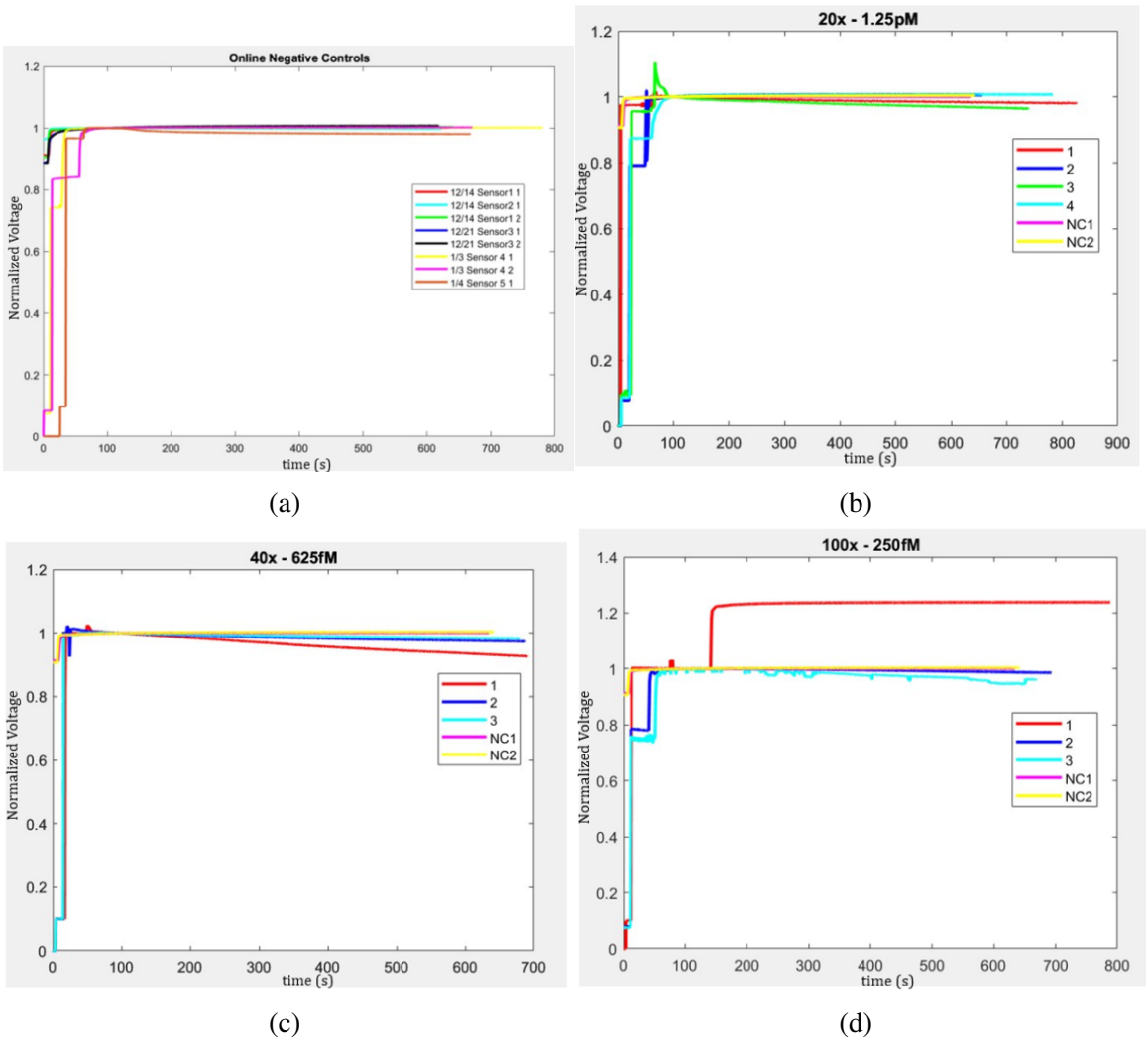

Figure A.16: Real-time voltage output responses for integrated impactor/ nanowell online experiments. a) Negative control (C = 0), b) C = 1.25 pM, c) C = 625 fM, d) C = 250 fM.

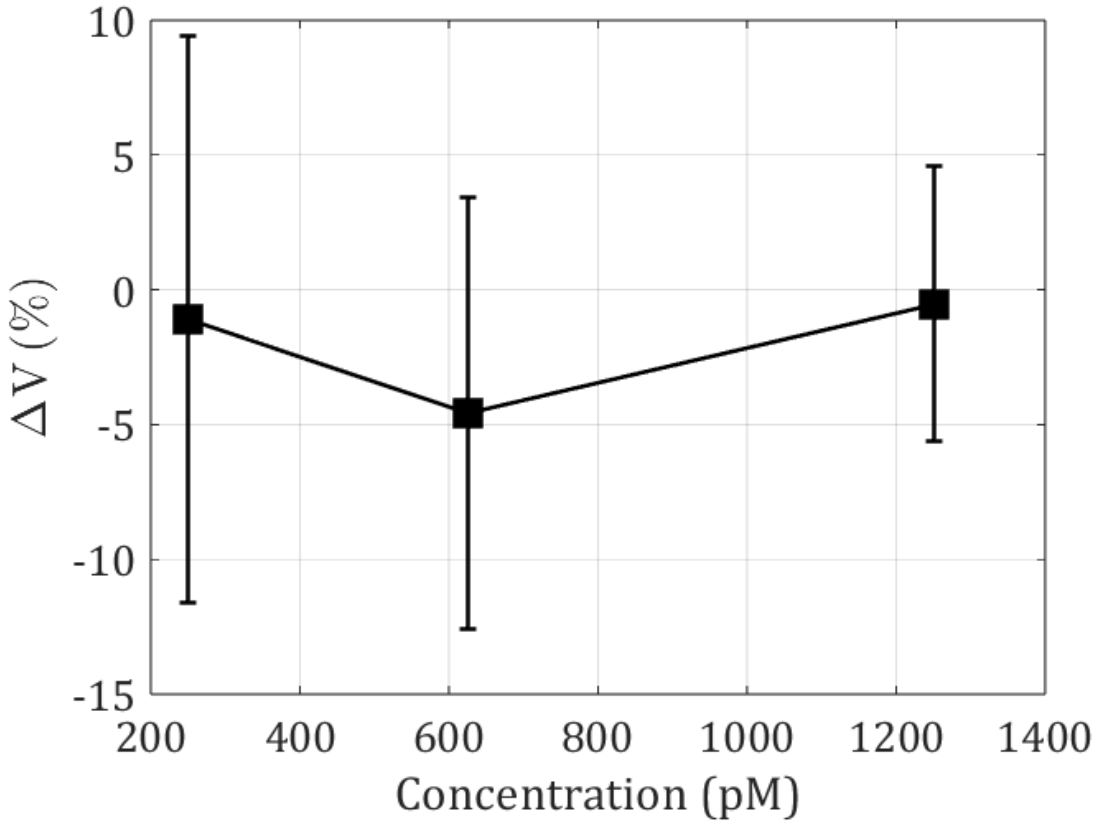

Figure A.17: Titration curve for integrated breathalyzer experiments. Inconsistent results across experiments with at least N = 3 iterations are an area for future work.